Force-displacement response of unreinforced masonry walls for seismic design

THÈSE N^{O} 6462 (2015)

PRÉSENTÉE LE 20 FÉVRIER 2015
À LA FACULTÉ DE L'ENVIRONNEMENT NATUREL, ARCHITECTURAL ET CONSTRUIT
LABORATOIRE DU GÉNIE PARASISMIQUE ET DYNAMIQUE DES STRUCTURES
PROGRAMME DOCTORAL EN GÉNIE CIVIL ET ENVIRONNEMENT

ÉCOLE POLYTECHNIQUE FÉDÉRALE DE LAUSANNE

POUR L'OBTENTION DU GRADE DE DOCTEUR ÈS SCIENCES

PAR

Sarah PETRY

acceptée sur proposition du jury:

Prof. R. Bernier-Latmani, présidente du jury
Prof. K. Beyer, directrice de thèse
Prof. E. Brühwiler, rapporteur
Prof. E. Fehling, rapporteur
Prof. A. Penna, rapporteur

ÉCOLE POLYTECHNIQUE
FÉDÉRALE DE LAUSANNE

Suisse
2015

Don’t only practice your art,
but force your way into it’s secrets,
for it and knowledge can
raise wo-men to the divine.

(adapted from Ludwig van Beethoven)

To my beloved family …
… to Mutti and Bompa,
… to Marc.

Preface

For centuries, unreinforced masonry (URM) has dominated the European built environment for cultural, historical and architectural reasons because it has offered affordable, sustainable and energy efficient building solutions with sufficient fire resistance. URM buildings are, however, also known for being among the most vulnerable structures when subjected to seismic loading and are often responsible for the high death toll after earthquakes.

With her thesis Sarah Petry contributes to the mitigation of seismic risk by developing improved models for predicting the displacement capacity of modern URM buildings. In combination with displacement-based assessment approaches, such models will allow to differentiate buildings that are in need of retrofitting from buildings that do not satisfy code requirements for new buildings but which do not lead to disproportionate risks.

Sarah conducted two test series on URM walls, which set themselves apart from previous tests with regard to the applied boundary conditions, the instrumentation-the entire displacement field was recorded using an optical measurement system-and the fact that all data was made publically available in digital format. Sarah proposes new empirical drift capacity models for URM walls made of clay bricks and also developed an analytical model for predicting the drift capacity of URM walls that fail in flexure. This model yields new insights into parameters that govern the drift capacity and sets the path for our future research projects in this field. For her thesis Sarah was awarded the 2014 Arnold Hendry Postgraduate Project Prize by the International Masonry Society.

Lausanne, December 2014

Katrin Beyer

Acknowledgements

First and foremost, I would like to address my greatest gratitude to my supervisor Prof. Katrin Beyer for always trusting me and my work and for taking the time to listen to my ideas. I admire her unlimited thirst for knowledge with which she often encouraged me to look up things more in depth. This thesis and especially its quality has been only possible thanks to her guidance and her continuous encouragement. Thank you.

I would also like to acknowledge the members of my thesis jury: Prof. R. Bernier-Latmani from the EPFL (president of the jury), Prof. A. Penna from the University of Pavia, Prof. E. Fehling from the University of Kassel and Prof. E. Brühwiler from the EPFL. I was honored by their interesting comments and suggestions on my work as well as by their proposition to nominate me for the EPFL doctorate award. In particular, I would like to acknowledge Prof. A. Penna who followed my work throughout my PhD and gave several times good advices on how to continue.

I thank Morandi Frèrès SA for the donation of the bricks and in particular, Philipp Piguet for all the interest he showed in my research throughout my PhD.

During these past four years, a lot of people contributed to the herein presented work. In particular, I would like to thank the technical staff from the structural laboratory at EPFL, namely Gérald Rouge for his never-stopping ambitions for finding an improved solution, François Perrin on who you could always count, Sylvian Demierre for making a joke in the most desperate moment and also Fréd, Gilles, Patrice and Armin. Without their technical and mental support the experimental part would have been much less fun. In addition, my colleagues Michael Rupf and Pia Hannewald gave me some valuable advices when starting the experiments. Salvatore Marino helped me performing the small-scale wall tests and Nikita and Nicholas helped me during the preparation of the full-scale walls.

This research was carried out at the EESD laboratory and I profitted a lot from the feedback I obtained during group meetings and at other occasions. In specific, I thank João, Panagotios and Prof. Sri for their comments. I thank my two office mates, Pia and Angelica, for all the talks and moments we shared together. Angelica translated also the thesis abstract in Italian and Pia and Maléna helped me with the German and French translation. I thank Marco for reviewing parts of the thesis and for all the collaborations on the CoMa-Wall project. It was a great project to work on. Shenghan and Francesco were the first to try my model and gave me thus immediate feedback on what to improve. I thank them both as well as Georgia and Ovidiu for all the coffee breaks and Raluca and Alessandro for the nice experiences we shared together when discovering new cities during conferences. Finally, I thank Marie-Madeleine and Yvonne for their help with all kind of bureaucratic stuff; often they made life quite easier.

This four years would have been also much less fun without my friends and colleagues outside EESD, without all the runs and hikes with Jürgen, without all the lunch discussions with Filip and Ioannis, without the German talks with Ben and of course, without my Spanish tandem María. Not to forget the famous apple cake competition and all the other things I shared with Maléna, Marie-Rose and the others.

Finally, I dedicate my thesis to my beloved family. I thank Marc, Ria and Winfried for all their unconditional support—especially when it came to correcting my writing—and Michel who put the idea in my head of becoming a civil engineer.

Lausanne, November 2014

Sarah Petry

Abstract

In regions with low to moderate seismicity, unreinforced masonry (URM) is commonly used for the construction of low to mid-rise buildings and a large stock of existing and new residential buildings contains modern URM walls as structural elements. When these structures are subjected to seismic loading, the stiff URM walls attract considerable part of the lateral forces and need therefore to be considered in seismic design and assessment. Nevertheless, the response of URM walls subjected to lateral in-plane loading is not yet fully understood and given estimates for some of the crucial design and assessment parameters are unsatisfactory, e.g. the displacement capacity and the effective stiffness.

This thesis contributes to the improvement of the design and assessment methods for URM wall structures built with modern hollow core clay bricks by several means: First an experimental campaign on the lateral nonlinear in-plane response of URM walls is presented; second, an existing dataset on URM walls is extended and reanalyzed; third, a new mechanical model is developed which describes the full force-displacement response of URM walls developing a significant flexural mode up to Near Collapse.

Two series of URM walls tested under lateral in-plane loading are presented. First series was built at full-scale using a typical Swiss hollow clay brick and a commercially available standard cement-based mortar. Second series represented the same walls at half-scale. During all tests, the walls were subjected to quasi-static cycles of increasing drift demands, while controlling the boundary conditions (axial load and moment restraint at the top of the walls) such to simulate the typical loading of a ground floor wall in an URM building. From the experiments several new insights on the kinematics of URM walls are drawn. For instance, it is identified that once several diagonal cracks develop in the walls, the deformation capacity of the walls is governed by the separation of the rectangular wall into two triangles. From comparison between both test series at different scales, new recommendations for the correct scaling of hollow core masonry are derived and proposed.

In order to compare our own results to wall tests from literature, an existing dataset of URM walls is extended and reanalyzed. Finally, a dataset of 64 quasi-static tests on modern URM walls of different heights and masonry types is presented. The comparison throughout the dataset confirms the influence of the boundary conditions on the drift capacity. Moreover, it reveals the presence of a strong size effect. Hence, an empirical equation is proposed to estimate the ultimate drift capacity while accounting for the boundary conditions and size effect. In order to account for other factors (e.g. load history) a method is proposed on how to adopt the drift capacity from quasi-static cyclic tests in future codes' recommendations.

Throughout the quasi-cyclic tests of all URM walls, the deformations were recorded using a digital photogrammetric measurement system tracking the displacement field of the walls. This measurement was synchronized with the force measurement such that global and local engineering demand parameters of the walls could be linked. This point was crucial for the following contributions of this thesis: (i) proposition of two sets of limit states (LSs) that link local damage states to characteristic points of the global force-displacement curve of URM walls; (ii) the study of different deformation parameters for the validation of mechanical and numerical models at local level.

Based on these findings, a new mechanical model is proposed which describes the nonlinear force-displacement response of flexural dominated URM walls up to Near Collapse. The model is developed in two steps. First, an analytical part is derived based on the plane section hypothesis and a non-tension material with a linear-elastic constitutive material law in compression. It assumes that only the compressed part of the wall contributes to the wall resistance and accounts for a softening due to the reduction of the effective area. In a second step, new criteria are developed which predict the occurrence of the previous proposed local LSs, which are then incorporated in the analytical model. The new complete model links local performance levels to global displacement capacities of modern URM walls developing a significant flexural mode. The model is validated through the comparison with results from own and others' wall tests yielding to good estimates for the effective stiffness and the displacement capacity of in-plane loaded URM walls.

Keywords:

Unreinforced masonry; Small-scale testing; Seismic design; Displacement capacity; Effective stiffness; Quasi-static cyclic testing.

Résumé

Dans les régions avec une sismicité faible à moyenne, la maçonnerie non-armée est couramment utilisée pour la construction des bâtiments de basse à moyenne hauteur et une grande part des constructions nouvelles et existantes contiennent cet élément structural. Quand ce type de structure est sollicité par un chargement sismique, les murs en maçonnerie rigides reprennent une grande partie des charges horizontales et ils ne peuvent pas être négligés lors de la conception ou de l'évaluation du bâtiment. Pourtant, le comportement des murs en maçonnerie non-armée soumis à des charges latérales dans le plan n'est pas encore complètement compris et les valeurs recommandées pour certains paramètres essentiels pour la conception et l'évaluation sont non-satisfaisants, par exemple la capacité de déplacement et la rigidité effective.

Cette thèse contribue à l'amélioration des méthodes de conception et d'évaluation des structures contenant des murs construits avec des briques creuses en terre cuite. Premièrement, une campagne d'essais sur des murs en maçonnerie est présentée. Deuxièmement, une base de données sur des murs en maçonnerie non-armée est étendue et analysée de nouveau. Troisièmement, un nouveau modèle mécanique est élaboré. Ce dernier estime la courbe complète force-déplacement jusqu'à l'état limite correspondant à la quasi-rupture pour des murs développant un mode de rupture par flexion.

Deux séries d'essais sur des murs en maçonnerie non-armée soumis à des charges latérales dans le plan sont présentées. La première série d'essais porte sur des murs construits à l'échelle en utilisant des briques creuses en terre cuite courantes en Suisse et un mortier standard à base de ciment. La deuxième série est identique à la première, mais avec des dimensions réduites de moitié (demi-échelle). Durant tous les essais, les murs ont été soumis à des cycles de déplacement quasi-statiques d'amplitude croissante et les conditions aux limites (charge axiale et moment de torsion en haut du mur) étaient contrôlées. Ces dernières ont été choisies afin d'être représentatives du chargement d'un mur situé au rez-de-chaussée d'un bâtiment en maçonnerie typique. Les résultats d'essais permettent de tirer différentes conclusions sur la cinématique d'un mur en maçonnerie soumis à des charges latérales. Par exemple, il a été identifié que lorsque plusieurs fissures diagonales s'ouvrent, la capacité de déformation est déterminée par la séparation du mur rectangulaire en deux triangles. Par la comparaison des deux séries d'essais réalisées à différentes échelles, de nouvelles recommandations pour l'usage de spécimen à échelle réduite sont élaborées et proposées.

Afin de comparer nos résultats avec d'autres essais de la littérature, une base de données existante est étendue et analysée de nouveau. La nouvelle base de données contient 64 essais quasi-statiques sur des murs en maçonnerie moderne construits à des hauteurs et avec des briques différentes. L'analyse de la base de données confirme l'importance des conditions aux limites sur la capacité de déplacement et révèle aussi l'influence de l'effet de taille. Suite à cela, une nouvelle équation empirique est proposée pour estimer la capacité ultime de déformation en fonction des conditions aux limites et des effets de taille. Afin de traduire la capacité de déformation extraite des essais quasi-statiques cycliques en recommandations à adopter dans les futures générations de codes, il est également proposé de prendre d'autres facteurs en considération, tel que l'historique de chargement.

Pendant tous les essais quasi-statiques un système photogrammétrique numérique a mesuré le champ de déplacement des murs. Ces mesures ont été synchronisées avec les mesures de forces créant un lien entre les déformations locales et les paramètres globaux. Ce point a été déterminant pour les contributions suivantes de cette thèse : (i) proposition de deux groupes d’état limite qui lient l’état de fissuration locale à des points caractéristiques de la courbe globale force-déplacement d’un mur en maçonnerie non-armée ; (ii) l’étude de différents paramètres de déformation pour la validation locale du modèle mécanique et numérique.

Basé sur ces résultats, un nouveau modèle mécanique est proposé, lequel décrit la relation force-déplacement non-linéaire jusqu’à l’occurrence de l’état limite de quasi-rupture. Ce modèle est développé en deux pas. Premièrement, une équation analytique est dérivée, laquelle est basée sur l’hypothèse de section plane et sur un matériau avec une résistance à la traction négligeable et un comportement linéaire en compression. Le modèle considère que seule la partie du mur en compression contribue à la résistance et modélise la réduction de la rigidité due à la réduction de la surface effective. Deuxièmement, de nouveaux critères liés à l’occurrence des états limites locaux proposées précédemment sont incorporés dans l’équation analytique. Le nouveau modèle lie les niveaux de performance locale à la capacité de déplacement globale pour des murs développant un mode de rupture par flexion. Le modèle est validé par la comparaison entre les résultats de nos propres essais et les essais d’autres. Il est démontré que le modèle estime bien la rigidité effective et la capacité de déplacement des murs sollicités dans le plan.

Mots clés :

Maçonnerie non-armée ; Essais à échelle réduite ; Conception parasismique ; Capacité de déplacement ; Rigidité effective ; Essais quasi-statiques cycliques.

Kurzfassung

In Regionen mit geringer bis moderater Erdbebengefährdung wird oft modernes, unbewehrtes Mauerwerk für den Bau von kleinen bis mittelgrossen Gebäuden verwendet und ein grosser Anteil der bestehenden und neugebauten Wohnhäuser enhält unbewehrte Mauerwerkswände als Tragelemente. Wenn diese Gebäude unter Erdbebenlasten stehen, ziehen die Mauerwerkswände aufgrund ihrer Steifigkeit einen beträchtlichen Teil der Horizontallasten an und müssen daher im Tragnachweis berücksichtigt werden. Das Last-Verschiebungsverhalten von Mauerwerkswänden unter Horizontallasten parallel zur Ebene ist allerdings nicht vollkommen erfasst und manche der physikalischen Grössen, welche für den Tragnachweis erforderlich sind, sind nur mit unzureichender Genauigkeit bekannt (z. Bsp. die Verformungskapazität oder die effektive Anfangssteifigkeit von Mauerwerkswänden).

Diese Arbeit trägt zu einem verbesserten Erdbebennachweis von Mauerwerkstragwerken aus modernen Ziegelsteinen in mehrerer Hinsicht bei: zuerst werden zwei Serien von Wandversuchen zum nichtlinearen Verhalten in der Ebene vorgestellt; als Nächstes wird anhand einer Literaturrecherche eine bestehende Datenbank für Versuche an Mauerwerkswänden neu aufgegriffen und durch weitere Versuche ergänzt; als Letztes wird ein mechanisches Modell entwickelt, welches das Last-Verschiebungsverhalten von Mauerwerkswänden bis zum Punkt ”erheblicher Horizontallastabfall” erfasst.

Im Rahmen dieser Doktorarbeit wurden zwei Serien von Wandversuchen zum Last- Verschiebungsverhalten von Mauerwerkswänden unter Horizontallasten parallel zur Ebene durchgeführt. Für den Bau der Wände der ersten Testreihe wurde ein typischer Schweizer Hochlochziegel und ein kommerziel erhältlicher Zementmörtel verwendet. Die Wände der zweiten Testreihe entsprachen denen der Ersten mit dem Unterschied, dass sie im halben Maßstab gebaut wurden. Während der Versuche wurden die Wände quasi-statischen Verformungszyklen ausgesetzt und die Amplituden der Zyklen nach und nach gesteigert. Die vertikale Auflast und das aufgebrachte Moment wurden dabei stets kontrolliert, so dass die Randbedingungen denen entsprachen, die für eine Erdgeschosswand eines realen Gebäudes zu erwarten sind. Aus den Versuchen wurden einige neue Erkenntnisse zur Kinematik von Mauerwerkswänden gewonnen. Zum Beispiel wurde erkannt, dass sich die rechteckigen Wände nach dem Auftreten erster Diagonalrisse in zwei Dreiecke teilen, welche daraufhin das Verformungsverhalten der Wände bestimmen. Der Vergleich der zwei Testreihen untereinander lieferte zusätzlich Erkenntnisse zu den Skalierungseffekten. Darauf basierend werden neue Empfehlungen zur bestmöglichen Skalierung von Mauerwerk gegeben.

Um unsere eigenen Experimente mit Anderen zu vergleichen, wird eine bestehende Datenbasis aufgegriffen und mit anderen Wandversuchen ausgeweitet. Daraus entsteht eine Datenbank mit 64 Mauerwerkswänden, welche alle aus unterschiedlichen modernen Ziegeln gebaut wurden. Der Vergleich der unterschiedlichen Wandversuche bestätigt den Einfluss der aufgebrachten Randbedingungen auf die Verformungskapazität. Zusätzlich wird ersichtlich, dass auch die Grösse der Probekörper einen starken Einfluss hat. Basierend auf diesen Erkenntnissen, wird eine neue empirische Formel vorgeschlagen, welche den Einfluss von Randbedingungen und Grösse der Wände berücksichtigt. Um andere maßgebende Faktoren miteinzubeziehen (z. Bsp. Belastungsgeschichte), wird vorgeschlagen, wie die Verformungskapazität von zyklischen Wandversuchen in Empfehlungen zukünftiger Regelwerke übernommen werden könnte.

Während der quasi-statischen Wandversuche wurde das Verschiebungsfeld der Wände kontinuierlich mit digitalen fotogrammetrischen Messkammern aufgenommen. Diese Messungen wurden mit den Kraftmessgebern synchronisiert, so dass eine Verbindung zwischen globalen und lokalen physikalischen Grössen geschaffen wurde. Diese lokalen Messungen waren entscheidend für folgende zwei Beiträge dieser Arbeit: (1) Vorschlag zweier Sätze lokaler Grenzzustände, welche charakteristische Punkte der globalen Last-Verschiebungskurve von Mauerwerkswänden auf lokale Schadensgrade zurückführen; (2) Ermittlung lokaler Verformungsgrössen welche für die Bewertung mechanischer und numerischer Modelle geignet sind.

Basierend auf diesen Erkenntnissen, wird ein neuartiges mechanisches Modell entwickelt, welches das Last-Verschiebungsverhalten von Mauerwerkswänden unter Biegeverformunegn bis zum erheblichen Horizontallastabfall vorhersagt. Das Modell wird in zwei Schritten entwickelt. Zuerst wird ein analytischer Ansatz hergeleitet, welcher das Ebenbleiben der Querschnitte, vernachlässigbarer Zugwiderstand und linear-elastisches Materialverhalten auf Druck vorrausetzt. Es basiert somit auf der Annahme, dass nur der komprimierte Teil der Wand zum Widerstand beiträgt und berücksicht den Abfall der Steifigkeit wenn sich die mitwirkende Fläche reduziert. In einem zweiten Schritt werden basierend auf zuvor vorgeschlagenen lokalen Grenzzuständen, neue Bruchkriterien entwickelt, die in den analytischen Ansatz zu einem kompletten mechanischen Modell eingebaut werden. Das Modell wird mit den Ergebnissen unserer eigenen Testserie und anderen Wandversuchen aus der Literatur verglichen die auf Biegung versagten. Es zeigt sich, dass das Modell gute Vorhersagen für die Verschiebungskapazität und effektive Anfangssteifigkeit von Mauerwerkswänden erzielt werden, wenn diese hauptsächlich unter Biegung belastet werden.

Schlagworte:

Unbewehrtes Mauerwerk; Experimentieren im reduzierten Maßstab; Erdbebenbemessung; Verformungskapazität; Anfangssteifigkeit; Quasi-statisch zyklische Versuche;

Riassunto

La muratura non armata, in regioni a bassa e moderata sismicità, è comunemente utilizzata per la costruzione di edifici di bassa o media altezza e in un grande numero di edifici esistenti la struttura portante è costituita di pareti in muratura non armata. Quando queste strutture sono soggette ad azione sismica, le pareti in muratura non armata assorbono la maggior parte della forza orizzontale e pertanto devono essere tenute in considerazione nella fase di progettazione e riqualificazione sismica dell'edificio. Nonostante ciò, il comportamento delle pareti in muratura non armata soggette ad azioni nel piano non è ancora del tutto definito e i valori prescritti per alcuni parametri fondamentali nella progettazione e nella riqualificazione, quali ad esempio la capacità di spostamento e la rigidezza effettiva, non sono del tutto soddisfacenti. Questa tesi vuole essere un contributo al miglioramento dei metodi di progettazione e riqualificazione delle strutture che presentano muri costituiti da tipici mattoni forati e comune malta cementizia. Inizialmente viene presentata una campagna sperimentale sulla risposta non lineare nel piano di pareti in muratura non armata; successivamente è stata esaminata e rianalizzata una raccolta di dati sperimentali su test di pareti in muratura non armata effettuati in passato; infine, viene sviluppato un nuovo modello meccanico capace di descrivere la risposta completa in termini di forza-spostamento delle pareti in muratura non armata che presentano a collasso un marcato comportamento flessionale.

Inizialmente vengono presentate due serie di test sperimentali di pareti realizzate in muratura non armata e testate sotto l'azione di un carico nel proprio piano. La prima serie è composta da muri a grandezza naturale costruiti con i tipici mattoni forati svizzeri e comune malta cementizia. La seconda è costituita dagli stessi muri, ma realizzati in scala 1:2. Durante i test i muri sono stati soggetti a carichi ciclici quasi-statici, incrementando il drift imposto e mantenendo controllate le condizioni al contorno (carico assiale e momento alla sommità del muro), in modo da simulare le condizioni di vincolo tipiche di una parete in muratura non armata situata al piano terra di un edificio. Dai risultati sperimentali si è ottenuta una maggiore comprensione del comportamento cinematico delle pareti in muratura non armata. Ad esempio, è stato osservato che quando molteplici fessure diagonali si sviluppano nel muro, la capacità di deformazione è governata dalla separazione della parete rettangolare in due singoli elementi triangolari. Dal confronto dei risultati sperimentali dei provini costruiti a a diversa scala sono state sviluppate e proposte nuove raccomandazioni per l'esecuzione di test a scala ridotta.

Al fine di confrontare i risultati dei test da noi realizzati con altri presenti in letteratura, un dataset esistente riguardante esperimenti su pareti in muratura non armata è stato rianalizzato ed esteso. Al termine di questo lavoro è stato ottenuto un dataset composto da 64 test quasi-statici su pareti in muratura non armata di differente altezza e diversa tipologia di muratura. Dall'analisi dei risultati contenuti nel dataset è stato confermato come le condizioni al contorno influenzino la capacità di spostamento. Inoltre è stata osservata l'importanza dell'effetto di scala. Pertanto, viene proposta un'equazione per la valutazione della capacità ultima di sposamento che prende in considerazione sia l'effetto di diverse condizioni al contorno che l'effetto di scala. Inoltre, è stato sviluppato un metodo che permette di tenere in considerazione altri fattori, quali ad esempio la storia di carico, per definire la capacità di spostamento partendo dai risultati dei test ciclici quasi-statici e che potrà essere implementato in future norme e codici.

Durante i test ciclici delle pareti in muratura non armata, le deformazioni dei muri sono state registrate utilizzando un sistema di fotogrammetria digitale in grado di registrare l'intero campo di spostamento del muro nel corso dell‘esperimento. Questo sistema di misura è stato sincronizzato con il sistema di misurazione della forza applicata, in modo da correlare parametri locali e globali. Questo punto è stato di cruciale importanza nello sviluppo dei seguenti contributi della tesi: (i) formulazione di due serie di stati limite in grado di correlare lo stato di danneggiamento locale con alcuni punti caratteristici della curva di risposta forza-spostamento delle pareti in muratura non armata; (ii) studio di differenti parametri di deformazione per la validazione di modelli meccanici e numerici a livello locale.

Basandosi sui risultati ottenuti, un nuovo modello meccanico è stato proposto per descrivere la risposta non lineare forza-spostamento di pareti in muratura non armata che presentano un comportamento flessionale a collasso. Il modello è stato sviluppato in due fasi: inizialmente è stata derivata un‘equazione analitica basata sull‘ipotesi di conservazione delle sezioni piane e assumendo un materiale non resistente a trazione con legge costitutiva lineare-elastica a compressione. Inoltre è stato ipotizzato che solo la parte in compressione del muro contribuisca alla resistenza, tenendo conto di un effetto di softening dovuto alla riduzione dell’area effetiva. Nella seconda fase, sono stati derivati nuovi criteri in grado di predire l’occorrenza di uno degli stati limite locali precedentemente proposti; tali criteri sono poi stati implementati nel modello analitico. Il modello finale così ottenuto lega le deformazioni a livello locale con la capacità di spostamento globale per pareti in muratura non armata che presentano un marcato comportamento flessionale. Questo modello è stato validato utilizzando i risultati dei nostri test e di altri in letteratura, ottenendo buoni risultati per la stima della rigidezza effettiva e della capacità di spostamento di pareti in muratura non armata caricate nel proprio piano.

Parole chiave:

Muratura non armata; Esperimenti a scala ridotta; Progettazione sismica; Capacità di spostamento; Rigidezza effettiva; Esperimenti sotto carichi ciclici quasi-statici.

Contents

Introduction

1 Motivation and scope

Unreinforced masonry (URM) is one of the oldest types of construction used by humans and the term URM stands nowadays for many different kinds of masonry typologies (as shown in Fig. 1). Despite its popularity and continued use, URM buildings are still among the most vulnerable building classes when subjected to seismic loading. Most likely because they were treated as non-engineered structures for a long time, their seismic behavior is not yet fully understood and scientists and practicing engineers demand more research to improve the seismic design and assessment of these structures [Abr01, Mag06, PLBL11, BP$^+$14].

The continued use of URM results from its numerous advantages: good acoustical and thermal insulation properties, ease of construction, durability, sustainability, good fire resistance, etc. [Mag06]. For instance, in Switzerland, 35 to 40% of new residential buildings constructed between 2005 and 2012 comprise URM structural elements [SBV12]. Despite these advantages, the use of URM for new constructions has slowly decreased over the last decades [SBV12]. In Switzerland—a country with low to moderate seismicity—an important reason for the decrease of use of URM has been the introduction of the seismic verification rules in design codes. First generations of seismic codes included only force-based (FB) methods, which are based on elastic analysis and a force reduction factor q that accounts in an approximate manner for overstrength and inelastic deformation capacity. FB methods are thus not well suited for capturing the nonlinear behavior of structures under seismic loading and tend to be rather conservative [PCK07]. This can be quite undesirable in particular for the assessment of existing structures [Mag06]. As an alternative to FB methods, displacement-based (DB) methods have been developed. These methods account directly for the nonlinear behavior of a structure [PCK07] and lead usually to less conservative results than FB methods [Mag06]. In particular for the assessment of existing structures, DB methods are better suited as they allow to distinguish more accurately between buildings that need to be retrofitted to meet minimum safety standards and buildings that might not be conform to today's building standards but are expected to display an acceptable seismic performance. This is important since the financial means of a society that can be spent on retrofitting existing buildings are limited. Therefore, DB should be put forward also from a socio-economic point of view.

This thesis focuses on the improvement of seismic design and assessment methods for modern URM buildings assembled with hollow clay bricks and standard cement mortar as shown in Fig. 2.

Figure 1. Examples of different masonry structures: (a) Porta Nigra in Trier, Germany built probably in the 2nd century (courtesy of Kolja Schulin), (b) masonry bridge nearby Domodossola, Italy (date of construction unknown), (c) stone columns inside Sagrada Familia in Barcelona, Spain begin of construction in the 19th century and (d) residential Trulli nearby Alberobello, Italy built in the traditional way in the 21st century

Figure 2. (a) Brick used for the construction of the wall tests, (b) walls in construction in the laboratory before painting and (c) typical Swiss residential building with modern clay URM walls and RC slabs

In masonry buildings, two modes of damage generally occur during an earthquake [Mag06]:

- The *first damage mode* mainly involves out-of-plane failure of single walls or parapets. Even though it can also involve a whole overturning of a building facade, in modern URM buildings with RC slabs the mechanism takes place mostly locally and is thus referred to as *local collapse mechanism.*
- The *second damage mode* occurs as in-plane failure of the walls, parapets, piers and spandrels. This mechanism activates the global resistance of the structure and can only develop when the first damage mode is avoided. Accordingly, it is referred to as *global collapse mechanism.*

Despite the fact that a complete seismic design or assessment of an URM building implies the verification of both failure modes, only the in-plane failure of URM walls is addressed in this thesis.

URM buildings are often relatively regular in plan and elevation and their seismic behavior is typically studied by means of 2D wall structures parallel to the two main directions of the building, as illustrated in Fig. 3. The 2D wall structures are often analyzed by means of equivalent frame models, e.g. [LP$^+$13]. In these frame models the walls are represented as vertical elements and the spandrels and slabs as horizontal elements. Each wall element extends over the height of one story. In external walls the effective wall height can be reduced due to the presence of spandrels and lintels (see Fig. 3). To compute the force-displacement response of the entire structure, detailed knowledge on the force-displacement response of each vertical and horizontal element is required. This thesis makes a contribution to the force-displacement response of the wall elements. To this purpose, in particular the wall elements of the ground floor will be studied. These wall elements are subjected to the highest shear forces and are therefore also often the first vertical elements to fail [Tom99].

In case of modern URM structures, masonry walls are often combined with reinforced concrete (RC) slabs. The in-plane stiffness and strength of these RC-slabs is considerable. Thus, when considering a building with regular floor plan, where torsional effects are relatively low, it can be assumed that the RC slabs impose an equal-displacement to all walls of one story [Mag06, LV13]. The out-of-plane stiffness and strength of slabs can vary significantly between building typologies and three levels of coupling are distinguished in the literature [Lan02, Oro11]: (a) weak coupling where the horizontal elements impose only equal displacements at

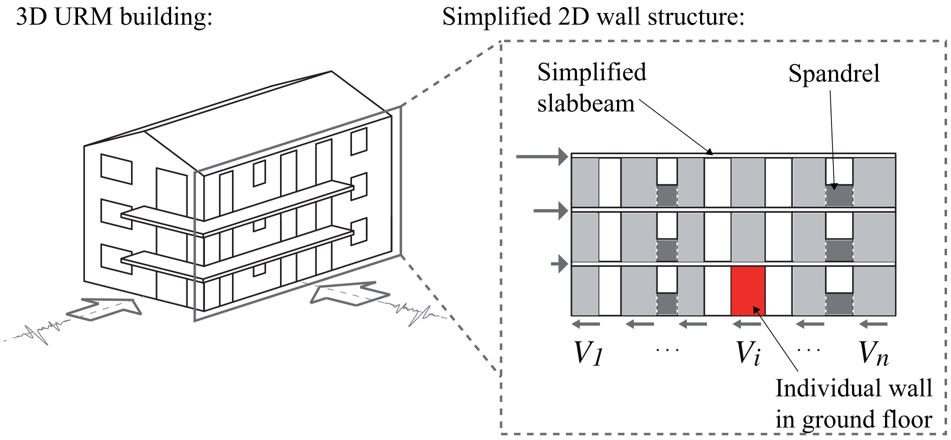

Figure 3. Simplified 2D evaluation for 3D an URM building

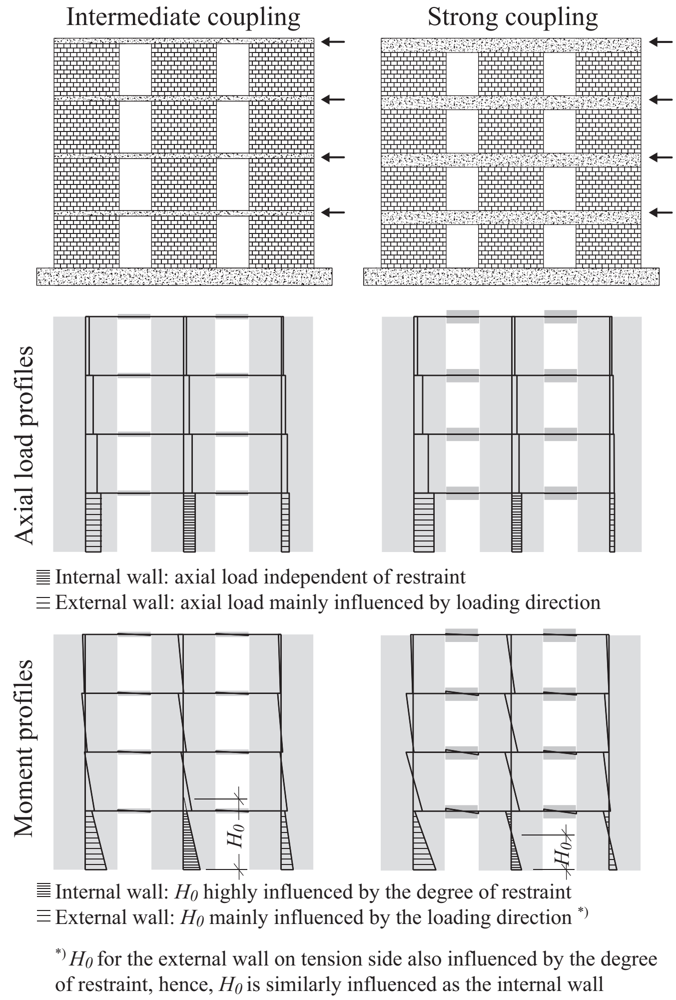

Figure 4 Results from a pushover analysis using the macro-element software Tremuri [LP$^+$13, PLG14] on URM wall structures with intermediate coupling (left) and strong coupling (right) [PB14]

the story levels but do not transfer significant shear forces or bending moments, (b) strong coupling where vertical and horizontal elements develop together a strong framing action and (c) intermediate coupling. For modern URM buildings with RC-slabs, intermediate to strong coupling can be expected resulting in shear spans of the first story walls that often vary between 0.5-1.5 H, where H is the story height (see Fig. 4). The global in-plane response of 2D equivalent frame models as shown in Fig. 3 is composed by the nonlinear response of all URM walls of the ground floor (see Fig. 5), e.g. [Tom99]. Their boundary conditions at the top depend on the walls of the upper storys and the horizontal elements (e.g. slabs and spandrels).

The aim of this thesis is to contribute to this understanding of the nonlinear behavior of an individual URM wall of the ground floor as highlighted in Fig. 3. More specifically, the thesis will focus on the deformation capacity of the URM walls, which are assembled with modern hollow clay bricks and standard cement mortar and which have mortar joints of approximately 1 cm thickness (see Fig. 2). In Section 2 of this introductory chapter, the seismicity in Switzerland is explained. The basic concepts of seismic design and assessment are introduced including the particularities of modern URM structures and walls. The specific objectives of this thesis are explained in Section 3 and the methodology applied to reach them in Section 4. The organization of the thesis is finally outlined in Section 5.

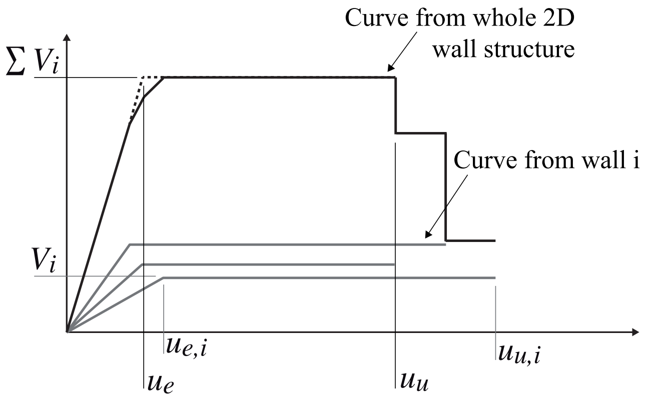

Figure 5 Force-displacement curve for a 2D wall structure obtained from the sum of the capacity of the individual walls

2 Problem statement

2.1 Switzerland, an example for a region of low to moderate seismicity

In the seismic engineering community, URM structures are believed to offer poor performance under earthquake loads [Mag06, LV13]. This idea originated several centuries ago when heavy earthquakes struck densely populated regions destroying large parts of the existing masonry building stock, e.g. Lisbon, Portugal (1755), San Francisco, USA (1906), Messina, Italy (1908) and Tokyo, Japan (1923) [LV13]. In more recent earthquakes—Molise (2002), L'Aquila (2009), Christchurch (2010–2011) and Emilia-Romagna (2012)—masonry building suffered again significant damage [DS⁺04, DI⁺10, DI⁺11, WB⁺12, RTS12].

From these examples only the damage caused by the earthquakes from L'Aquila (2009) and Emilia-Romagna (2012) are briefly introduced. These two examples are considered to be representative for the damage that could be expected in Switzerland as the masonry typologies are similar in the two countries and the magnitudes recorded in L'Aquila and Emilia-Romagna similar to the magnitudes of a 100-year-event in the canton Valais (VS) [DB09, WB⁺12].

- In April 2009, an earthquake of magnitude 6.3 struck the region around the city of L'Aquila. The epicenter of the earthquake was near the city center (5 km away from the center with a depth of 9 km) causing tremendous damages. A total of 15,000 buildings were damaged and more than 70,000 people lost their homes at least temporarily. Most of the observed damage on masonry buildings occurred to old rubble stone masonry but some damage on newer brick and concrete block masonry was also reported [DB09].
- In May 2012 the region of Emilia-Romagna was struck by a series of earthquake shocks, the largest of which had a magnitude of 5.9. Most damage was reported on existing masonry structures and recent industrial buildings. As a consequence a total of 14,000 people lost their homes and 12,000 people lost their jobs [RTS12]. In this region, seismic considerations were not mandatory until 2003. Most of the destroyed buildings were constructed before this date [WB⁺12, RTS12].

In Table 1, the ten strongest earthquakes recorded in Switzerland are summarized. It can be noted that both earthquakes in Italy—L'Aquila (2009) and Emilia-Romagna (2012)—reached magnitudes similar to the ones recorded in Switzerland. Most collapsed buildings during these earthquakes did not comply with current existing code recommendations [DS⁺04]. Scientists recommend therefore that the seismic assessment of existing buildings should be mandatory for regions where a seismic design standard has just been relatively recently introduced [WB⁺12, RTS12].

Table 1 Ten strongest earthquakes recorded in Switzerland (source: www.seismo.ethz.ch)

City	Canton	Magnitude	Intensity	Year
Churwalden	GR	6.2	VIII	1295
Basel$^{*)}$	BS	6.6	IX	1356
Ardon	VS	5.8	VII	1524
Aigle$^{*)}$	VD	5.9	VIII	1584
Unterwalden	NW	5.9	VIII	1601
Ftan	GR	5.4	VII	1622
Brig-Naters	VS	5.7	VIII	1755
Altdorf	UR	5.7	VII	1774
Stalden-Visp$^{*)}$	VS	6.2	VIII	1855
Sierre$^{*)}$	VS	5.8	VIII	1946

$^{*)}$ including strong aftershocks

2.2 Design and assessment methods of modern URM wall structures

As mentioned before, two main approaches are typically distinguished in the seismic design and assessment of structures. The first approach interprets the seismic loading as forces (the so-called force-based design (FBD) method), e.g. [CEN04, SIA03], while the second approach interprets the seismic loading in form of displacement demand (the so-called displacement-based design (DBD) method), e.g. [CEN05, SIA04, PLBL11].

Most current seismic design codes are based on FBD, which consist in determining the acceleration demand from the effective period $T_e = 1/(2\pi)\sqrt{k_e/m_e}$ on the basis of the effective stiffness k_e. The lateral force demand is then obtained by dividing the acceleration demand by the effective mass and the so-called q-factor, which accounts for the overstrength and the inelastic deformation capacity of the structure up to failure. For URM structures, most codes give a factor of $q = 1.5$–2.5 , e.g. [CEN04], considering hence only a very limited displacement ductility of the URM structure. Different DBD methods have been developed so far. The most advanced ones are the capacity spectrum method (CSM) developed in the 80s by Freeman et al. [FNT75], the N2-method by Fajfar et al. [FF88, FG96] and the direct displacement-based design (DDBD) developed in the 90s by Priestley et al. [PCK07].

The DDBD-method [PCK07] is initially based on the idea of the Substitute Structure from Shibata and Sozen [SS76], which represents an inelastic multi degree of freedom (MDOF) system through an equivalent elastic single degree of freedom (SDOF) system with the secant stiffness at peak displacement and the effective damping ratio. The CSM [FNT75] defines the seismic demand via the acceleration-displacement response spectrum and the seismic capacity by means of a pushover analysis. To compare demand with capacity, the pushover curve of the MDOF system is transformed into the pushover curve of an equivalent SDOF system and the base shear divided by the effective modal mass of the first mode. The performance point is the intersection of the capacity curve and the demand curve (see Fig. 6). In the case of CSM [FNT75], the demand is represented by a highly damped elastic spectra. In the N2-method by Fajfar et al. [FF88, FG96], an inelastic spectrum instead of a highly damped elastic spectrum is used.

In Switzerland, DB methods have been adopted for buildings in general with the introduction of SIA 2018 [SIA04] and specifically for URM buildings with the introduction of the

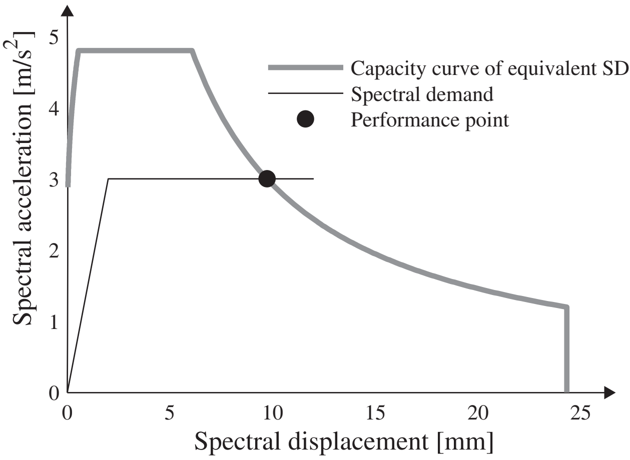

Figure 6 N2-method developed by Fajfar et al. [FF88, FG96]

SIA D0237 [PLBL11]. Both verify the in-plane resistance of URM wall structures based on the N2-method by Fajfar et al. [FF88, FG96]. The methodology for the evaluation of URM buildings in Switzerland is similar to the one described in Figs. 3 and 6, with the difference that the frame effect coming from the coupling beams is implicitly considered through the shear span H_0 [Lan02, PLBL11] (see Fig. 4).

2.3 Force-deformation behavior of URM walls

As stated before, the global force-displacement response of an URM building will be governed by the force-displacement response of individual URM walls at the base of the building. The force-displacement behavior of this individual URM walls depends on the dominant failure mode (flexural rocking, diagonal shear, sliding [MC97]), which in turn depends on the boundary conditions, the aspect ratio of the wall, the brick and mortar quality, etc. Three parameters are needed to describe the bi-linear approximation of the load-displacement curve of an individual wall i (see Fig. 7). These are: (a) the force capacity V_i, (b) the effective stiffness $k_{e,i}$ and (c) the ultimate displacement $u_{u,i}$. Note that the elastic displacement $u_{e,i} = V_i / k_{e,i}$ is often used instead of the effective stiffness $k_{e,i}$, as shown in Fig. 5.

Several experimentally validated mechanical models are available to compute the force capacity V_i of URM walls. Examples of such models are the ones by Mann and Müller [MM82], Ganz [Gan85]—which forms the basis of the Swiss masonry code SIA 266 [SIA05]—and Turnšek et al. [TC71, TS81]. These models account for the geometry of the wall, the boundary conditions as well as the mechanical properties of the masonry.

There are two types of models for computing the ultimate displacement capacity $u_{u,i}$ of URM walls: empirical and mechanical models. Empirical models were derived from quasi-static tests on URM walls which revealed the dependency between the deformation capacity and the failure mechanism [MC97]. These kinds of models assign either (a) a specific drift capacity to each failure mode [MC97], or (b) express the drift capacity as a function of parameters that influence the failure mode. Parameters can be the mean axial stress ratio or the slenderness ratio of the wall [Lan02, Oro11]. In most countries, the empirical models of type (a) have been adopted in codes and standards (such as in [CEN05]), with the exception of Switzerland where the empirical model of type (b) has been implemented in the SIA D0237 [PLBL11].

Concerning the mechanical models, three different approaches have been reported in the

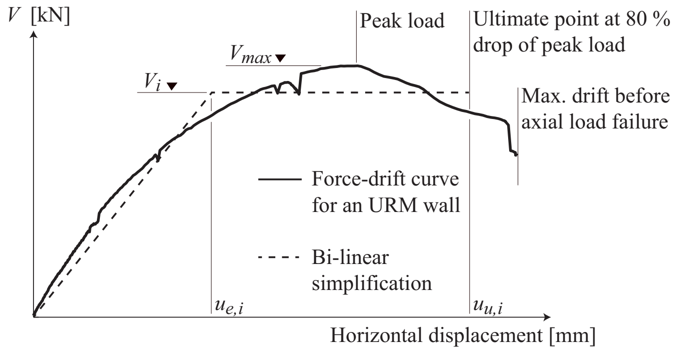

Figure 7 Force-drift curve for an URM wall subjected to lateral in-plane loading

literature: (i) the mechanical model for the ultimate drift by Priestley et al. [PCK07], (ii) the analytical model for the force-displacement relationship described by Benedetti et al. [BS08, BB13] and (iii) the model developed by Penna et al. [PLG14][1] for the macro-element formulation implemented in the software Tremuri [LP$^+$13]. The first two models were derived for flexural dominated walls assuming a non-tension constitutive relationship for the URM. Benedetti and Benedetti [BB13] implemented a shear failure criterion in the model initially proposed by [BS08]. Nevertheless, nonlinear effects are only partially considered when determining shear deformations. The model by Penna et al. [PLG14] is the only one which accounts implicitly for damage due to shear solicitation by means of an implemented shear damage model [GL97].

Most of the previous models (including the empirical models) for the displacement capacity of URM walls estimate only the ultimate displacement capacity, being not suitable for estimating the effective stiffness $k_{e,i}$. Therefore, most codes recommend to compute $k_{e,i}$ by applying a reduction factor of 30 to 50% to the gross sectional stiffnesses [CEN05, PLBL11]. Recent evaluations of quasi-static cyclic tests on URM walls have, however, revealed that the ratio of effective to gross sectional stiffness can vary significantly [FM$^+$09, Tom09].

3 Objectives

The objective of this thesis is to contribute to the general understanding of the force-displacement response of modern URM clay brick walls and in particular of their displacement capacities at different limit states. The thesis addresses in particular the following aspects:

1. the influence of boundary conditions, i.e. axial load ratio and shear span, on the force-displacement response of URM walls;
2. the influence of scaling on the seismic behavior of URM walls;
3. the definition of local limit states influencing the global force-displacement response of URM walls;
4. the development of a mechanical model which captures the kinematics of an URM wall and yields an accurate force-displacement response of URM walls.

The methodology adopted in order to fulfil these objectives is outlined in the next section.

---

[1] The model by Penna et al. [PLG14] is strictly speaking only a semi-mechanical model which accounts for softening in the pre-peak response by mechanical and phenomenological approaches and in the post-peak response by phenomenological approaches only. However, the model is the most complete as it also considers also damage in URM walls due to shear. It is therefore included in this list.

4 Methodology and main contributions

In order to gain a better insight into the nonlinear force-displacement response of URM walls, two test series on URM elements were performed. Each of these test series comprises different standard material tests and 5 to 6 quasi-static cyclic tests on masonry walls. In addition to the conventional hard-wired measurement system, a LED-based optical system was used to record the displacement field of the walls continuously throughout the quasi-static tests. These measurements allow to link the local deformations to the global force-displacement curve of the walls. The test series set themselves apart from previous experimental research, e.g. [GT84, MC92, BP$^+$03, MMP08, GT13, SMS13], with regard to three aspects:

- continuous measurement of displacement field of the URM walls;
- variation of the applied shear span over a large range ($H_0 = 0.5H, 0.75H$ and $1.5H$);
- publication of local and global measurement data on an open access platform.

In order to provide a simplified tool for the estimation of the displacement capacity of URM walls suitable for future codes adaptation, an empirical drift capacity model is developed. For this an existing dataset on URM wall tests [FM$^+$09] is extended by other wall tests, e.g. [GT84, MC92, BP$^+$03, MMP08] and our own wall tests. The analysis of the experimental data confirmed the dependency of the ultimate drift capacity on the axial stress ratio [Lan02, Oro11], the normalized shear span [PLBL11] and the following new factors:

- influence of the size of wall unit on the ultimate drift capacity;
- influence of the load history on the ultimate drift capacity.

As a first step towards the development of mechanical models capturing the nonlinear behavior of URM walls, two new sets of local limit states (LSs) are proposed which are typically observed for URM walls assembled with modern hollow core clay bricks. These limit states are partly based on observations by others [ATC98, MM82, Hey92, GM$^+$98, Cal99, Abr01, Lan02, BP$^+$03, LG06, Tom07] and are extended by evaluation of local deformations, e.g. curvature and strain profiles at the limit states. The two sets of limit states set themselves apart from previous research with regard to the following aspects:

- separation of the limit states according to the predominate mode, i.e. flexural or shear solicitations;
- new local limit states are linked to characteristic points of the global load-displacement response.

A new analytical formulation is developed which captures the force-displacement behavior of URM walls developing a significant flexural mode. It is based on the same assumptions as existing models [BS08, PLG14], i.e. plane section hypothesis and a linear-elastic constitutive material law in compression, but sets itself apart with regard to the following two points:

- a coupling of the shear and flexural stiffness. This is achieved by accounting for the reduction of the effective section when computing the displacement due to shear and flexural solicitation;
- comparison of local measurement shows that the analytical formulation yields an excellent prediction of the relative contributions of shear and flexural deformations.

In order to create a link between local performance levels and global force-displacement capacity, the new set of local limit states due to flexure are incorporated in the analytical formulation. This complete mechanical model sets itself apart to previous mechanical models [PCK07, BS08] with regard to the following points:

- confinement of the foundation and compression failure of masonry in second mortar joint are considered;
- model yields a good prediction of the force-displacement response of flexural dominated URM walls up to the Near Collapse limit state.

5 Organization

The work of the herein presented thesis is summarized in four journal articles and one additional chapter. The list of the articles includes:

I Influence of boundary conditions and size effect on the drift capacity of URM wallsCyclic test data of six unreinforced masonry walls with different boundary conditions
II Scaling unreinforced masonry for reduced-scale seismic testing
III Limit states of modern unreinforced clay brick masonry walls subjected to in-plane loading
IV Force-displacement relationship for in-plane loaded URM walls

In Paper I, the different force-displacement response of the full-scale wall tests is discussed and conclusions on the influence of the applied boundary conditions are done. In addition, existing recommendations on the drift capacity of URM walls are reviewed and discussed. The results from own wall tests are compared to other 58 quasi-static tests on URM walls of different heights and masonry types. The comparison confirms the influence of the boundary conditions on the drift capacity and reveals the influence of size of wall units and load history. A new empirical formulation is thus proposed which accounts for all these factors and which could be adopted in future codes' recommendations.

Within the framework of a shake table test on a half-scale mixed URM-RC wall structure the influence of scaling of modern clay masonry needed to be investigated. Paper II addresses therefore the influence of scaling on the in-plane force-displacement response of URM walls built of hollow clay brick masonry with fully mortared head and bed joints. It commences with a detailed literature review on scaling for structural testing and scaling of masonry in particular. Different choices of scaling brick units and mortar joints are investigated and the final half-scale brick is presented. Material tests and quasi-static cyclic tests, which are presented in Paper I for the full-scale masonry, are repeated using the half-scale masonry and the differences between both test series are compared in terms of material properties and structural behavior. To conclude, recommendations for the scaling of modern hollow core clay brick masonry are formulated, i.e. scaling of the hollow core brick by reduction of numbers of webs and scaling of mortar joint has a negligible effect when dealing with hollow core clay bricks.

In Paper III, the full-scale test series is evaluated in terms of local and global engineering demand parameters (EDPs). The two sets of limit states (LSs) are derived linking local damage states to characteristic points of the global force-displacement response of URM wall. The two sets define LSs for walls developing a shear or a flexural mechanism respectively. In a second part of this paper, parameters deemed suitable for the validation of mechanical and numerical models at local level are evaluated from optical measurement data of the quasi-static cyclic wall tests presented in Appendix A, i.e. effective compression length , curvature, shear strains, etc.

In Paper IV, a new mechanical model is developed which describes the nonlinear force-displacement response of URM walls developing a flexural rocking mode up to Near Collapse. It is based on the plane section hypothesis and constitutive law for the masonry assuming zero tensile strength and a linear-elastic behavior in compression. The new proposed model is compared to existing models and experimental evidence in terms of local and global engineering demands parameters. It is shown that the model captures well the kinematics of flexural developed walls and yields thus to improved estimates for the three key parameters defining the force-displacement response of URM walls, i.e. force capacity, effective stiffness and ultimate displacement.

Chapter V summarizes all attempts to develop a model which describes the force-displacement behavior for URM walls where a significant diagonal shear crack develops. The basic ideas of a possible mechanical model are presented and the limitation of the model are discussed.

In the conclusions the main contributions and outcome of this thesis are summarized and an outlook on further work is given.

In Appendix A, the first test series of the six full-scale URM walls tested under quasi-static cyclic lateral in-plane loading is summarized. All test data of this EPFL test series including that of the optical measurements is shared publicly via the doi 10.5281/zenodo.8443 allowing hence any researcher to reuse the data. In Appendix A, the test setup, the material used for the walls and the test program are briefly presented, the optical and conventional measurement devices are explained and a detailed description on the postprocessing of the test data is given. The same is done for the half-scale wall tests in Appendix B.

References

[Abr01] Abrams, DP. Performance-based engineering concepts for unreinforced masonry building structures. *Progress in Structural engineering and Materials*, 3:48–56, 2001.

[ATC98] ATC. Evaluation of earthquake damaged concrete and masonry wall buildings. Technical Report FEMA-306, Basic Procedures Manual, Applied Technology Council (ATC), Washington, DC, USA, 1998.

[BB13] Benedetti, A and Benedetti, L. Interaction of shear and flexural collapse modes in the assessment of in-plane capacity of masonry walls. In *Proceedings of the 12th Canadian Masonry Symposium*, Vancouver, Canada, 2013.

[BP$^+$03] Bosiljkov, V, Page, AW, Bokan-Bosiljkov, V and Zarnič, R. Performance based studies of in-plane loaded unreinforced masonry walls. *Masonry International*, 16(2):39–50, 2003.

[BP$^+$14] Beyer, K, Petry, S, Tondelli, M and Paparo, A. *Towards displacement-based design of modern unreinforced masonry structures.* Istanbul, Turkey, 2014.

[BS08] Benedetti, A and Steli, E. Analytical models for shear-displacement curves of unreinforced and frp reinforced masonry panels. *Construction and Buildings Materials*, 22:175–185, 2008.

[Cal99] Calvi, GM. A displacement-based approach for vulnerability evaluation of classes of buildings. *Journal of Earthquake Engineering*, 3:411–438, 1999.

[CEN04] CEN. Eurocode 8: Design of structures for earthquake resistance, Part 1: General rules, seismic actions and rules for buildings. Construction Code EN 1998-1:2004, European Committee for Standardisation, Brussels, Belgium, December 2004.

[CEN05] CEN. Eurocode 8: Design of structures for earthquake resistance, Part 3: Assessmemt and retrofitting of buildings. Technical Report EN 1998-3, European Committee for Standardisation, Brussels, Belgium, June 2005.

[DB09] Dazio, A and Beyer, K. Schäden an Mauerwerksbauten beim Erdbeben vom 6.April 2009 in L'Aquila. pages 33–42, 2009.

[DI+10] Dizhur, D, Ismail, N, Knox, C, Lumantarna, R and Ingham, J. Performance of unreinforced and retrofitted masonry buildings during the 2010 Darfield Earthquake. *Bulletin of the New Zealand Society for Earthquake Engineering*, 43:321–339, 2010.

[DI+11] Dizhur, D, Ingham, J, Moon, L, Griffith, M, Schultz, A, Senaldi, L, Magenes, G, Dickie, J, Lissel, S, Centeno, J, Ventura, C, Leite, J and Lourenço, PB. Performance of masonry buildings and churches in the 22 February 2011 Christchurch Earthquake. *Bulletin of the New Zealand Society for Earthquake Engineering*, 44:279–296, 2011.

[DS+04] Decanini, L, Sortis de , A, Goretti, A, Langenbach, R, Mollaioli, F and Rasulo, A. Performance of masonry buildings during the 2002 Molise, Italy, earthquake. *Earthquake Spectra*, 20:191–220, 2004.

[FF88] Fajfar, P and Fischinger, M. N2 – a method for non-linear seismic analysis of regular buildings. In *Proceedings of Ninth World Conference on Earthquake Engineering*, volume V, pages V–111–V–116, Tokyo-Kyoto, Japan, August 1988.

[FG96] Fajfar, P and Gačperšič, P. The N2 method for the seismic damage analysis of RC buildings. *Earthquake Engineering and Structural Dynamics*, 25:31–46, 1996.

[FM+09] Frumento, S, Magenes, G, Morandi, P and Calvi, GM. *Interpretation of experimental shear tests on clay brick masonry walls and evaluation of q-factors for seismic design*. Technical Report, IUSS PRESS, Pavia, Italy, 2009.

[FNT75] Freeman, SA, Nicoletti, JP and Tyrell, JV. Evaluations of existing buildings for seismic risk – a case study of puget sound naval shipyard, bremerton, washington. In *Proceedings of U.S. National Conference on Earthquake Engineering*, pages 113–122, Berkeley, USA, 1975.

[Gan85] Ganz, HR. *Mauerwerksscheiben unter Normalkraft und Schub*. Phd thesis, ETH Zürich, Institute of Structural Engineering, Zürich, Switzerland, 1985.

[GL97] Gambarotta, L and Lagomarsino, S. Damage models for the seismic response of brick masonry shear walls. Part I: The mortar joint model and its applications. *Earthquake Engineering and Structural Dynamics*, 26:423–439, 1997.

[GM+98] Gruenthal, G, Musson, R, Schwarz, J and Stucchi, M. European macroseismic scale 1998. Technical report, Cahiers de Centre Européen de Géodynamique et de Seismologie, Luxembourg, 1998.

[GT84] Ganz, HR and Thürlimann, B. Versuche an Mauerwerksscheiben unter Normalkraft und Querkraft. Technical Report Test Report 7502-4, ETH Zürich, Zürich, Switzerland, 1984.

[GT13] Gams, M and Tomaževič, M. Influence of different types of units and mortars on seismic resistance of masonry walls. In *Proceedings of the 12th Canadian Masonry Symposium*, Vancouver, Canada, 2013.

[Hey92] Heyman, J. Leaning towers. *Meccanica*, 27:153–159, 1992.

[Lan02] Lang, K. *Seismic vulnerability of existing structures*. Phd thesis, ETH Zürich, Institute of Structural Engineering, Zürich, Switzerland, February 2002.

[LG06] Lagomarsino, S and Giovinazzi, S. Macroseismic and mechanical models for the vulnerability and damage assessment of current buildings. *Bulletin of Earthquake Engineering*, 4:415–443, 2006.

[LP+13] Lagomarsino, S, Penna, A, Galasco, A and Cattari, S. Tremuri program: an equivalent frame model for the nonlinear seismic analysis of masonry buildings. *Engineering Structures*, 56:1787–1799, 2013.

[LV13] Lourenço, PB and Vasconcelos, G. Modern masonry structures and earthquakes: reinforced or unreinforced? 2013.

[Mag06] Magenes, G. Masonry building design in seismic areas: recent experiences and prospects from a European standpoint. In *Keynote at the First European conference on earthquake engineering and seismology*, Geneva, Switzerland, 2006.

[MC92] Magenes, G and Calvi, GM. Cyclic behaviour of brick masonry walls. In *Proceedings of the*

10th world conference on earthquake engineering, pages 3517–22, Madrid, Spain, 1992.

[MC97] Magenes, G and Calvi, GM. In-plane seismic response of brick masonry walls. *Earthquake Engineering and Structural Dynamics*, 26:1091–112, 1997.

[MM82] Mann, W and Müller, H. Failure of shear-stressed masonry—an enlarged theory, tests and application to shear walls. In *Proceedings British Ceramic Society*, volume 30, pages 223–235, 1982.

[MMP08] Magenes, G, Morandi, P and Penna, A. Enhanced safety and efficient construction of masonry structures in europe, 7.1c test results on the behaviour of masonry under static cyclic in plane lateral loads. Technical Report ESECMaSE D7.1c, University of Pavia, Pavia, Italy, 2008.

[Oro11] Oropeza, M. *Fragility functions for seismic risk in regions with moderate seismicity*. Phd thesis, EPFL, School of Architecture, Civil and Environmental Engineering, Lausanne, Switzerland, September 2011.

[PB14] Petry, S and Beyer, K. Influence of boundary conditions and size effect on the drift capacity of URM walls. *Engineering Structures*, 65:76–88, 2014.

[PCK07] Priestley, MJN, Calvi, GM and Kowalsky, MJ. *Displacement-Based Seismic Design of Structures*. Pavia, Italy, 2007.

[PLBL11] Pfyl-Lang, K, Braune, F and Lestuzzi, P. Evaluation de la sécurité parasismique des bâtiments en maçonnerie. Technical Report SIA D0237, Documentation, Swiss Society of Engineers and Architects SIA, Zürich, Switzerland, 2011.

[PLG14] Penna, A, Lagomarsino, S and Galasco, A. A nonlinear macroelement model for the seismic analysis of masonry buildings. *Earthquake Engineering and Structural Dynamics*, 43:159–179, 2014.

[RTS12] Rosin, J, Taddei, F and Schmitt, T. Die Erdbebenserie in der Emilia-Romagna im Mai 2012: DGEB-Erkundungsmission. *D-A-CH-Mitteilungsblatt, Der Bauingenieur*, 87:8–14, 2012.

[SBV12] SBV. Zahlen und Fakten. Report, Schweizerischer Baumeisterverband, Zürich, Switzerland, 2012.

[SIA03] SIA. SIA261:2003 actions on structures. Construction code, Swiss Society of Engineers and Architects SIA, Zürich, Switzerland, 2003.

[SIA04] SIA. SIA2018:2004 vérification de la sécurité parasismique des bâtiments existants. Construction code, Swiss Society of Engineers and Architects SIA, Zürich, Switzerland, 2004.

[SIA05] SIA. SIA266: Masonry. Construction Code, Swiss Society of Engineers and Architects SIA, Zürich, Switzerland, 2005.

[SMS13] Salmanpour, A, Mojsilovič, N and Schwartz, J. Deformation capacity of unreinforced masonry walls subjected to in-plane loading: a state-of-the-art review. *International Journal of Advanced Structural Engineering*, 5:1–12, 2013.

[SS76] Shibata, A and Sozen, M. Substitue structure method for seismic design in reinforced concrete. *Journal of the Structural Division*, 102(6):1–18, 1976.

[TC71] Turnšek, V and Cašovič, F. Some experimental results on the strength of brick masonry walls. In *Second International Brick Masonry Conference*, pages 149–156, 1971.

[Tom99] Tomaževič, M. *Earthquake-resistant design of masonry buildings*, volume 1 of *Series on Innovation in Structures and Construction*. Imperial College Press, London, UK, 1999.

[Tom07] Tomaževič, M. Damage as a measure for earthquake-resistant design of masonry structures: Slovenian experience. *Canadian Journal of Civil Engineering*, 34:1403–1412, 2007.

[Tom09] Tomaževič, M. Shear resistance of masonry walls and eurocode 6: shear versus tensile strength of masonry. *Materials and Structures*, 42:889–907, 2009.

[TS81] Turnšek, V and Sheppard, P. The shear and flexural resistance of masonry walls. In *Proceedings of the International Research Conference on Earthquake Engineering*, pages 517–573, Skopje, 1981.

[WB$^+$12] Wenk, T, Baur, M, Duvernay, B and Paparo, A. Die Erdbebenserie in der Emilia-Romagna im Mai 2012: Schäden an Industriehallen und geotechnische Aspekte. *D-A-CH-Mitteilungsblatt, Der Bauingenieur*, 87:2–7, 2012.

Paper I

Influence of boundary conditions and size effect on the drift capacity of URM walls

Petry, S and Beyer, K; *Engineering Structures* (2014), 65:76–88,
DOI: 10.1016/j.engstruct.2014.01.048

Abstract

In codes the drift capacity of unreinforced masonry (URM) walls is often estimated as a function of the failure mode and the aspect ratio. The empirical relationships are based on results from quasi-static cyclic tests on single URM walls, which were tested simulating either fixed-fixed or cantilever boundary conditions. In real structures, the stiffness and strength of slabs and spandrels define the boundary conditions of the walls and therefore the moment, shear force and axial force imposed on a wall during an earthquake. Depending on the exact configuration of wall, slab and spandrel, the boundary conditions can vary significantly. In order to investigate the influence of these boundary conditions on the force-deformation behavior of URM walls, six quasi-static cyclic tests were performed. Different boundary conditions were simulated by varying the axial load ratio and the ratio of top and bottom moment applied to the wall. This article presents the test results and discusses the influence of the boundary conditions on the failure mechanism and the drift capacity of the walls. In addition, the results from 64 quasi-static tests on URM walls of different heights and masonry types are evaluated. These tests confirm the influence of the boundary conditions on the drift capacity. Moreover, they show that a strong size effect is present which leads to smaller drift capacities with increasing wall height. For this reason, an empirical drift capacity equation is proposed which accounts for the moment profile, the axial load ratio and the size effect.

Keywords:

Unreinforced masonry; Drift capacity; Boundary conditions; Size effects; Quasi-static cyclic tests; Walls;

1 Introduction

In unreinforced masonry (URM) buildings, walls are connected by horizontal structural elements such as slabs and masonry spandrels. When walls are subjected to in-plane loading, these horizontal elements act as coupling elements between the walls and the system is often analyzed using equivalent frame models [LP^{+}13]. The stiffness and strength of these coupling elements can vary significantly and three levels of coupling are distinguished in the literature, see Fig. 1, e.g. [Tom99, Lan02]: (i) weak coupling, where the horizontal elements impose only equal displacements on the walls of each story but do not transfer significant shear forces or bending moments, (ii) strong coupling, where vertical and horizontal elements develop together a framing action and where the coupling elements remain largely elastic when the structure is subjected to horizontal loading, (iii) intermediate coupling, where the moments transferred by the coupling elements are limited but not negligible. The coupling elements influence the rotational restraint at the top of the wall and therefore, the moment profile. For outer walls, the coupling elements cause also a variation of axial force in the wall. For inner walls in symmetrical structures, the axial force variation due to the horizontal loading is small and can often be neglected. In most codes, such as EC8-Part 3 [CEN05], the drift capacity of URM walls is estimated as a function of the failure mode and the aspect ratio. These empirical relationships are based on results from quasi-static cyclic tests on URM walls, which were tested simulating either fixed-fixed or cantilever conditions. Hence, as only two types of boundary conditions were applied, a detailed investigation on the influence of the boundary conditions on displacement capacities of URM walls was not possible. To complement previous tests, this study comprises six wall tests with different boundary conditions typical for internal or external walls in URM buildings with RC slabs. The findings are compared to the results of a dataset comprising 64 wall tests and the relationship between axial stress, degree of coupling and displacement capacity is discussed. The dataset also shows that the displacement capacity of URM walls is affected by a strong size effect: tests on walls with smaller height lead to higher drift capacities than full story height walls. New equations for drift capacity should therefore account for the boundary conditions (moment profile, axial load ratio) and the size effect.

2 Quasi-static cyclic tests on masonry walls

To investigate the effect of the boundary conditions (axial load ratio and moment profile) on the deformation capacity of URM walls, a series of six wall tests was designed. The boundary conditions to be applied in the tests were derived from pushover analyzes of a 4-story masonry wall with RC slabs using the macro-element program Tremuri [LP^{+}13, PLG14]. The wall was analyzed for two different moment capacities of the RC beam elements representing a case of intermediate coupling (Fig. 2 left) and strong coupling (Fig. 2 right). The walls were tested using the test stand shown in Figs. 3 and 4. The test stand allowed applying one horizontal force and two vertical forces by means of three servo-hydraulic actuators, which were controlled in a fully coupled mode. All six walls had the same height H, length L and thickness T (H = 2.25 m, L = 2.01 m, T = 0.20 m). The first three tests (PUP1–3) simulated an internal wall and the next three tests (PUP4–6) an external wall. All tests represented walls at the first floor where failure in URM buildings is expected. The following section summarizes the analysis results and the boundary conditions derived for the tests.

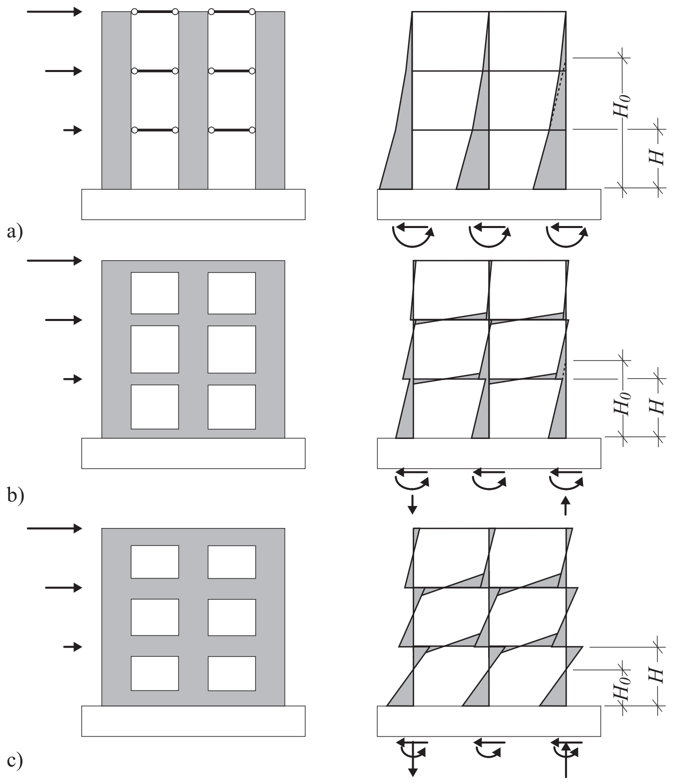

Figure 1 Moment profiles of masonry wall structures with (a) weak coupling, (b) intermediate coupling and (c) strong coupling, taken from [Lan02]

2.1 Simulating the boundary conditions of internal walls: PUP1 to PUP3

In URM buildings with a regular wall layout, the axial force in an internal wall does not vary significantly when the wall is subjected to horizontal loading. Hence, the axial load in internal walls can be assumed independent from the degree of coupling and only the rotational top restraint was changed between PUP1–3. For the 4-story reference building, the axial load acting on an internal wall at the ground floor is $N = 419$ kN. This corresponds to a normal stress ratio of $\sigma_0 / f_u = 0.18$, where f_u represents the average compressive strength of the investigated masonry and σ_0 the applied normal stress.

2.1.1 Reference test specimen PUP1

For the first test specimen PUP1 standard fixed-fixed boundary conditions were applied, i.e. the rotation of the top beam was controlled to be zero, while the total normal force was kept constant:

$$N = F_{ver,1} + F_{ver,2} = constant \tag{1}$$

where N is the total normal load and $F_{ver,1}$ and $F_{ver,2}$ the force applied through the two vertical actuators (see Fig. 2).

2.1.2 Reduced rotational top constraints for PUP2 and PUP3

The effect of different degrees of coupling on the axial load and moment profiles is shown in Fig. 2. It can be seen that fixed-fixed boundary conditions are not representative for the moment profiles over the height of an internal wall of the first story. For most building configurations, the bottom moment of the wall is significantly larger than the top moment.

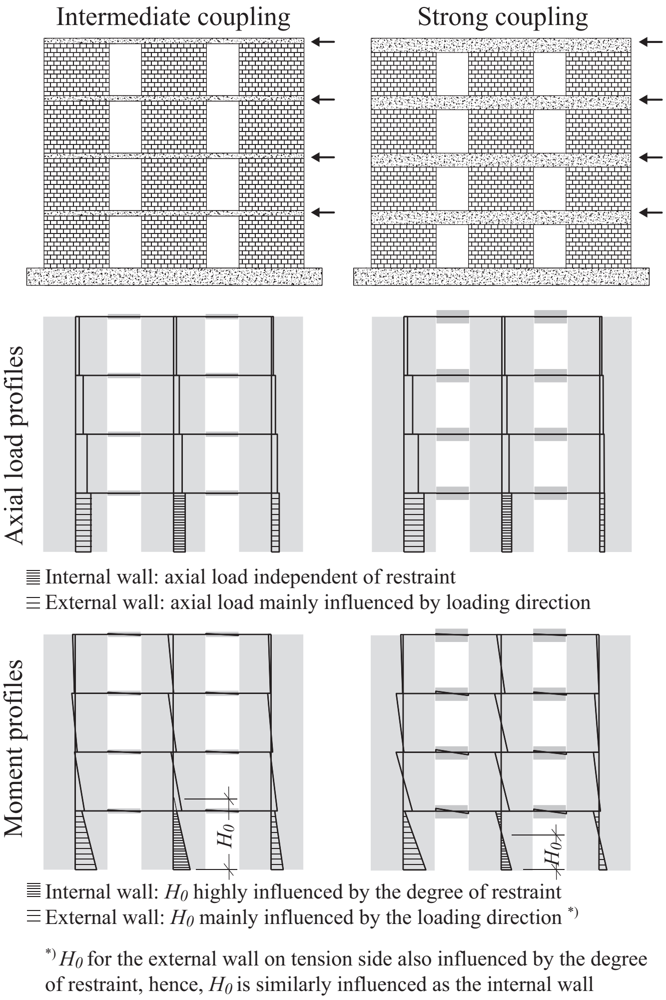

≣ Internal wall: axial load independent of restraint
☰ External wall: axial load mainly influenced by loading direction

≣ Internal wall: H_0 highly influenced by the degree of restraint
☰ External wall: H_0 mainly influenced by the loading direction *)

*) H_0 for the external wall on tension side also influenced by the degree of restraint, hence, H_0 is similarly influenced as the internal wall

Figure 2 Results from a pushover analyzes on URM-wall structures with intermediate coupling (left) and strong coupling (right)

For weak to intermediate coupling, the top and bottom moment might even have the same sign. Thus, PUP2 and PUP3 were allowed a limited top rotation. Instead of controlling this top rotation, the height of the shear span H_0 was kept constant throughout the test, i.e. the applied moment at the top was a function of the applied horizontal force. The total axial load applied by the two vertical actuators was maintained constant throughout the test. For PUP2 and PUP3, the shear span was fixed at $H_0 = 0.75H$ and $1.5H$, respectively, where H is the height of the wall (Table 1).

2.2 Simulating the boundary conditions of an external wall: PUP4 to PUP6

2.2.1 PUP4 and PUP5 with constant axial load and constant shear span

In an external wall, a unilateral coupling moment is introduced and affects thus the axial load in the wall. Figure 2 shows that the axial load in an outer wall at the first story fluctuates by approximately ± 50 %. Hence, PUP4 and PUP5 were tested under a constant axial load of 619 kN and 219 kN, respectively. However, with varying axial force also the shear span changed (Fig. 2) and therefore for PUP4 and PUP5 shear spans of $H_0 = 1.5H$ and $0.75H$ were chosen, respectively (Table 1).

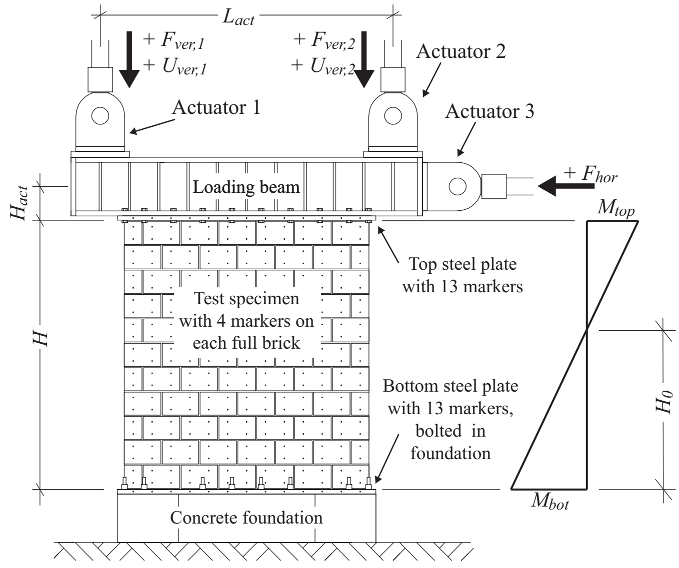

Figure 3 Drawing of EPFL test stand

Table 1. Boundary conditions of PUP1–6

Specimen	Wall	Normal stress ratio	σ_0/f_u	Degree of coupling	Shear span H_0
PUP1	Internal	Intermediate	0.18	Strong	$0.5H$
PUP2	Internal	Intermediate	0.18	Strong	$0.75H$
PUP3	Internal	Intermediate	0.18	Intermediate	$1.5H$
PUP4	External	High	0.26	Intermediate	$1.5H$
PUP5	External	Low	0.09	Strong	$0.75H$
PUP6	External	High–low	0.26–0.09	Intermediate–strong	$1.5H$–$0.75H$

2.2.2 Varying axial load and shear span for PUP6

In a real building, the axial load in an external wall varies with the direction of the lateral load. While for one loading direction the axial load in the wall increases, it decreases for the opposite loading direction (see Fig. 2). Hence, when simulating an external wall, the boundary conditions applied to PUP4 and PUP5 should be combined. Therefore for PUP6, the axial load and shear span were taken as linear functions of the horizontal load F_{hor}. Hence, the boundary conditions of PUP6 approached in the negative and positive directions, those of PUP4 and PUP5, respectively:

$$N = \frac{N_{max} + N_{min}}{2} - F_{hor} \cdot \frac{N_{max} - N_{min}}{F_{hor,max} - F_{hor,min}} \tag{2}$$

$$H_0 = \frac{H_{0,max} + H_{0,min}}{2} - F_{hor} \cdot \frac{H_{0,max} - H_{0,min}}{F_{hor,max} - F_{hor,min}} \tag{3}$$

Figure 4 Photo of EPFL test stand

where N_{max} = 619 kN, N_{min} = 219 kN, $H_{0,min}$ = 0.75H and $H_{0,max}$ = 1.5H correspond to the boundary conditions of PUP4 and PUP5, while $F_{hor,max}$ = -$F_{hor,min}$ = 133 kN was determined as the average of the horizontal force capacities obtained from PUP4 and PUP5.

2.3 Instrumentation and testing procedure

A set of conventional hard-wired measurements was used to measure the forces in all three actuators, the displacement at the top of the wall and local deformations in bricks and joints at all four corners of the wall. In addition, a LED-based optical measurement system was used to follow the displacements of the wall and at the steel plates at the top and bottom of the wall (see markers in Fig. 3). The force-drift hysteresis in Figs. 6c to 11c were obtained from the average displacement of the markers on the top steel plate. Note that the drift herein this article stands for the interstory drift, which is obtained when dividing the top displacement by the height of the walls. In the reinforced concrete community, the drift is often defined as chord rotation which is computed as the displacement at the inflection point divided by the shear span. While for walls tested as cantilever or under fixed-fixed boundary conditions chord rotation and interstory are the same, they diverge from each other for walls tested under different boundary conditions. From our own tests, which included tests with shear span

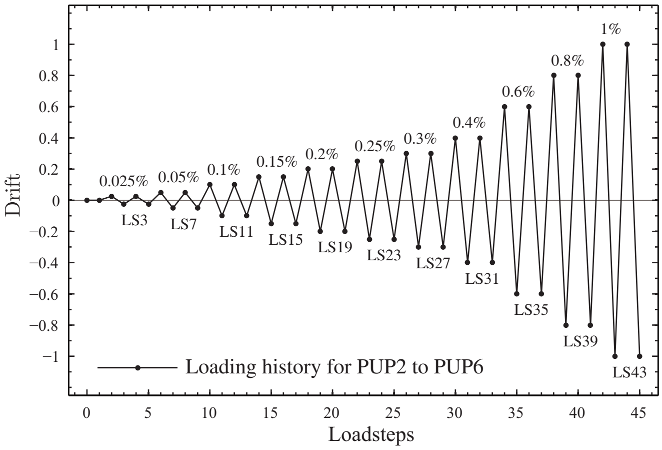

Figure 5. Loading history for walls PUP2–6. For PUP1 the cycles with amplitudes of 0.15% and 0.25% were not applied.

Table 2 Brick and mortar properties

Brick strength		
Compression, ‖ to perforation	35.0 ± 7%	MPa
Compression, ⊥ to perforation	9.4 ± 8%	MPa
Flexural tensile, ⊥ to perforation	1.27 ± 38%	MPa
Mortar properties		
Compression strength	11.2 ± 20%	MPa
Flexural tensile strength	2.7 ± 25%	MPa

ratios different to 1 or 0.5, we found that interstory drift approximates chord rotation in general reasonably well. The ratio of interstory drifts to chord rotations are approximately 1.05 for $H_0/H = 0.75$ and 0.85 for $H_0/H = 1.5$. After applying the axial load, the test unit was subjected to drift cycles with the following amplitudes: 0.025%, 0.05%, 0.1%, 0.15%, 0.2%, 0.3%, 0.4%, 0.6%, 0.8% and 1.0% (see Fig. 5). Note that the cycles with amplitudes of 0.15% and 0.25% were not included in the loading history applied to PUP1, but added from PUP2 onwards since the performance of PUP1 deteriorated rapidly within the cycles with amplitudes of 0.2% and 0.3%.

3 Material properties

The walls were constructed with a typical modern Swiss hollow clay brick unit. The head and bed joints were fully mortared and were 10–12 mm thick. The outer dimensions of the bricks were 190 x 300 x 195 mm (H x L x W). Webs and shells were 8–10 mm thick and the void ratio was 49 %. The mean strength values and coefficients of variation obtained from material tests on the bricks are summarized in Table 2. The cement mortar WEBER MUR MAXIT 920, used for the construction of the walls, is one of the most commonly used mortars in Switzerland. Mortar samples were taken while constructing walls and wallettes for material tests. The mortar samples were tested at the same time as the corresponding walls and wallettes. The mortar properties are summarized in Table 2. To determine the material properties of the masonry, three types of standard material tests were conducted: (i) 5 compression tests on masonry wallettes [CEN02], (ii) 8 shear tests on masonry triplets [CEN07] and (iii) 5 diagonal tensile tests on square masonry wallettes [RIL91]. The results are summarized in Table 3.

Table 3 Masonry properties

Results from compression tests		
Compression strength f_u	5.87 ± 5%	MPa
E-modulus E	3550 ± 9%	MPa
Poisson ratio ν	0.20 ± 19%	-
Results from shear tests		
Peak strength τ_{peak}	$0.94\sigma + 0.27$	MPa
Residual strength τ_{res}	0.91σ	
Results from diagonal tensile tests		
Diagonal tensile strength	0.50 ± 10%	MPa

4 Results from wall tests

For all test units, the loading was continued until the walls were no longer able to carry the applied vertical load. Therefore, within this series, two different failure limit states are distinct: (i) the horizontal load failure is defined as the drift where the strength dropped to 80 % of the peak strength and (ii) the vertical load failure is attained, when the walls can no longer sustain the load applied by the vertical pistons. The horizontal failure corresponds to the limit state "Near Collapse" as defined in EC8-Part 3 [CEN05]. Figs. 6 to 11 show the crack pattern of PUP1–6 after horizontal and vertical load failure, the applied boundary conditions and the hysteretic response. The following sections discuss the influence of the shear span, the axial load ratio and the loading history on the deformation behavior of the test units.

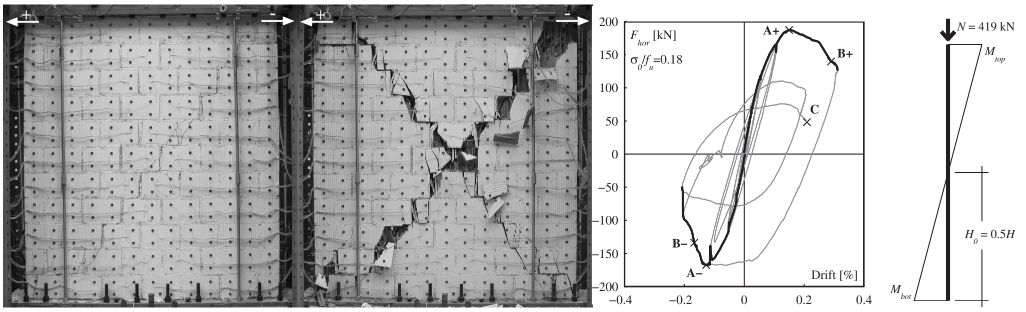

Figure 6. PUP1: (a) after reaching the horizontal failure (B+), (b) after vertical failure (C), (c) interstory drift-force hysteresis and (d) moment diagram

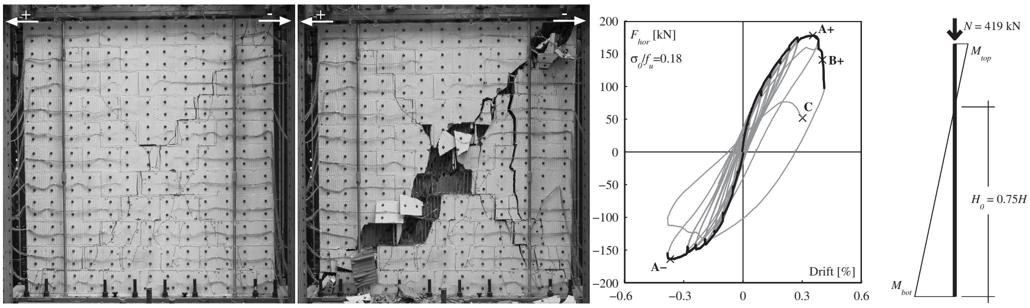

Figure 7. PUP2: (a) after reaching the horizontal failure (B+), (b) after vertical failure (C), (c) interstory drift-force hysteresis and (d) moment diagram

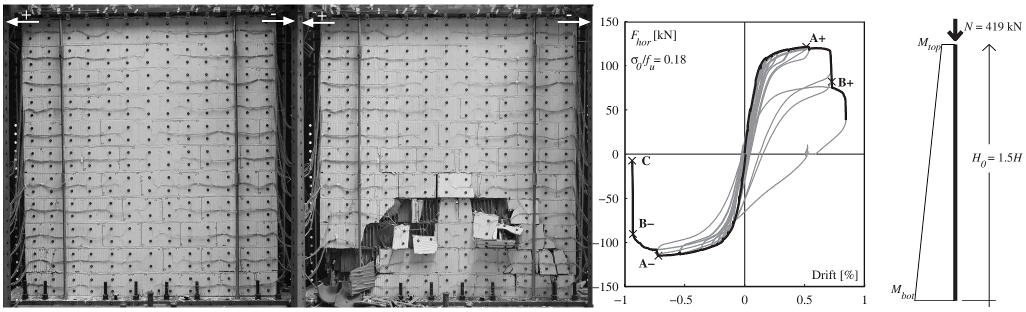

Figure 8. PUP3: (a) after reaching the horizontal failure (B+), (b) after vertical failure (C), (c) interstory drift-force hysteresis and (d) moment diagram

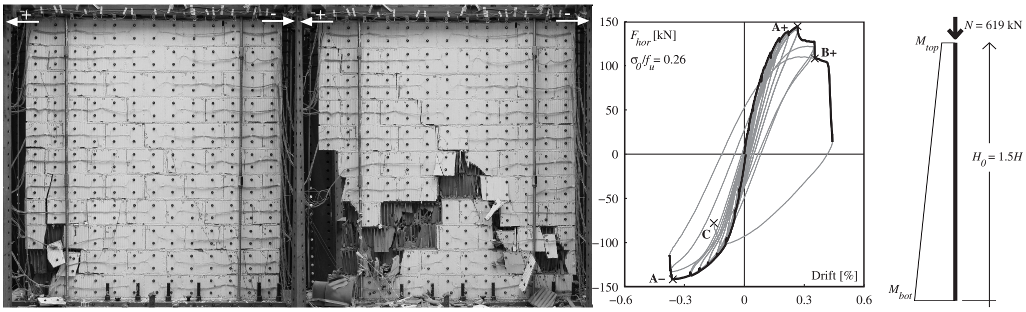

Figure 9. PUP4: (a) after reaching the horizontal failure (B+), (b) after vertical failure (C), (c) interstory drift-force hysteresis and (d) moment diagram

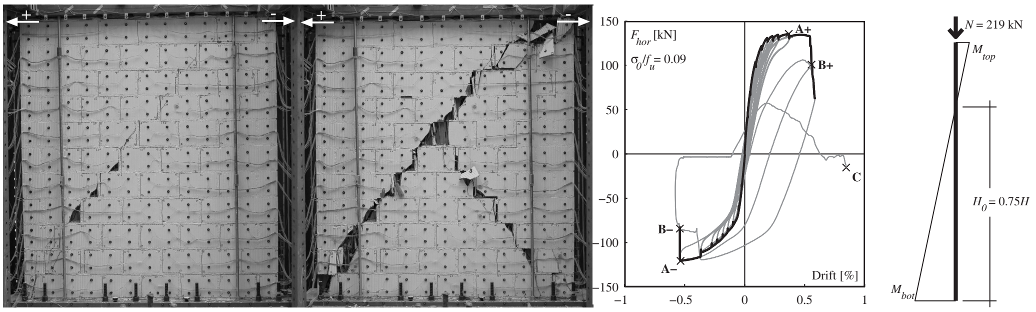

Figure 10. PUP5: (a) after reaching the horizontal failure (B+), (b) after vertical failure (C), (c) interstory drift-force hysteresis and (d) moment diagram

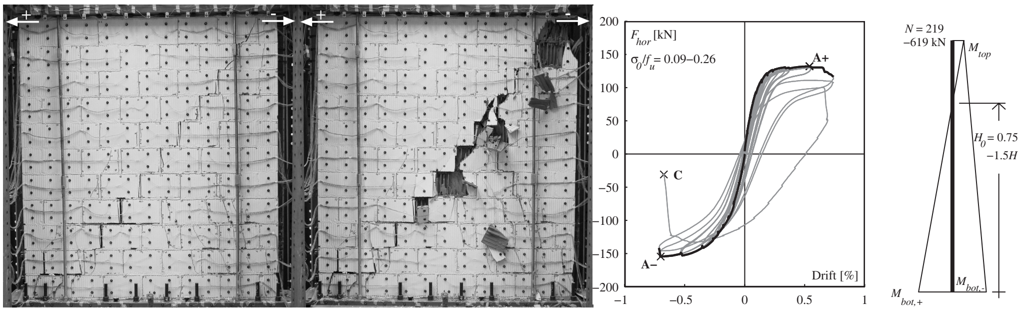

Figure 11. PUP6: (a) after strength deterioration (~A+), (b) after vertical failure (C), (c) interstory drift-force hysteresis and (d) moment diagram

4.1 Influence of the shear span H_0

PUP1–3 were tested under the same constant average normal stress but the three tests differed with respect to the applied shear span ratio (PUP1: $H_0/H = 0.5$, PUP2: $H_0/H = 0.75$, PUP3: $H_0/H = 1.5$). PUP1 and PUP2 developed a shear failure while PUP3 failed due to rocking. All three walls developed first horizontal cracks in the mortar joints. While horizontal cracks appeared simultaneously at the top and bottom of PUP1, the horizontal joints at the top of PUP2 and PUP3 remained almost uncracked due to the smaller top moment. The horizontal cracks at the base of PUP2 and PUP3, however, opened up wider and spread over a larger height than in PUP1. In PUP1 and PUP2 the first diagonal cracks appeared at a nominal drift of 0.1 %. Differences could be observed with regard to the initial inclination of the diagonal cracks, which were steeper for PUP2 (30–35° with respect to the vertical, Fig. 7a) than for PUP1 (cracks followed from the beginning the diagonal of the wall, Fig. 6a). With continuing loading and degradation, further inclined cracks developed in PUP2 and finally, the deformations concentrated along one diagonal crack spanning from one corner of the wall to the other, similar to PUP1 (compare Figs. 7a and b). In PUP3, the first inclined cracks appeared not before the cycles with a nominal drift of 0.4 % and did not influence the failure mode (see Figs. 8a and b). When comparing the displacement capacity of PUP1–3 (see Table 4), it can be noticed that the capacity increased with increasing shear span. This applied to the displacement capacity associated with horizontal as well as vertical load failure. The increased displacement capacity was mainly due to the increased flexural deformations of the walls: while in PUP1 only few horizontal cracks developed at the top and bottom of the wall before deformations concentrated in one diagonal crack, horizontal cracking in PUP2 and PUP3 spread over a larger portion of the wall. An increased shear span leads therefore to an increase in deformation capacity.

4.2 Effect of the axial load ratio σ_0/f_u

PUP2 and PUP5 were both tested applying a constant shear span of $0.75H$. The two test units differed with respect to the applied axial load (PUP2: $\sigma_0/f_u = 0.18$, PUP5: $\sigma_0/f_u = 0.09$). Both walls showed at the beginning a similar crack pattern: the first cracks were horizontal cracks at the base of the wall. Shortly after, the first diagonal cracks appeared (at a nominal drift of 0.1 % for PUP2 and 0.15 % for PUP5). In both cases the first diagonal crack was steeper than the dominating crack at failure (see Figs. 7a, 7b and 10a, 10b). However, the larger normal force of PUP2 seemed to provoke more inclined cracks through the bricks, while in PUP5 the inclined cracks followed at the beginning the joints (stair step cracks) and passed only later through the bricks leading to a smaller strength degradation than for PUP2. Although both test units developed a shear failure mode, the displacement capacity of PUP5 was approximately 40 % larger than the one of PUP2 (this applied to horizontal load failure and vertical load failure). It is assumed that the reduced degradation of the diagonal crack increased the displacement capacity for PUP5 (see Table 4). Also PUP3 and PUP4 were both tested with a constant shear span of $1.5H$ and differed with respect to the applied axial load (PUP3: $\sigma_0/f_u = 0.18$, PUP4: $\sigma_0/f_u = 0.26$). Both walls developed first a flexural behavior, while inclined cracks formed only at a later stage. PUP3 and PUP4 failed eventually due to a flexural and a hybrid failure, respectively. Due to the higher level of normal stresses and shear stresses in PUP4, the inclined cracks and local crushing at the toe appeared for PUP4 at smaller displacement demands than for PUP3 (see Table 4) leading to a faster strength degradation of PUP4. Thus, similar to PUP2/PUP5, the increase in axial load led to a reduced drift capacity.

Table 4. Summary of failure modes, maximum force capacity, drift at peak load, drift at horizontal failure and maximum drift

Specimen	Failure mechanism	Axial load ratio σ_0/f_u	Shear span H_0	Peak load A	Drift at peak load A	Drift at hor. failure B	Max. drift
PUP1	Diagonal shear	0.18	0.5H	187 kN	0.15%	0.29%	0.31%
				-167 kN	-0.12%	-0.17%	-0.21%
PUP2	Diagonal shear	0.18	0.75H	178 kN	0.35%	0.40%	0.41%
				-164 kN	-0.37%	-	-0.38%
PUP3	Flexural rocking	0.18	1.5H	121 kN	0.51%	0.72%	0.84%
				-115 kN	-0.72%	-0.93%	-0.94%
PUP4	Hybrid failure	0.26	1.5H	145 kN	0.27%	0.35%	0.44%
				-142 kN	-0.36%	-	-0.38%
PUP5	Diagonal shear	0.09	0.75H	135 kN	0.37%	0.56%	0.58%
				-121 kN	-0.53%	-0.54%	-0.55%
PUP6	Hybrid failure	0.26	1.5H	132 kN	0.54%	-	0.74%
		0.09	0.75H	-154 kN	-0.70%	-	-0.71%

4.3 Asymmetrical loading

The boundary conditions of PUP6 approached for the positive loading direction those of PUP5 and for the negative loading direction those of PUP4. Figures 12 and 13 show the applied axial load and shear span ratio as function of the applied horizontal load and drift. The critical loading direction of PUP6 was the negative direction where the boundary conditions of PUP4 were approached. For horizontal and vertical load failure, the drift capacities of PUP6 were 2.0 and 1.6 times larger than those of PUP4 (Table 4), i.e. the results suggest that the displacement capacity of symmetrical loaded walls is smaller than the displacement capacities of walls that are asymmetrically loaded and do not reach failure for one of the loading directions.

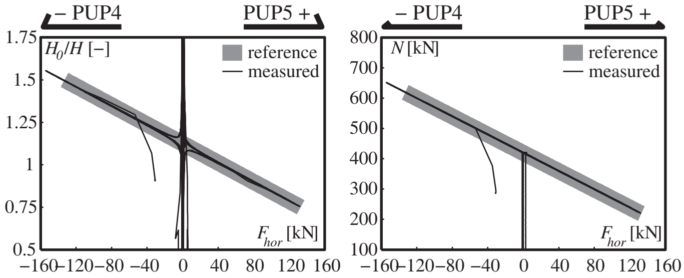

Figure 12. Shear span ratio and axial load for PUP6 as a function of the applied horizontal load

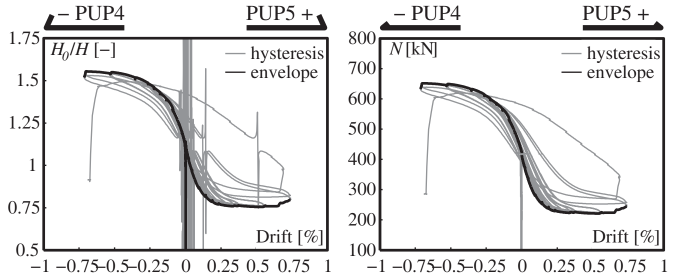

Figure 13. Shear span ratio and axial load for PUP6 as a function of the applied horizontal drift

5 Empirical models for the drift capacity of URM walls

Deformation-based seismic assessment methods for URM structures require as input parameter estimates of the drift capacity of URM walls. The objective of this section is to review existing drift estimates for URM walls by comparing these to a dataset of 64 walls (Table 5). Hereinafter, the term drift capacity refers to the minimum drift capacity associated with horizontal load failure. If the horizontal failure was not measured before vertical failure was reached, the maximum drift is taken (see Table 4).

5.1 Drift capacity models in codes

The Eurocode, the Italian, New Zealand and Swiss code as well as several FEMA guidelines include drift capacity equations for URM walls, which are summarized in the following. EC8-Part 3 [CEN05] estimates the drift capacity as a function of the failure mode. According to EC8-Part 3 [CEN05] the "Significant Damage" (SD) drift capacity is 0.4 % for shear failure and 0.8 % H_0/L for flexural failure where L is the length of the wall. The German national annex to EC8 [CEN04] limits the use of 0.4 % drift for shear failure for walls with an axial stress ratio of $\sigma_0/f_k \leq 0.15$ where f_k is the characteristic compression strength of the masonry. For walls loaded to higher axial stress ratio the SD drift capacity is reduced to 0.3 % for shear. The NC drift capacities are estimated as 4/3 times the SD drift capacities: 4/3 x 0.4 % = 0.53 % for shear failure and 4/3 x 0.8 % H_0/L = 1.07 % H_0/L for flexural failure. In EC8-Part 3, the limit state "Near Collapse" (NC) corresponds to a 20 % loss of peak strength and therefore to the definition of horizontal load failure adopted in this paper. The Italian code only provides drift limits for the ultimate limit state (ULS) [NTC08]. The shear drift capacity corresponds to the SD limit state drift capacity in EC8-Part 3 but for flexural failure the Italian code provides a fixed drift value of 0.8 %, which is hence independent of the slenderness ratio H_0/L [NTC08, MIT08]. The supplement on masonry structures [NZS11] to the New Zealand Standard for seismic assessment [NZS06] proposes ULS drift capacities which are equal to the values in EC8-Part 3 for the SD limit state. The only difference relates to the drift capacity of walls with flanges, which is assumed 50 % larger than for walls with a rectangular cross section when failing in shear (0.6 % instead of 0.4 %).

FEMA 306 [ATC98] distinguishes drift capacities for different damage levels and failure modes. The following drift capacities are specified for the "heavy damage" limit state: For a failure comprising only horizontal cracking due to rocking, FEMA 306 assumes 0.8 % H_s/L, where H_s is the free height between two storys. For a failure mode comprising only sliding along the joints (in form of stair step cracks), FEMA assumes 0.4 %. For walls failing due to diagonal cracking no drift capacities but only ductility capacities are specified. For mixed modes comprising toe crushing, flexural cracking and bed joint sliding, FEMA 306 specifies a drift capacity of 1.2 % and for mixed modes with flexural cracking and toe crushing only a drift capacity of 0.3 %. Both mixed failure modes apply only to squad walls with $L/H_s > 1.25$. Hence, if one stipulates that "heavy damage" corresponds to the SD limit state and neglects the mixed modes, the drift capacities proposed by FEMA 306 are very similar to those in EC8-Part 3 [CEN05]. FEMA 273 [ATC97], a guideline for the seismic rehabilitation of buildings, distinguishes also between shear and flexural failure modes when defining drift capacities. NC limit state drift limits for walls of primary structural importance are 0.4 % for shear failure and 0.4 % Hs/L for flexural failure. Assuming that $\delta_{NC}/\delta_{SD} = 4/3$, the drift capacities in FEMA 273 are 33 % lower than those in EC8-Part 3.

Unlike most codes, the Swiss guideline on the seismic assessment of URM structures SIA D0237 [PLBL11] does not estimate the drift capacity as a function of the failure mode but expresses the drift capacity as a function of the axial stress ratio σ_0/f_d, where f_d is the design value of the masonry compressive strength. This approach originates from [Lan02] and was developed to be used in conjunction with the Swiss Masonry code SIA 266 [SIA05], which determines the strength capacity of a masonry wall using stress fields and therefore does not distinguish explicitly between different failure modes. Drift estimates that are independent of the failure mode might also be convenient for vulnerability studies of large building stocks as axial load and shear span ratio can be roughly estimated from the geometry of the building and the SIA D0237 estimates the drift capacity ULS at the life safety limit state [PLBL11] which can be assumed to correspond approximately to the SD limit state:

$$\delta_{SD} = \delta_0 \cdot (1 - \frac{\sigma_0}{f_d}) \tag{4}$$

where σ_0 is the drift capacity at zero overburden stress, σ_n is the design value of the normal stress and f_d is the design value of the compressive strength of the masonry. For the life safety limit state, SIA D0237 proposes values of 0.8 % if the wall is loaded as a cantilever and 0.4 % if the boundary conditions are fixed-fixed. Unlike other codes, it accounts explicitly for the boundary conditions to which the wall is subjected. To compare the predicted values to the experimental values, SD needs to be converted to NC and the design values of the masonry strength fd to the mean strength f_u. For the ratio δ_{NC}/δ_{SD} a value of 4/3 is assumed (EC8-Part 3 [CEN05]). If the probabilistic distribution is not known, EN 1052-1 [CEN02] proposes that the mean strength f_u is 20 % larger than the characteristic value. The Swiss masonry code applies a safety factor of $\gamma_M = 2.0$ for transforming the characteristic strength into a design value. Hence, with $f_u = 2.4\ f_d$ and $\delta_{NC} = 4/3\delta_{SD}$, Eq. (4) can be rewritten as:

$$\text{Cantilever:}\delta_{NC} = \frac{3}{4} \cdot 0.8 \cdot (1 - 2.4\frac{\sigma_0}{f_u}) \tag{5}$$

$$\text{Fixed-fixed:}\delta_{NC} = \frac{3}{4} \cdot 0.4 \cdot (1 - 2.4\frac{\sigma_0}{f_u}) \tag{6}$$

SIA D0237 intended these equations to yield conservative estimates of the drift capacity obtained from quasi-static cyclic tests [PLBL11]. They were determined on the basis of a dataset comprising walls of different heights tested as cantilevers or with fixed-fixed boundary conditions.

5.2 Dataset of quasi-static wall tests including PUP-series

The dataset comprises results from quasi-static tests on URM walls constructed with clay brick units and normal cement mortar. All walls were constructed with full-size brick units. Own tests with fully mortared and unfilled head joints as well as results reported in the literature, e.g. [FM+09], suggested that the type of head joints has relatively little influence on the deformation behavior of masonry walls. For this reason, quasi-static tests on URM walls with fully mortared head joints, unfilled head joints, mortar pocket as well as tongue and groove masonry are considered. Table 5 summaries the dimensions of the walls, the ratio H_0/H, the applied axial stress σ_0, the mean masonry strength f_u, the brick height h_B, the observed failure mode as well as the drift capacity δ_u. The dataset includes in total 64 tests that stem from 13 test series conducted in 8 different structural engineering laboratories. The information on test units 1–42 is taken from [FM+09]. It collects data on a large variety of masonry wall tests, assesses the failure modes and determines the drift capacity of the walls in a uniform manner. Tests 43–64 were added from different primary sources and include also the six tests PUP1–6 presented in the first part of this paper. The data was processed as in [FM+09]. Thus, the ultimate drift δ_u is determined as the minimum value of the drifts attained at horizontal and vertical load failure. Apart from the PUP-series, all walls were subjected to boundary conditions corresponding either to fixed-fixed or to a cantilever. The ratio H_0/H was therefore for these tests either 0.5 or ≥ 1.0. For the cantilever tests the shear span H_0 was defined as the distance between the center line of the horizontal actuator and the base of the walls (see Table 5).

5.3 Consideration of loading history and strain rate

During seismic loading, URM walls are subjected to loading histories substantially different to the symmetric cycles with increasing amplitudes applied in most quasi-static tests. Furthermore, the strain rates under seismic loading are much larger than in quasi-static tests. For this reason, drift limits derived from quasi-static cyclic tests (δ_{CT}) should not be adopted directly in code recommendations for δ_{NC} but need to be modified to account for loading history (ψ_{LH}) and strain rate (ψ_{SR}) effects. In the absence of mechanical models that account for these effects in an explicit manner, we propose the following simple relationship to estimate the seismic drift capacity associated with the NC limit state from quasi-static cyclic test results:

$$\delta_{NC} = \delta_{CT} \cdot \psi_{LH} \cdot \psi_{SR} \tag{7}$$

At present, the dataset for determining the correction factor ψ_{SR} is very limited. Abrams and Paulson [Abr96, PA90] report a more important crack propagation in URM structures when tested quasi-static cyclically than when tested dynamically. However, Tomaževič [Tom00] and Elgawady [Elg04] report similar displacement capacities for masonry walls tested quasi-statically or dynamically suggesting hence $\psi_{SR} = 1$. With regard to loading history effects (ψ_{LH}) the data is also rather limited: the dataset (Table 5) contains five tests which were not subjected to symmetric cycles. Nevertheless, a comparison between cycles from real seismic loading and symmetric cycles with increasing amplitude is missing. The five tests are PUP6, which was subjected to an asymmetric loading history, and four tests conducted as monotonic tests. For four of these five tests also counterparts subjected to a symmetric cyclic loading

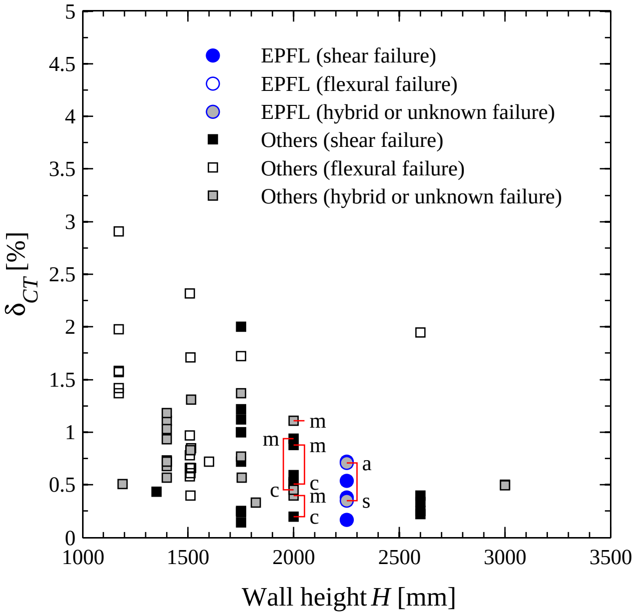

Figure 14 Drift capacities obtained from quasi-static tests vs height of wall specimens (c=symmetric cyclic tests, a=asymmetric cyclic tests, m=monotonic test)

history are available and allow to draw first conclusions regarding the effect of the load history: as outlined in Section 4.3, PUP6 can be compared to PUP4 while the counterparts of tests 43, 44 and 52, which had been subjected to monotonic loading, are the cyclic test 46, 47 and 53. Figure 14 shows that the drift capacity of monotonically or asymmetrically loaded test units is larger than of symmetrically loaded test units. The ratios of drift capacities varied between 1.75 and 2.10. The drift capacity of a monotonically or asymmetrically loaded wall is therefore approximately twice the drift capacity of a cyclically loaded wall. This suggests that ψ_{LH} could be significantly larger than unity. Based on own experience with quasi-static cyclic and shake table tests, we estimate that $\psi_{SR} \cdot \psi_{LH}$ could be in the order of 2–3. Since quasi-static cyclic tests will most likely remain the standard test for URM walls in the future, further research on ψ_{SR} and ψ_{LH} is needed but is out of the scope of this paper.

5.4 Size effect on drift capacity

Empirical drift capacity models, e.g. [PLBL11], were developed as best fit lines to datasets similar to the one presented in Table 3. Many of the wall tests documented in the literature were conducted on walls with heights less than a story. Such walls are present in facades with masonry spandrels while walls at the interior of the building and walls in modern URM buildings typically span over the entire story height. Assuming a story height of $H_s = 2.4$ m, out of the 64 test units documented in Table 3, only 7 were conducted on story-high walls ($H \geq 2.4$ m). The next smaller test units are the six test units of the PUP-series, which had a height of 2.25 m ($H = 0.94\ H_s$). 27 test units were conducted with heights smaller than $2/3 H_s$. Including test units of different heights in the dataset when developing simple empirical models has, however, a significant implication: Figure 14 shows that the experimentally determined drift capacity is strongly dependent on the height of the test unit. Hence, there is a strong size effect on the drift capacity of URM walls, which leads to larger drift capacities for walls of smaller heights. To our knowledge, this effect has been disregarded when developing empirical drift capacity models from experimental results, which might potentially lead to unsafe drift predictions

Table 5. Dataset of wall tests

No	Test unit	Type	Ref.	L [mm]	T [mm]	H [mm]	H_0/H [-]	h_B [mm]	σ_0 [MPa]	f_u [MPa]	σ_0/f_u [-]	Load history	Fail mech.	δ_u [%]
1	10_1	F	[BT03, FM$^+$09]	1028	300	1510	1.06$^{1)}$	240	0.60	4.00	0.15	C	F	1.71
2	10_2	F	[BT03, FM$^+$09]	1030	300	1510	1.06$^{1)}$	240	1.19	4.10	0.29	C	F	0.66
3	10_3	F	[BT03, FM$^+$09]	1033	300	1515	1.06$^{1)}$	240	0.60	4.00	0.15	C	D	1.31
4	10_4	F	[BT03, FM$^+$09]	1025	300	1514	1.06$^{1)}$	240	1.19	4.10	0.29	C	F	0.85
5	10_5	F	[BT03, FM$^+$09]	1027	300	1511	1.06$^{1)}$	240	1.19	4.10	0.29	C	D	0.83
6	10_6	F	[BT03, FM$^+$09]	1026	300	1508	1.06$^{1)}$	240	0.60	4.00	0.15	C	F	2.32
7	10_7	No	[BT03, FM$^+$09]	989	300	1513	1.06$^{1)}$	237	1.19	4.25	0.28	C	F	0.66
8	10_8	No	[BT03, FM$^+$09]	987	300	1511	1.06$^{1)}$	237	1.19	4.25	0.28	C	F	0.83
9	10_9	No	[BT03, FM$^+$09]	988	300	1507	1.06$^{1)}$	237	1.19	4.25	0.28	C	F	0.97
10	10_10	MP	[BT03, FM$^+$09]	985	300	1508	1.06$^{1)}$	236	1.19	6.26	0.19	C	F	0.66
11	10_11	MP	[BT03, FM$^+$09]	985	300	1509	1.06$^{1)}$	236	1.19	6.26	0.19	C	F	0.78
12	10_12	MP	[BT03, FM$^+$09]	986	300	1507	1.06$^{1)}$	236	1.19	6.26	0.19	C	F	0.66
13	10_13	TG	[BT03, FM$^+$09]	988	300	1510	1.06$^{1)}$	235	1.19	6.26	0.19	C	F	0.40
14	10_14	TG	[BT03, FM$^+$09]	987	300	1512	1.06$^{1)}$	235	1.19	6.26	0.19	C	F	0.61
15	10_15	TG	[BT03, FM$^+$09]	986	300	1508	1.06$^{1)}$	235	1.19	6.26	0.19	C	F	0.58
16	14_1	F	[BT06, FM$^+$09]	2567	297	1750	1.10$^{1)}$	236	0.59	4.21	0.14	C	H	1.37
17	14_2	F	[BT06, FM$^+$09]	2572	297	1753	1.10$^{1)}$	236	1.19	4.10	0.29	C	H	0.57
18	14_3	F	[BT06, FM$^+$09]	2584	297	1751	1.10$^{1)}$	236	0.89	4.05	0.22	C	H	0.77
19	14_4	TG	[BT06, FM$^+$09]	2482	296	1750	1.10$^{1)}$	237	0.95	4.32	0.22	C	S	0.72
20	14_5	TG	[BT06, FM$^+$09]	2484	296	1750	1.10$^{1)}$	237	0.53	2.41	0.22	C	F	1.72
21	14_6	MP	[BT06, FM$^+$09]	2359	247	1600	1.11$^{1)}$	188	0.85	3.86	0.22	C	F	0.72
22	14_7	F	[BT06, FM$^+$09]	2712	172	1820	1.10$^{1)}$	188	2.07	9.41	0.22	C	H	0.33
23	15_5	TG	[MDPG05, FM$^+$09]	992	300	1170	1.09$^{1)}$	225	0.94	5.53	0.17	C	F	1.42
24	15_6	TG	[MDPG05, FM$^+$09]	992	300	1170	1.09$^{1)}$	225	1.24	5.64	0.22	C	S	1.57
25	15_7	TG	[MDPG05, FM$^+$09]	992	300	1170	1.09$^{1)}$	225	1.55	5.74	0.27	C	F	1.58
26	15_8	MP	[MDPG05, FM$^+$09]	992	300	1170	1.09$^{1)}$	225	0.89	5.24	0.17	C	F	2.91
27	15_9	MP	[MDPG05, FM$^+$09]	992	300	1170	1.09$^{1)}$	225	1.14	5.18	0.22	C	F	1.98
28	15_10	MP	[MDPG05, FM$^+$09]	992	300	1170	1.09$^{1)}$	225	1.46	5.41	0.27	C	F	1.37
29	16_1	MP	[FM$^+$09]$^{3)}$	2500	300	1750	0.50	238	0.40	5.71	0.07	C	S	0.25
30	16_2	MP	[FM$^+$09]$^{3)}$	2500	300	1750	0.50	238	0.60	6.00	0.10	C	S	0.14
31	16_3	MP	[FM$^+$09]$^{3)}$	2500	300	1750	0.50	238	0.60	6.00	0.10	C	S	0.24
32	18_1	MP	[FM$^+$09]$^{3)}$	2500	300	1750	0.50	238	0.60	6.00	0.10	C	S	1.00
33	18_2	MP	[FM$^+$09]$^{3)}$	2500	300	1750	0.50	238	0.60	6.00	0.10	C	S	1.00
34	18_3	MP	[FM$^+$09]$^{3)}$	2500	300	1750	0.50	238	0.60	6.00	0.10	C	S	2.00
35	18_4	MP	[FM$^+$09]$^{3)}$	2500	300	1750	0.50	238	0.60	6.00	0.10	C	S	1.22
36	18_5	MP	[FM$^+$09]$^{3)}$	2500	300	1750	0.50	238	0.60	6.00	0.10	C	S	1.12
37	18_6	MP	[FM$^+$09]$^{3)}$	2500	300	1750	0.50	238	0.60	6.00	0.10	C	S	1.00
38	CL04	F	[MMP08, FM$^+$09]	2500	300	2600	0.50	190	0.68	9.71	0.07	C	S	0.34
39	CL05	F	[MMP08, FM$^+$09]	2500	300	2600	0.50	190	0.68	9.71	0.07	C	S	0.25
40	CL06	F	[MMP08, FM$^+$09]	1250	300	2600	0.50	190	0.50	10.00	0.05	C	F	1.95
41	CL07	TG	[MMP08, FM$^+$09]	1250	300	2600	0.50	190	0.50	7.14	0.07	C	S	0.22
42	CL08	TG	[MMP08, FM$^+$09]	2500	300	2600	0.50	190	0.68	6.80	0.10	C	S	0.40
43	W1	F	[GT84]	3600	150	2000	1.04	190	0.77	8.25	0.09	M	S	0.94
44	W2	F	[GT84]	3600	150	2000	1.04	190	2.38	8.25	0.29	M	H	0.40
45	W4	F	[GT84]	3600	150	2000	2.11	190	0.78	8.25	0.09	M	H	1.11
46	W6	F	[GT84]	3600	150	2000	1.04	190	0.77	8.25	0.09	C	D	0.45
47	W7	F	[GT84]	3600	150	2000	1.04	190	2.39	8.25	0.29	C	S	0.20
48	MR-A1	MP	[SG10]	1500	150	1190	1.43$^{1)}$	190	1.00	9.40	0.11	C	H	0.51
49	MR-B1	MP	[SBG10]	1800	150	1400	1.36$^{1)}$	190	0.50	9.40	0.05	C	F	0.72
50	CM01	F*	[BP$^+$03]	950	120	1400	1.00$^{2)}$	65	2.72	14.98	0.18	C	D	0.57
51	CM02	F*	[BP$^+$03]	950	120	1400	1.00$^{2)}$	65	2.72	14.98	0.18	C	D	1.11
52	MI1m	F*	[MC92, MC97]	1500	150	2000	0.50	55	1.02	7.92	0.13	M	S	0.88
53	MI1	F*	[MC92, MC97]	1500	150	2000	0.50	55	1.12	7.92	0.14	C	S	0.51
54	MI2	F*	[MC92, MC97]	1500	150	2000	0.50	55	0.68	7.92	0.09	C	S	0.60
55	MI3	F*	[MC92, MC97]	1500	150	3000	0.50	55	1.24	7.92	0.16	C	H	0.48
56	MI4	F*	[MC92, MC97]	1500	150	3000	0.50	55	0.69	7.92	0.09	C	S	0.50
57	ISP1	F*	[MC92, MC97]	1000	250	1350	0.50	55	0.60	6.20	0.10	C	S	0.44
58	ISP3	F*	[MC92, MC97]	1000	250	2000	0.50	55	1.08	6.20	0.17	C	F	0.53
59	PUP1	F	EPFL-Test	2010	200	2250	0.50	190	1.05	5.86	0.18	C	S	0.25
60	PUP2	F	EPFL-Test	2010	200	2250	0.75	190	1.05	5.86	0.18	C	S	0.40
61	PUP3	F	EPFL-Test	2010	200	2250	1.50	190	1.05	5.86	0.18	C	F	0.80
62	PUP4	F	EPFL-Test	2010	200	2250	1.50	190	1.54	5.86	0.26	C	H	0.40
63	PUP5	F	EPFL-Test	2010	200	2250	0.75	190	0.55	5.86	0.09	C	S	0.60
64	PUP6	F	EPFL-Test	2010	200	2250	1.55	190	1.54	5.86	0.26	A	S	0.75
	Min			950	120	1170	0.50	55	0.40	2.41	0.05			0.14
	Max			3600	300	3000	2.11	240	2.72	14.98	0.29			2.91

Legend:
Type of masonry: F=Hollow clay brick masonry with fully mortared joints, F*= Solid clay brick masonry with fully mortared joints, No= Hollow clay brick masonry with unfilled head joints, MP=Mortar pocket masonry, TG=Tongue and groove masonry (unfilled head joints).
Loading history: C=symmetric cycles, M=monotonic loading, A=asymmetric cycles.
Failure modes: S= Shear failure, F=Flexural failure, H=Hybrid failure, D=Failure mechanism doubtful/unknown
The data on test units 1-42 was taken from [FM$^+$09]. The first references indicated are the primary references given in [FM$^+$09].

$^{1)}$ Shear span estimated from drawing or photo of test setup in corresponding reference.
$^{2)}$ Shear span could not be estimated from corresponding reference.
$^{3)}$ Primary reference was not specified in [FM$^+$09].

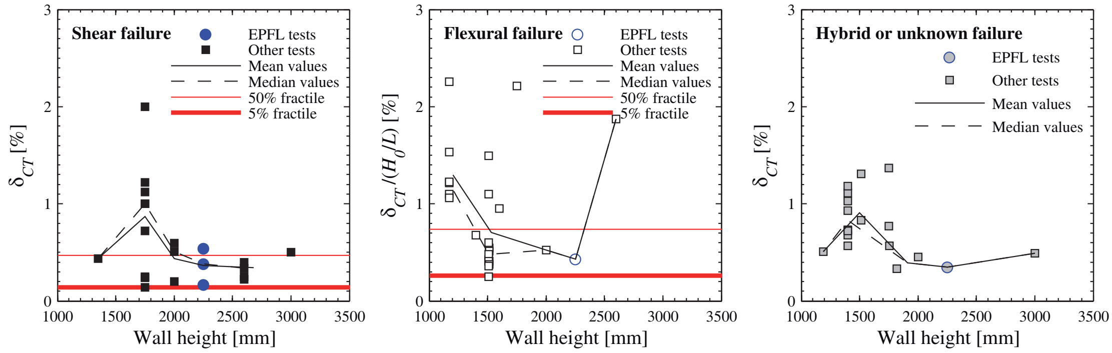

Figure 15. Modified EC8-Part 3: Comparison of best-fit drift capacities to drift capacity obtained from quasi-static tests on walls with different heights

for story-high walls. The trend in the experimental data agrees, with results of a numerical study by Lourenço [Lou97] who analyzed masonry structures at different scales by means of simplified micro models. Lourenço [Lou97] found that the maximum strength of masonry walls increased as the size of the specimen was reduced. This applied if failure occurred due to tensile failure of bricks or due to crushing of the masonry. For sliding failure, the strength was independent of the size as sliding is a ductile mechanism. For compression failure modes, which are characterized by a softening regime after reaching the peak strength, also the slope of the post-peak branch depended strongly on the size of the test unit: the larger the wall, the steeper the drop in strength after peak strength and thus the smaller the displacement capacity associated with horizontal load failure. Lourenço acknowledged that the adopted modeling approach might not be adequate for capturing correctly compression failure. However, his results are confirmed qualitatively by the experimental data in Fig. 14: most walls subjected to horizontal displacements fail eventually due to crushing of the compression zone or the failure along a diagonal crack passing through bricks. For such failure modes, size effects are expected to play a role. A pure sliding failure, which would not be affected by size effects, is hardly observed. Most failure modes are in fact hybrid modes and depending on the contribution of the different mechanisms, the size effect might influence the drift capacity to different extents. At present, mechanical models that predict the deformation capacity of URM walls are, however, lacking and one must fall back on simple empirical models. To account for the size effect in empirical drift capacity models a height dependent term should be introduced; a simple model including such a term is proposed in Section 5.5.

5.5 Revised empirical relationships for the drift capacity of URM walls

In the following, the coefficients of three different drift capacity models of walls are evaluated from the dataset of Table 5. These are: (i) the model in EC8-Part 3 [CEN05] which distinguishes between failure modes, (ii) the model in SIA D0237 [PLBL11] which accounts for the boundary conditions (axial stress ratio and moment profile), and (iii) a new model which introduces a height dependent term to the SIA-model. In accordance with the definition of CT, only walls subjected to symmetric cycles are considered.

5.5.1 Drift capacity models based on failure modes (Modified EC8 model)

Figure 15 plots for three different failure modes (shear, flexural, hybrid/unknown) the experimentally determined drift capacities as a function of the test units' height. For all three

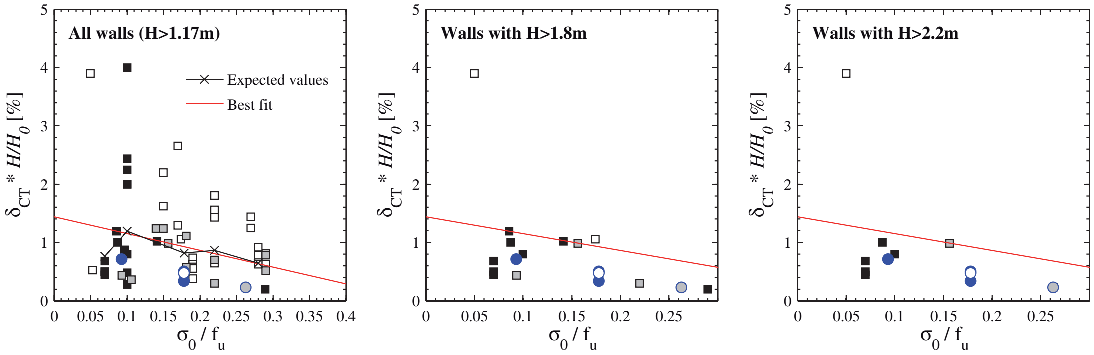

Figure 16. Modified SIA-model: Comparison of best-fit drift capacities to drift capacities obtained from quasi-static cyclic tests on walls with different heights

failure modes, the drift capacities decrease with the wall height. Based on the cyclic tests of the dataset in Table 5, the 5 and 50 % fractile values of the drift capacity of walls of all heights failing in shear and flexure are:

Shear failure (22 test units, Fig. 15a): $\delta_{CT,5\%} = 0.14\%$ $\delta_{CT,50\%} = 0.47\%$

Flexural failure (25 test units, Fig. 15b): $\delta_{CT,5\%} = 0.26\% H_0/L$ $\delta_{CT,50\%} = 0.74\% H_0/L$

Including the slenderness ratio H_0/L does not improve the goodness of fit. It is therefore suggested to omit, as the Italian code does [NTC08, MIT08], the slenderness ratio and to estimate the flexural drift capacity also by a constant value:

Flexural failure (25 test units): $\delta_{CT,5\%} = 0.41\%$ $\delta_{CT,50\%} = 1.00\%$

The ratios between 5 and 50 % fractile values are for shear and flexural failure modes approximately 2.5–3. Assuming a drift ratio $\delta_{NC}/\delta_{SD} = 4/3$ [CEN05] and $\psi_{SR} \cdot \psi_{LH} = 2–3$ one obtains the following drift capacities at the SD limit state:

Shear failure: $\delta_{SD,5\%} \simeq 0.20 - 0.30\%$ $\delta_{SD,50\%} \simeq 0.70 - 1.05\%$

Flexural failure: $\delta_{SD,5\%} \simeq 0.60 - 0.90\%$ $\delta_{SD,50\%} \simeq 1.50 - 2.25\%$

The values were rounded to the nearest 0.05. The 5% fractile values are slightly smaller than the drift capacities proposed in EC8-Part 3 [CEN05], which would correspond for the assumed correction factors to 10–30% fractile values of the dataset in Table 5.

5.5.2 Drift capacity model based on boundary conditions (Modified SIA-model)

To generalize the effect of the shear span on the wall's drift capacity, Eqs. (5) and (6) are condensed into:

$$\delta_{CT} = \delta_0 \cdot (1 - \alpha \frac{\sigma_0}{f_u}) \cdot \frac{H_0}{H} \tag{8}$$

The best fit line obtained for the dataset of Table 5 yields the following coefficients:

$$\delta_{CT,50\%} = 1.45\% \cdot (1 - 2.0 \frac{\sigma_0}{f_u}) \cdot \frac{H_0}{H} \tag{9}$$

Equation (9) should only be applied to test units with $0.07 \leq \sigma_0/f_u \leq 0.30$ and $0.5\ H_0/H \leq 1.5$. Assuming again a lognormal distribution of the drift capacities, the values should be divided by 3.0 if 5%-fractile values of the drift capacity are sought. The best fit line was obtained as follows: (i) the drift capacities $\delta_{CT} \cdot H/H_0$ were plotted against σ_0/f_u and the data points grouped in intervals of 0.05 σ_0/f_u; (ii) for tests within one interval, the drift values were assumed lognormally distributed and independent of σ_0/f_u (the expected drift value was determined for each interval); (iii) Eq. (9) is the linear approximation of these expected drift values. Fig. 16a shows for the entire dataset the expected values of the σ_0/f_u intervals and the best fit line (Eq. 9). When compared to two subsets including walls with $H \geq 1.8$ m and $H \geq 2.2$ m, respectively (16b, 16c), Eq. (9) overestimates the drift capacity but one can also note that the scatter reduces considerably as walls of smaller height intervals are considered. Note that the data for $H \geq 2.2$ m walls comprises all three failure modes and test data from three different types of masonry typologies, i.e. hollow clay brick masonry, solid clay brick masonry and tongue and groove masonry (F, F*, TG). The results presented in Fig. 16 underscore that the drift capacity should decrease with increasing wall height (Section 5.4).

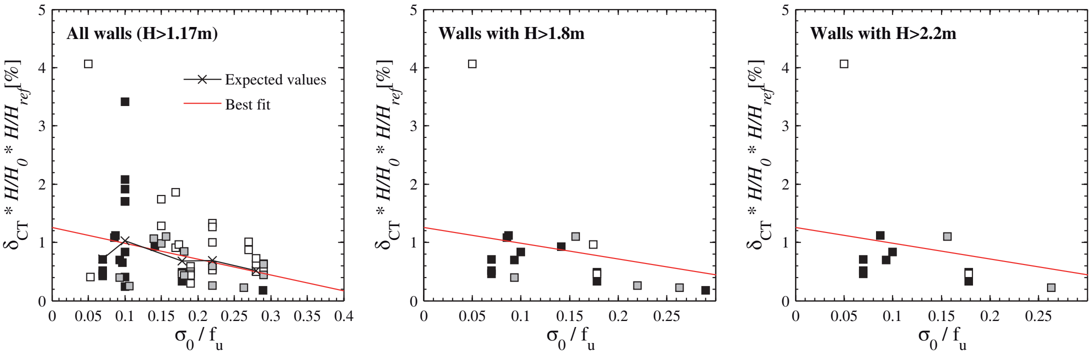

Figure 17. New-model: Comparison of best-fit drift capacities to drift capacities obtained from quasi-static cyclic tests on walls with different heights

5.5.3 Drift capacity model based on boundary conditions and size effect (New model)

In order to account for the decreasing drift capacity with increasing height, an additional term is introduced into Eq. (9).

$$\delta_{CT,50\%} = \delta_0 \cdot (1 - \alpha \frac{\sigma_0}{f_u}) \cdot \frac{H_0}{H} \cdot (\frac{H_{ref}}{H})^{\beta} \tag{10}$$

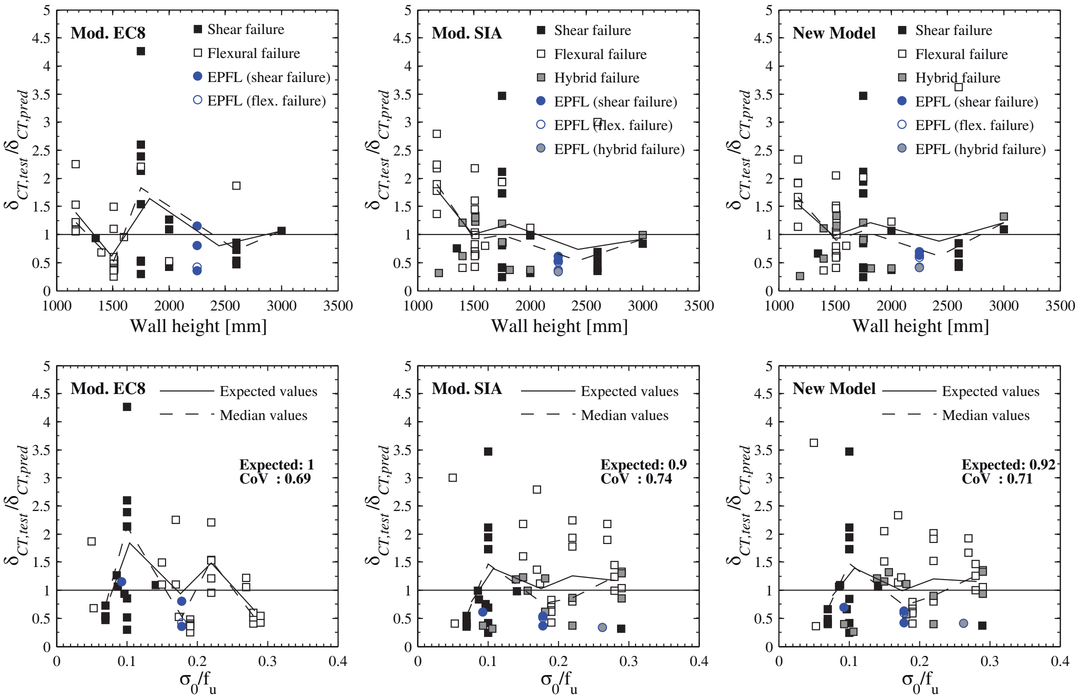

Figure 18. Ratio of predicted to observed drift ratios for (a) and (b) modified EC8 model (Shear failure: $\delta_{CT,50\%} = 0.47\%$, Flexural failure: $\delta_{CT,50\%} = 1.00\%$), (c) and (d) modified SIA model (Eq. 9), (e) and (f) the new model (Eq. 11)

Ideally, the form and coefficients of the term accounting for size effect should be derived from a mechanical model. In the absence of the latter, this simple form is chosen: the coefficient β set to 0.5 and H_{ref} to a constant value of 2400 mm. The best-fit line is computed as outlined in the previous section and the following coefficients are obtained:

$$\delta_{CT,50\%} = 1.3\% \cdot (1 - 2.2\frac{\sigma_0}{f_u}) \cdot \frac{H_0}{H} \cdot (\frac{H_{ref}}{H})^{0.5} \tag{11}$$

When compared to the two subsets (walls with $H \geq 1.8$ m and $H \geq 2.2$ m), Eq. (11) yields reasonable approximations of the expected drift capacities although it was calibrated on the entire dataset (Fig. 17a). Assuming again a lognormal distribution of the drift capacities, the values should be divided by 2.8 if 5%-fractile values of the drift capacity are sought. For a drift ratio $\delta_{NC}/\delta_{SD} = 4/3$, $\psi_{LH} \cdot \psi_{SR} = 2 - 3$ and $f_u = 2.4 f_d$ one obtains as drift limits for the δ_{SD} limit state:

$$\delta_{CT,50\%} = (0.7\% \div 1.0\%) \cdot (1 - 0.9\frac{\sigma_0}{f_d}) \cdot \frac{H_0}{H} \cdot (\frac{H_{ref}}{H})^{0.5} \tag{12}$$

Figure 18 shows the ratio of predicted to observed drift capacities. It is clear that the uncertainty remains also for the new model considerable. However, noticeable trends of the ratio of observed to predicted drift capacities with σ_0/f_u and wall height have been eliminated.

6 Conclusions

In a first part, the paper presents results of six quasi-static cyclic tests on URM walls which investigated the effect of the boundary conditions on the deformation behavior of URM walls. The boundary conditions were characterized in terms of applied axial load ratio and moment restraint provided at the top of the wall, which was expressed in terms of the shear span. The results showed that the larger the axial load ratio or the smaller the shear span, the smaller the drift capacity of URM walls. For larger axial load ratios, shear cracks tended to pass through bricks rather than joints leading to faster strength degradation and hence, to a smaller drift capacity of the walls. For a smaller shear span, the contribution of the flexural deformations of the masonry, which result from the opening of horizontal joints, was significantly reduced, resulting in a smaller total drift capacity of the walls. In the second part of the paper a dataset comprising the results of 64 quasi-static tests on URM walls was analyzed. This dataset confirmed the trends observed with regard to the boundary conditions from the first part of the paper. The analysis of the dataset showed further the importance of size effects on the deformation capacity of URM walls: with increasing test unit size, the drift capacity of the walls reduced. Empirical estimates of drift capacities that are included in today's codes do not account for this effect and drift capacity models are independent of the wall's height (e.g. [PLBL11]). As a result, when applied to story-high walls, drift capacities are overestimated. For seismic analysis of URM structures, a new drift capacity model was proposed, which consists of three components: A drift capacity CT derived from quasi-static cyclic tests and two correction factors - ψ_{LH} and ψ_{SR} - accounting for loading history and strain rate effects. Determining the two correction factors was out of the scope of this article and significant further research is required; as a first rough value we estimate from own tests a value of 2–3 for $\psi_{SR} \cdot \psi_{LH}$. For δ_{CT} a new model accounting for boundary conditions (axial load ratio and moment profile) and size effects was proposed. Unlike previous models (EC8-Part 3 [CEN05], SIA D0237 [PLBL11]), this model reflects the reduced drift capacity with the increasing wall height. For the time being, this size effect is only accounted by means of the simple term $(H_{ref}/H)^{0.5}$, which lacks a sound justification. H_{ref} is a reference height and is for the time being set equal to a typical story height (H_{ref} = 2400 mm). Future research should aim at developing a mechanical model for the drift capacity of URM walls, which allows deriving the parameters controlling the size effect. Furthermore, an improved link between drift capacities obtained from quasi-static cyclic tests and drift capacities attained during real seismic loading must be established.

7 Acknowledgments

The authors would like to thank the three reviewers for their comments that helped to improve the quality and increase the scope of the paper. The authors also thank Morandi Frères SA for the donation of the bricks and the staff of the structural engineering laboratory at EPFL for the support during testing.

References

[Abr96] Abrams, DA. Effects of scale and loading rate with tests of concrete and masonry structures. *Earthquake Spectra*, 12(1):13–28, 1996.

[ATC97] ATC. Nehrp guidelines for the seismic rehabilitation of buildings. Technical Report FEMA-273, Basic Procedures Manual, Applied Technology Council (ATC), Washington DC, USA, 1997.

[ATC98] ATC. Evaluation of earthquake damaged concrete and masonry wall buildings. Technical Report FEMA-306, Basic Procedures Manual, Applied Technology Council (ATC), Washington, DC, USA, 1998.

[BP+03] Bosiljkov, V, Page, AW, Bokan-Bosiljkov, V and Zarnič, R. Performance based studies of in-plane loaded unreinforced masonry walls. *Masonry International*, 16(2):39–50, 2003.

[BT03] Bosiljkov, V and Tomaževič, M. test report, Ljubljana, Slowenia, 2003.

[BT06] Bosiljkov, V and Tomaževič, M. Optimization of shape of masonry units and technology of construction for earthquake resistant masonry buildings. Research report - part three, ZAG, Ljubljana, Slowenia, 2006.

[CEN02] CEN. EN 1052-1: Methods of test for masonry, Part 1: Determination of compressive strength. Technical Report EN 1052-1:1998-12, European Committee for Standardisation, Brussels, Belgium, 2002.

[CEN04] CEN. Eurocode 8: Design of structures for earthquake resistance, Part 1: General rules, seismic actions and rules for buildings. Construction Code EN 1998-1:2004, European Committee for Standardisation, Brussels, Belgium, December 2004.

[CEN05] CEN. Eurocode 8: Design of structures for earthquake resistance, Part 3: Assessmemt and retrofitting of buildings. Technical Report EN 1998-3, European Committee for Standardisation, Brussels, Belgium, June 2005.

[CEN07] CEN. EN 1052-3: Methods of test for masonry, Part 3: Determination of the initial shear strength. Technical Report EN 1052-3:2002+A1:2007 D, European Committee for Standardisation, Brussels, Belgium, 2007.

[Elg04] Elgawady, M. *Seismic in-plane behavior of URM walls upgraded with composites.* Phd thesis, EPF Lausanne, Lausanne, Switzerland, 2004.

[FM+09] Frumento, S, Magenes, G, Morandi, P and Calvi, GM. *Interpretation of experimental shear tests on clay brick masonry walls and evaluation of q-factors for seismic design.* Technical Report, IUSS PRESS, Pavia, Italy, 2009.

[GT84] Ganz, HR and Thürlimann, B. Versuche an Mauerwerksscheiben unter Normalkraft und Querkraft. Technical Report Test Report 7502-4, ETH Zürich, Zürich, Switzerland, 1984.

[Lan02] Lang, K. *Seismic vulnerability of existing structures.* Phd thesis, ETH Zürich, Institute of Structural Engineering, Zürich, Switzerland, February 2002.

[Lou97] Lourenço, PB. *Two aspects related to the analysis of masonry structures: size effect and parameter sensitivity.* Technical report, tu-delft no 03.21.1.31.25/ tno-bouw no 97-nm-r1533, Faculty of Engineering, TU Delft, Netherlands, 1997.

[LP+13] Lagomarsino, S, Penna, A, Galasco, A and Cattari, S. Tremuri program: an equivalent frame model for the nonlinear seismic analysis of masonry buildings. *Engineering Structures*, 56:1787–1799, 2013.

[MC92] Magenes, G and Calvi, GM. Cyclic behaviour of brick masonry walls. In *Proceedings of the 10th world conference on earthquake engineering*, pages 3517–22, Madrid, Spain, 1992.

[MC97] Magenes, G and Calvi, GM. In-plane seismic response of brick masonry walls. *Earthquake Engineering and Structural Dynamics*, 26:1091–112, 1997.

[MDPG05] Modena, F, Da Porto, F and Garbin, F. Ricerca sperimentale sul comportamento di sistemi per muratura portante in zona sismica. Draft 2005/01, University of Padua, Padua, Italy, 2005.

[MIT08] MIT. Circ. c.s.ll.pp. no. 617 of 2/2/2009: Istruzioni per l`applicazione delle nuove norme tecniche per le costruzioni di cui al decreto ministeriale 14 gennaio 2008. Technical Report G.U. S.O. n. 27 of 26/2/2009 No. 47, Ministry of Infrastructures and Transportation, 2008.

[MMP08] Magenes, G, Morandi, P and Penna, A. Enhanced safety and efficient construction of masonry structures in europe, 7.1c test results on the behaviour of masonry under static cyclic in plane lateral loads. Technical Report ESECMaSE D7.1c, University of Pavia, Pavia, Italy, 2008.

[NTC08] NTC. Decreto ministeriale 14/1/2008: Norme tecniche per le costruzioni. Technical Report G.U.S.O. n.30 on 4/2/2008, Ministry of Infrastructures and Transportations, 2008.

[NZS06] NZSEE. Assessment and improvement of unreinforced masonry buildings for earthquake resistance. Technical report, New Zealand Society of Earthquake Engineering, University of Auckland, New Zealand, 2006.

[NZS11] NZSEE. Assessment and improvement of unreinforced masonry buildings for earthquake resistance, supplement to assessment and improvement of the structural performance of buildings in earthquakes. Technical report, New Zealand Society of Earthquake Engineering, University of Auckland, New Zealand, 2011.

[PA90] Paulson, TJ and Abrams, D. Correlation between static and dynamic response of model masonry structures. *Earthquake Spectra*, 6:573–591, 1990.

[PLBL11] Pfyl-Lang, K, Braune, F and Lestuzzi, P. Evaluation de la sécurité parasismique des bâtiments en maçonnerie. Technical Report SIA D0237, Documentation, Swiss Society of Engineers and Architects SIA, Zürich, Switzerland, 2011.

[PLG14] Penna, A, Lagomarsino, S and Galasco, A. A nonlinear macroelement model for the seismic analysis of masonry buildings. *Earthquake Engineering and Structural Dynamics*, 43:159–179, 2014.

[RIL91] RILEM. RILEM TC76-LUM: Diagonal tensile strength tests of small wall specimens. Technical Report TC76-LUM, RILEM Publications SARL, Brussels, Belgium, 1991.

[SBG10] Suter, R, Broye, A and Grisanti, M. Essais de cisaillement de murs en maçonnerie renforcesm, serie experimentale mr–a. Technical Report Report Projet de recherche AGP 21´159, Ecole d´ingénieurs et d´architectes de Fribourg, Fribourg, Switzerland, 2010.

[SG10] Suter, R and Grisanti, M. Essais de cisaillement de murs en maçonnerie renforces, serie experimentale mr–b. Technical Report Report Projet de recherche AGP 21´159, Ecole d´ingénieurs et d´architectes de Fribourg, Fribourg, Switzerland, 2010.

[SIA05] SIA. SIA266: Masonry. Construction Code, Swiss Society of Engineers and Architects SIA, Zürich, Switzerland, 2005.

[Tom99] Tomaževič, M. *Earthquake-resistant design of masonry buildings*, volume 1 of *Series on Innovation in Structures and Construction.* Imperial College Press, London, UK, 1999.

[Tom00] Tomaževič, M. Some aspects of experimental testing of seismic behaviour of masonry walls and models of masonry buildings. *ISET Journal of Earthquake Technology*, 37:101–117, 2000.

Paper II

Scaling unreinforced masonry for reduced-scale seismic testing

Petry, S and Beyer, K; *Bulletin of Earthquake Engineering* (2014), 12(6):2557–2581, DOI: 10.1007/s10518-014-9605-1

Abstract

When testing multi-story structures, most testing facilities require the testing of a reduced-scale model. A literature review on tests of scaled masonry structural components revealed that scaling of masonry was rather challenging and often significant differences in stiffness, strength and failure mechanisms between the different sized masonry were reported. This paper addresses the scaling of hollow clay brick masonry with fully mortared head and bed joints. We investigate different choices of scaling brick units and mortar joints. Based on the results of an extensive test program including standard material tests and quasi-static cyclic tests on masonry walls subjected to horizontal and axial loads, we formulate recommendations for the production of a half-scale model of unreinforced masonry structures. The experimental results show a good match between full-scale and half-scale masonry. We discuss the differences in material properties that remained and compare the force-displacement hysteresis obtained for the wall tests.

Keywords:

Unreinforced masonry; Small-scale testing; Displacement capacity; Force capacity; Mechanical properties;

1 Introduction

A general problem in experimental testing of civil engineering structures relates to the required size of the test unit: the examined structures are normally of such large dimensions (buildings, bridges, etc.) that it is usually impossible to test entire structures at full-scale. As a consequence, either only parts of the whole structure are tested or the test units are model structures which are scaled down to a size that can be accommodated in the testing facility. The latter is typically required for shake table tests of multi-story structures. With respect to the scaling of unreinforced masonry structures, the results reported in the literature are inconclusive: While some early works report a good similitude with regard to the global behavior of URM panels at different scales [SH69, HS71] more recent works on scaling of masonry reported unsatisfactory similitude of stiffness, strength and failure mechanisms, e.g. [ECA91, Abr96]. All reports in the literature relate to the scaling of solid brick masonry. The aim of this article is to provide recommendations for the scaling of bricks and mortar joints for hollow clay brick masonry. When dealing with seismic tests, the model masonry at half-scale should behave as similar as possible as the prototype masonry when subjected to axial and horizontal loads. The similitude should extend to stiffness, strength, hysteretic behavior, failure mode and deformation capacity of the masonry. This study was conducted as preparation for a shake table test on a modern 4-story building with reinforced concrete and unreinforced masonry walls.

Since the scaling of hollow clay brick masonry has not been discussed in the literature before, our investigation builds on the findings of studies on the scaling of solid clay brick masonry, which was investigated in several research projects.We modify these where required and address also questions that are specific to the scaling of hollow clay brick masonry such as for example the scaling of web and shell thicknesses of the brick. Furthermore, most previous investigations addressed the similarity of small-scale and full-scale masonry on the basis of force-based tests on material components and small masonry assemblies. With the introduction of performance-based design, the focus of seismic tests lies next to the strength also on the deformation capacity of the structure. For this reason, studies on the scale effect need to address the similitude with regard to the entire force-displacement response up to failure. To do so, we conduct besides standard material tests quasi-static cyclic tests at full and half-scale and compare stiffness, strength, hysteretic energy, deformation capacity, crack widths and failure mode.

This article commences with a review of studies on the scaling of solid clay masonry (Sec. 2). Based on these findings and own tests on hollow clay brick masonry, guidelines for the scaling of the brick unit and the mortar joint are proposed (Sec. 3). The resulting model masonry is compared to the prototype masonry through standard material tests (Sec. 4) and quasi-static cyclic tests on walls (Sec. 5). Section 6 concludes on the main points that need to be considered when developing hollow clay brick masonry for small-scale testing.

2 Scaling of masonry: literature review

According to Tomaževič, three similarities are important for obtaining a good similitude in the overall behavior of reduced-scale and full-scale masonry structures [Tom87]: (i) the similarity in failure mechanism, (ii) the similarity of stresses and (iii) the similarity in mass and stiffness. The similarity in failure mechanism is important for a correct simulation of energy dissipation. The type of failure mechanism that forms depends on shear and axial stresses acting on the

Variable	Scaling	Variable	Scaling
Length	S_l	Strain	1
Time	$\sqrt{S_l}$	Stress	1
Frequency	$1/\sqrt{S_l}$	Strength	1
Velocity	$\sqrt{S_l}$	E-modulus	1
Gravity	1	Displacement	S_l
Acceleration	1	Force	S_l^2
Mass density	1	Moment	S_l^3

Table 1 Scaling laws for an artificial mass simulation [Kra79]

masonry, which in a dynamic test are controlled by the mass and the dynamic properties of the structure. The following sections outline the scaling laws for dynamic tests on small-scale specimens, the effect of scaling on the mechanical properties of masonry and the approaches documented in the literature aiming at reducing the differences in mechanical properties between small and full-scale masonry.

2.1 Dimensional analysis for a masonry specimen

Several theoretical scaling laws exist, which describe the ideal relationship between different physical properties that are affected by the scaling (e.g. [Kra79, TV92]). For the scaling of masonry structures, the Artificial Mass Simulation scaling law is typically applied [Kra79]. This scaling law requires that the reduced scale masonry has the same mechanical properties (density, stiffness, strength, drift capacity) as the full-size masonry. Attempts in the past to apply scaling laws to masonry that require a modification of the small-scale masonry properties and therefore the usage of different materials for the brick at small- and full-scale led often to a compromise between required mass and strength of the model material. Poor similitude in the behavior of the model and prototype masonry allowed only a qualitative comparison of the seismic response of model and full size structure [Tom87].

When applying the Artificial Mass Simulation scaling law, the density of the material at reduced- and full-scale is the same. If the length is divided by a factor of S_l, the area reduces by S_l^2. Since the gravity forces are related to the volume (S_l^3) and the gravitational constant g remains unaltered, a mass equal to (S_l^1) times the mass of the scaled structure has to be added in order to guarantee equal stresses due to gravity loads. As previously noted, equal vertical stresses are essential for obtaining a similar behavior at small- and full-scale. In order to obtain also equal horizontal accelerations and therefore shear stresses, the time has to be scaled by $\sqrt{S_l}$ since the displacements are S_l times smaller at small-scale than at full-scale. The resulting scaling laws for the Artificial Mass Simulation are summarized in Table 1.

2.2 Scaling effects on the mechanical properties of solid clay brick masonry

As outlined in the previous paragraph, applying the Artificial Mass Simulation scaling law requires that small- and full-scale masonry have the same mechanical properties, i.e. in particular the same density, stiffness, strength and deformation capacity. While the scaling of hollow clay brick masonry has not been addressed in the literature, scaling of solid clay brick masonry has been the subject of several research projects. This section summaries the findings from studies on scaled solid clay brick masonry while the following sections (Sects. 2.3, 2.4) outline different attempts documented in the literature that aim at modifying the model bricks and joints in order to minimize these differences.

2.2.1 Compressive strength of masonry

The most recent detailed experimental study on scaling of solid clay brick masonry is presented by Mohammed [Moh06] and Mohammed and Hughes [MH11] which comprises different standardized material tests at different scales (1/6-, 1/4-, 1/2- and full-scale). When comparing the results of compression tests, similar failure patterns were observed for the specimens at all scales. Despite this, the compressive strength was significantly higher for the masonry panels tested at 1/6- and 1/4-scale than the compressive strength of the full-scale masonry. The 1/2-scale masonry developed a compressive strength similar to the full-scale masonry. This is in agreement with the findings by previous studies (e.g. [HM65]), which also found an increased compressive strength for small-scale masonry.

The increase in strength was attributed to the following two phenomena: (1) the burning of a reduced-scale brick can lead to an increased brick strength [ECA91] and (2) the scaling of the mortar joint affects the percentage of water sucked from the mortar by the brick during the curing of the mortar and thus the strength of the mortar joint [DH08, MH11]. Mohammed [Moh06] reported that the brick unit at 1/6- and 1/4-scale was indeed slightly stronger in compression than the prototype brick. Nevertheless, the brick strength at different scales varied less than the masonry strength and it was therefore concluded that both phenomena contribute to the difference in compressive strength between full-scale and small-scale masonry. One alternative could be to scale only the width of the bricks but neither length, nor height of the brick nor the thickness of the mortar joints. However, Hamid et al. [HAH86] showed that the compressive strength is related to the number of the brick courses and also Frumento et al. [FM$^+$09] noted that walls with less courses yielded different results when subjected to lateral loading due to the larger restraint provided by the beams at the top and bottom. Therefore, the scaling of brick size and mortar joint thickness is recommended.

2.2.2 Axial stiffness of masonry

Other researchers reported that the scaling affects also the axial stiffness due to the different overburden stresses during construction [HM65, ECA91]. Since the additional masses required by the Artificial Mass Simulation scaling law are typically only installed after the construction of the entire structure has been completed, the compressive stresses acting on the bed joints during curing of the mortar of the small-scale masonry are only half of those of the full-scale masonry. To avoid the difference in overburden stresses, Mohammed and Hughes [MH11] built their specimens horizontally and obtained from compression tests similar stiffnesses in the elastic range for the small- and full-scale masonry. While such a construction practice is feasible when conducting material tests on small specimens, it is not possible to construct entire shake table test units in a horizontal position nor does this construction practice reflect the stiffness of real masonry structures. Such an approach is therefore valid for investigating the effect of different parameters on the scaling but cannot be part of recommendations for the construction of scaled test units for shake table tests.

2.2.3 Shear behavior of masonry

Although scaling of unreinforced masonry structures is particularly relevant for shake table testing, most research projects on scaling investigated chiefly masonry panels subjected to vertical loads and not to horizontal loads. Exceptions are (i) the study by Benjamin and Williams [BW58] who investigated the scale effect on the shear strength of infill masonry walls with concrete frames; (ii) the study by Sinha and Hendry [SH69] and Hendry and Sinha [HS71] who compared the shear behavior of masonry panels at full- and reduced-scale, (iii) the study by Abrams [Abr96] who compared the behavior of a 2-story URM building at full- and reduced-scale when subjected to lateral loading; and (iv) the study by Mohammed and Hughes [MH11] who studied the influence of the scaling on the masonry shear strength through triplet tests and diagonal compression tests.

In the first study, Benjamin and Williams [BW58] tested one story, single bay RC frames with masonry infills with solid bricks. They compared models at different scales up to 1:4 to prototype specimens. Infills at all scales were constructed using the same solid brick type and the width of the walls was varied by changing the orientation of the bricks. As a result, the number of brick layers changed between scales. According to the literature (e.g. [HAH86, DH08], changing the number of layers affects the shear strength of the masonry and thus a comparison of the models and prototypes is somewhat questionable. Furthermore, as reported by Benjamin and Williams [BW58], the scatter of the results within each test series was so significant that a clear trend with the scaling factor could not be identified.

Sinha and Hendry [SH69] and Hendry and Sinha [HS71] compared full-size URM panels with and without openings with experiments on 1/6-scale panels. The panels were first subjected to a uniform axial compression and then to a lateral monotonic load. Generally, they observed a good agreement between the behavior of prototype and model panels and only with regard to the post peak behavior, the model panels tended to have an increased displacement capacity. While the compression strength reported in Sinha and Hendry [SH69] and Hendry and Sinha [HS71] is similar for both model and prototype brick, this study misses further discussion on the differences between both masonries at full- and 1/6-scale, e.g. surface properties of the model brick, thickness of mortar joints.

Abrams [Abr96] compared the lateral behavior of a reduced-scale 2-story URM building tested dynamically with a test performed on an equivalent structure at full-scale subjected to quasi-static cyclic loading. Since the test type varied between both tests, a comparison was difficult and Abrams [Abr96] associated most differences to the different loading histories.

In the last study [MH11], the model bricks were cut after the burning from prototype bricks leading to a smaller surface roughness when compared to the prototype brick that were wire-cut before the burning. As a result, Mohammed and Hughes [MH11] observed for the shear triplet tests on full-size masonry a significant higher cohesion and friction than for the model masonry. For the shear triplet tests on the three model masonries, an increase in initial shear strength and a decrease in friction coefficient were observed with increasing scaling factor. Concerning the diagonal compression test, on the contrary, no significant difference between the four scales was observed. Concerning the effect of the scaling on the deformation capacity, Mohammed and Hughes [MH11] observed a slight increase in post peak deformation capacity for reduced-scale specimens when tested in diagonal compression; unfortunately a similar statement with regard to the shear deformation capacity obtained from triplet tests is missing.

2.3 Producing solid clay brick units for model masonry

Model bricks are typically produced using the clay from the same pit and applying the same burning procedure as for the prototype bricks. As outlined above, the resulting model brick tends to be stronger than the prototype brick. Different approaches for reducing the difference in brick strength are reported in the literature. These can be grouped as follows: (i) using a different brick material for the model brick, (ii) reducing the burning temperature for the model brick, or (iii) cutting the model brick from a prototype brick after the burning.

Tomaževič [Tom87] showed that using a different material for the model brick proved to be too complicated and should be avoided, since not only the brick strength but also the brick density, stiffness and deformation capacity need to be matched. Egermann et al. [ECA91] experimented with a reduced burning temperature for producing solid clay model bricks but could not obtain a perfect match for the resulting compression strength of the brick. Tomaževič et al. [TW+90] reported good experiences with the use of model bricks cut after the burning from prototype bricks. Nevertheless, some differences might still be present: Mohammed [Moh06] noticed for solid bricks the importance of the orientation of the model brick within the original brick, which was also observed by Shrive and Jessop [SJ80]. Also the roughness of the cut surface should be considered [DHT95, MH11] since it determines the shear resistance of the mortar-brick interface.

2.4 Reducing scaling effects on mortar joint properties

In the model masonry the mortar joints have a smaller thickness than in the prototype masonry. The sucking behavior of the bricks is the main mechanism that affects the properties of the mortar and the joint-brick interface in solid clay brick masonry. The literature reports that for thinner joints the suction of the brick has a larger effect on mortar and interface properties, e.g. [DH08]. Due to the suction, the water-cement ratio of the mortar is changed and the crystallization process in the mortar modified. It is, however, difficult to quantify this effect. If the water-cement ratio is only slightly reduced, the strength in the mortar tends to increase. If it reduces significantly, not enough water might be left for the mortar to crystallize completely and the mortar strength might reduce rather than increase. Hence, dependent on the amount of water absorbed by the brick and the initial water-cement ratio of the mortar, the strength of the masonry will either increase or decrease [Moh06].

Several researchers investigated parameters that could help to control the reduction of the water-cement ratio in the mortar due to the suction process. Brocken et al. [BS+98] investigated the effect of pre-wetting the bricks but found that this affects the suction process only in a significant manner, if the water content of the brick reaches nearly saturation. They also studied the use of water retention products but concluded that the addition of water retention products does not influence significantly the quantity of water extracted, but only slows down the suction [BS+98]. Also Green et al. [GC+99] mentioned that only very large quantities of water retention products would show significant changes in the amount of water absorbed by the bricks - which could even for small-scale test units become eventually too costly.

3 Scaling hollow clay brick masonry

The objective of this project is to develop a half-scale masonry with hollow clay brick units that has very similar properties as the corresponding full-scale masonry. The behavior of modern masonry with hollow clay brick units is strongly influenced by the anisotropy of the bricks. Hence, when scaling such masonry not only the points outlined for solid brick masonry need to be considered but it is also important to maintain the anisotropy of the units.

3.1 Producing hollow clay brick units for model masonry

Modern hollow clay brick units are produced by extruding a clay strand through a form. Producing a new form for a model brick is rather expensive; moreover at the start of this project we did not know which characteristics this form should have. After discussions with several manufacturers we decided to take the form of an existing brick unit and adapt the outer dimensions of the brick by covering parts of the form; the latter can be done relatively easily. The following paragraphs summaries our considerations when developing a half-scale hollow clay brick unit.

The vertical compressive strength of hollow clay brick units is mainly influenced by the net area of the brick [Gan85]. While the shape of the perforation is not decisive for the vertical strength, it has a significant influence on the compressive strength parallel to the bed joints (in the following referred to as horizontal strength). Lourenço et al. [LV+10] showed that the horizontal compressive strength of bricks with continuous and straight webs and shells was significantly higher than for bricks with rice-shaped holes. When scaling hollow clay brick units it is therefore important to maintain the ratio of net to gross area and to choose a model brick that has a similar hole layout as the prototype brick. The hole layout of a brick can be scaled in two different ways, both respecting the similarity of the void ratio, of the effective width (defined as the net width of the brick) and the hole layout: (i) the geometry is scaled completely, including web and shell thicknesses, or (ii) shell and web thicknesses remain identical and the number of webs is decreased.

After testing several potential model bricks, we opted for a model brick which shell and web thicknesses were similar to those of the prototype brick unit. This yielded the best match of model and prototype brick with regard to the strength of the bricks. Note that this observation is also in good agreement with recommendations given by Eurocode 6 [CEN05], which classifies the robustness of masonry bricks according to void ratio, minimum thickness of web and shells and effective width of bricks. With the chosen model brick, all three parameters matched rather well between model and prototype brick.We assume further that the good similitude is based on the following phenomenon: While for solid bricks the development of the temperature in the center of the brick depends on the total size of the brick, for hollow clay bricks the web and shell thicknesses rather than the brick size are decisive. Keeping the web and shell thicknesses identical is therefore advantageous, because it allows the same drying and burning procedure to be used for the model brick as for the prototype brick. Scaling the web and shell thickness rather than reducing the number of webs and shells led also to a reduced strength and a very brittle behavior of the brick. The final choice of model brick for the prototype brick of this study is shown in Fig. 1 and the mechanical properties of both bricks are summarized in Table 2. Small differences remained with regard to the void ratio and effective width. When loaded perpendicular to the perforation, the model brick was therefore slightly stronger than the prototype brick.

3.2 Mortar for model masonry

The mortar joints of both masonries were fully filled using the cement-based mortar WEBER MUR MAXIT 920. It is one of the most commonly used mortars in Switzerland. The thickness of the joints of the model masonry was scaled. For the full-scale masonry, the measured mortar joint thickness varied between 10 and 12 mm and for the half-scale masonry between 5 and 7 mm. For both types of masonry, head and bed joints had the same thickness and were fully filled. As a result of the different joint thicknesses, the suction process described in the literature review led to a smaller effective water-cement ratio of the mortar for the model masonry than for the prototype masonry. The literature review showed that neither adding water retention products to the mortar nor saturating fully the brick proved to be an ideal

Table 2. Mechanical and geometrical properties of all investigated bricks (resulting material strength in bold)

	Full-scale brick	Half-scale brick	Ratio half- and full-scale
Average dimensions of a brick			
Length (mm)	297	148	-
Width (mm)	194	96	-
Height (mm)	189	94	-
Average mass and density of a brick			
Mass brick (kg)	9.9	1.3	-
Volumetric mass (kg/m^3)	901	996	1.10
Void ratios and effective length / width of a brick			
Void ratio (%)	49.3	39.5	0.80
Effective length [a] (%)	30.6	37.8	1.24
Effective width [a] (%)	28.9	36.5	1.26
Average strength and deviation			
Compression, $\parallel$ to perforation (MPa)	35.0 ± 7%	33.3 ± 25%	0.95
Compression, $\perp$ to perforation (MPa)	9.4 ± 8%	10.8 ± 17%	1.15
Flexural tensile strength, $\perp$ to perforation (MPa)	1.27 ± 38%	1.61 ± 41%	1.27

[a] The effective length / width describe the percentage of filled material to voids over the gross length / width

option for modifying the properties of the mortar for the model masonry. Own compression tests with different water retention products and pre-wetting of the bricks confirmed these results. Thus, it was decided to construct the half-scale masonry using the same mortar recipe as for the prototype masonry. As discussed in Sect. 2.4, measures such as constructing the

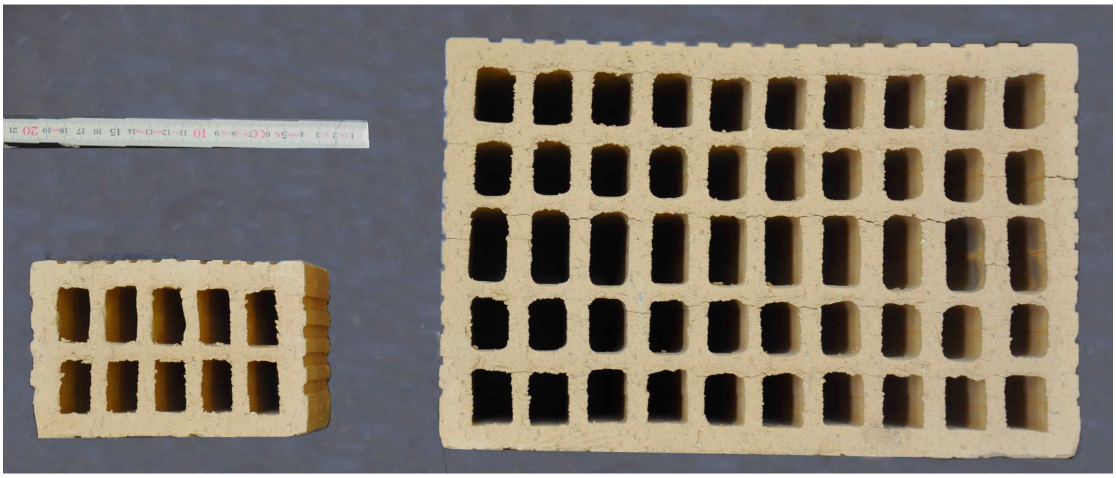

Figure 1. Final half-scale and full-scale brick from Morandi Frères SA, Switzerland

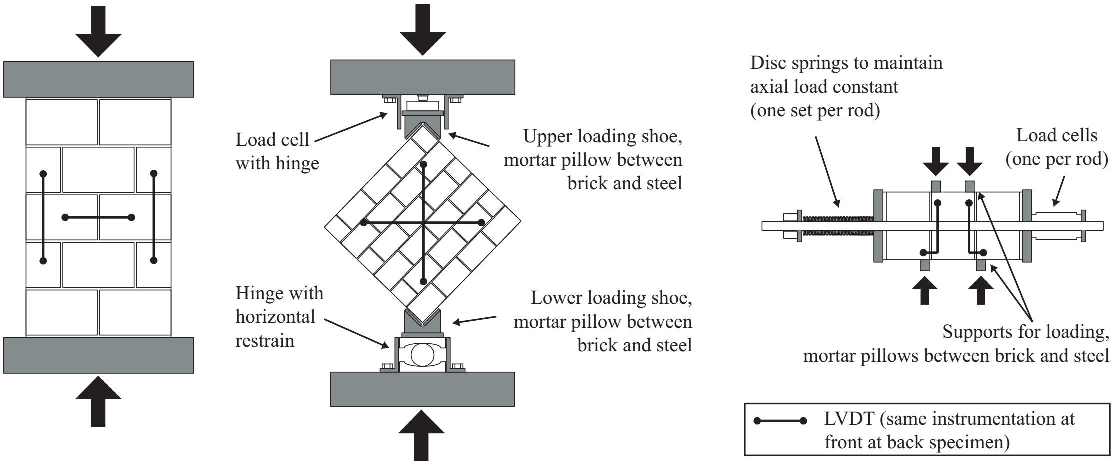

Figure 2. Material tests performed on half- and full-scale masonry: (a) compression test on masonry wallette, (b) diagonal compression test on square masonry wallette and (c) shear test on masonry triplet

masonry horizontally were not considered. In addition, the vertical construction assured a good penetration of the mortar inside the perforation of the brick, which is important for the shear transfer between mortar joint and brick in hollow clay brick masonry.

4 Similitude of the material properties of half- and full-scale masonry

Three kinds of material tests were performed on half- and full-scale masonry, i.e. compression tests, shear triplet tests and diagonal compression tests. The different setups for the material tests are illustrated in Fig. 2. The following sections compare the results obtained from these standard tests for the model masonry to those of the prototype masonry.

4.1 Compression tests

For the standard compression test [CEN02], a series of five specimens was constructed at each scale. During testing, the deformations of the panels were measured with four vertical and two horizontal LVDTs (Fig. 2). Figure 3 shows the stress-strain curves obtained from the compression tests. For solid brick masonry several researchers had reported an increase in compressive strength for smaller scales,which they attributed partly to the scaling of the brick and partly to the scaling of the mortar thickness (see Sect. 2). In this study, similar strength values were obtained for both brick units (see Table 2). Hence, an increase in masonry strength due to a stronger model brick was avoided and also the scaling of the joint did not affect the compressive strength significantly. As a result, a good match of the compressive strength values was obtained.

The modulus of elasticity E_c was determined as the secant modulus when reaching 1/3 of the maximum stress [CEN02]. The Poisson's ratio v was evaluated by comparing the vertical and horizontal strain for the same load point (see position of LVDTs in Fig. 2). While the two types of masonry match perfectly with regard to the Poisson's ratio, the E-modulus of the model masonry is 50% higher than the E-modulus of the prototype masonry. However, masonry is not isotropic. Thus, the herein determined Poisson's ratio describes the lateral expansion under vertical compression but is not suitable for determining the shear modulus G. In order to compare the E-modulus of model and prototype masonry for larger stress values,

Table 3. Results from the compression tests performed on half- and full-scale masonry panels (resulting material strength in bold)

	f_u (MPa)	$E_c = E_{0-1/3}$ (GPa)	E_c/f_u (-)	ν (-)	$E_{1/3-2/3}$ (GPa)	$E_{2/3-3/3}$ (GPa)	$E_{0-3/3}$ (GPa)
Full-scale masonry	5.87	3.55	613	0.20	4.26	4.28	4.00
	±5%	±9%	±10%	±19%	±7%	±11%	±8%
Half-scale masonry	5.66	5.46	965	0.20	4.74	4.08	4.50
	±4%	±8%	±11%	±65%	±11%	±16%	±9%
Ratio half- / full-scale	0.94	1.54	1.57	1.00	1.11	0.95	1.13

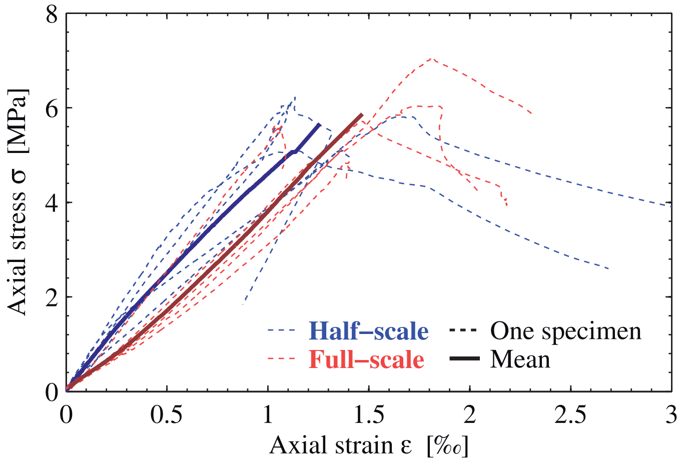

Figure 3. Stress-strain curves of the compression tests

the E-modulus is also evaluated comparing the vertical strain and the vertical stress at 1/3 and 2/3 f_u ($E_{1/3-2/3}$, the footnote stands for the stress and strain used, i.e. $\epsilon_{1/3} = \epsilon(\sigma = 1/3 f_u)$ and $E_{1/3-2/3} = (2/3 f_u - -1/3 f_u)/(\epsilon_{2/3}\epsilon_{1/3})$), at 2/3 f_u and f_u ($E_{2/3-3/3}$) and as secant stiffness at peak strength ($E_{0-3/3}$). The values are summarized in Table 3 and show that for larger stresses the E-moduli of the two types of masonry are rather similar.

Figure 3 also shows that the post-peak deformation capacity is subjected to considerable scatter but in average the post-peak deformation capacity of the half-scale masonry is larger for the model masonry than for the full-scale masonry. Lourenço [Lou97] pointed out that the deformation capacity of masonry failing in compression is affected by size effects, i.e. that reduced-scale masonry possesses a larger deformation capacity than full-scale masonry. The results of the compression tests and the quasi-static cyclic tests on the walls.as will be shown later.confirm this observation.

4.2 Shear triplet tests

Ten shear triplet tests [CEN07] were carried out at each scale. The triplets were tested for normal stresses between 0.2 and 0.6 MPa. The friction coefficient μ and the cohesion c characterizing the peak strength were obtained from a best-fit line. The residual shear strength was

	c (MPa)	μ (-)
Full-scale masonry	0.28	0.91
Half-scale masonry	0.23	0.70
Ratio half- / full-scale	0.82	0.77

Table 4 Results from the shear tests performed on half- and full-scale masonry triplets (resulting material strength in bold)

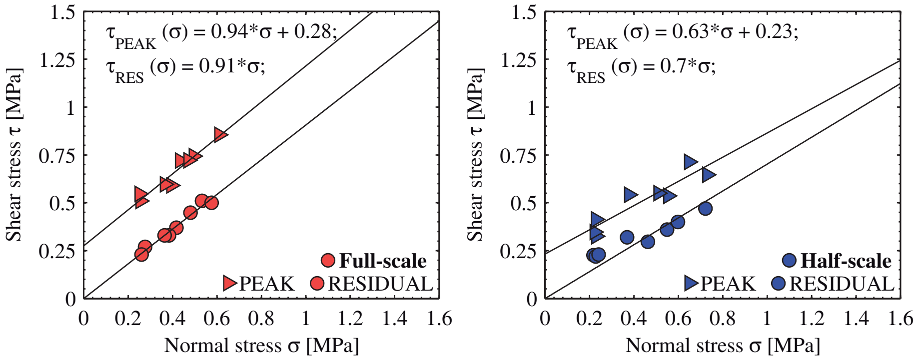

Figure 4. Results from shear tests on half- and full-scale masonry

determined when the shear strength reached for large sliding displacements an approximately constant value. The friction coefficient describing the residual strength regime was obtained from the best fit line passing through the origin (see Fig. 4). The friction coefficients and the cohesion of the model masonry are approximately 20% smaller than those of the prototype masonry (Table 4). To the authors' opinion, this discrepancy results from the difference in void ratio of the half- and full-scale brick units ($\vartheta_M/\vartheta_P = 0.8$, see Fig. 1 and Table 2). Assuming that the shear strength results mainly from the shearing off of the mortar pillars, which form when the mortar is pressed inside the voids of the perforated bricks, the shear strength should be proportional to the void ratio. This is confirmed by the shear triplet results. To improve the match of the interface shear strength one should therefore aim for equal void ratios of the half- and full-scale brick unit (Table 4).

4.3 Diagonal compression tests

To determine the diagonal tensile strength, five specimens at each scale were tested under a local compression load at the corners as illustrated in Fig. 2 [RIL91]. The lower and upper shoes applying this compression load were scaled with the test unit. Note that no pre-compression perpendicular to the bed joints was applied (Fig. 2). The diagonal tensile strength f_t was computed from the peak force F_{PEAK} :

$$f_t = \frac{F_{PEAK}}{\sqrt{2} \cdot A_N} \tag{1}$$

where A_N represents the average cross section:

$$A_N = \frac{L+H}{2} \cdot T \tag{2}$$

Table 5 Results from the diagonal compression tests performed on half- and full-scale masonry panels (resulting material strength in bold)

	L (mm)	H (mm)	f_t (MPa)
Full-scale masonry	1230	1190	0.496 ±9.7%
Half-scale masonry	615	595	0.336 ±15%
Ratio half- / full-scale	-	-	0.68

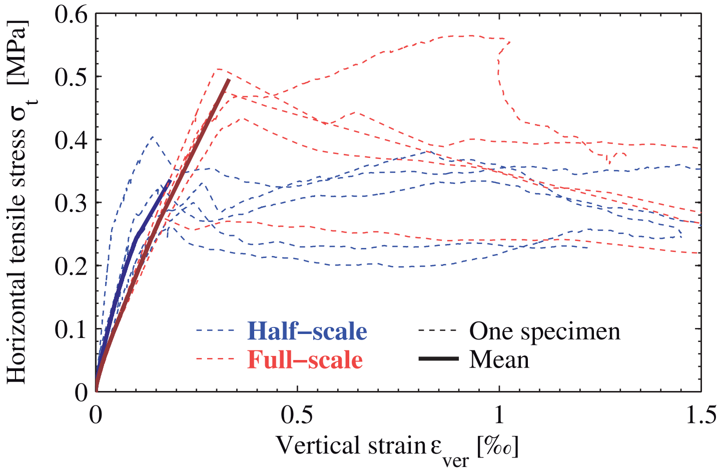

Figure 5. Stress-strain curves of the diagonal tensile strength

where L, H and T are the length, height and thickness of the panel, respectively. The resulting diagonal tensile strengths for the half- and full-scale masonry are summarized in Table 5. The diagonal tensile strength of the half-scale masonry underestimates the strength of the full-scale masonry by around 30% ($f_{t,M}/f_{t,P}$ = 0.68). All panels failed along one diagonal crack, which started at the center of the panels and followed the mortar joint. The diagonal tensile strength was therefore controlled by the joint-brick interface properties. Hence, similar to the shear strength obtained from the triplet tests, the diagonal tensile strength of the model masonry is lower for the model masonry than for the prototype masonry because the void ratio of the model brick unit is lower (see Fig. 5).

4.4 Summary of differences in material properties

The standard material tests showed that the model masonry agreed well with the prototype masonry with regard to the compressive strength f_u, the axial stiffness E_c and the Poisson's ratio ν. A key factor seems to be the brick strength as the compression failure is associated with the failure of the brick. The model and prototype masonry differed with respect to the deformation capacity of the masonry when subjected to compression. The deformation capacity of the model masonry was 10-50% larger than the deformation capacity of the prototype masonry. The shear strength of the brick-mortar interface of the model masonry was ~20% less than for the prototype masonry. This was linked to the different void ratios of the model and prototype brick units which could not be avoided since the number of holes but not the web and shell thickness were reduced. The interface properties also governed the tensile strength obtained from diagonal compression tests. On the whole the correspondence

Figure 6. (a) Photos of test stands for quasi-static cyclic wall tests on prototype walls (PUP1–5) and (b) Model walls (PUM1–5)

in terms of strength is rather satisfactory while the compression tests indicated that the displacement capacity of the model masonry is larger for the model masonry than for the prototype masonry. This will be investigated further in the next section, which compares the behavior of half- and full-scale masonry walls subjected to quasi-static cyclic loading.

5 Similitude of seismic behavior of URM walls at half- and full-scale

To investigate the similitude of the model and prototype masonry when subjected to seismic loading, quasi-static cyclic tests on walls were conducted. The following sections outline the test program, the test setup, the applied loading history and compare the response of the half- and full-scale walls in terms of crack pattern, failure mode and force-deformation characteristics.

5.1 Test program, test setup and loading history

For the quasi-static cyclic tests, a series of five walls was constructed at each scale using the brick units and mortar that had been used for the material tests. The walls at one scale had all the same dimensions (Table 6) and were tested in the test stands shown in Fig. 6. Each test stand allowed applying two vertical forces and one horizontal force. The control of the three actuators could be fully coupled. For each wall (exception: PUP1, see following section), the applied axial force and the shear span remained constant throughout the test. The horizontal actuator (master) was displacement-controlled. The vertical actuators were force-controlled. The forces to be applied by the two vertical actuators $F_{ver,1,2}$ were computed as a function of

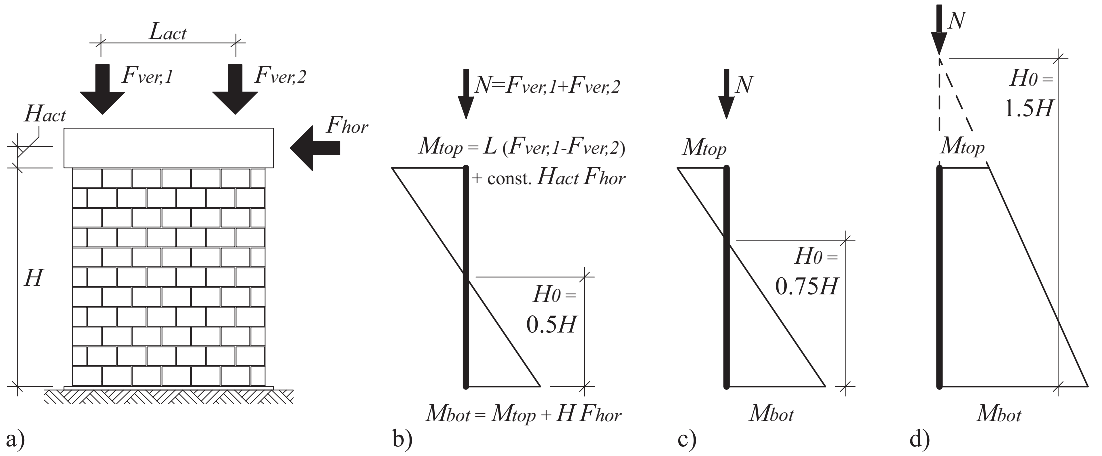

Figure 7. (a) Boundary conditions for the URM walls at half- and full-scale with the resulting moment profiles for (b) PUM1/PUP1, (c) for PUM2/PUP2 and PUM5/PUP5 and (d) for PUM3/PUP3 and PUM4/PUP4

the force applied by the horizontal actuator F_{hor} and the axial force N (Fig. 7):

$$F_{ver,1,2} = \frac{N}{2} \pm \mathrm{C} \cdot F_{hor} \tag{3}$$

The constant C is a function of the shear span H_0 and the geometry of the test setup. Figure 7 shows the three different shear spans that were applied in the test series. The walls were subjected to a cyclic loading history with the following peak drifts: 0.025, 0.05, 0.1, 0.15, 0.2, 0.3, 0.4, 0.6, 0.8, 1.0, 1.5, 2.0%. At each drift level, two cycles of equal amplitude were imposed. The deformations of the walls were measured by an optical measurement system. The average drift of the wall was computed as the horizontal displacement at the top of the wall divided by the wall height H.

A set of conventional hard-wired measurements was used to measure the forces of all three actuators, the global displacement at the top of the wall and the local deformations in bricks and joints at all four corners of the wall. In addition, a LED-based optical measurement system was used to follow the displacements of the wall and at the steel plates at the top and bottom of the wall (see markers in Fig. 6; for the half-scale walls, the markers were fixed on the back of the specimen and are not visible in Fig. 6).

The test parameters that were varied between the five walls were the applied axial stress and the shear span. Table 6 summarizes the test program and introduces the labels of the wall units for the prototype walls (PUP1–5) and the model walls (PUM1–5). The first three walls were subjected to the same vertical load, while the rotational restraint at the top was varied. For the first wall fixed-fixed boundary conditions were simulated. For the second and third walls the moment applied at the top of the wall was proportional to the applied horizontal load and therefore, the shear span H_0 was constant and equal to 0.75 and 1.5 times the wall height H for the second and third wall, respectively (see Fig. 7). The fourth wall was subjected to the same shear span as the third wall ($H_0 = 1.5H$) but the axial load was increased by ~ 50%. The fifth wall was subjected to the same shear span as the second wall ($H_0 = 0.75H$) but the normal load was reduced by ~ 50%.

Table 6. Dimensions and boundary conditions of the quasi-statically tested walls PUM1-5/PUP1-5

Wall unit	H (m)	L (m)	t (m)	H_0/H (-)	N (kN)	σ_0 (MPa)	σ_0/f_u (-)
PUP1	2.225	2.010	0.200	0.5^a	419	1.04	0.18
PUM1	1.113	1.005	0.100	0.5	105	1.04	0.18
PUP2	2.225	2.010	0.200	0.75	419	1.04	0.18
PUM2	1.113	1.005	0.100	0.75	105	1.04	0.18
PUP3	2.225	2.010	0.200	1.5	419	1.04	0.18
PUM3	1.113	1.005	0.100	1.5	105	1.04	0.18
PUP4	2.225	2.010	0.200	1.5	619	1.54	0.26
PUM4	1.113	1.005	0.100	1.5	155	1.54	0.27
PUP5	2.225	2.010	0.200	0.75	219	0.54	0.09
PUM5	1.113	1.005	0.100	0.75	55	0.54	0.10

[a] For PUP1 a fixed-fixed boundary condition was simulated by applying a zero rotation at the top of the wall. For all other specimens the boundary conditions were simulated in controlling the moment ratio, and thus, the shear span H_0 of the walls

The objective of the research program was to compare the behavior of the model and prototype masonry for different performance limit states. For this reason, the quasi-static cyclic loading was continued until the walls were no longer able to carry the applied vertical load. Hence, two different failure limit states are distinct: (i) the ”horizontal load failure” refers to the drift where the strength dropped to 80% of the peak strength; (ii) the ”axial load failure” is attained, when the wall could no longer sustain the vertical load applied by the pistons. The first failure criterion—horizontal load failure—corresponds to the limit state ”near collapse” (NC) as defined in the Eurocode 8, Part 3 [CEN05] and aims at limiting the damage in order to avoid collapse of the structural element. The second failure criterion ”axial load failure” would correspond to the collapse or partial collapse of the structure.

5.2 Comparison of crack pattern and failure mode

Pictures of all ten specimens after axial load failure and the hysteresis for the half- and full-scale walls are shown in Fig. 8. In order to compare the hysteretic curves of the model and prototype walls, the average shear stress $\sigma_0 = V/A$ is plotted against the average drift where A is the gross sectional area of the wall and V the lateral force applied by the horizontal actuator.

All five wall configurations tested at half-scale (PUM1–5) produced similar failure modes and damage patterns as the equivalent full-scale walls (PUP1–5, Fig. 8): PUM1/PUP1, PUM2/PUP2 and PUM5/PUP5 displayed a diagonal shear failure, PUM3/PUP3 a flexural failure and PUM4/PUP4 a hybrid failure mode. In addition, to the failure mechanism also the shape of the hysteresis is well reproduced for all walls resulting thus in similar energy dissipation (Fig. 9). Only for PUM4 and PUP4, the form of the hysteresis differed slightly (Fig. 8) which resulted also in different equivalent hysteretic damping factors (Fig. 9). Both walls failed in a hybrid failure mode and it seems to the authors that it was difficult to reproduce exactly the same behavior when two failure modes were dominant at the same time. Even though, both walls developed generally the same crack pattern, the hysteretic behavior of PUM4 resembled more a rocking failure, while the hysteretic behavior of PUP4 is characteristic for a diagonal shear failure. Accordingly, the equivalent damping obtained for PUM4 was lower than for PUP4.

For PUM1/PUP1, the boundary conditions were imposed slightly differently: PUP1 was tested under fixed-fixed boundary conditions and PUM1 was tested with a constant shear span $H0 = 0.5H$. Nevertheless, the resulting average shear strength and the drift capacity showed a good similitude (see Fig. 8). For both PUP1 and PUM1 shear cracks started forming during the cycles with a nominal drift of 0.1%. The peak strength occurred slightly earlier for the model wall than for the prototype wall but the deterioration in the post-peak branch was more significant for PUP1 than for PUM1, resulting therefore in very similar drift capacities for the two walls. For PUM1, the vertical pistons were controlled to keep the shear span constant at $0.5H$. This resulted in very small rotations of the top beam in the post peak branch. Nevertheless, these rotations were very small and are neglected in the following discussion.

In general, horizontal and diagonal cracks tended to appear later in the half-scale walls than in the full-scale walls. Especially at small drifts–when the walls behaved still largely in an elastic manner–the crack opening was generally smaller in the half-scale walls than in the full-scale walls and it seemed to the authors that the crack width was scaled accordingly to the scaling of joints and bricks. Thus, the initial cracks in the half-scale walls were simply too small to be detected at the same stage as the full-scale walls and onset of cracking was observed later in the half-scale walls. For PUM5/PUP5, the first diagonal cracks were noticed at the same nominal drift of 0.15%. However, even though throughout the testing the crack formation was similar, the cracks appeared generally at more important drifts for PUM5. In the walls where flexural deformations contributed in a significant manner to the total deformations–PUM3/PUP3, PUM4/PUP4 and PUM5/PUP5–the horizontal cracks developed generally later in the half-scale walls than in the full-scale walls. Nevertheless, the delay of the onset of horizontal cracking was less than for diagonal cracking and might thus explain why PUM4 displayed a stronger rocking behavior than PUP4.

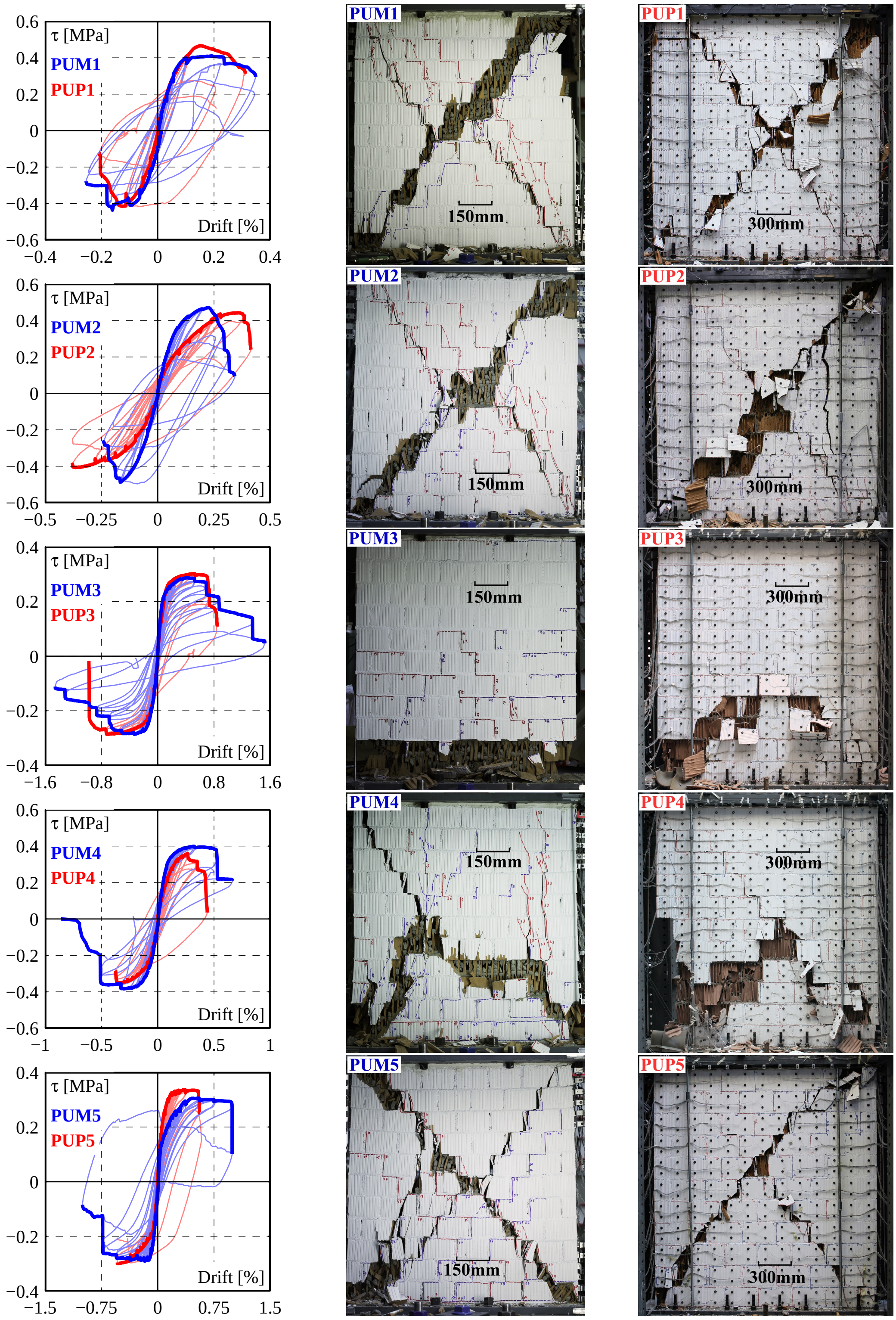

Figure 8. Comparison of the results from the quasi-static tests on the half-scale (PUM1–5) and the full-scale masonry walls (PUP1–5): hysteresis loops with envelopes (left) and damages of the photo of the walls after axial load failure (center: half-scale, right: full-scale)

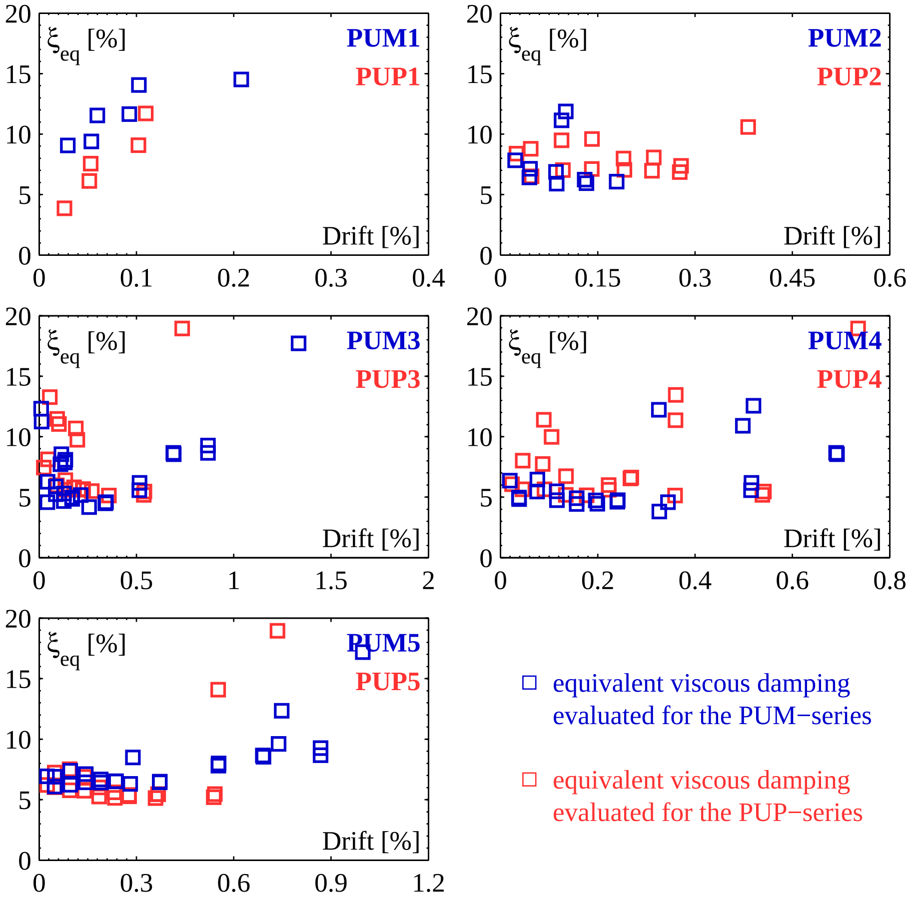

Figure 9. Comparison of equivalent viscous damping ratios; The equivalent viscous damping ratios are evaluated according to Magenes and Calvi [MC97]

This observation is also confirmed by the crack widths, which we determined from the optical measurements. Figure 10 shows the 98 %-fractile value of the crack widths ($w_{ver,M}$ and $w_{ver,P}$ refer to vertical cracks which developed through bricks or head joints and $w_{hor,M}$ and $w_{hor,P}$ to the horizontal crack width measured in bed-joints). The 98%-fractile value is determined for all locations of potential cracks using the LED-measurements shown in Fig. 6. For all plots the crack opening for the half-scale walls is plotted using the double scale than for the prototype masonry ($2w_{hor,M} = w_{hor,P}$ and $2w_{ver,M} = w_{ver,P}$). Hence, when blue curves and red curves match, the crack width of the model masonry is half the crack width of the prototype masonry and therefore perfectly scaled. The parameters δ_e and δ_u in Fig. 10 represent the elastic and ultimate drift values and refer to the limit of the linear elastic behavior and the horizontal drift capacity. They will be explained more in detail in the next section. However, it can be noted that for drift demands in the linear-elastic domain ($\delta < \delta_e$), the crack widths of the model masonry tend to be approximately half the crack widths of the prototype masonry. Thus, the measurement confirms the good similitude in the elastic behavior. For larger drifts, the agreement is slightly less satisfactory and the cracks in the prototype walls tended to be wider than $2w_M$. Hence, for the prototype walls the deformations were concentrated in fewer cracks than in the model masonry.

Table 7. Comparison of the characteristic properties of the half- and full-scale walls (resulting material strength in bold)

Wall unit	H_0/H (-)	σ_0/f_u (-)	Failure mode	δ_e (%)	δ_u (%)	δ_{max} (%)	τ_u (MPa)	k_e (kN/m^2)	$f_{c,m}$	$E_{LS0-LS1}$ (GPa)
PUP1	0.5	0.18	S	0.083	0.168	0.210	0.416	50.3	8.99	4.86
PUM1	0.5	0.18	S	0.073	0.193	0.268	0.395	53.8	9.27	6.03
Ratio 1	-	-	-	0.89	1.15	1.28	0.95	1.07	1.03	1.24
PUP2	0.75	0.18	S	0.189	0.383	0.383	0.413	21.8	9.75	4.05
PUM2	0.75	0.18	S	0.108	0.193	0.243	0.456	42.3	11.3	11.7
Ratio 2	-	-	-	0.57	0.50	0.63	1.10	1.94	1.16	2.89
PUP3	1.5	0.18	F	0.133	0.717	0.843	0.280	21.0	12.0	3.05
PUM3	1.5	0.18	F	0.110	0.691	1.459	0.274	25.0	12.3	3.70
Ratio 3	-	-	-	0.82	0.96	1.73	0.98	1.19	1.03	1.21
PUP4	1.5	0.26	H	0.139	0.352	0.382	0.336	24.2	11.7	4.05
PUM4	1.5	0.27	H	0.111	0.518	0.665	0.375	33.8	9.45	7.58
Ratio 4	-	-	-	0.80	1.47	1.74	1.12	1.40	0.81	1.87
PUP5	0.75	0.09	S	0.134	0.543	0.546	0.306	22.9	9.87	4.94
PUM5	0.75	0.10	S	0.151	0.740	0.993	0.288	19.1	11.9	11.6
Ratio 5	-	-	-	1.13	1.36	1.82	0.94	0.83	1.21	2.35
Average ratio	-	-	-	0.84	1.09	1.44	1.02	1.29	1.05	1.91

5.3 Comparison of stiffness, force and displacement capacities

In order to compare the stiffness, force and displacement capacities in more detail, the force-drift envelopes are approximated by bi-linear curves, following the method outlined in Frumento et al. [FM$^+$09]. In this method, the elastic stiffness k_e is estimated as secant stiffness when the force capacity reaches 70% of the peak force ($0.7V_{max}$). The ultimate displacement Δ_u corresponds to the so-called "horizontal load failure" (see Sect. 5.1) when the force drops to 80% of the peak strength. The ultimate strength V_u is computed such that the area under the envelope up to ultimate displacement Δ_u is the same as under the bilinear curve. The elastic displacement Δ_e is the intersection point of the elastic branch with stiffness k_e and the horizontal line determined by V_u. In addition to the bi-linear method as applied by Frumento et al. [FM$^+$09], we determined the maximum displacement Δ_{max} which is associated to the previously defined "axial load failure" (Sect. 5.1). Furthermore, in order to simplify the comparison of the results of the walls at different scales, the displacement and force quantities are replaced by quantities which are independent of the scale, i.e. the interstory drift $\delta = \Delta/H$ (Δ_e, Δ_u and Δ_{max} change to δ_e, δ_u and δ_{max}) and the mean shear stress $\tau_u = V_u/A$ where H is the height of the wall (see Fig. 7) and A the area of the gross cross section of the wall. The envelopes and the bilinear approximations of all 5 PUM/PUP-pairs are illustrated in Fig. 11.

The characteristic values obtained from the bilinear approximations of the force displacement envelopes are summarized in Table 7. The table also indicates the compressive strength $f_{c,m}$ of the mortar at the day of the wall tests and the axial stiffness $E_{LS0-LS1}$ of the wall which

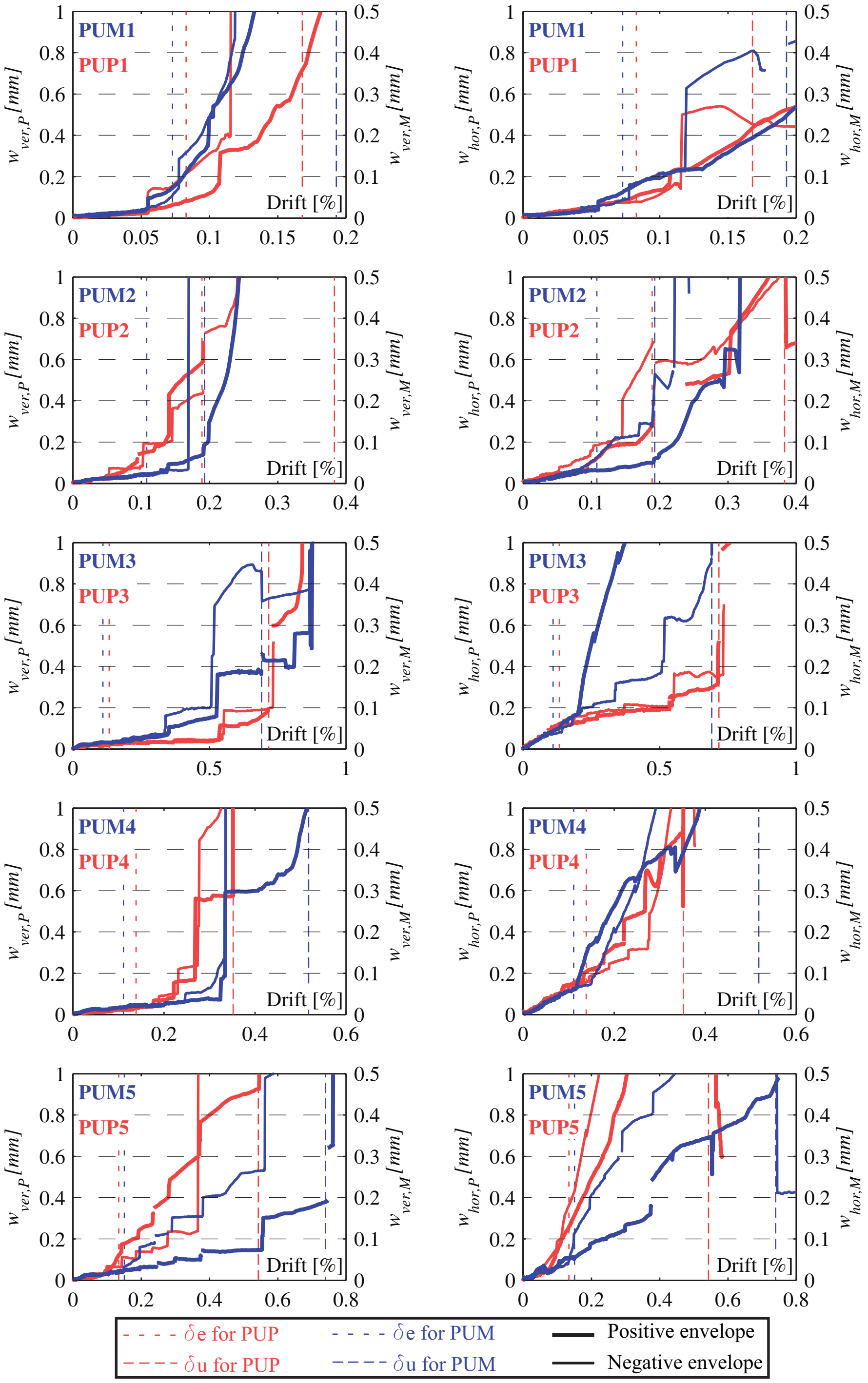

Figure 10. 98 %-fractile of the width of vertical cracks (w_{ver}) in bricks and head joints (indicator for diagonal cracks, at the left) and of the width of the horizontal cracks (w_{hor}) in bed joints (indicator for flexural cracking, at the right

was computed from the shortening of the wall when applying the axial load at the beginning of each quasi-static cyclic test. Figures 12, 13 and 14 illustrate the ratio of the characteristic

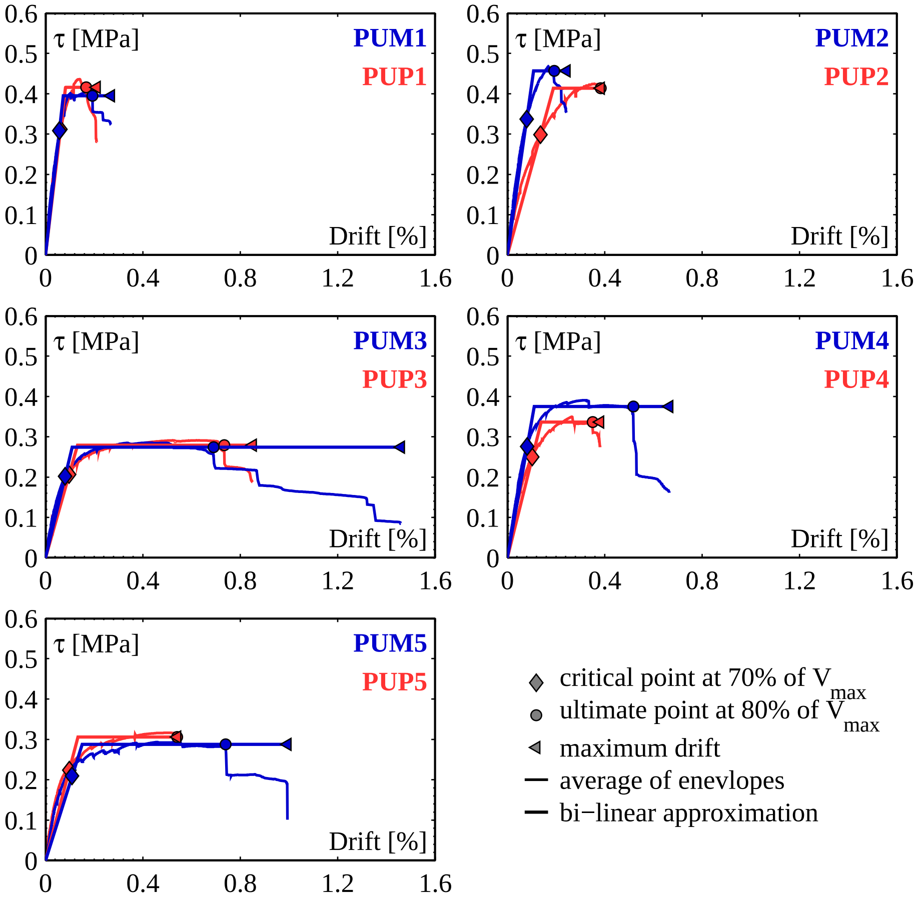

Figure 11. Mean envelope for PUP1–5/PUM1–5 and resulting bilinear approximation, until horizontal failure and maximum drift at vertical failure

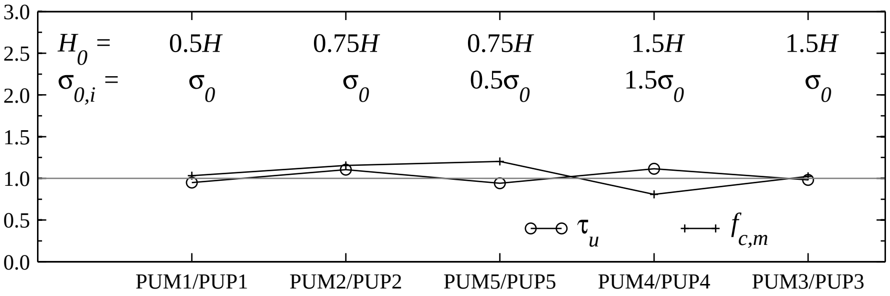

Figure 12. PUM/PUP ratio of the shear capacity τ_u and of the compressive strength $f_{c,m}$ of the corresponding mortar cubes

properties for each PUM/PUP-pair. In order to compare the walls according to their failure mechanism, in Figs. 12, 13 and 14, the walls are ordered first according to their shear span ($H_0 = 0.5H$, $0.75H$ and $1.5H$) and then according to the axial load ratio ($\sigma_{0,i} = 50\%\sigma_0$, 100% σ_0 and 150% σ_0).

The age of the walls at the day of testing varied between ~40 and 120 days within one series. To obtain similar mortar strength values for the model and prototype walls, each

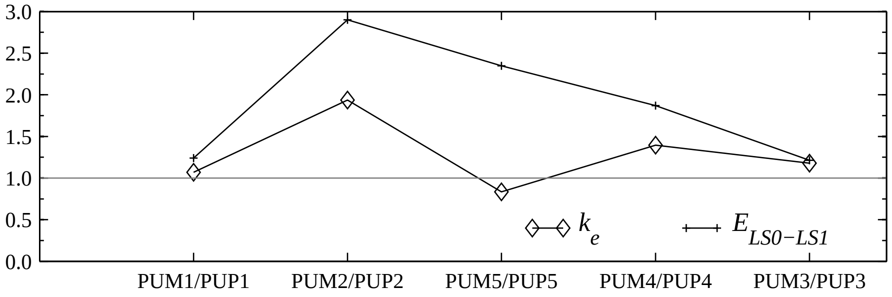

Figure 13. PUM/PUP ratio of the initial stiffness k_e and of the measured axial stiffness $E_{LS0-LS1}$ during the first axial load application from LS0 to LS1

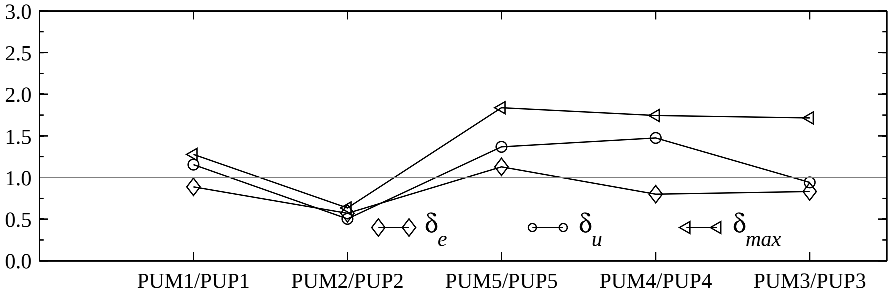

Figure 14. PUM/PUP ratio of the drift capacities δ_e, δ_u and δ_{max}

PUM/PUP-pair was tested at a similar age. Even though the mortar strength $f_{c,m}$ showed a slight tendency to increase with age (Table 7), it did not vary significantly within each PUM/PUP-pair and thus did not affect the shear strength similitude of the walls (Fig. 12). For instance, for the first two pairs, PUM1/PUP1 and PUM2/PUP2, the shear strength obtained at half-scale matches perfectly with the one obtained at full-scale (Fig. 12). Due to the larger net area of the model brick, the tensile strength of the model brick was larger than the tensile strength of the prototype brick while the interface strength is smaller for the model brick (see Sects. 4 and 5). The mismatch in net area might therefore change the relative contributions of the different mechanisms to the shear resistance while the total shear strength of the walls remains largely unaffected. In PUM5/PUP5, few cracks developed in the bricks. Cracks through bricks developed only for larger drift demands and these cracks seemed to be caused by geometrical incompatibility when sliding occurs along the joints. Hence, for these walls, the shear strength seems to stem mainly from the sliding mechanism and therefore the full-scale wall is slightly stronger. The pairs PUM3/PUP3 failed due to rocking while PUM4/PUP4 developed a mixed failure mode. Compression tests on model and prototype masonry showed that the compressive strengths f_u were very similar (Table 3) and consequently for both pairs the similitude of strength between model and prototype walls is excellent (Fig. 12).

The axial stiffness $E_{LS0-LS1}$ of the model masonry is in average larger than the axial stiffness of the prototype masonry (Fig. 13). In the case of PUM2/PUP2, the difference in axial stiffness amounts to more than 150% while the average ratio of axial stiffness for the model to prototype walls is 1.9. When neglecting the pair PUM2/PUP2, the agreement of the elastic horizontal stiffness k_e between model and prototype wall depends on whether the wall is developing a shear or rocking behavior: For walls developing a shear failure mode

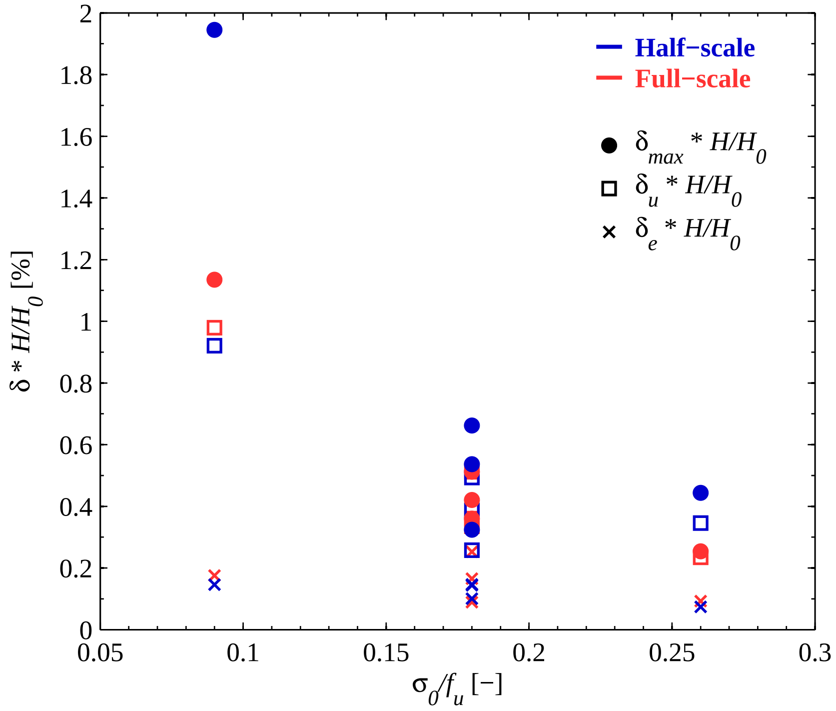

Figure 15. Comparison of the displacement capacities δ_e, δ_u and δ_{max} in dependency of the boundary conditions (axial stress ratio σ_0/f_u and shear span ratio H_0/H)

(PUM1/PUP1 and PUM5/PUP5), the agreement of the stiffness is better than for walls with a hybrid (PUM4/PUP4) or rocking failure mode (PUM3/PUP3); for the latter the horizontal stiffness of the model walls is in average 30% larger than the stiffness of the prototype walls. This is in agreement with findings from the material tests where the E-modulus of the half-scale masonry exceeded the E-modulus of the full-scale masonry by ±50% (Table 3). Figure 14 shows the ratios of the drift capacities of the model and prototype walls. As previously noted, the similitude of the elastic drift δ_e is generally good. The drift capacity associated with horizontal load failure is in average 9% larger for the model walls than for the prototype walls. The drift δ_{max} at vertical failure is for all model walls (with the exception of PUM2) larger than for the corresponding prototype walls. The average ratio of the drifts δ_{max} is 1.44. Our observation of an increased displacement capacity in the post peak branch agrees hence with the observation done by Hendry and Sinha [HS71]. However, in Fig. 15 the drift capacity is plotted following the approach of Petry and Beyer [PB14] in dependency of the boundary conditions—shear span ratio and axial stress ratio—and it can be noted that generally a good similitude is obtained for the elastic and ultimate drift. At axial load failure the model walls tend to have a significant higher maximum drift capacity (Figs. 14 and 15).

6 Conclusions

Shake table tests of entire buildings often require testing at a reduced-scale. This paper provides guidelines for the scaling of modern unreinforced masonry buildings with hollow clay brick units. Based on the results of tests on brick units, standard material tests and quasi-static cyclic tests on walls, we recommend the following geometry for a model hollow clay brick unit:

- Similar absolute web and shell thicknesses as the prototype brick,
- Similar void ratio and similar effective width of webs and shells as the prototype brick (ratio of the sum of the web and shell thicknesses to the total width of the bricks),
- Similar layout of the hole pattern as the prototype brick (e.g. rectangular webs with straight, continuous webs vs. rice-shaped holes).).

The model brick should be produced from the same clay as the prototype brick. Since the web and shell thicknesses are similar to those of the prototype brick, it should be dried and burnt using the same procedure as for the prototype brick. The bricks should be wire-cut before the burning in order to obtain similar mortar-brick interface properties as for the prototype masonry.

It is clear that such scaling of the brick is restricted to rather moderate scaling factors. In this study, masonry at half- and full-scale was compared. Using these guidelines, we obtained an excellent match of the bricks' compressive strengths in the vertical and horizontal direction. Comparison of the results from standard material tests on brick units and masonry wallettes as well as results from quasi-static cyclic tests on walls indicate further:

- Due to the excellent match in brick strength, also the compressive strengths of the masonry at half- and full-scale are very similar. As a result, the flexural capacity of the walls is well reproduced. The axial stiffness of the model and prototype masonry differed by almost a factor of two. However, the horizontal elastic stiffnesses of the walls were rather similar. Previous studies suggested that the different axial stiffnesses are caused by the different overburden pressures during curing of the mortar.
- The net areas of the model and prototype brick units used in this study differed by 20%. As a result the interface shear strength of the model masonry was 20% lower and the tensile brick strength 27% higher than for the prototype masonry. The shear strength of the walls was, however, not that different indicating that in most cases both resisting mechanisms contributed to the shear strength of the wall. The differences in net brick areas were due to the fact that (i) the web and shell thicknesses were identical for the model and prototype brick and (ii) an existing form of a full-scale brick unit was modified rather than a new form designed for the model brick. If a new form is designed for the model brick, it is suggested to aim for a slightly reduced net area of the brick by reducing slightly the web and shell thickness. This should increase the interface shear strength of the model masonry and reduce the tensile strength of the brick. Hence, such a model brick is expected to yield an even improved similitude between model and prototype masonry.
- The least satisfying match between half- and full-scale masonry was obtained with regard to the drift capacities at axial load failure. While the ultimate drift capacity associated with horizontal load failure corresponds still rather well between model and prototype masonry (average difference of 9%), the drift capacities associated with axial load failure were significantly larger for the half-scale masonry than for the full-scale masonry. This is most likely related to size effects that can lead to larger deformation capacities of small-scale specimens than for full-scale specimens. The results suggest that the proposed scaling of the masonry did not reduce the fracture energy associated with the compression failure of the masonry correctly. At present, mechanical models that link material properties to ultimate wall drifts are missing. In addition, standard material tests address only the strength and not the deformation capacity of masonry. Such models and tests would be

necessary in order to estimate already on the material test level, whether a similar drift capacity of the walls at reduced- and full-scale can be expected. Existing empirical models only consider the slenderness ratio and the failure mode, which was always correctly reproduced. Once mechanical models for the drift capacity are available it might be possible to refine the recommendations for the scaling of masonry.

Which of the above properties is the most important property to be matched, depends of course on the objectives of the reduced-scale test that is to be conducted and on the limit states to be addressed. If, for example, only limit states up to the ”Significant Damage” limit state [CEN05] are addressed, the difference in drift capacity associated with axial load failure might be of lesser importance as the behavior up to peak strength and even up to horizontal load failure (20% drop in peak strength) is rather well reproduced by the model masonry.

7 Acknowledgments

The authors thank the two reviewers for their comments that helped improving the manuscript. The authors would also like to thank Morandi Frères SA and in particular Philip Piguet, Switzerland, for the effort put into the production of the small-scale bricks and for the donation of the small- and full-scale bricks. Thanks also to Salvatore Marino for his help during testing of the reduced-scale walls.

References

[Abr96] Abrams, DA. Effects of scale and loading rate with tests of concrete and masonry structures. *Earthquake Spectra*, 12(1):13–28, 1996.

[BS+98] Brocken, HJP, Spielmann, ME, Pel, L, Kopinga, K and Larbi, JA. Water extraction out of mortar during brick laying: a NMR study. *Material Structures*, 31:49–57, 1998.

[BW58] Benjamin, JR and Williams, HA. The behavior of one-story brick shear walls. In *Journal Struct Division, Proceedings of the American Society of Civil Engineers*, pages 1–30, 1958.

[CEN02] CEN. EN 1052-1: Methods of test for masonry, Part 1: Determination of compressive strength. Technical Report EN 1052-1:1998-12, European Committee for Standardisation, Brussels, Belgium, 2002.

[CEN05] CEN. Eurocode 8: Design of structures for earthquake resistance, Part 3: Assessmemt and retrofitting of buildings. Technical Report EN 1998-3, European Committee for Standardisation, Brussels, Belgium, June 2005.

[CEN07] CEN. EN 1052-3: Methods of test for masonry, Part 3: Determination of the initial shear strength. Technical Report EN 1052-3:2002+A1:2007 D, European Committee for Standardisation, Brussels, Belgium, 2007.

[DH08] Drysdale, RG and Hamid, AA. *Masonry structures: behavior and design.* The Masonry Society, Boulder, US, 3rd edition, 2008.

[DHT95] Davies, M, Hughes, T and Taunton, P. Considerations in the small scale modelling of masonry arch bridges. In *Arch bridges*, pages 365–374, London, UK, 1995. Thomas Telford.

[ECA91] Egermann, R, Cook, D and Anzani, A. An investigation into the behaviour of scale model brick walls. In *Proceedings of the ninth international Brick/Block Masonry conferences*, pages 628–635, Berlin, Germany, 1991.

[FM+09] Frumento, S, Magenes, G, Morandi, P and Calvi, GM. *Interpretation of experimental shear tests on clay brick masonry walls and evaluation of q-factors for seismic design.* Technical Report, IUSS PRESS, Pavia, Italy, 2009.

[Gan85] Ganz, HR. *Mauerwerksscheiben unter Normalkraft und Schub.* Phd thesis, ETH Zürich, Institute of Structural Engineering, Zürich, Switzerland, 1985.

[GC+99] Green, K, Carter, M, Hoff, W and Wilson, M. The effects of lime and admixtures on the water-retaining properties of cement mortars. *Cement Concrete Research*, 29:1743–1747, 1999.

[HAH86] Hamid, AA, Abboud, B and HG, Harris. Direct small scale modeling of grouted concrete block masonry. In *U.S.-PRC joint workshop on seismic resistance of masonry structures*, Harbin, China, 1986.

[HM65] Hendry, AW and Murthy, CK. Comparative tests on 1/3- and 1/6-scale models brickwork piers and walls. In *Proceedings of the British Ceramic Society*, volume 4, pages 44–66, 1965.

[HS71] Hendry, AW and Sinha, BP. Shear tests on full-scale single-storey brickwork structures subjected to precompression. *J. Civil Eng. Public Works Rev*, pages 1339–1344, 1971.

[Kra79] Krawinkler, H. Possibilities and limitations of scale-model testing in earthquake engineering. In *Proceedings of the second US national conference on earthquake engineering*, pages 283–292, Stanford, California, 1979.

[Lou97] Lourenço, PB. *Two aspects related to the analysis of masonry structures: size effect and parameter sensitivity.* Technical report, tu-delft no 03.21.1.31.25/ tno-bouw no 97-nm-r1533, Faculty of Engineering, TU Delft, Netherlands, 1997.

[LV⁺10] Lourenço, PB, Vasconcelos, G, Medeiros, P and Gouveia, J. Vertically perforated clay brick masonry for loadbearing and non-loadbearing masonry walls. *Construction Material*, 24:2317–2330, 2010.

[MC97] Magenes, G and Calvi, GM. In-plane seismic response of brick masonry walls. *Earthquake Engineering and Structural Dynamics*, 26:1091–112, 1997.

[MH11] Mohammed, A and Hughes, T. Prototype and model masonry behaviour under different loading conditions. *Journal Civil Engineering Public Works Review*, 44:53–65, 2011.

[Moh06] Mohammed, A. *Experimental comparison of brickwork behaviour at prototype and model scales.* Phd thesis, Cardiff University, UK, 2006.

[PB14] Petry, S and Beyer, K. Influence of boundary conditions and size effect on the drift capacity of URM walls. *Engineering Structures*, 65:76–88, 2014.

[RIL91] RILEM. RILEM TC76-LUM: Diagonal tensile strength tests of small wall specimens. Technical Report TC76-LUM, RILEM Publications SARL, Brussels, Belgium, 1991.

[SH69] Sinha, BP and Hendry, AW. *Racking tests on storey-height shear-wall structures with openings subjected to precompression.* Designing, engineering and constructing with masonry products, Gulf Publication Co., Houston, Texas, 1969.

[SJ80] Shrive, NG and Jessop, EL. Anisotropy in extruded clay units and its effect on masonry behaviour. In *Proceedings of the 2nd Canadian masonry symposium*, pages 39–50, Ottawa, 1980.

[Tom87] Tomaževič, M. Dynamic modelling of masonry buildings: storey mechanism model as a simple alternative. *Earthquake Engineering and Structural Dynamics*, 15:731–749, 1987.

[TV92] Tomaževič, M and Velechovsky, T. Some aspects of testing small-scale masonry building models on simple earthquake simulators. *Earthquake Engineering and Structural Dynamics*, 21:945–963, 1992.

[TW⁺90] Tomaževič, M, Weiss, P, Velechovsky, T and Modena, C. Seismic behaviour of masonry buildings - shaking table study of masonry buildings with different structural configuration - summary report, models 1,2,3 and 4. Test report, ZAG, Ljubljana, Slovenia, 1990.

Paper III

Limit states of modern unreinforced clay brick masonry walls subjected to in-plane loading

Petry, S and Beyer, K; *Special Issue of Bulletin of Earthquake Engineering* (2014),
DOI: 10.1007/s10518-014-9695-9

Abstract

Recent research showed that the in-plane horizontal displacement capacity of unreinforced masonry (URM) walls depends on numerous factors that are not yet captured by current empirical drift capacity models; e.g., axial stress, shear span, geometry of the walls and the material used. In order to improve the performance-based assessment of URM wall buildings, future research should aim at developing numerical and mechanical models that link the global force-displacement response of URM walls to local deformation measures such as strains. This paper addresses the behavior of modern clay brick masonry and makes first contributions to such an endeavor by the evaluation of experimental results: first, two sets of limit states are proposed that link local damage limit states to characteristic points of the global force-displacement response of the URM wall. The two sets define limit states for walls developing a shear or a flexural mechanism respectively. Second, local deformation measures deemed suitable for the characterization of these limit states are evaluated from optical measurement data of quasi-static cyclic wall tests. These include strains, compression zone depth and the ratio of shear to flexural deformations.

Keywords:

Unreinforced masonry; Displacement capacity; Limit states; Performance limits;

1 Introduction

With the implementation of performance-based principles in design codes, e.g. [CEN05], not only estimates of the structural elements' stiffness and strength but also of their deformation capacity are required. For URM structural elements, the deformation capacity for in-plane loading is expressed in terms of story drift. Today's codes include only rather simple empirical drift capacity models for URM walls, e.g. [CEN05], which define the drift capacity as a function of only two parameters, i.e. the expected failure mode and the ratio between the shear span and the length of the wall H_0/L. This results in significant dispersion of predicted to observed drift capacities [FM$^+$09, PB14b]. To promote the use of performance-based design of URM buildings, improved drift capacity models are required. One approach for improving drift capacity models is to consider additional parameters in empirical drift capacity models, e.g. [PLBL11, PB14b]. However, in the long term, the development of analytical drift capacity models seems desirable. Such models should estimate the drift capacity of a certain limit state (LS) using a mechanical model which links the drift capacity to limits of local deformation measures such as strains and curvatures. For reinforced concrete and steel structures analytical models for predicting the displacement capacity are well established (e.g. plastic hinge models). For URM walls, first models have been put forward by Priestley et al. [PCK07] and Benedetti and Steli [BS08]. These models are limited to cantilever or fixed-fixed walls responding in a rocking mode. The model by Benedetti and Benedetti [BB13] includes a shear failure check based on the Mohr-Coulomb criterion; however, their model is still based on a flexural displacement mechanism. In future developments it would be desirable to generalize these models to boundary conditions different to cantilever walls and to develop models that are applicable to walls developing a shear or mixed failure mode.

Thus the objectives for this article are twofold: First, based on findings by other researchers, our own test results on URM walls and the LSs defined in FEMA 306 [ATC98], we propose two new sets of LSs which link local damage to the global force-displacement response of URM walls. The two sets define LSs for walls developing a shear or a flexural mechanism respectively. They shall serve as basis for the development of improved mechanical models for the force-displacement behavior of URM walls [PCK07, BS08, PLG14]. Second, local deformation measures are evaluated that are suited to characterize these LSs. They are computed from optical measurements taken during the test. This information on the local response shall also provide other researchers the input required for validating their models (numerical or mechanical) not only on the global but also on the local level. In the past, often the tests by Ganz and Thürlimann [GT84] were used for validation purposes, e.g. [Lou96, FT11, FPV14]. In Zhang et al. [ZPB14], we use the EPFL test data to validate the model developed by Facconi et al. [FPV14] with regard to global displacements and local strains. Note that all data of this EPFL test series including that of the optical measurements is shared publicly via the doi 10.5281/zenodo.8443 allowing hence any researcher to reuse the data [PB14a].

After introducing briefly the EPFL tests in Section 2, we develop in Section 3 the two sets of LSs. In Section 4, we evaluate different local deformation measures from the EPFL tests and draw conclusions regarding their suitability to characterize the different LSs. Section 5 summarizes the findings and discusses the possibilities and challenges related to the development of analytical models for the drift capacity of URM walls.

2 Quasi-static cyclic tests on masonry walls

The literature reports the results of a large number of quasi-static tests on URM walls; a summary of these can be found in [FM$^+$09]. In almost all test series the walls were subjected to either cantilever or fixed-fixed conditions and parameters such as the axial stress ratio and aspect ratio rather than the moment profile over the height of the walls were investigated. Only few test series compare explicitly the behavior of walls subjected to cantilever and fixed-fixed conditions, e.g. [FSA07, MMP08]. These test series demonstrated that the displacement capacity of walls depended on the applied moment profile even if the walls developed the same failure mode.

To complement existing data, a test series of six walls was designed at EPFL to investigate the influence of the two boundary conditions axial stress ratio and moment profile on the force-displacement response of the walls and in particular on their in-plane deformation capacity [PB14b, PB14a]. In addition to the conventional instrumentation, a LED-based optical measurement system was used to measure the displacement field of the walls, which yielded continuous measurements of local deformation quantities over the entire duration of the tests. In Section 2.1, we introduce briefly the test series and compare the walls to other existing series. Section 2.2 discusses the global force-displacement response of the walls and the importance of the discrepancy between chord rotation and interstory drifts for shear spans different to 1.0 or $0.5H$, where H is the wall height.

2.1 Testing program

The test series comprised six quasi-static cyclic tests of walls with identical dimensions. The parameters that were varied between the tests were the axial stress ratio σ_0/f_u and the ratio between shear span H_0 and wall height H. Both parameters were kept constant in each of the first five tests; for the sixth wall, σ_0/f_u and H_0/H varied in function of the applied lateral force. This test is not included here but more information on the entire test series can be found in [PB14b, PB14a]. In order to simulate an internal wall in buildings with slabs of different stiffness, the first three walls (PUP1–3) were subjected to the same axial stress ratio of $\sigma_0/f_u = 0.18$ but three different shear spans of $H_0 = 0.5$, 0.75 and $1.5H$. The first test, PUP1, was a reference test which applied standard fixed-fixed boundary conditions to the wall. The axial stress ratio σ_0/f_u corresponds to the axial load N divided by the cross section of the wall A and the compression strength of the masonry f_u. Walls 4 and 5 represented external walls. Thus, PUP4 was subjected to an increased axial stress ratio of $\sigma_0/f_u = 0.26$ and an increased shear span of $H_0 = 1.5H$, while PUP5 was tested with $\sigma_0/f_u = 0.09$ and $H_0 = 0.75H$.

The dimensions of all walls were 2.01 m x 2.25 m x 0.20 m (length x height x width). The walls were constructed using a typical modern Swiss hollow-core clay brick and a standard cement mortar [PB14a]. To record local and global quantities, two kinds of measurement systems were used: a set of conventional instruments recorded forces in all three actuators, the displacement at the top of the wall and average strains of bricks and joints at all four corners of the wall and a LED-based optical measurement system was used to record the displacements of 312 points on the wall. From the optical measurements, the displacement field as well as strains in bricks and deformations in joints could be derived.

In [PB14b] the resulting displacement capacity of this test series is compared to other 58 existing quasi-static monotonic or cyclic tests on unreinforced clay brick masonry. Comparison showed that the global results from this test series follow the general trends; according to these, the drift capacity decreases with (i) increasing wall size, (ii) increasing moment restraint at the top of the wall, and (iii) increasing axial stress ratio. In addition, a detailed comparison of global and local quantities, e.g. force-displacement behavior or crack width, with an equivalent test series at half-scale [PB14c] showed that the results could be reproduced at reduced scale. From these two studies, we concluded that the behavior of the EPFL tests is representative of the seismic behavior of hollow core clay brick masonry with cement mortar.

2.2 Force-displacement envelopes and a comparison of chord rotation and interstory drift

The test units PUP1–3 were tested applying the same average normal stress ratio but different shear spans. With the pairs PUP2/PUP5 and PUP3/PUP4 the influence of the axial stress ratio was investigated. First cycle envelopes of all five test units are shown in Fig. 1.

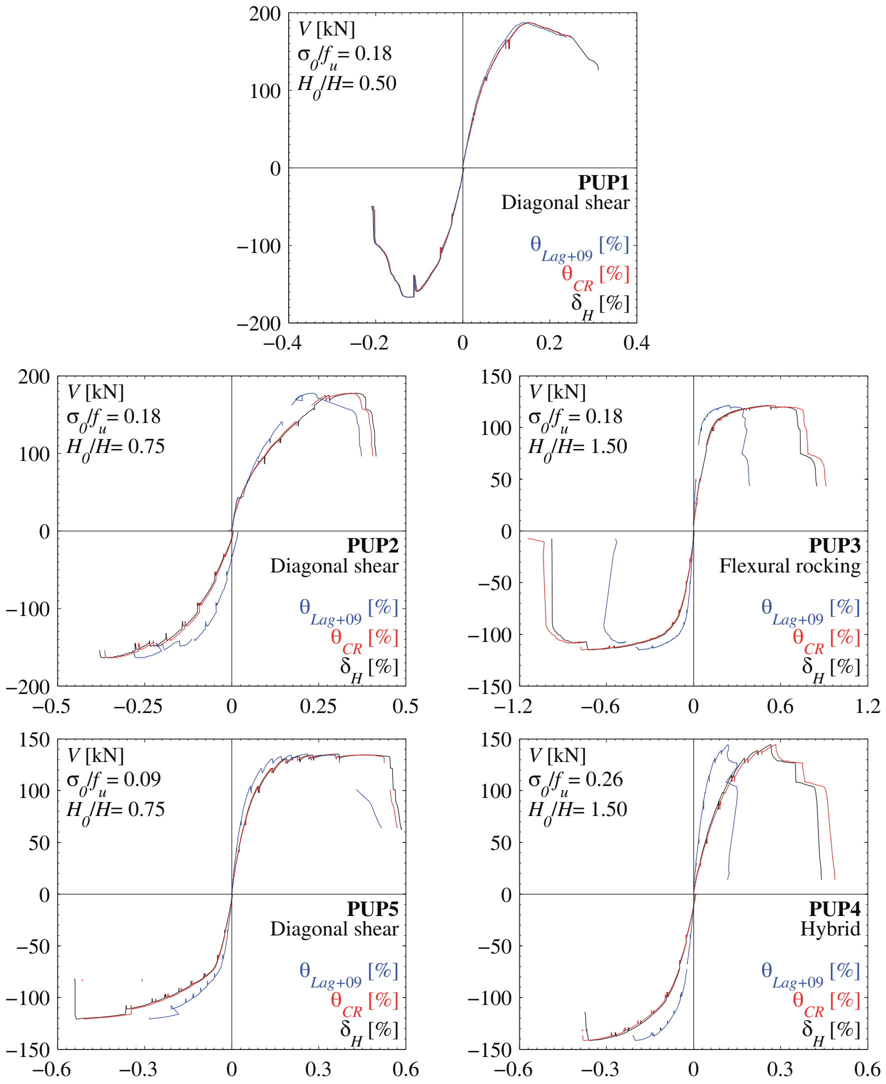

Figure 1. Force-drift envelopes obtained with the chord rotation θ_{CR} and the interstory drift δ_H and the drift measure θ_{Lag+09} proposed by Lagomarsino et al. [LP+13]

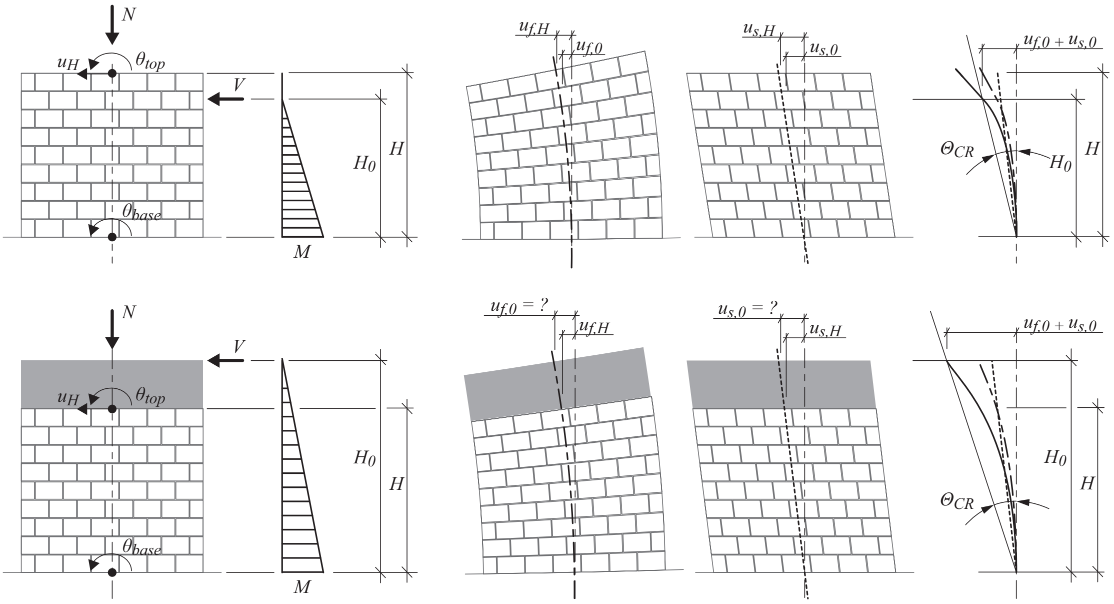

Figure 2. Definition of the chord rotation for shear spans $H_0 < H$ and $H_0 > H$

While current codes express the displacement capacity of URM walls as interstory drifts, the deformation of steel or reinforced concrete structural element is often described in terms of chord rotation, see Fig. 2. When subjected to cantilever or fixed-fixed boundary conditions, interstory drift and chord rotation are per definition equal (note that, strictly speaking, this assumption does not hold for fixed-fixed boundary conditions if the damage to the top and base of the wall is not identical). Since wall tests reported in the literature applied either of the two boundary conditions, the difference between interstory drift and chord rotation had not been investigated. The EPFL campaign comprised tests with $H_0/H = 0.75$ and 1.5 and therefore the difference between chord rotation and interstory drift is of interest. In addition, the drift measure proposed by Lagomarsino et al. [LP$^+$13] is compared to the interstory drift and the chord rotation. This drift measure is based on the assumption that the in-plane shear deformation is a better indicator of the wall damage, was originally proposed for the structural member's drift, although in some cases it may coincide with the interstory drift (Penna, personal communication, Oct. 2014).

The interstory drift (short: drift) is the total lateral displacement at the top of the wall divided by the story height (in our case the story height is equal to the height of the wall H):

$$\delta_H = \frac{u_H}{H} \tag{1}$$

where u_H is the relative horizontal displacement between the top and base of the story-high wall.

The drift measure proposed by Lagomarsino et al. [LP$^+$13], which is used to determine the limit states of the bi-linear element in Tremuri, subtracts from the interstory drift the average rotation at the top and base of the wall:

$$\theta_{Lag+09} = \frac{u_H}{H} - \frac{\theta_{top} + \theta_{base}}{2} \tag{2}$$

where θ_{top} and θ_{base} are the rotation at top and base of the wall respectively. Note that the sign convention is such that (i) θ_{top} is positive if the rotation at the top has the same orientation as the rotation at the top of a cantilever wall subjected to a horizontal load leading to a positive displacement u_H, (ii) θ_{base} is positive in the same sense as the top rotation (see Fig. 2).

The chord rotation is defined as the lateral displacement at the inflection point divided by the shear span, see Fig. 2.

$$\theta_{CR} = \frac{u_0}{H_0} = \frac{u_{f,0}}{H_0} + \frac{u_{s,0}}{H_0} \tag{3}$$

where $u_{f,0}$ is the flexural component and $u_{s,0}$ is the shear component of the total lateral displacement u_0 at the height H_0. For the walls tested with a shear span $H_0 \leq H$ the displacement at the height of the inflection point can be obtained directly from the LED measurements. For the walls subjected to $\alpha = H_0/H > 1$, however, additional assumptions are required.

Assuming a simple Timoshenko beam with a constant section along its length, we developed the following expression in order to compute the chord rotation from the deformation quantities measured at the top of the wall:

$$\theta_{CR} = \frac{2H_0^2 u_{f,H}}{3H^2(H_0 - \frac{H}{3})} + \frac{u_{s,H}}{H} \tag{4}$$

where $u_{f,H}$ and $u_{s,H}$ are the flexural and shear component of the total lateral displacement at the top of the wall. The first term of the equation is based on a cubic extrapolation of the flexural deformations determined at the top of the wall up to the inflection point, while the second term of the equation is based on a linear extrapolation of the shear deformations. The flexural deformations at wall height are computed from the difference in rotation at the top and base of the wall; the shear displacement at the top of the wall is computed as difference between total and flexural displacement ($\alpha \leq 1$):

$$u_{f,H} = (\theta_{top} - \theta_{base}) \cdot \frac{H}{2} \cdot \frac{\alpha - \frac{1}{3}}{\alpha - \frac{1}{2}} \tag{5}$$

$$u_{s,H} = u_H - u_{f,H} \tag{6}$$

For a cantilever wall Eq. (5) yields $2/3 \cdot \theta_{top} \cdot H$, which corresponds to the flexural deformation of a Timoshenko beam. Figure 1 shows the first-cycle envelopes of the five walls, once as function of the drift and once as function of the chord rotation. PUP1 was tested for fixed-fixed condition and accordingly the difference between drift and chord rotation is negligible. PUP2 and PUP5 were both tested with a constant shear span of $0.75H$ and it can be noted that the interstory drift is slightly larger than the chord rotation. For walls with $H_0 \geq H$ (PUP3 and PUP4) the interstory drift is slightly smaller than the chord rotation. However, at all stages, the difference between chord rotation and drift is less than 15% and therefore relatively small. In agreement with the convention in codes, e.g. EC8-P3 [CEN05], this paper uses the interstory drift rather than the chord rotation as measure for the horizontal deformation of the wall.

The drift measure proposed by Lagomarsino et al. [LP$^+$13] can yield considerable smaller values than the interstory drift or the chord rotation and therefore the three definitions should not be mixed up. The difference increases with increasing relative rotation between top and base of the wall. This is in particular the case for the walls where $H_0 = 1.5H$. Hence, if the failure of a wall is defined by means of a constant value for θ_{Lag+09} walls with a larger shear span fail at a larger horizontal displacement u_H. Recent research has shown that this failure criterion corresponds better to the observed drift capacities than a constant value of interstory drift [PB14b].

3 Limit states of unreinforced hollow core clay brick masonry walls responding in shear and flexure

The two most common in-plane failure modes of URM walls with hollow core clay bricks subjected to vertical and horizontal in-plane loads are the flexural rocking failure mode and the diagonal shear failure mode. The third failure mode often mentioned in the literature is sliding shear failure along a bed joint. However, for load bearing URM walls with hollow core bricks this failure mode is rarely reported in the literature and was also not observed in the EPFL test series; for this reason it is not included in the following discussion.

As a first step towards describing the kinematics of URM walls, the typical LSs of the walls of the EPFL test series failing in shear and flexure are identified. A LS refers to the first occurrence of a particular crack type or the local failure of parts of the wall. The crack pattern is chosen as parameter for distinguishing the LSs because the appearance of a new type of crack or the concentration of the crack width in a single crack leads typically to a change in the kinematics of the wall. As a result, the modeling hypotheses need to be reconsidered at the LSs. These LSs are then linked to characteristic points of the force-displacement curve of the wall (Section 3.1). In a second part, the order of occurrence of these LSs is discussed for the first five walls of the EPFL test series and a link between boundary conditions and the sequence of LSs (Section 3.2) is established. The last part of this section shows amplified deformed shapes on which basis the kinematics at the different LSs are discussed (Section 3.3).

3.1 Definition of LSs for URM walls

When developing mechanical models for the displacement capacity of URM walls, LSs of the URM walls need to be defined and related to local deformation measures such as strains or crack widths. The LSs should distinguish phases of wall behavior with different kinematics and describe when local failure mechanisms such as crushing of the bricks occur. As a first step towards such an endeavor, this section defines LSs by means of crack patterns observed for the walls PUP1-5. Two sets of LSs are defined that characterize the behavior of a shear and flexural prevailing behavior, respectively. Many walls develop mixed failure modes and feature therefore LSs from both sets.

Note that several researchers defined LSs for URM structures [ATC98, GM$^+$98, Cal99, Abr01, Lan02, BP$^+$03, LG06, Tom07]. Most of these LSs were developed for whole structures. Only FEMA 306 [ATC98] and Bosiljkov et al. [BP$^+$03] address the LSs of individual elements. The newly proposed LSs build on the FEMA 306 LSs in particular for the flexural failure mode. However, the newly proposed LSs differ in two aspects: (i) they focus on crack patterns typical for modern hollow clay brick masonry while FEMA 306 addresses solid clay brick masonry; (ii) each LSs is described by the appearance of a new type of crack which affects the kinematics rather and does not include the crack width nor the extent of the crack as criteria for the LSs. At the end of this section, the newly proposed LSs are compared to those defined in FEMA 306 [ATC98] and Bosiljkov et al. [BP$^+$03].

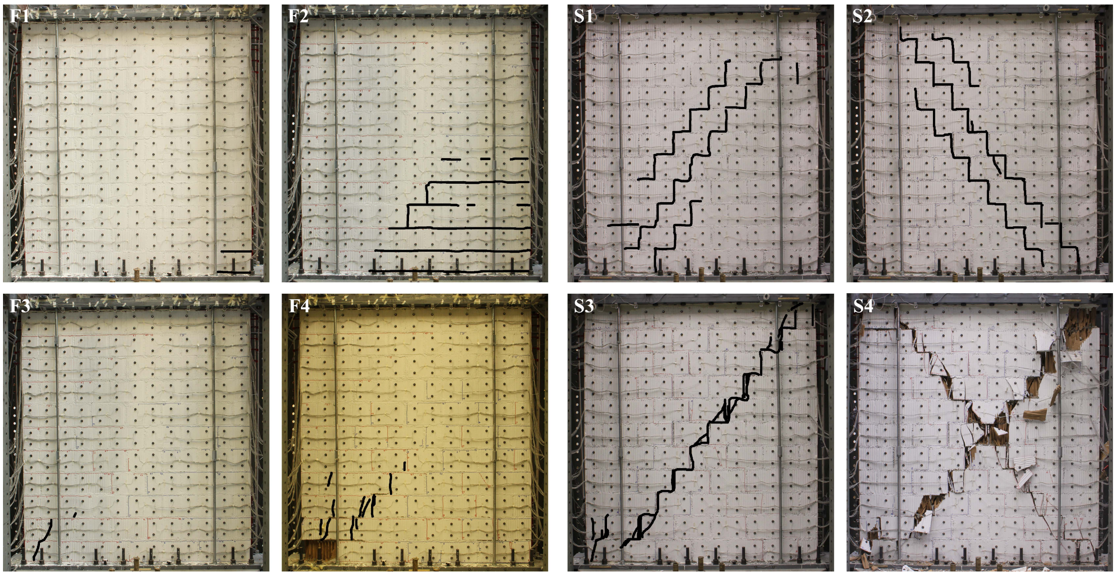

Figure 3. Photos of different walls of the EPFL test series with accentuated cracks to show the different LSs caused by flexure (left) and shear (right): (F1) first crack in bed joint, (F2) separation of wall visible, (F3) cracks in bricks in compressed zone, (F4) loss of compressed zone, (S1) first stair step crack visible, (S2) diagonal shear crack propagates through brick, (S3) concentration of deformation in one diagonal crack and (S4) shearing off of the corner bricks

F1 to F5 describe five LSs which can be observed when the walls develop a significant flexural behavior. They are described in Table 1 and illustrated in Fig.3 with photos of corresponding crack patterns. In Fig.3 the occurrence of the LSs is indicated in the load-displacement envelopes of the walls. It can be noted that the LS-F1 is associated with a first reduction in wall stiffness. LS-F2, although very apparent in the crack pattern, is not reflected in the force-displacement response of the wall because the masonry below the crack that forms is not an essential part of the load transfer mechanism. LS-F3 refers to the point where the stress capacity was exceeded in the compressed toe. In the global force-displacement response this LS is typically associated with the maximum shear capacity. After developing the first cracks in the brick at the toe, it was observed that the force capacity did not reduce immediately and only the occurrence of LS-F4 could be associated with a significant loss of lateral resistance. The axial load failure (LS-F5) was attained shortly after.

S1 to S5 describe five LSs which can be observed for shear solicitations. The LSs S1-S5 are described in Table 2 and the corresponding crack patterns are shown in Fig. 3. The first stair step crack (LS-S1) appeared directly over a significant part of the height of the wall and in Fig. 4, it can noted that LS-S1 was always preceded by a first reduction of stiffness, indicating that the internal load path changed before the stair step crack became visible. The stiffness reduced further with the occurrence of the next LS-S2 and S3. The LS-S3 could be associated with the peak load and the LS-S4 with a significant loss of the lateral resistance. However, once the corner started shearing off (LS-S4), it was observed that strong degradation was introduced to the diagonals under cyclic loading and axial load failure (LS-S5) occurred during the first or second cycles after LS-S4 without increasing significantly the displacement demand.

During testing it was observed that the cracks developing at the LS-S1, F1 and F2 closed

Table 1. Five LSs which can be observed when walls develop a significant flexural behavior

LS-F	Local crack pattern	Influence on global response
LS-F1	First appearance of a crack in a bed joint	First reduction of stiffness
LS-F2	Visible separation of the unloaded zone from the compression zone [Hey92]	Negligible influence on force-displacement relationship
LS-F3	Appearance of vertical splitting cracks in compressed corner	Peak load is typically attained shortly afterwards
LS-F4	Loss of part of the toe region due to crushing	Significant loss of the lateral resistance
LS-F5	Crushing of entire compression zone	Axial load failure

Table 2. Five LSs which can be observed when walls develop a significant shear behavior

LS-S	Local crack pattern	Influence on global response
LS-S1	First appearance of diagonal stair step cracks in mortar joints [MM82]	Preceded by a first reduction of stiffness
LS-S2	First appearance of vertical and inclined cracks through bricks along the diagonals	Negligible influence on force-displacement relationship
LS-S3	Deformations start concentrating in one diagonal crack	Peak load is typically attained shortly afterwards
LS-S4	Shearing off of the corners of the bricks	Significant loss of the lateral resistance
LS-S5	Crushing of bricks along the diagonal crack	Axial load failure

again when reversing the loading direction. This observation is also confirmed by the shape of the hysteresis which leads to approximately zero residual drifts at the LS-S1, F1 and F2 [PB14b]. In fact, these LSs correspond to kinematic states where cracks did not propagate through the bricks yet (see also Tables 3 and 4). On the other hand, the LSs which comprise cracks in bricks (S2-S4 and F3-F4) must depend on the type of brick used for the construction of the URM walls, e.g. brittleness of the brick, and the possibility of the cracks to propagate, e.g. loading velocity and loading history.

To set the newly proposed LSs into context, we compare in Tables 3 and 4 the proposed LSs to the LSs of URM walls defined in FEMA 306 [ATC98] and Bosiljkov et al. [BP$^+$03]. The FEMA 306 defines the LSs ”insignificant damage” to ”extreme damage” for different kinds of structural elements, including URM walls, in function of crack pattern and crack width. The LSs defined by Bosiljkov et al. [BP$^+$03] are based on the performance rather than the crack pattern. The comparison in Tables 3 and 4 is thus to a certain degree subjective as the three different scales use different identifiers. In addition, FEMA 306 [ATC98] provides λ-factors which describe the ratio of the remaining to the initial properties once a certain LS was attained. Such λ-factors are defined for the stiffness (λ_K), the strength (λ_Q) and the displacement capacity (λ_D) and allow therefore defining the bi-linear force-displacement relationship of an element that reached a certain LS. To compare the different definitions

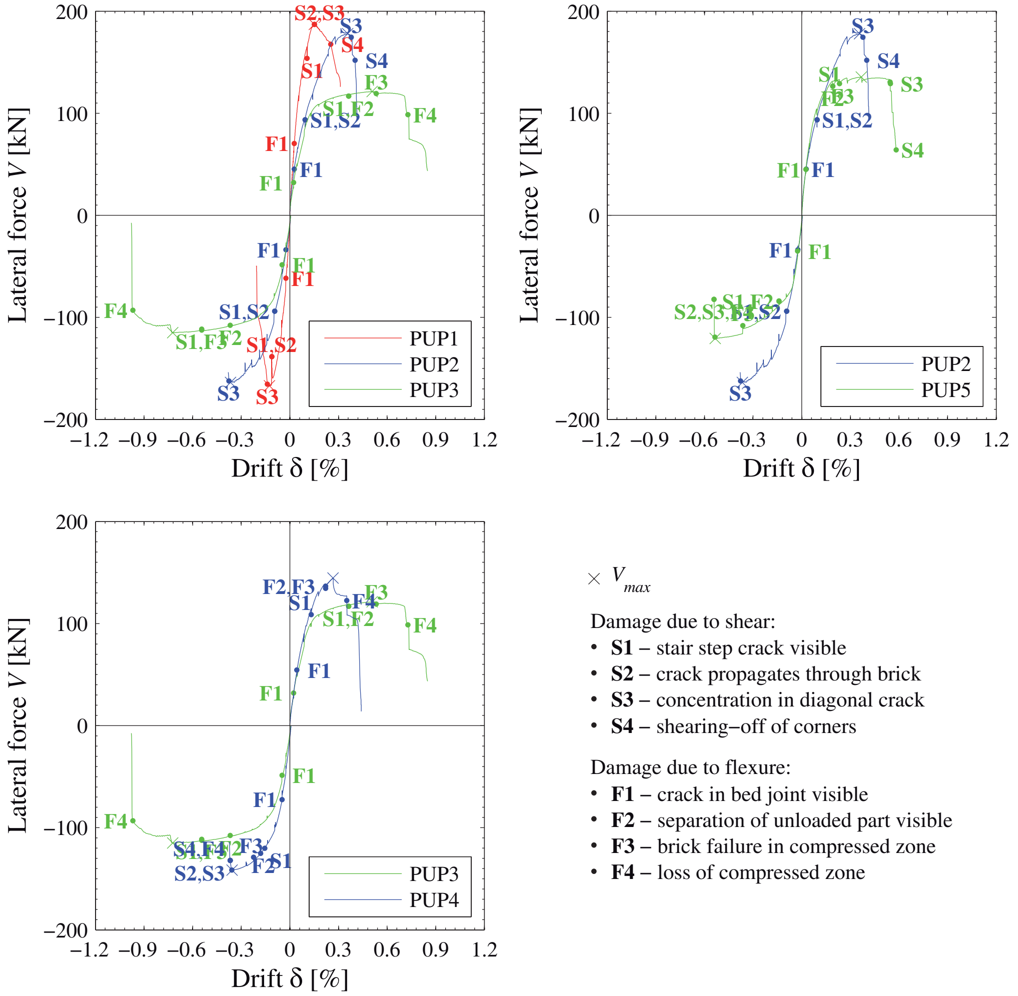

Damage due to shear:
- **S1** – stair step crack visible
- **S2** – crack propagates through brick
- **S3** – concentration in diagonal crack
- **S4** – shearing–off of corners

Damage due to flexure:
- **F1** – crack in bed joint visible
- **F2** – separation of unloaded part visible
- **F3** – brick failure in compressed zone
- **F4** – loss of compressed zone

Figure 4. First loading envelope of the force-interstory drift hysteresis for all walls, regrouped according to boundary conditions

of LSs, we determine these factors on the basis of the test results for PUP1 and PUP3 and compare these to the values in FEMA 306 in Tables 3 and 4. It can be seen that the values in FEMA 306 give good estimates which are rather conservative. Only for LS-S4, FEMA 306 overestimates the remaining capacity, which might be due to the fact that the hollow clay brick masonry is more brittle than the solid clay masonry walls, on which FEMA 306 is based.

3.2 Influence of boundary conditions on the drift for which the LSs are attained

In Fig. 4, the different LSs are indicated in the first cycle envelopes of the five EPFL walls. Figure 4a compares the walls subjected to the same axial stress ratios but different shear spans. As expected, the stiffness decreases with increasing shear span. The larger the shear span, the smaller the drift for which flexural cracks developed in bed joints (F1) and for which the unloaded part separated from the loaded part of the wall (F2). As a result, the larger the shear span, the smaller the drift for which a first decrease in stiffness was observed. A smaller shear span caused, however, significant diagonal stair step shear cracks (S1 of PUP1 and PUP2).

Table 3. Comparison of the newly proposed set of LSs for flexure with existing LSs for URM walls and their recommended reduction of stiffness (λ_K), strength (λ_Q) and displacement capacity (λ_D) after occurrence

Newly proposed LSs				Bosiljkov et al. [BP+03]	FEMA 306 [ATC98]			
LS-F	Reduction (PUP3)			Performance levels	Damage levels	Reduction		
	λ_K	λ_Q	λ_D			λ_K	λ_Q	λ_D
LS-F1	1.0	1.0	1.0	first crack	insignificant	1.0	1.0	1.0
LS-F2	1.0	1.0	1.0	-	moderate	0.8	1.0	1.0
LS-F3	0.8	1.0	1.0	life safety	heavy	0.6	0.9	1.0
LS-F4	0.35	0.65	1.0	collapse prevention	extreme	0.4	0.8	0.7
LS-F5	-	-	-	-	-	-	-	-

Table 4. Comparison of the newly proposed set of LSs for shear with existing LSs for URM walls and their recommended reduction of stiffness (λ_K), strength (λ_Q) and displacement capacity (λ_D) after occurrence

Newly proposed LSs				Bosiljkov et al. [BP+03]	FEMA 306 [ATC98]			
LS-S	Reduction (PUP1)			Performance levels	Damage levels	Reduction		
	λ_K	λ_Q	λ_D			λ_K	λ_Q	λ_D
LS-S1	1.0	1.0	1.0	immediate occupancy	insignificant	1.0	1.0	1.0
LS-S2	0.95	1.0	1.0	-	insignificant	1.0	1.0	1.0
LS-S3	0.8	0.9	0.9	life safety	moderate	0.8	0.9	1.0
LS-S4	0.5	0.55	0.25	collapse prevention	heavy / extreme	0.4	0.8	0.7
LS-S5	-	-	-	-	-	-	-	-

These spread also quickly through the bricks (S2) and provoked thus a significantly more abrupt horizontal and axial load failure than for walls with a larger shear span (PUP3), which failed in a flexural mode due to crushing of the toe (F4). However, in Fig. 4, it can be noted that the LSs associated with the loss of the corner bricks (LS-S4/F4) are both immediately succeeded in the envelope by axial load failure. Therefore, S5 and F5 are omitted in the following.

Figures 4b and c show walls subjected to the same shear span but different axial stress ratios: Walls tested with the same shear span had similar initial stiffnesses. The lower axial stress ratio favored the development of flexural deformations in PUP3 and PUP5 (e.g. F1 and F2) and caused thus an earlier softening of these walls. On the other hand the increased axial stress ratio favored the development of non-reversible LSs (e.g. S2 and F3) and provoked thus a more abrupt failure for these walls (PUP2/PUP4 versus PUP5/PUP3). The drift values for which the different damage states were observed are summarized in Tables 5 and 6. When a LS was observed for both loading directions, the average drift is given. These tables show that the drifts for which the different LSs are attained decrease with increasing axial stress ratio.

Table 5. Drift in (%, rounded at 0.05%) for which the LSs (F1/F2/F3/F4) associated to flexural solicitation occurred (”NO” = not observed)

σ_0/f_u ; H_0/H	0.5	0.75	1.5
0.09	-	0.025 / 0.15 / 0.25 / 0.55	-
0.18	0.025 / NO / NO / NO	0.025 / NO / NO / NO	0.025 / 0.35 / 0.55 / 0.9
0.26	-	-	0.05 / 0.15 / 0.2 / 0.35

Table 6. Drift in (%, rounded at 0.05%) for which the LSs (S1/S2/S3/S4) associated to shear solicitation occurred (”NO” = not observed)

σ_0/f_u ; H_0/H	0.5	0.75	1.5
0.09	-	0.15 / 0.35 / 0.55 / 0.6	-
0.18	0.1 / 0.15 / 0.15 / 0.25	0.1 / 0.1 / 0.35 / 0.4	0.45 / NO / NO / NO
0.26	-	-	0.15 / 0.35 / 0.35 / 0.35

3.3 Kinematics of URM walls at different LSs

The kinematics of URM walls depend first of all on the prevailing behavior mode (flexure vs. shear) but vary also throughout the loading history. The LSs defined in the previous section identify points when the kinematics of the walls changes due to the appearance of a new type of crack. In order to visualize the different kinematics of the walls, we show the amplified deformed shapes of the wall that developed the most significant flexural mode (PUP3) and shear mode (PUP1), respectively. The displacements are shown with respect to the zero measurement before the axial load was applied (LS0, [PB14a]).

3.3.1 Amplified deformed shapes at flexural LSs

Figure 5 shows the amplified deformed shapes of the wall which developed the most significant flexural mode (PUP3, note that due to the high amplification factor for smaller displacements the brick seem to overlap). The deformed shapes are plotted for LS-F1 (crack in bed joint visible), F3 (splitting cracks in compressed zone) and F4 (partial loss of compressed zone). The figure shows that for LS-F1 the lateral deformations develop mainly through a shortening of the wall on the compression side. Once bed joints start to open up (F1), the compressed length of the wall reduces until first splitting cracks appear (F3) and the onset of toe crushing (F4). When LS-F3 and F4 are reached, the compressed length has reduced so much that large deformation concentrate in the bottom brick layers of the wall and the wall seems to rotate as a rigid body around its base.

3.3.2 Amplified deformed shapes at shear LSs

Figure 6 shows the amplified displaced shapes of the wall which developed the most significant shear mode (PUP1, note that due to the high amplification factor for smaller displacements the brick seem to overlap). The displaced shapes are plotted at LS-S1 (stair step crack visible), S3 (concentration of deformation in one diagonal crack) and S4 (shearing-off of bricks in corner). At LS-S1, a clear diagonal compression strut develops, along which first inclined stair step cracks open up. With increasing displacement demands, deformations start to concentrate along one crack which follows the geometric diagonal of the walls. Thus, at LS-S3,

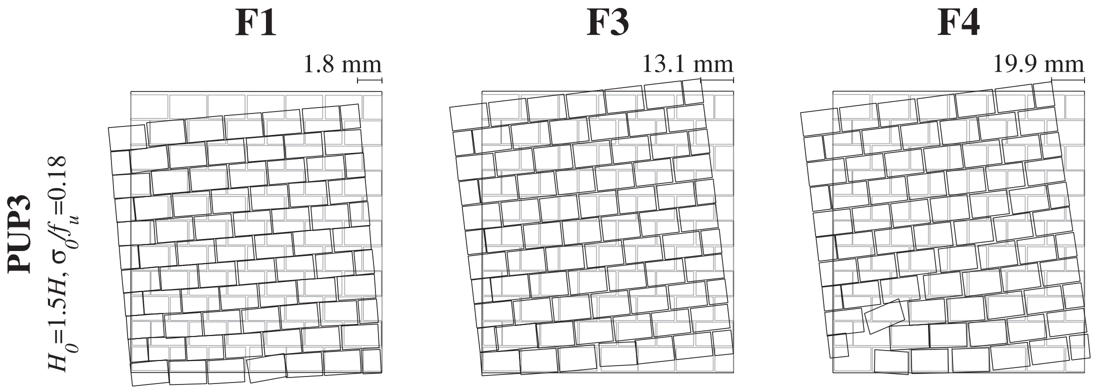

Figure 5. Amplified deformation shapes for a wall (PUP3) developing a significant flexural mode at LS-F1, F3 and F4

the wall separates into two triangles, which are held together by the corner bricks and form two almost independent parts. This separation of the wall into two triangles is a continuous process which initiates at LS-S1 and causes the softening in the force-displacement curve, which we observed in Section 3.2 from LS-S1 onwards.

However, once the deformation start concentrating in one diagonal crack, sliding occurs at the center of the diagonal crack (see the relative displacement between both triangles in Fig. 6 at LS-S3). At this state, the global displacement capacity of the walls is given by the flexural and shear deformation of the separated triangles (see the bended triangles in Fig. 6 at LS-S3) and further by the ability of the triangles to transfer the shear stresses through their tips. Thus, the corner bricks are highly solicited and once the brick strength is exceeded there, the corner bricks collapse (LS-S4). This causes a significant sliding movement that occurs along the whole length of the diagonal crack (see Fig. 6) and involves always a significant loss of lateral strength. Note that similar damage are described in the literature for numerical models of URM walls, e.g. for the solid clay URM wall modeled by Lourenço and Rots [LR97] with a multi-surface interface model.

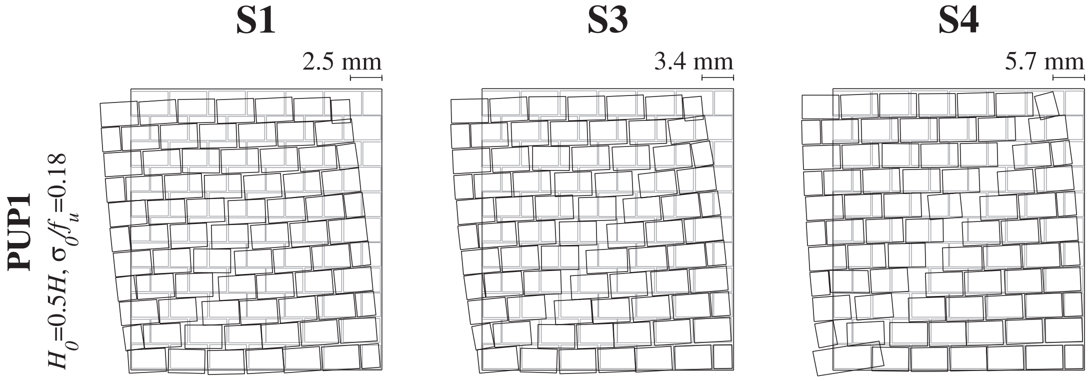

Figure 6. Amplified deformation shapes for a wall (PUP1) developing a significant shear mode at LS-S1, S3 and S4

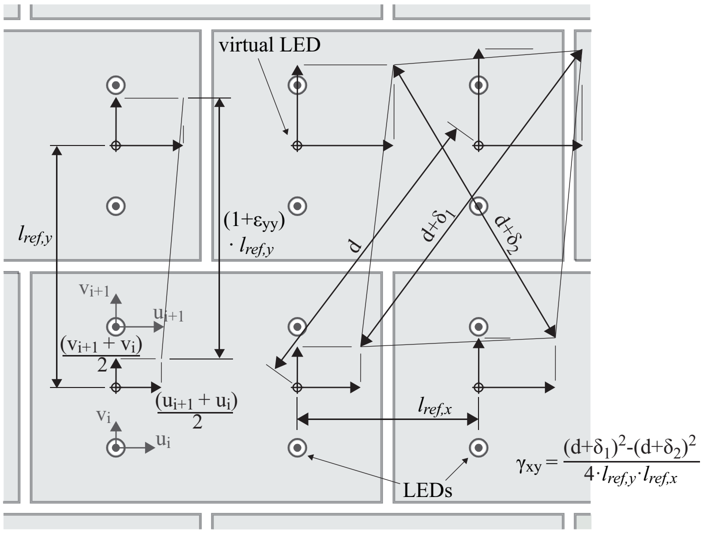

Figure 7. Schema showing how vertical strains ϵ_{yy} and the shear strains γ_{xy} are computed

4 Local deformation measures for characterizing different LSs

In a mechanical model, global and local deformation quantities have to be linked through a kinematic model. Since failure occurs locally, LSs should be identified through limits of local deformation (e.g. strains and crack width) or local strength (e.g. compression and shear strength). To investigate which local deformation measures could be suitable for such an endeavor, different deformation quantities are computed from the optical measurement results and their properties at different LSs are discussed. The considered deformation measures are vertical and shear strain fields (Section 4.1) as well as strain profiles at the outer edges of the wall (Section 4.2), bed joint openings (Section 4.3), curvatures (Section 4.4) and shear strains (Section 4.5).

4.1 Vertical strain and shear strain fields at different LSs

In Section 3.3, it is mentioned that large parts of the deformations originate from the shortening of the compression struts (see Figs. 5 and 6) which results thus in a bending of the wall. This can be best visualized by strain fields. In order to homogenize the anisotropy of the masonry, strains are computed as average strains of one brick and one mortar layer. To do so, virtual LEDs are defined at midheight of the bricks. Their displacement is computed from the average displacement of the LEDs above and below, which are glued onto the same brick (see Fig. 7). Vertical strains ϵ_{yy} and shear strains γ_{xy} of the masonry are computed on the basis of the displacements of these virtual LEDs (see Fig. 7). All deformations are computed with reference to the measurement taken before the vertical load was applied (LS0, [PB14a]).

4.1.1 Strain fields at flexural LSs

Figures 8 and 9 show the vertical and shear strain fields of PUP3, which developed a significant flexural mode at LS-F1, F3 and F4. The considered wall (PUP3) was tested with a shear span larger than the wall height and accordingly, the compression strains concentrate along one side (left wall edge in Fig. 8), while tension strains developed on the other side (right wall edge in Fig. 8). Once the compressed length is significantly reduced, deformations start concentrating at the wall base, which is reflected in the large axial strains and shear strains in

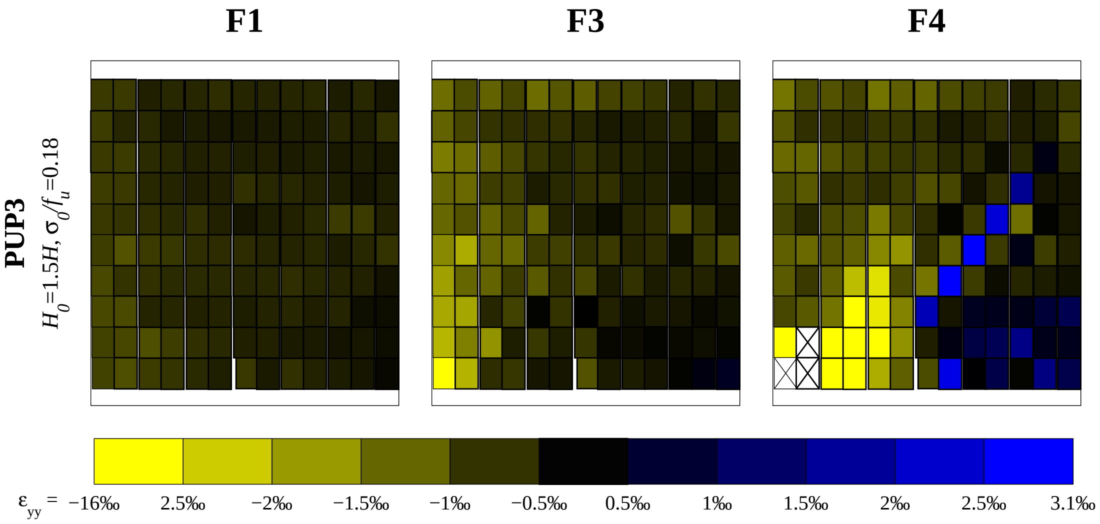

Figure 8. Vertical strain ϵ_{yy} measured between two layers of brick for a wall (PUP3) developing a significant flexural mode at LS-F1, F3 and F4

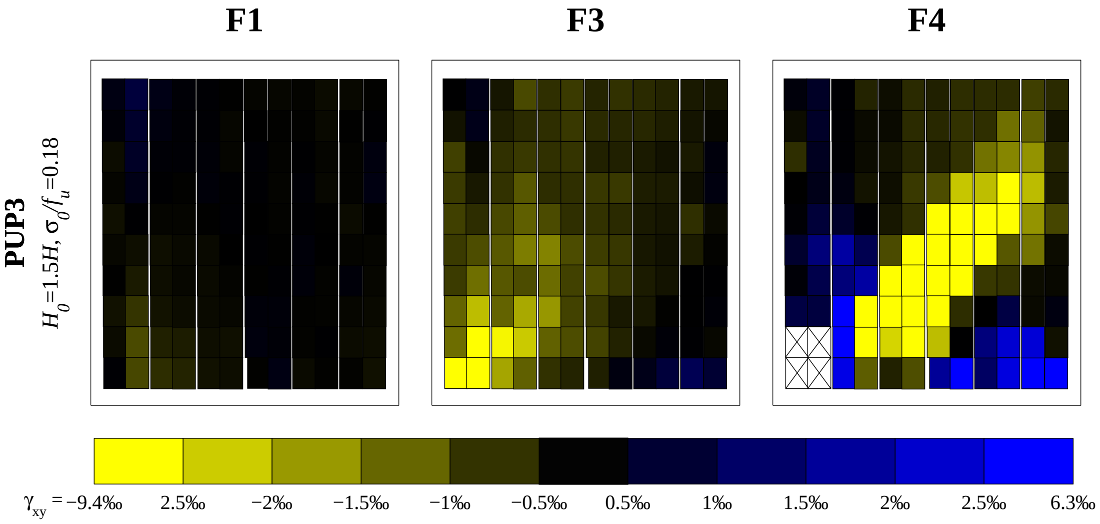

Figure 9. Shear strain γ_{xy} measured between two layers of brick for a wall (PUP3) developing a significant flexural mode at LS-F1, F3 and F4

the bottom left corner for LS-F3/F4 in Figs. 8 and 9.

4.1.2 Strain fields at shear LSs

Figures 10 and 11 show the vertical and shear strains for a wall (PUP1) developing a significant shear mechanism at LS-S1, S3 and S4. In Fig. 10, the diagonal crack opening is clearly visible in form of a stair step dark blue line. Assuming that the vertical head joints are stress free, the shear stresses γ_{xy} are transferred from brick layer to brick layer solely by the bed joints. This subjects the brick to a torque moment, which is countered by a pair of differential vertical stresses $\Delta\sigma_{yy}$ that are superimposed to the mean vertical stresses σ_{yy} [MM82]. When this pair

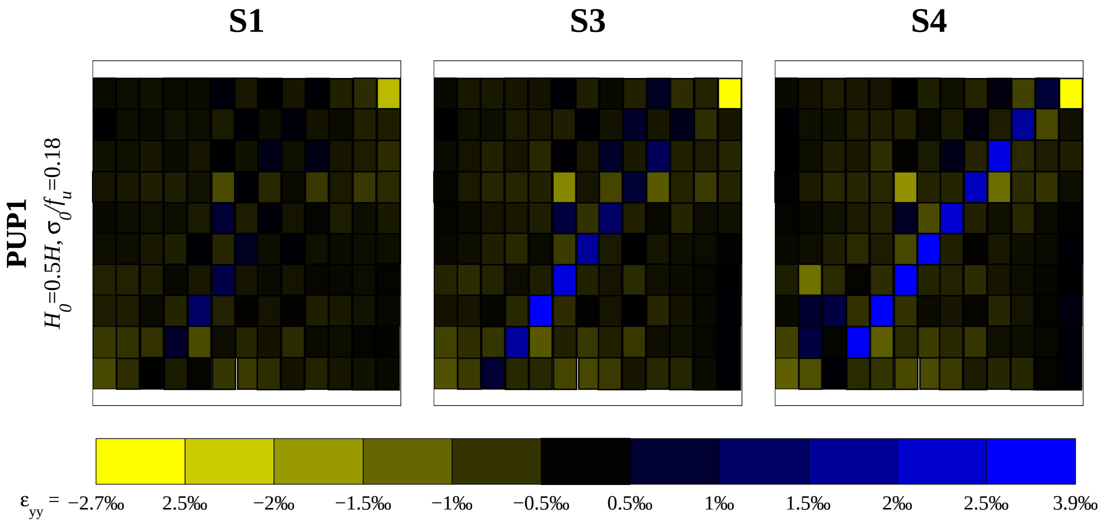

Figure 10. Vertical strain ϵ_{yy} measured between two layers of brick for a wall (PUP1) developing a significant shear mode at the LS-S1, S3 and S4

of differential stresses $\Delta\sigma_{yy}$ exceeds the mean vertical stresses σ_{yy}, the brick starts to uplift on one side resulting in an opening of the bed joint over half the brick length (Fig. 12). This is reflected in Fig. 10 by the alternating blue and yellow rectangles along the diagonal of the wall.

In Section 3, it was noted that first several parallel diagonal cracks developed (LS-S1/S2) but eventually the crack opening tends to concentrate in a single diagonal crack (LS-S3). After that, two triangles form which are held together at the corners until local stresses exceed the capacity of the corner bricks (LS-S4), see Fig. 13. Figure 10 confirms these observations: once separation of the two triangles occurs (LS-S3), the vertical strains next to the diagonal crack increase. This indicates that one load path passes through the upper and one load path through the lower triangle. In both triangles the major compression struts run parallel to the diagonal crack. These struts force the triangles to bend and to develop flexural cracks in the bed joints as shown in Fig. 13.

4.2 Vertical and shear strain profiles at the outer edges of the walls at the different LSs

The strain fields in the previous section visualized the force flow through the masonry walls. The axial and shear strain fields highlighted on one hand the high demands on the compressed toes of the walls, i.e. compression failure of the toe (LS-F3/F4) or shearing off of the corner bricks (LS-S4), and the flow of forces along the diagonal crack (LS-S3). As a first step towards quantifying admissible deformation limits for the compressed toes, the strain profiles of the compressed edge are shown. The vertical strains ϵ_{yy} and the shear strains γ_{xy} are computed as described in Fig. 7 using the outmost lines of LEDs (the distance between the first outmost line of LEDs and the edge of the walls is approximately 8 cm). In order to differentiate between the two loading directions, the origin of the x-axes is slightly offset (see Fig. 14).

In Fig. 14, a significant increase of vertical strains towards the lower layers of the wall can be noted. Even though the compression strains are higher for the walls developing a significant flexural mode (PUP3), the concentration of vertical strains in the bottom layers of the masonry

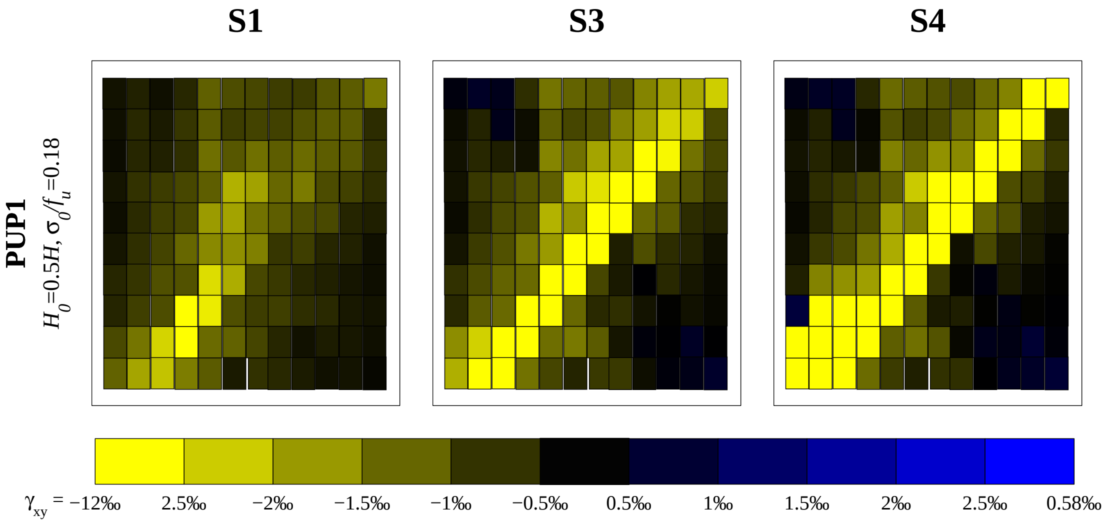

Figure 11. Shear strain γ_{xy} measured between two layers of brick for a wall (PUP1) developing a significant shear mode at the LS-S1, S3 and S4

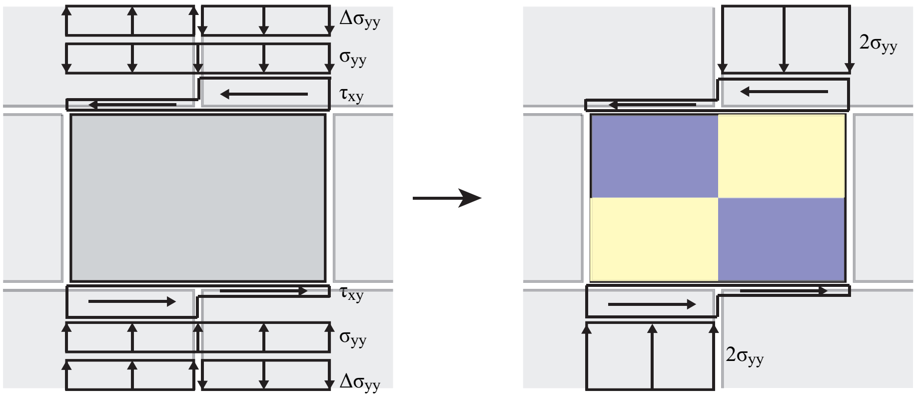

Figure 12. Partial uplift of bricks due to local torque of brick; adapted from Mann and Müller [MM82]

is visible for both walls. In addition, also the shear strains concentrate in the lower brick layers of the masonry wall and confirm thus the high solicitation of the corner bricks. Independent of the prevailing mechanism, the shear strains in the corner bricks are of the same amplitude for both walls before reaching LS-S3/F3.

4.3 Bed joint opening for the different walls at the different LSs caused by flexure

The opening of the first horizontal joint occurred for nearly all walls for rather small drift demands (0.025%, Fig. 4) leading to a first reduction of stiffness. The effective stiffness of the wall depends on the compressed length. If mechanical models shall be able to describe fully the flexural mode, good estimates for the actual compressed length are required. In the following, we investigate whether plane section analysis and neglecting the tension strength of the URM, e.g. [BS08], leads to good estimates of the compressed length. Hence, for flexural failure, the maximum moment is limited by the overturning moment and once the compressed length

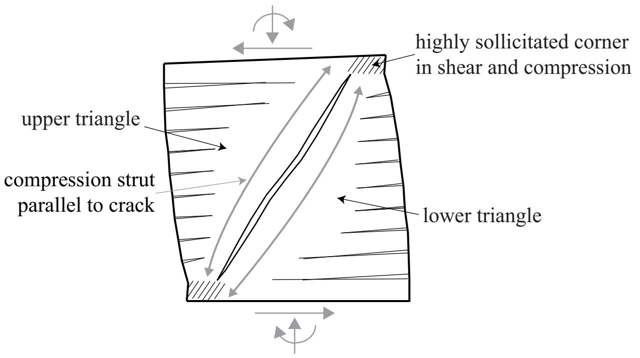

Figure 13 Crack pattern and force flow after occurrence of LS-S3

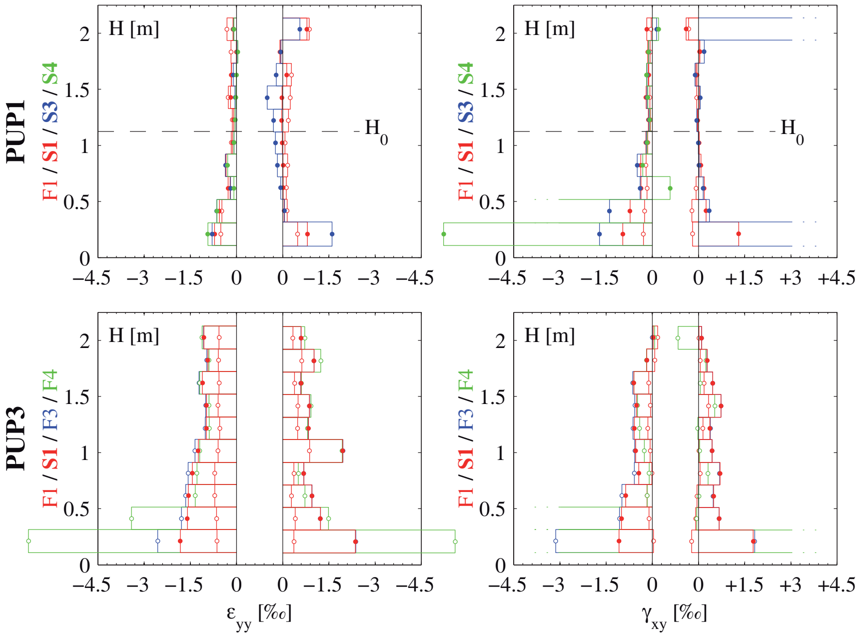

Figure 14. Strain profiles of the compressed edges for the different LSs for a wall (PUP3) developing a significant flexural mode and a wall developing a significant shear mode (PUP1)

is reduced significantly, the moment starts approaching the overturning moment $M = NL/2$ asymptotically, e.g. [PLG14]. The theoretical point of decompression of the bed joints is computed from the axial load N, the length of the wall L and the moment M using plane section analysis ($M = NL/6$). For the wall tests considered here, N is constant throughout the test, while the moment M depends on the applied horizontal force, the shear span H_0 and the distance of the bed joint to the base of the wall. Assuming a linear-elastic behavior for the masonry in compression and zero tensile strength, the compressed length can be estimated as, e.g. [BS08]:

$$\text{Ł}_c = 3(\frac{L}{2} - \frac{M}{N}) \tag{7}$$

For computing the compressed length from the optical measurements the following approach was used (see Fig. 15): first the rigid body displacements (u_b, v_b) and rotation (θ_b) and the deformations ($\epsilon_{b,xx}$, $\epsilon_{b,yy}$ and $\gamma_{b,xy}$) of each brick are evaluated from the displacement of the

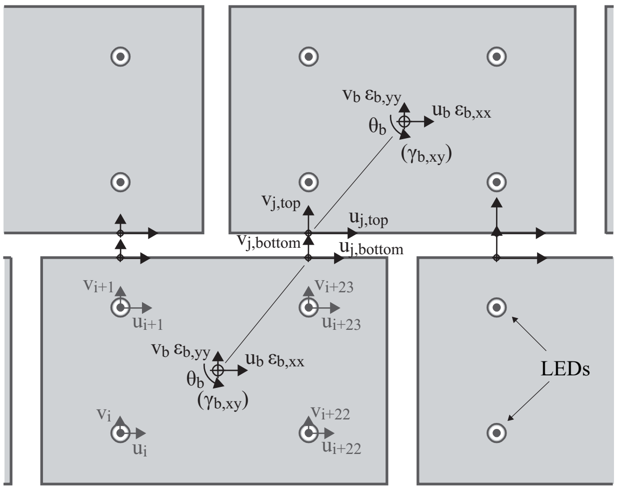

Figure 15. Schema showing how the opening of the bed joints is evaluated

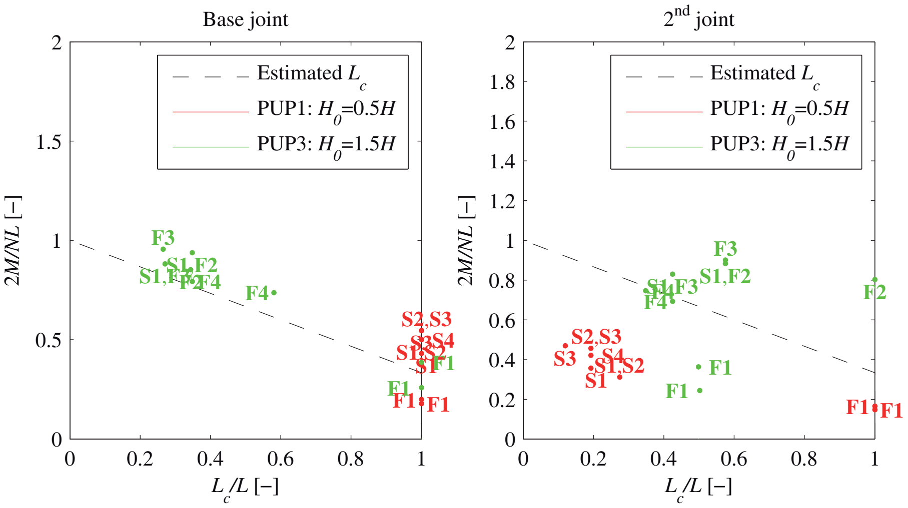

Figure 16. Moment vs captured compressed length portion in base and second joint at the observed LSs for a wall (PUP3) developing a significant flexural mode and a wall developing a significant shear mode (PUP1)

four LEDs on one brick. All deformations are computed with reference to the measurement LS0 performed before axial load application [PB14a]. Assuming that the strain state is uniform in the entire brick, the vertical and horizontal displacements at the top and bottom edge of each brick are computed ($u_{j,top}$, $v_{j,top}$ and $u_{j,bottom}$, $v_{j,bottom}$, see Fig. 15) and the deformation of a joint is obtained by comparing the displacement of two adjacent bricks. Finally, the compressed length is defined as the distance between the external wall edge in compression and the position at which the joint first opens ($v_{j,top} - v_{j,bottom} > 0$).

In Fig. 16, the measured compressed length for a wall showing a significant flexural (PUP3) and a wall showing a significant shear failure mode (PUP1) are plotted versus the theoretical compressed length L_c for the base joint and the second joint using Eq. (7). The moment is normalized by dividing it by the limit overturning moment $NL/2$. It can be observed that the moment demand in the shear dominated wall (PUP1) is too small to develop a significant opening at the base, while for the flexural dominated wall (PUP3) the compressed length of the bottom and second joint decreases to 0.2 and $0.25L$, respectively. Hence, we concluded that Eq.(7) leads to good estimates of the compressed length as long as no significant diagonal crack has formed.

4.4 Curvature at the different LSs caused by flexure

In previous sections we show that an important part of the total displacement capacity of all walls originates from flexural deformations. This applies also to the walls that eventually failed in shear (e.g. PUP1, Fig. 6). In general, flexural deformations can be best described by curvatures and therefore the evaluation of curvatures suggests itself. Hence, in the following we compute the curvatures using the vertical strains ϵ_{yy} from Section 4.1. Since the part in compression controls the wall's behavior, first the theoretical compressed length L_c is estimated using Eq. (7) and then the curvature is determined as slope of the best fit line of the vertical strains obtained from the LEDs for which the distance to the edge in compression is shorter than L_c (see Fig. 17).

In Fig. 18, the resulting curvature profiles are plotted for the different LSs for the walls PUP1

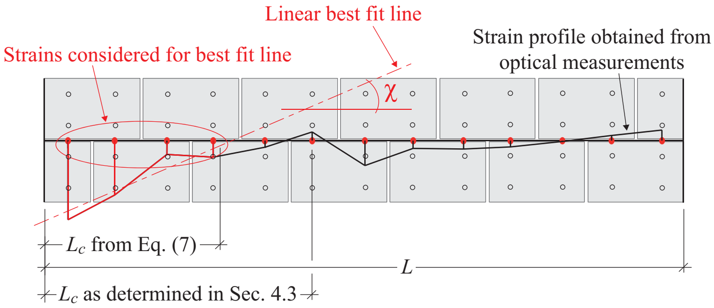

Figure 17. Schema showing how the curvature is obtained from the vertical strain profile

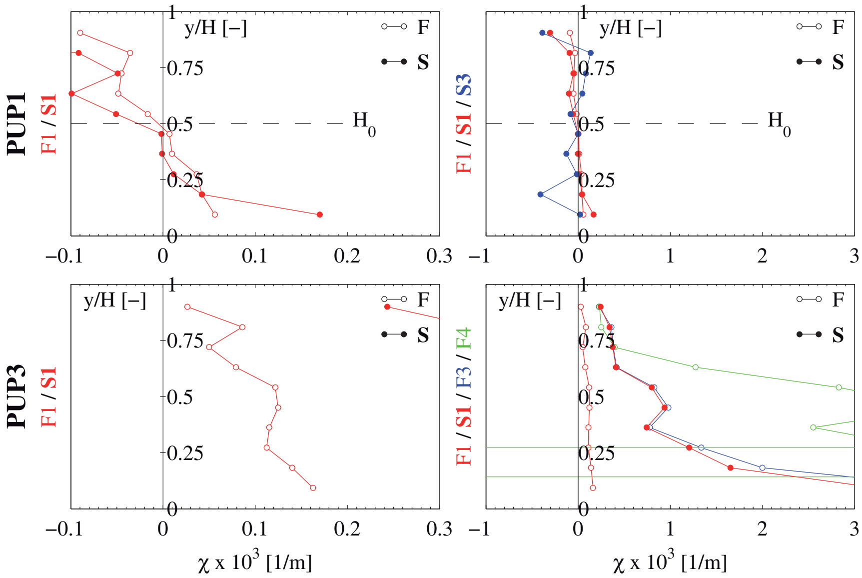

Figure 18. Average curvature profiles from the curvature profiles obtained at the LS-F1 to S4, when considering only the part of the masonry in compression

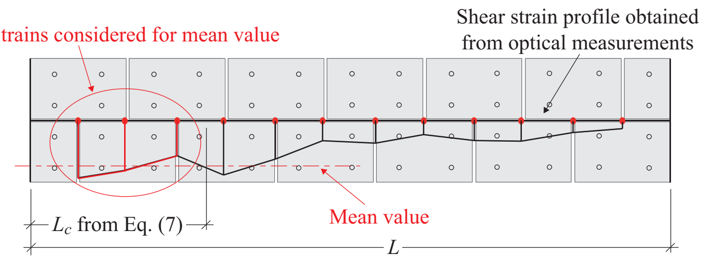

Figure 19. Schema showing how the average shear strain is obtained from the shear strain profile

and PUP3. The curvature profiles correspond to average values from curvatures in the positive and negative loading direction at the same LS. Hence, the curvature profiles are only included when the LSs are obtained for both loading directions. For PUP1 it can be noted that once the deformation start concentrating along one diagonal crack at LS-S3 and the hypothesis of plane sections clearly no longer holds, the curvature profile turns very irregular. This conclusion is in agreement with the conclusion from Section 4.3 on the prediction of the bed joint opening using Eq. (7). By contrast, the shapes of the curvature profiles before S3 are rather regular and it seems feasible to estimate these by a simple analytical model. For example, the height of zero curvature of these profiles intersects with the y-axes at approximately the height of zero moment. Furthermore, for LSs up to F1 (opening of bed joints) the curvature profile is approximately linear. Once the bed joints start opening, the compressed area reduces and the deformations start concentrating in the lower brick layers of the masonry (see Figs. 8, 10 and 14 in Sections 4.1 and 4.2). In Fig. 18, it can be seen that for the LSs succeeding LS-F1 this concentration of deformations is reflected in an over proportional increase of curvatures at the base.

4.5 Shear strains at the different LSs caused by shear solicitation, when considering only the part of the wall in compression

The curvature profiles are an indicator for the flexural deformability. However, taking into account that URM walls can be rather squat, shear deformations can contribute in equal measure to the total deformations as flexural deformations. Thus, in this section the shear strain profiles are investigated. Assuming again that the compressed part of the wall controls the wall's behavior, the shear strain at a particular height is computed as average of the shear of the compressed section at this height (see Fig. 19). The shear strains themselves are computed using the approach described in Fig. 7.

In Fig. 20, the shear strain profiles correspond to average values of the shear strains in the positive and negative loading direction at the same LS. The shear strain profiles are only included when the LSs are attained for both loading directions. It can be noted that the shear strains are rather constant over the height for small displacement demands (LS-S1/F1), while for higher displacement demands the shears strains tend to augment towards the base. This is due to the fact that after the first opening of the base joint at LS-F1, the effective section reduces and shear and compression stresses concentrate in the compressed zone. Since stresses and strains are related, this phenomenon is well visible for PUP3 (see also Fig. 14). Similar to the curvature profiles (see previous section), the shear strain profiles turn quite irregular once the walls start separating into two triangles (LS-S3).

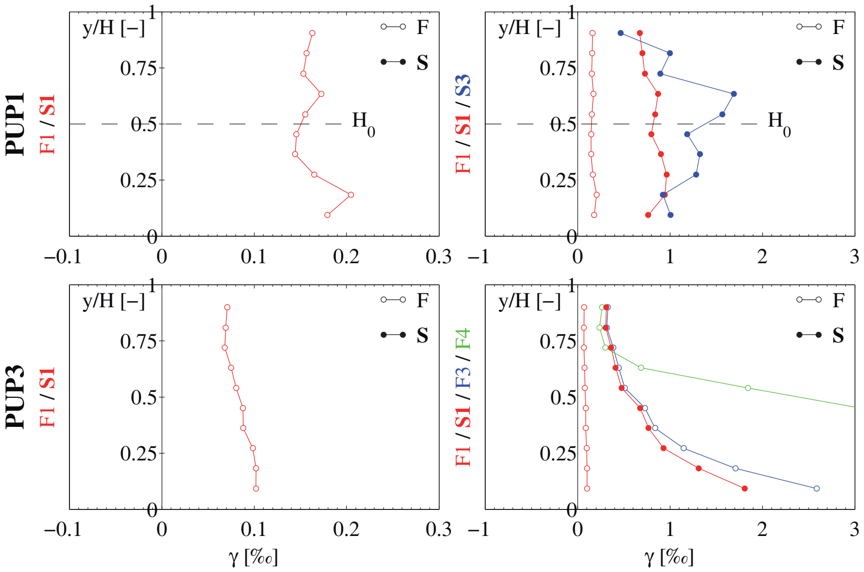

Figure 20. Average shear strain profiles from the shear strain profiles obtained at LS-F1 to S4, when considering only the part of the masonry in compression

5 Conclusions

Drift capacity models in current codes are based on empirical relationships but in the long term a replacement with analytical drift capacity models seems desirable [PB14b]. Such models should estimate the drift capacity at a certain limit state (LS) using a mechanical model which links the global force-displacement relationship of URM walls to local deformation measures such as strains and curvatures. However, in order to develop such models, local deformation measures that characterize the different LSs need to be identified.

Based on the observations by others [MM82, Hey92], results of our own tests and the LSs defined in FEMA 306 [ATC98], we define two sets of local LSs which are based on the occurrence of new cracks and therefore involve changes in the kinematics of the walls. For flexural modes, LS-F1 to F5 describe five LSs from the first appearance of a horizontal crack in the bed joint (F1) up to the instant when the wall loses its axial load bearing capacity (F5). For shear modes LS-S1 to S5 describe the behavior of the wall from the appearance of first stair step crack (S1) up to the instant when the upper triangle slips abruptly downwards (S5), which leads to both horizontal and axial load failure. We discuss the cause of these different LSs and we show that the drifts for which the different LSs are attained decrease with increasing axial stress and with decreasing shear span. We then link these LSs to characteristic points of the global force-displacement response.

In a second part of the paper we evaluate different local deformation measures at these LSs for two walls developing a shear and flexural failure mode respectively. The vertical and shear strain fields underline the high solicitation of the corner regions and along the diagonal crack. Furthermore, the strain fields show that the deformation behavior of the considered URM walls is controlled by the compressed part of the wall. Accordingly, in the following, the deformations of the compressed part of the wall are investigated in detail and the curvature and shear strain profiles of the compressed wall part are evaluated from the experimental measurements. The results suggest that before the formation of a diagonal shear crack, the wall behavior can be described by a Timoshenko beam where the variable cross section over the height of the wall corresponds to the compressed part of the wall. After the formation of the diagonal crack, the kinematics of the wall change and the wall behaves like two triangles above and below the diagonal crack. From this point onwards, a new kinematic model needs to be applied, which is yet to be developed.

6 Acknowledgments

The authors would like to thank Morandi Frères SA for the donation of the bricks and the staff of the structural engineering laboratory at EPFL for the support during testing.

References

[Abr01] Abrams, DP. Performance-based engineering concepts for unreinforced masonry building structures. *Progress in Structural engineering and Materials*, 3:48–56, 2001.

[ATC98] ATC. Evaluation of earthquake damaged concrete and masonry wall buildings. Technical Report FEMA-306, Basic Procedures Manual, Applied Technology Council (ATC), Washington, DC, USA, 1998.

[BB13] Benedetti, A and Benedetti, L. Interaction of shear and flexural collapse modes in the assessment of in-plane capacity of masonry walls. In *Proceedings of the 12th Canadian Masonry Symposium*, Vancouver, Canada, 2013.

[BP+03] Bosiljkov, V, Page, AW, Bokan-Bosiljkov, V and Zarnič, R. Performance based studies of in-plane loaded unreinforced masonry walls. *Masonry International*, 16(2):39–50, 2003.

[BS08] Benedetti, A and Steli, E. Analytical models for shear-displacement curves of unreinforced and frp reinforced masonry panels. *Construction and Buildings Materials*, 22:175–185, 2008.

[Cal99] Calvi, GM. A displacement-based approach for vulnerability evaluation of classes of buildings. *Journal of Earthquake Engineering*, 3:411–438, 1999.

[CEN05] CEN. Eurocode 8: Design of structures for earthquake resistance, Part 3: Assessmemt and retrofitting of buildings. Technical Report EN 1998-3, European Committee for Standardisation, Brussels, Belgium, June 2005.

[FM+09] Frumento, S, Magenes, G, Morandi, P and Calvi, GM. *Interpretation of experimental shear tests on clay brick masonry walls and evaluation of q-factors for seismic design.* Technical Report, IUSS PRESS, Pavia, Italy, 2009.

[FPV14] Facconi, L, Plizzari, G and Vecchio, F. Disturbed stress field model for unreinforced masonry. *Journal of Structural Engineering*, 140, 2014.

[FSA07] Fehling, E, Stuerz, J and A, Emami. Enhanced safety and efficient construction of masonry structures in europe - d 7.1a test results on the behaviour of masonry under static (monotonic and cyclic) in plane lateral loads. Technical Report Report ESECMaSE D 7.1a, University of Kassel, Kassel, Germany, 2007.

[FT11] Furtmüller T, Adam C. Numerical modeling of the in-plane behavior of historical brick masonry walls. *Acta Mechanica*, 221:65–77, 2011.

[GM+98] Gruenthal, G, Musson, R, Schwarz, J and Stucchi, M. European macroseismic scale 1998. Technical report, Cahiers de Centre Européen de Géodynamique et de Seismologie, Luxembourg, 1998.

[GT84] Ganz, HR and Thürlimann, B. Versuche an Mauerwerksscheiben unter Normalkraft und Querkraft. Technical Report Test Report 7502-4, ETH Zürich, Zürich, Switzerland, 1984.

[Hey92] Heyman, J. Leaning towers. *Meccanica*, 27:153–159, 1992.

[Lan02] Lang, K. *Seismic vulnerability of existing structures.* Phd thesis, ETH Zürich, Institute of Structural Engineering, Zürich, Switzerland, February 2002.

[LG06] Lagomarsino, S and Giovinazzi, S. Macroseismic and mechanical models for the vulnerability and damage assessment of current buildings. *Bulletin of Earthquake Engineering*, 4:415–443, 2006.

[Lou96] Lourenço, PB. *Computational strategies for masonry structures.* Phd thesis, Faculty of Engineering, TU Delft, Netherlands, 1996.

[LP$^+$13] Lagomarsino, S, Penna, A, Galasco, A and Cattari, S. Tremuri program: an equivalent frame model for the nonlinear seismic analysis of masonry buildings. *Engineering Structures*, 56:1787–1799, 2013.

[LR97] Lourenço, PB and Rots, JG. Multisurface interface model for analysis of masonry structures. *Journal of Engineering Mechanics*, 123:660–668, 1997.

[MM82] Mann, W and Müller, H. Failure of shear-stressed masonry—an enlarged theory, tests and application to shear walls. In *Proceedings British Ceramic Society*, volume 30, pages 223–235, 1982.

[MMP08] Magenes, G, Morandi, P and Penna, A. Enhanced safety and efficient construction of masonry structures in europe, 7.1c test results on the behaviour of masonry under static cyclic in plane lateral loads. Technical Report ESECMaSE D7.1c, University of Pavia, Pavia, Italy, 2008.

[PB14a] Petry, S and Beyer, K. Cyclic test data of six unreinforced masonry walls with different boundary conditions. *Earthquake Spectra*, 2014.

[PB14b] Petry, S and Beyer, K. Influence of boundary conditions and size effect on the drift capacity of URM walls. *Engineering Structures*, 65:76–88, 2014.

[PB14c] Petry, S and Beyer, K. Scaling unreinforced masonry for reduced-scale seismic testing. *Bulletin of Earthquake Engineering*, 12:2557–2581, 2014.

[PCK07] Priestley, MJN, Calvi, GM and Kowalsky, MJ. *Displacement-Based Seismic Design of Structures.* Pavia, Italy, 2007.

[PLBL11] Pfyl-Lang, K, Braune, F and Lestuzzi, P. Evaluation de la sécurité parasismique des bâtiments en maçonnerie. Technical Report SIA D0237, Documentation, Swiss Society of Engineers and Architects SIA, Zürich, Switzerland, 2011.

[PLG14] Penna, A, Lagomarsino, S and Galasco, A. A nonlinear macroelement model for the seismic analysis of masonry buildings. *Earthquake Engineering and Structural Dynamics*, 43:159–179, 2014.

[Tom07] Tomaževič, M. Damage as a measure for earthquake-resistant design of masonry structures: Slovenian experience. *Canadian Journal of Civil Engineering*, 34:1403–1412, 2007.

[ZPB14] Zhang, S, Petry, S and Beyer, K. Investigating the in-plane mechanical behavior of URM piers via DSFM. In *Proceedings of the 2nd European Conference on Earthquake Engineering and Seismology*, Istanbul, Turkey, 2014.

Paper IV

Force-displacement response for in-plane loaded URM walls with a dominating flexural mode

Petry, S and Beyer, K; *Submitted to Earthquake Engineering and Structural Dynamics* (September 2014)

Abstract

This article presents a new mechanical model for the nonlinear force-displacement response of unreinforced masonry (URM) walls developing a flexural rocking mode including their displacement capacity. The model is based on the plane section hypothesis and a constitutive law for the masonry with zero tensile strength and linear-elastic behavior in compression. It is assumed that only the compressed part of the wall contributes to the stiffness of the wall and therefore the model accounts for a softening of the response due the reduction of the effective area. Stress conditions for limit states are proposed that characterize the flexural failure. The new model allows therefore to link local performance levels to global displacement capacities. The limit states criteria describe the behavior of modern URM walls with cement mortar of normal thickness and clay bricks. The model is validated through comparison of local and global engineering demand parameters with experimental results. The model is shown to provide good prediction of the effective stiffness, the force capacity and the displacement capacity of URM walls at different limit states.

Keywords:

Unreinforced masonry; Flexural rocking; Walls; Displacement capacity; Effective stiffness;

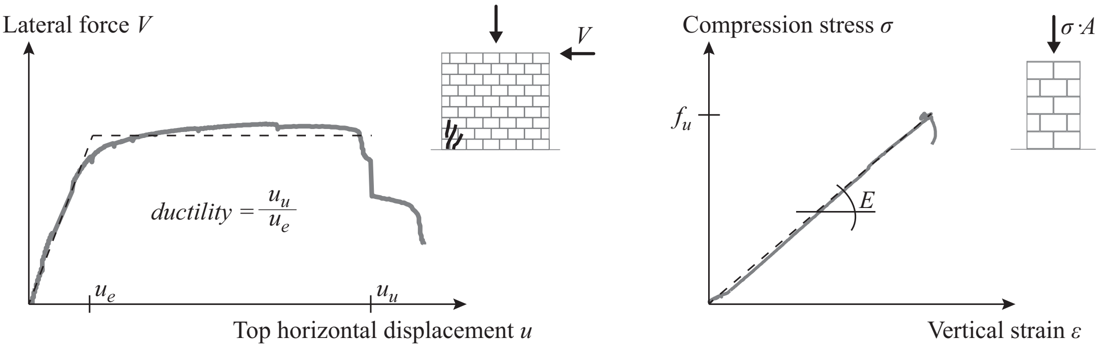

Figure 1. Schematic force-displacement response for a wall developing a flexural rocking mode and stress-strain relationship of masonry in compression

1 Introduction

Previous generations of seismic design codes were based on force-based design approaches, which led in general to conservative designs and evaluations. For the assessment of existing buildings this is often undesirable and displacement-based methods, which tend to lead to more realistic and less conservative estimates, should be given preference [Mag06]. Displacement-based methods require not only estimates of the stiffness and strength but also of the deformation capacity. While several models exist which provide good estimates of the force-capacity of in-plane loaded unreinforced masonry (URM) walls [MC97, TC71, TS81, MM82, Gan85], estimating the displacement capacity and the effective stiffness of URM walls is a much more challenging task, which needs further research [Mag06, BP$^+$14]. One approach for improving existing empirical drift capacity models is to consider additional parameters [Lan02, PLBL11, PB14c]. The effective stiffness is currently computed as fixed portion of the elastic stiffness [CEN05b] which could potentially also be improved by replacing this fixed ratio by an empirical function of several parameters. In the long term it seems, however, desirable to move towards mechanical models for the force-displacement response of URM structural elements. Such models would foster an understanding for key parameters that influence the seismic behavior of URM walls and could also account for the large regional variability of masonry construction through standard material tests.

When URM walls are subjected to lateral in-plane loading, three kinds of failure modes are generally distinguished: rocking failure, diagonal shear failure and sliding failure [MC97]. In this article walls developing a rocking failure mode, i.e. a flexural failure, are discussed. Flexural failure is dominated by local compression failure of the wall toe [MC97] and Fig. 1 compares the global force-displacement response of an URM wall developing a flexural mode to the stress-strain curve obtained from a simple uniform compression test on a masonry wallette. Despite the brittle behavior of URM in compression (Fig. 1b), URM walls developing a flexural mode can develop a significant ductility due to its nonlinear elastic behavior (Fig. 1a) [MC97, PCK07]: an URM wall subjected to a constant normal load N and an increasing lateral force V behaves linear-elastically until the minimum stress in the bottom section is equal to zero (see Fig. 2, $V = V_e$). The tensile strength of URM is negligible. If V increases, the wall enters therefore the nonlinear elastic regime, horizontal cracks start opening at the wall base and the effective section reduces while the flexibility of the wall increases. The lateral load at

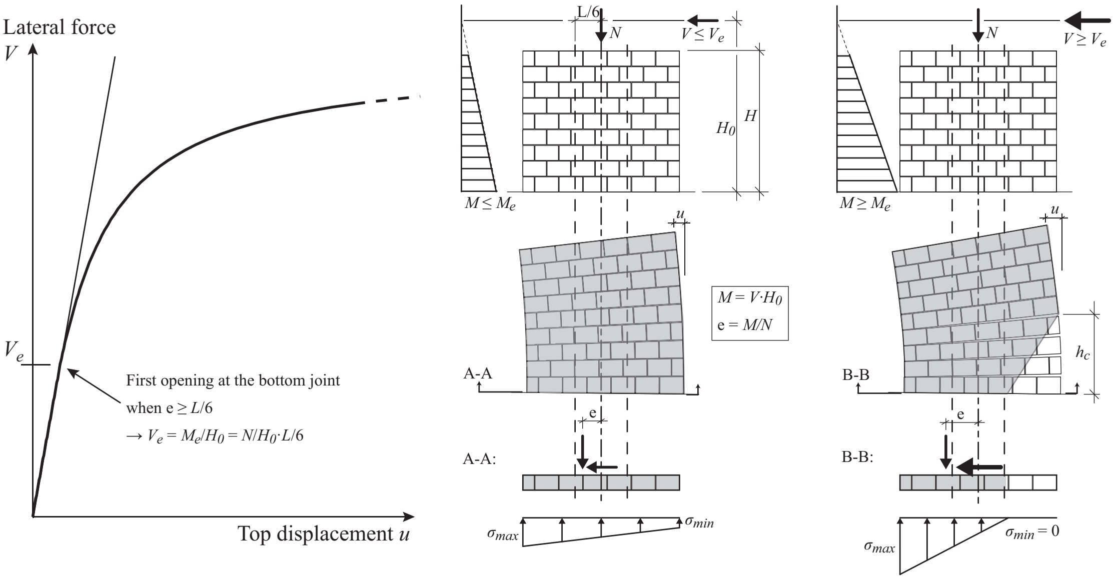

Figure 2. Force-displacement response of a wall assuming a material with zero tensile strength and linear-elastic behavior in compression

the onset of decompression is:

$$V_e = \frac{NL}{6H_0} \tag{1}$$

where N is the applied normal load, L the length of the wall and H_0 the shear span. Several researchers published models which describe the behavior of flexural URM walls. Some of these models are of analytical nature and derive a direct relationship between horizontal force and top displacement, e.g. the force-displacement relationship for leaning towers [Hey92] or the force-displacement response developed in [BS08, BB13] and [PLG14]; the latter is implemented as macro-element in the computer software Tremuri [LP$^+$13].

Section 2 reviews these existing models. Based on these models a new analytical formulation is developed and compared to the existing models in Section 3. In Section 4, local deformation limit states are implemented in the new analytical formulation and a link between local and global engineering demand parameters (EDPs) is thus established. The model is validated through comparison of local and global EDPs with own experiments in Section 5. In Section 6, the model is benchmarked against a larger dataset with regard to the predicted effective stiffness and displacement capacity. In Section 7, the model is used to determine key parameters that influence the ultimate drift capacity. Section 8 concludes the paper with a summary of the findings and an outlook on research needs.

2 Existing models for the prediction of the force-displacement relationship and the performance levels of URM walls

2.1 Analytical formulations for the force-displacement relationship of URM walls

Models that estimate analytically the force-displacement response of URM walls were published by Benedetti et al. [BS08, BB13] and by Penna et al. [PLG14]. The model by Benedetti and

Steli [BS08] is based on the plane section hypothesis and a non-tension material with a linear-elastic behavior in compression. Benedetti and Steli [BS08] describe the force-displacement behavior of URM walls in two parts: the linear-elastic part before the onset of decompression and the nonlinear elastic domain with opening of the base joint (see also Fig. 2). The model is derived for flexural dominated walls but includes also linear-elastic shear deformations (though-as the comparison in Section 3.4 will show-these are underestimated). Benedetti and Benedetti implemented a shear failure criterion into the existing model [BB13] but since damage due to shear solicitation is not considered the model's application remains restricted to walls whose response is dominated by flexure. The model developed by Penna et al. [PLG14] is based on the idea of separating the wall into a central part and two interfaces at the bottom and top of the wall. Shear deformations are allocated to the central part of the wall and flexural deformations to the interfaces. Section 3.4 contains a detailed discussion of the differences between both models and the newly proposed model.

2.2 Mechanical models for the prediction of the displacement capacity at certain performance levels

Models that use local performance limits for predicting the global displacement capacity of URM walls were published by Benedetti and Steli [BS08] and Priestley et al. [PCK07]. The two models have in common that they link local deformation and strength limits in the compressed toe with the global displacement capacity of flexural walls. Benedetti and Steli [BS08] predict in conjunction with their analytical formulation described in Section 2.1 the yield and ultimate displacement. The model by Priestley et al. [PCK07] gives a direct estimate for the ultimate drift capacity. Both models are based on the assumption of an elastic plastic material in the compression zone with a maximum compression strain of 3‰and 4‰respectively. A more detailed review of these models can be found in [PB14b].

3 New analytical model for the elastic force-displacement relationship for URM walls

Benedetti and Steli [BS08] developed an analytical formulation for the elastic force-displacement relationship of cantilever walls subjected to an increasing horizontal load and a constant vertical load. For walls subjected to fixed-fixed boundary conditions, Benedetti and Steli [BS08] propose calculating the displacement at half height of the wall and doubling it to obtain the displacement at the top of the wall. In real structures, the boundary conditions of a wall are often different to those of a cantilever or fixed-fixed boundary conditions [Lan02, PB14c]. Hence, in the following section the model is extended for a general normalized shear span $\alpha = H_0/H$. Shear and flexural deformations are treated separately in Sections 3.1 and 3.2 respectively. At any point of loading, the total horizontal displacement u can be computed as the sum of the displacements due to flexural and shear deformations:

$$u = u_{fl} + u_{sh} \tag{2}$$

Shear deformations are assumed to contribute only to the horizontal displacement but not to the vertical displacement w or the top rotation θ. Hence, the rotation at the top of the wall and the vertical displacement are treated in the section on flexural deformations (Section 3.1). The sign convention of all deformation quantities is illustrated in Fig. 3. Sections 3.1 and 3.2 apply to walls with $\alpha \geq 1.0$. The computation of the global deformation quantities u, w, θ for

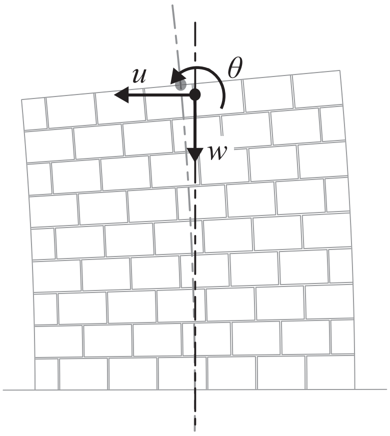

Figure 3 Definition and sign convention for the three global deformation quantities u, w, θ

walls with a normalized shear span $\alpha < 1.0$ are discussed in Section 3.3.

3.1 Deformation quantities caused by flexural solicitations for $\alpha \geq 1.0$

Based on the plane section hypothesis and a non-tension material, the following relationship is obtained between the length of the compression zone L_c and the base moment M (see Fig 2):

$$L_c = L \qquad \text{for} V \leq V_e \tag{3}$$

$$L_c = 3\left(\frac{L}{2} - \frac{M}{N}\right) \qquad \text{for} V > V_e \tag{4}$$

Considering further the linear-elastic material behavior of the masonry in compression (see Fig. 1b), the curvature after onset of decompression is estimated as follows:

$$\chi = \frac{M}{EI} \qquad \text{for} V \leq V_e \tag{5}$$

$$\chi = \frac{2N}{ET} \cdot \frac{1}{L_c^2} \qquad \text{for} V > V_e \tag{6}$$

where T is the thickness of the wall, $I = L^3 T/12$ is the moment of inertia of the full section and E the E-modulus for loading perpendicular to the bed joints. Assuming a simple Bernoulli beam with a constant section along its length for $V \leq V_e$ and a varying section for $V > V_e$, the flexural displacement u_{fl} is derived as follows:

$$u_{fl} = V \cdot \frac{H^3}{2EI}\left(\alpha - \frac{1}{3}\right) \qquad \text{for} V \leq V_e \tag{7}$$

$$\begin{aligned} u_{fl} = {} & u_{e,fl} \cdot \left(\left(1 - \frac{\alpha^2(3-\alpha)}{3\alpha - 1}\right) \cdot \frac{V}{V_e} + \frac{3\alpha^2(3-\alpha)}{3\alpha-1} \cdot \frac{V_e}{V} + \frac{2\alpha^3}{3\alpha-1} \cdot \left(\frac{V_e}{V}\right)^2 \right) \\ & + \theta_{cr}(V) \cdot \left(H(1-\alpha) + \frac{M_e}{V}\right) + \psi_{cr}(V) \qquad \text{for} V > V_e \end{aligned} \tag{8}$$

with

$$\theta_{cr}(V) = -\frac{2N^2}{9ETLV}\left(\mu - 6\eta\right) \tag{9}$$

$$\psi_{cr}(V) = -\frac{N^3}{9ETLV^2}\left(\frac{2}{3}\mu - 4\eta + 2\ln\frac{2}{3}\mu\right) \tag{10}$$

$$\mu = \frac{L\cdot N}{L\cdot N - 2\alpha H\cdot V} \tag{11}$$

$$\eta = \frac{\alpha H\cdot V}{L\cdot N - 2\alpha H\cdot V} \tag{12}$$

where H is the height of the URM wall. $u_{e,fl}$ is the flexural displacement at $V = V_e$ and is computed using Eqs. (1) and (7). In addition to a horizontal displacement, the vertical strains cause also the top of the wall to move vertically and to rotate. The rotation θ at the top of the wall equates to:

$$\theta = V\cdot\frac{H^2}{EI}\left(\alpha - \frac{1}{2}\right) \qquad \text{for} V \le V_e \tag{13}$$

$$\theta = V\cdot\frac{H^2}{2EI}\left(-(1-\alpha)^2 + \left(\alpha\cdot\frac{V_e}{V}\right)^2\right) + \theta_{cr}(V) \qquad \text{for} V > V_e \tag{14}$$

and the vertical displacement w to:

$$w = \frac{NH}{ELT} \qquad \text{for} V \le V_e \tag{15}$$

$$w = w_e\cdot(1-\alpha) + \frac{2N^2}{9ETV}\left(\frac{9}{4} - \mu + 3\ln\frac{2}{3}\mu\right) \qquad \text{for} V > V_e \tag{16}$$

3.2 Deformation quantities caused by shear solicitations for $\alpha \ge 1.0$

Assuming that only the compressed section contributes to the shear stiffness of the wall, the shear behavior as the flexural behavior will be influenced by the reduction of the effective section and the following relationship between the equivalent shear strain and the lateral load is derived:

$$\gamma = \frac{6V}{5GT}\cdot\frac{1}{L_c} \tag{17}$$

where G is the shear modulus and L_c the compression length according to Eqs. (3) or (4). Hence, assuming a simple Timoshenko beam with constant section along its length for $V \le V_e$, a varying section for $V > V_e$ and by integrating the equivalent shear strain computed with Eq. (17), the following relationship is established between shear displacement u_{sh} and V:

$$u_{sh} = V\cdot\frac{6H}{5GA} \qquad \text{for} V \le V_e \tag{18}$$

$$u_{sh} = u_{e,sh}\cdot\left(\alpha + (1-\alpha)\cdot\frac{V}{V_e}\right) + \psi_{sh}(V) \qquad \text{for} V > V_e \tag{19}$$

with

$$\psi_{sh}(V) = -\frac{2N}{5GT} \cdot \ln \frac{2}{3}\mu \tag{20}$$

$$\mu = \frac{L \cdot N}{L \cdot N - 2\alpha H \cdot V} \tag{21}$$

where $A = LT$ is the area of the full section.

3.3 Extension of the model to normalized shear spans of $\alpha \leq 1.0$

By applying the following procedure, the new model can be applied also to walls with a shear span smaller than the wall height. First, the horizontal displacement $u_{1,0}$ at the inflection point is computed using Eqs. (7) to (21) by replacing the wall height by the shear span and setting the normalized shear span to one, hence, $H^* = H_0$ and $\alpha^* = 1$. In a second step, the rotation $\theta_{1,0}$ and the vertical displacement $w_{1,0}$ at the inflection point are computed using the Eqs. (13) to (16) setting again $H^* = H_0$ and $\alpha^* = 1$.

The relative horizontal displacement between inflection point and top, $u_{2,0}$, is obtained using again the Eqs. (7) to (21), but replacing this time the wall height by the height remaining above the inflection point and setting the normalized shear span again equal to one, hence, $H^* = H - H_0$ and $\alpha^* = 1$. Note also that the limit $V \leq / > V_e$ changes to $V \leq / > H_0/(H - H_0)V_e$ for the part of the wall above the inflection point. In the next step, the rotation $\theta_{2,0}$ and the vertical displacement $w_{2,0}$ are computed for the part of the wall above the inflection point applying Eqs. (13) to (16) again with $H^* = H - H_0$ and $\alpha^* = 1$. Finally, the displacements and rotation at the top of the wall are computed as follows:

$$u = u_{1,0} + u_{2,0} + \left(\theta_{1,0} - \theta_{2,0}\right) \cdot (H - \alpha H) \tag{22}$$

$$\theta = \theta_{1,0} - \theta_{2,0} \tag{23}$$

$$w = w_{1,0} + w_{2,0} \tag{24}$$

3.4 Extension of the model to normalized shear spans of $\alpha = H_0/H > 1.5$ and $V > NL/(6H(\alpha - 1))$

For walls with a shear span higher to 1.5 times the wall height, the moment at top can exceed the moment at first cracking ($M_{top} > NL/6$) resulting thus in a reduction of the compression length also at top of the wall. This is the case when following condition is fulfilled:

$$V > \frac{NL}{6H} \cdot \frac{1}{\alpha - 1} \tag{25}$$

In order to account for this case, it is suggested to compute the deformation quantities $u_{1,0}$, $w_{1,0}$ and $theta_{1,0}$ by extending artificially the wall height to the shear span, hence, while assuming $H^* = H_0$ and $\alpha^* = 1$ and using the equations from Sections 3.1 and 3.2. Then, the deformation quantities $u_{2,0}$, $w_{2,0}$ and $theta_{2,0}$ which develop between in the artificially extended part are computed while applying $H^* = H_0 - H$ and $\alpha^* = 1$ to the equations from Sections 3.1 and 3.2. Finally, the displacements and rotation at the top of the wall are computed

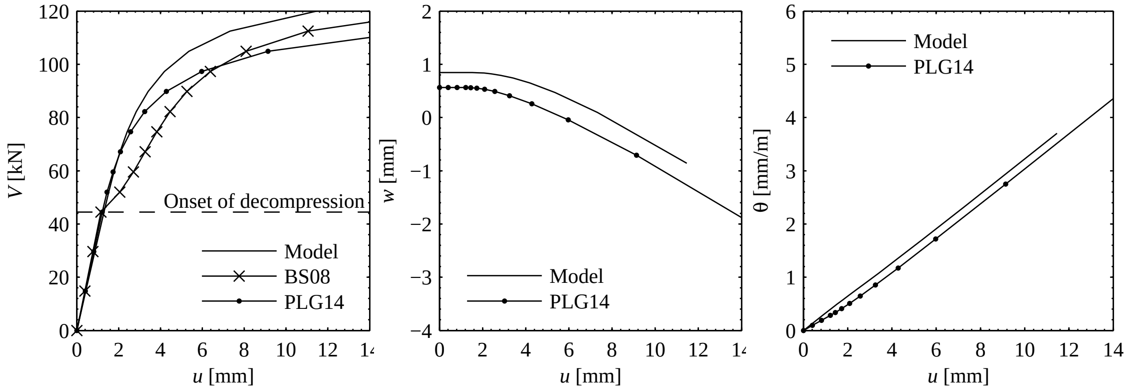

Figure 4. Global deformation quantities for a cantilever wall according to Benedetti and Steli [BS08], to Penna et al. [PLG14] and to the newly proposed model "Model"

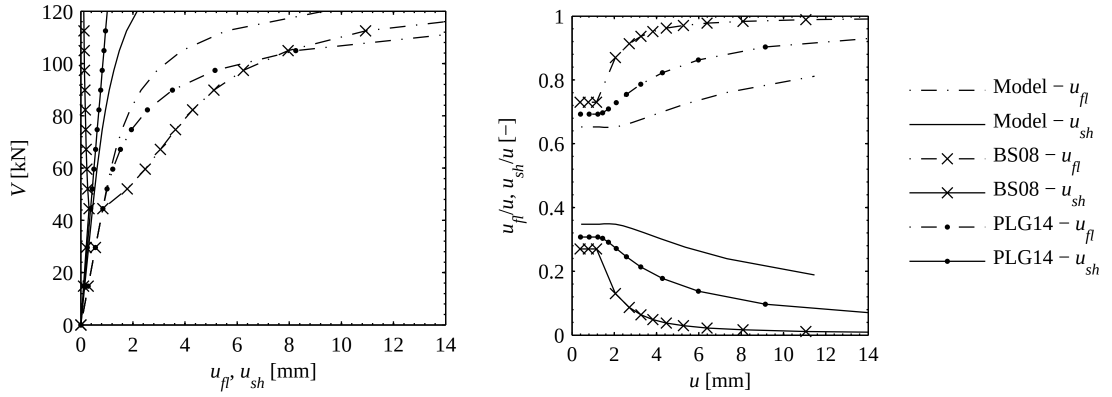

Figure 5. Horizontal displacement components due to shear and flexure for a cantilever wall according to Benedetti and Steli [BS08], to Penna et al. [PLG14] and to the newly proposed model "Model"

as follows:

$$u = u_{1,0} - u_{2,0} - \left(\theta_{1,0} - \theta_{2,0}\right) \cdot (H - \alpha H) \tag{26}$$

$$\theta = \theta_{1,0} - \theta_{2,0} \tag{27}$$

$$w = w_{1,0} - w_{2,0} \tag{28}$$

3.5 Differences between existing models and the newly proposed model

Figures 4 and 5 compare the predicted force-displacement curves using the new analytical formulation (Eqs. (2) to (21)) and the models developed by Benedetti and Steli [BS08] and by Penna et al. [PLG14] for a cantilever wall ($\alpha = 1.0$). The model by Benedetti and Steli [BS08] does not provide an estimate for the vertical displacement and the rotation at the top of the wall, thus for these two parameters only the model from Penna et al. [PLG14] is compared to the new analytical formulation. Even though all models are based on the same moment-curvature relationship, the resulting force-displacement relationships diverge notably after the onset of decompression in the base joint.

The model by Benedetti and Steli [BS08] predicts at the onset of the non-linearity an abrupt increase of the flexibility, which is also shown in the graphs reported in [BS08]. The shape of the curve resembles that of a moment-curvature relationship of reinforced concrete and it results probably from an error in the integration of the curvature profile. In addition, it can be noted that the model by Benedetti and Steli [BS08] predicts the shear deformation to decrease after the onset of decompression. As noted in [PB14b], this is not in line with experimental observations. The new analytical formulation accounts for the reduction of the effective section when computing shear deformations, predicting therefore an increase in shear flexibility with the onset of decompression. In the model by Penna et al. [PLG14], the reduction of the compression zone is only computed at the interfaces at the top and bottom of the wall, i.e., where the maximum curvatures develop. For cantilever walls, this simplification results in overestimating the flexural deformation by 1.5 and for double-fixed by a factor of 3. Therefore, it is suggested to counterbalance this phenomenon by increasing the E-modulus by 50% or 200% respectively. Nevertheless, the predicted softening of the flexural deformation after the onset of decompression is more important for the model by Penna et al. [PLG14] than for the new model. On the contrary, Penna et al. [PLG14] do not consider the reduction of the compression zone when computing the shear displacement and the shear force-shear displacement response remains linear-elastic throughout the force-displacement curve. Note that Penna et al. [PLG14] also included a damage model [GL97] that captures the nonlinear shear response for shear dominated walls. This part of the model is not considered here because only flexure dominated walls are treated. The shear displacements estimated with Penna et al. [PLG14] are 20% smaller with respect to the linear-elastic estimation obtained with the new analytical formulation. The new model includes a factor of 6/5 that accounts for the shear stress distribution of a rectangular cross section (Eq. (17)), which is not included in Penna et al. [PLG14].

4 Implementation of local limit states in the global force-displacement relationship

The new analytical formulation is based on the assumption of a linear-elastic material in compression with zero tensile strength and the hypothesis of plane sections remaining plane. Note that this second assumption only holds, as long as no significant diagonal crack separates the walls [PB14d]; this limits the application of the model to walls with a dominating flexural mode. For determining the displacement capacity of flexural dominated URM walls, local limit states (LSs) need to be predicted and their influence on the kinematics of the wall implemented in the model from Section 3. In Table 1, a set of local LSs is summarized which is typically observed for a modern URM wall that is (i) constructed with hollow clay bricks and normal cement mortar, (ii) subjected to lateral in-plane loading and (iii) whose behavior is dominated by flexure. LS-F2 does not alter the global force-displacement response of the wall and is therefore not considered in the following. LS-F4 results in a significant loss in lateral force capacity and it can be assumed that this limit state is equal to the performance level ”Near Collapse” according to EC8-P3 [CEN05b]. In the following, the characteristics of the LS-F1, F3 and F4 are discussed and local performance limits are proposed that allow estimating the global displacement at these LSs.

Table 1. Local LSs for in-plane loaded URM walls with a dominating flexural mode [PB14d]

Limit state	Local crack pattern	Influence on global response
LS-F1	First appearance of a crack in a bed joint	First reduction of stiffness
LS-F2	Visible separation of the unloaded zone from the compression zone [Hey92]	Negligible influence on force-displacement relationship
LS-F3	Appearance of vertical splitting cracks in compressed corner	Peak load is typically attained shortly afterwards
LS-F4	Loss of part of the toe region due to crushing	Significant loss of the lateral resistance
LS-F5	Crushing of entire compression zone	Axial load failure

4.1 Appearance of first horizontal cracks in bed joints (LS-F1)

The first appearance of a horizontal crack (LS-F1) is related to the onset of decompression in the base joint. The effect of decompression is considered in the model through the reduction of the effective section. The onset of decompression is reached when $V_{\mathrm{F1}} = V_e$ and the deformation vector at LS-F1 can be computed using Eqs. (1), (7), (13), (15) and (18).

4.2 First splitting cracks in bricks in the compression toe (LS-F3)

When the horizontal displacement is increased, at a certain point, vertical splitting cracks appear in the bricks of the compressed toe. Observations showed that cracks in bricks initiate often at the second bed joint ($y = h_B$, Fig. 6) and not always as one might expect at the base joint ($y = 0$). This is due to the confining effect of the foundation: masonry subjected to compression fails due to tensile failure of the bricks because mortar has a larger Poisson's ratio than bricks. At the base, the foundation confines the mortar layer and hinders the mortar from expanding. Hence, the typical tensile failure of the brick is observed only in relation to the second bed joint and not to the base joint. Furthermore, cracks initiating from the 2nd joint develop typically first half a brick width inwards from the external fiber of the wall. This is due to the fact that half bricks at the end of a row-irrespective whether they are in the first or second layer of bricks-have a certain flexibility to rotate inside the matrix of the surrounding mortar joints. Hence, considering the maximum masonry compression strength at the extreme fiber of the second mortar joint leads to too conservative estimates of the displacement capacity associated with LS-F3. This displacement capacity was found to correlate better with the instant when the masonry compression strength f_u is reached in the second joint ($y = h_B$) at a half-brick inwards ($x = l_B/2$) from the external fiber:

$$\sigma_y\left(\frac{l_B}{2}; h_B\right) = f_u \tag{29}$$

where $\sigma_y\left(x, y\right)$ is the vertical stress at the horizontal distance x from the extreme fiber at the height y of the wall. l_B is the length of the brick plus the width of one vertical mortar joint and h_B is the height of the brick plus the thickness of one horizontal mortar joint.

Depending on the relative size of bricks and walls, the compression stress at the base joint

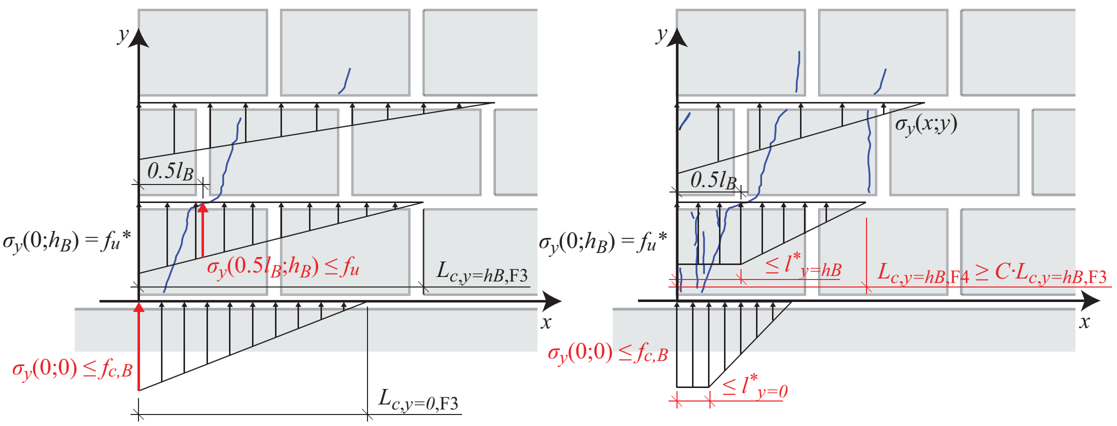

Figure 6. Crack pattern of compressed corner and assumptions for the stress states at (a) first cracks in brick (LS-F3) and (b) at loss of part of the toe region due to crushing (LS-F4)

can reach the compression strength of the brick itself before the limit given by Eq. (25) is reached. Therefore, as a second criterion for LS-F3, the compression strength $f_{c,B}$ of the brick has to be considered at the extreme fiber of the base section:

$$\sigma_y(0;0) = f_{c,B} \tag{30}$$

The two criteria for LS-F3 are illustrated in Fig. 6a. Whichever of the two criteria is reached first, will determine the global deformation quantities u_{F3}, w_{F3} and θ_{F3} at LS-F3, which can be computed using the equations given in Section 3 for $V > V_e$. Note that when LS-F3 occurs in the base joint, it is assumed that the ultimate capacity of the wall is reached (i.e. $u_{\text{F4}} = u_{\text{F3}}$). In that case, Section 4.3 does not apply.

The compression lengths at LS-F3 are required as input parameters for determining LS-F4. They can be computed for the second mortar joint as:

$$L_{c,y=hB,\text{F3}} = \frac{N + \sqrt{N^2 - N \cdot \sigma_y\left(\frac{l_B}{2}; h_B\right) \cdot T l_B}}{f_u T} \tag{31}$$

and for the base joint as:

$$L_{c,y=0,\text{F3}} = \frac{2N}{f_{c,B} T} \tag{32}$$

4.3 Loss of part of the toe region due to crushing (LS-F4)

Experiments showed that walls do not reach lateral load failure with the occurrence of first splitting cracks (LS-F3) but that at this instant the walls are still able to sustain the applied lateral load and that the load can even increase slightly until first parts of the compression zone break completely apart (LS-F4, [PB14d]).

Figure 6 shows the crack pattern in the compression zone just after reaching LS-F3 (Fig. 6a) and just before LS-F4 occurred (Fig. 6b). Between the two LSs, several cracks develop in the corners between the extreme fiber and the splitting crack that initiated at the point $\left(x = l_B/2, y = h_B\right)$. This allows a redistribution of the stresses in the compression zone. The maximum length l^* over which the stress can redistribute (see Fig. 6b) is assumed to be limited by the aforementioned splitting crack; it can be estimated as follows for the second joint and the base joint:

$$l^*_{y=hB} \leq \frac{l_B}{2} \tag{33}$$

$$l^*_{y=0} = l^*_{y=hB} - h_B \frac{V_{\mathrm{F3}}}{N} \tag{34}$$

It is assumed that the continued formation of cracks when loading beyond LS-F3 allows a certain stress redistribution in the compressed toe [PB14d]. The resulting reduction of the compression length at LS-F4 is restricted to account for the limited deformation capacity of masonry in compression. This is accounted for by confining the compression length at LS-F4 to $L_{c,\mathrm{F4}} \geq C \cdot L_{c,\mathrm{F3}}$, where C should depend on variables that control the deformation capacity of the brick in the post-splitting state (see Fig. 6b). Due to the lacking experimental evidence on this specific subject, a value of $C = 70\%$ is proposed. As in LS-F3 one should also account for compression failure of the brick itself and the maximum stress at the base should be limited to the compression strength $f_{c,B}$ of the brick (Eq. 26). The different limit criteria for LS-F4 are illustrated in Fig. 6b.

The deformation quantities at LS-F4 are computed as the sum of the deformations u_p, w_p and θ_p which develop in the zone of vertical splitting cracks and the nonlinear elastic deformations u_{ne}, w_{ne} and θ_{ne} which develop in the zone without vertical splitting cracks:

$$u_{\mathrm{F4}} = u_{ne} + u_p = u_{ne} + \theta_p \cdot \left(H - \frac{h_p}{2}\right) + u_{sh,p} \tag{35}$$

$$w_{\mathrm{F4}} = w_{ne} + w_p \tag{36}$$

$$\theta_{\mathrm{F4}} = \theta_{ne} + \theta_p \tag{37}$$

where h_p is the wall height over which vertical splitting cracks in bricks are expected (see Fig. 7) and which can be estimated as:

$$h_p = \frac{V_{\mathrm{F4}} \cdot H_0 - M_{FC}}{V_{\mathrm{F4}}} \geq h_B \tag{38}$$

where M_{FC} is the moment which leads to the first splitting crack and is equal to the moment which triggers LS-F3 ($M_{FC} = H_0^* \cdot V_{\mathrm{F3}}$), H_0^* is the shear span with respect to the critical section, i.e. the base joint or the second joint (see Fig. 7). It is assumed that the vertical splitting cracks form always over at least the height of one brick (h_B). The rotation θ_p which develops in the cracked zone is computed as follows:

$$\theta_p = \left(\chi_{y=0,\mathrm{F4}} + \chi_{y=hp,\mathrm{F4}}\right) \cdot \frac{h_p}{2} \tag{39}$$

where $\chi_{y=0,\mathrm{F4}}$ and $\chi_{y=hp,\mathrm{F4}}$ are the curvature at $y = 0$ and h_p respectively (see Fig. 7), which can be estimated from the strain at the external fiber (assuming a linear-elastic constitutive law as shown in Fig. 7) and the compression length:

$$\chi_{y=0,\mathrm{F4}} = \frac{\epsilon_y\,(0;0)}{L_{c,y=0,\mathrm{F4}}} = \frac{2N}{ETL_{c,y=0,\mathrm{F4}}\left(L_{c,y=0,\mathrm{F4}} + l^*_{y=0}\right)} \tag{40}$$

$$\chi_{y=hp,\mathrm{F4}} = \frac{\epsilon_y\left(0;h_p\right)}{L_{c,y=hp,\mathrm{F4}}} = \frac{2N}{ETL^2_{c,y=hp,\mathrm{F4}}} \tag{41}$$

The horizontal displacement component that originates from the shear strain in the zone of splitting can be computed using the same assumptions as in Section 3.2:

$$u_{sh,p} = \left(\gamma_{y=0,\mathrm{F4}} + \gamma_{y=hp,\mathrm{F4}}\right)\cdot\frac{h_p}{2} = \frac{V_{\mathrm{F4}}}{GT}\cdot\left(\frac{1}{L_{c,y=0,\mathrm{F4}}} + \frac{1}{L_{c,y=hp,\mathrm{F4}}}\right)\cdot\frac{h_p}{2} \tag{42}$$

and the vertical displacement that develops in the splitting zone can be obtained as follows:

$$w_p = \left(\chi_{y=0,\mathrm{F4}}\cdot\left(L_{c,y=0,\mathrm{F4}} - L/2\right) + \chi_{y=hp,\mathrm{F4}}\cdot\left(L_{c,y=hp,\mathrm{F4}} - L/2\right)\right)\cdot\frac{h_p}{2} \tag{43}$$

The force-deformation response of all global deformation quantities (u, w and θ) between LS-F3 and F4 can be estimated by linear interpolation, e.g. for the horizontal displacement u:

$$u = u_{\mathrm{F3}} + \frac{V - V_{\mathrm{F3}}}{V_{\mathrm{F4}} - V_{\mathrm{F3}}}\cdot\left(u_{\mathrm{F4}} - u_{\mathrm{F3}}\right) \tag{44}$$

5 Experimental validation - Part I

The model is validated in two steps: In this section, the analytical prediction is compared against two own tests for which detailed measurements of the displacement field are available. Hence, not only the global response but also the displacement components and local response at the wall base can be compared. In Section 6, the model is validated against a larger set of tests. For these tests the comparison is based on global engineering demand parameters (EDPs) only, i.e. effective stiffness, displacement and force capacity.

At EPFL six URM walls were tested under quasi-static cyclic loads; all walls were constructed with hollow clay bricks and normal cement mortar and had dimensions of $L \times H \times T = 2.01 \times 2.25 \times 0.20$ m [PB14c, PB14a]. Two walls of this series developed a significant flexural mode (PUP3 developed a typical flexural rocking and PUP4 showed a hybrid failure mode). These two walls are used in the following for the validation of the mechanical model on the global and local level. Both walls were tested keeping the normal force ($N = 419$ and 619 kN respectively) and the shear span constant ($H_0 = 1.5$ times the wall height H). The material properties that are relevant for the mechanical model are summarized in Table 2. The shear modulus could not be determined from experimental tests and was estimated as 25% of the elastic modulus. Note that current codes, e.g. EC6 [CEN05a], estimate the shear modulus as 40% of the elastic modulus; this is in general considered as too high [Tom09, Man14].

5.1 Global EDPs

In Fig. 8, the force-displacement relationship is estimated for the walls PUP3 and PUP4 using the model presented in Section 3 with the limit states defined in Section 4. Optical measure-

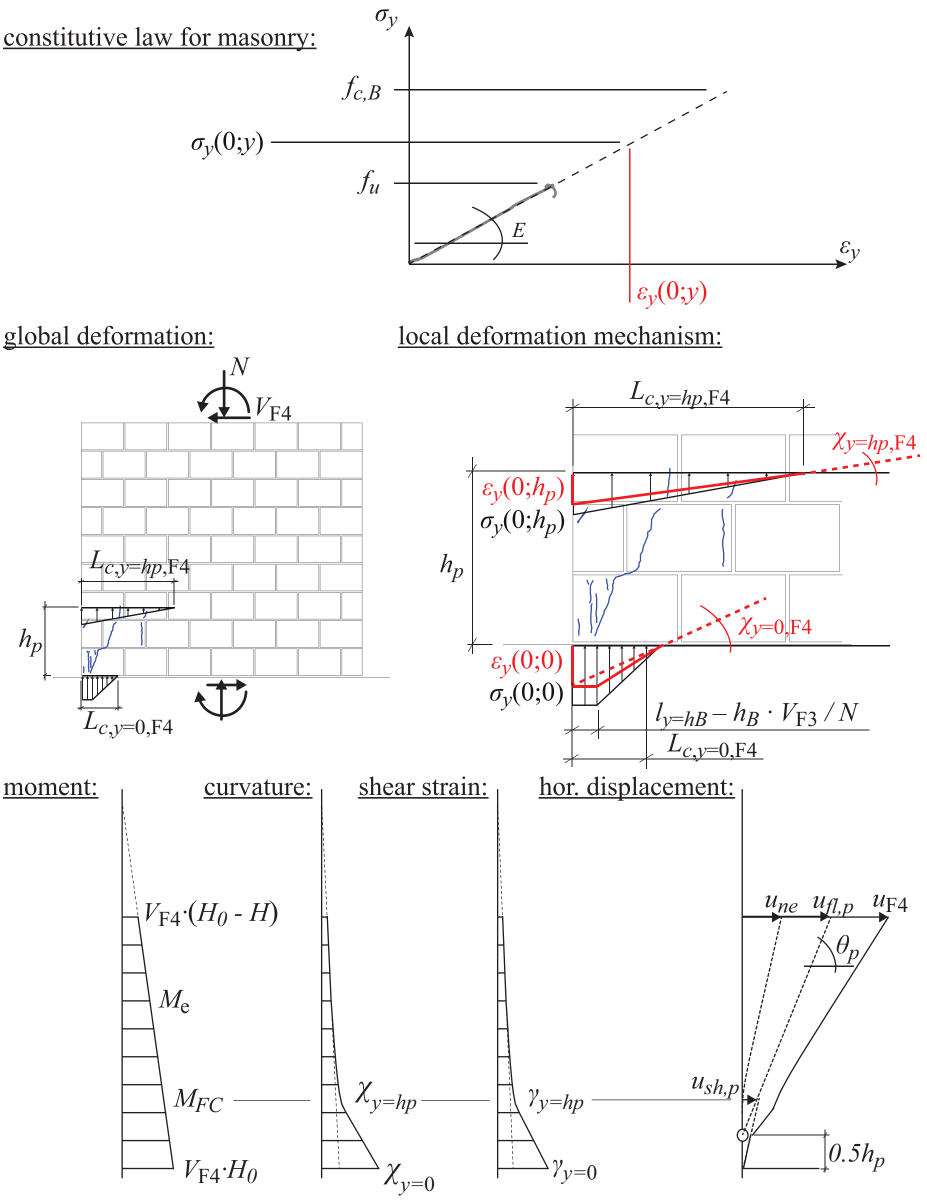

Figure 7. Displacement at LS-F4

ments taken during the testing of the walls yielded information on the walls' displacement fields. From these measurements, the shear and flexural horizontal displacement components are computed [PB14d] and compared to the predicted displacement components in Fig. 9. In Fig. 10, the vertical displacement and the top rotation are compared. The figures show that all three degrees of freedom (u, w, θ) as well as the shear and flexural components of u are well or very well predicted by the model. The largest discrepancies are observed for the vertical displacement, which the model tends to overestimate (see Fig. 10).

Brick properties			
Compression, ‖ to perforation	$f_{c,B}$	35.0	MPa
Masonry properties			
Compression strength	f_u	5.87	MPa
E-modulus	E	3550	MPa
Shear modulus	$G = 0.25 \cdot E$	890	MPa

Table 2 Brick and mortar properties

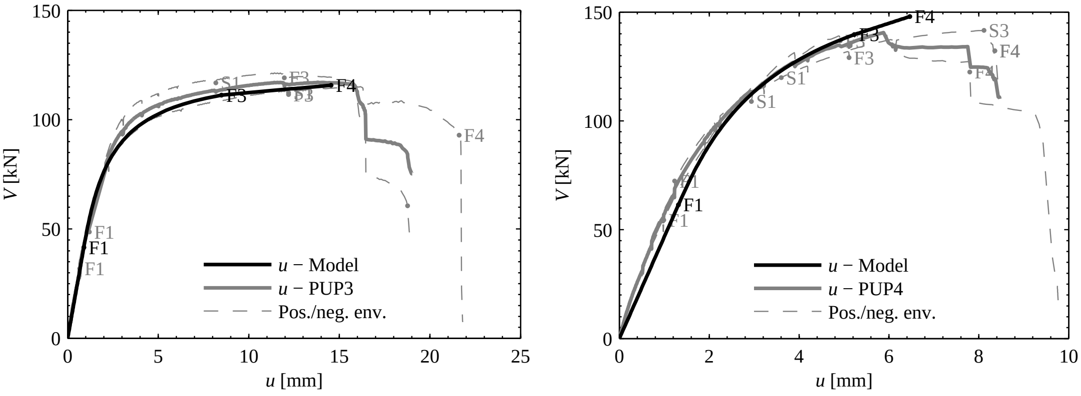

Figure 8. Lateral load versus horizontal displacement

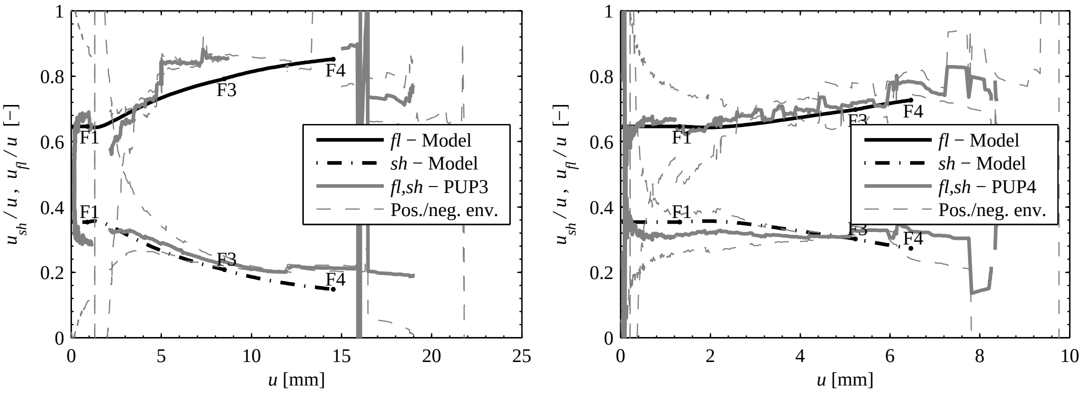

Figure 9. Contributions of the shear and flexural deformations to the total displacement

5.2 Local EDPs

The key hypotheses of the model are the assumptions (i) that plane section remained plane, (ii) that masonry in compression behaves linear elastically and (iii) that the kinematics of the wall can be represented by a Timoshenko beam with varying cross-section in the linear and nonlinear elastic phase (up to LS-F3) and by a plastic hinge model in the plastic phase (LS-F3–F4). To validate these hypotheses, local EDPs are compared to experimental results.

5.2.1 Validation of the plane section hypothesis and the assumption of the linear-elastic behavior in compression

Figure 11 compares the measured compressed portion of the base joint for the walls PUP3 and PUP4 with the compression length estimated with Eqs. (3) and (4). These equations are based

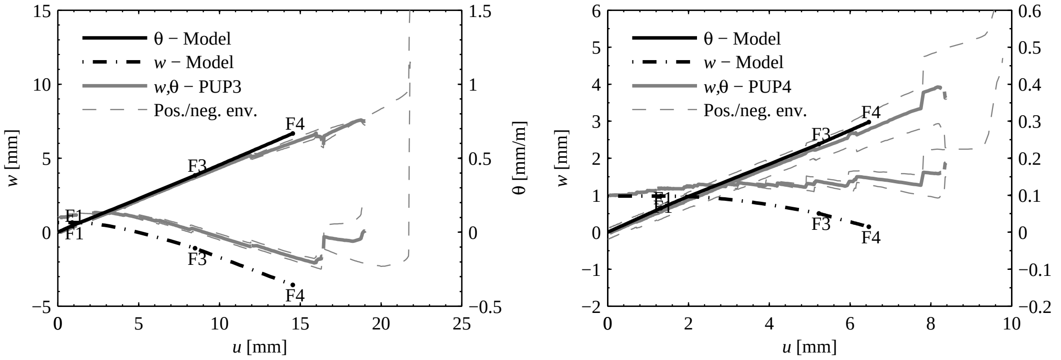

Figure 10. Vertical displacement and top rotation

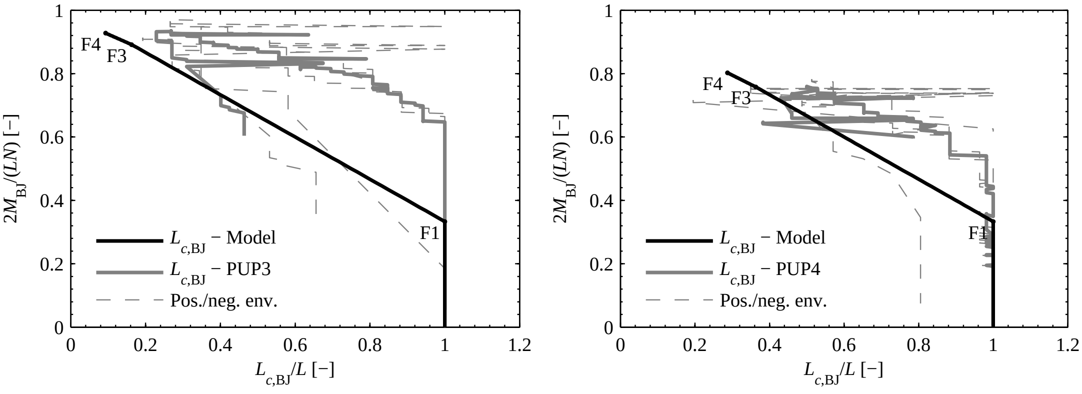

Figure 11. Compression length at the wall base versus moment ratio

on the plane section hypothesis and a linear-elastic material behavior in compression. Figure 11 shows the measured compression length at the base of the wall as a function of the applied base moment. The measured compression length is determined as the distance from the compressed edge to the location where tension strains are first observed [PB14d]. Equations (3) and (4) should therefore provide a lower bound estimate of this measured compression length, which is confirmed by Fig. 11.

Figure 13 shows the compression strains in the compressed toe; the location of the measurement devices is shown in Fig. 12. The strains are estimated at the same locations using the new proposed model and measurements are compared with theoretical results (Fig. 13). It can be seen that an excellent agreement is obtained. From comparison of compression strains and compression length, it can be concluded that the assumptions of plane sections remaining plane and a linear elastic material in compression hold satisfactorily.

5.2.2 Validation of the Timoshenko beam hypothesis

In Figs. 14 and 15, the curvature and the average shear strain profiles are estimated when reaching the predicted displacements for the limit states LS-F1, F3 and F4. The experimentally determined profiles are based on the part of the wall which is in compression [PB14d]. The figures show that experimental and theoretical results agree in average well; local deviations can, however, be significant.

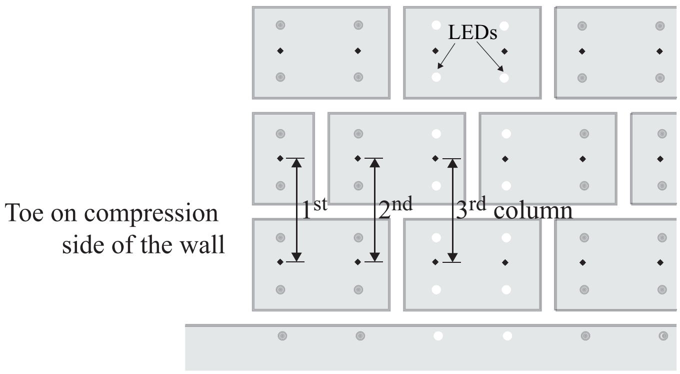

Figure 12 Schema showing the location of strain measurements at the wall toe

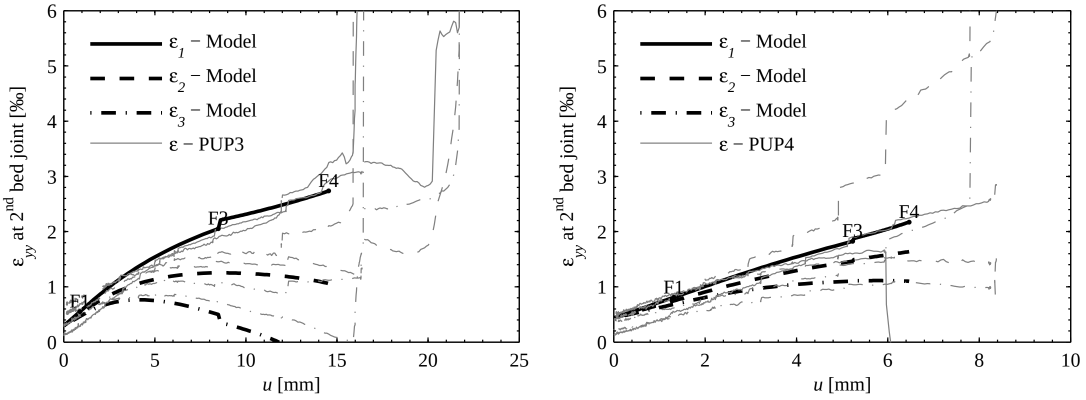

Figure 13. Vertical compression strains in toe base versus lateral top displacement

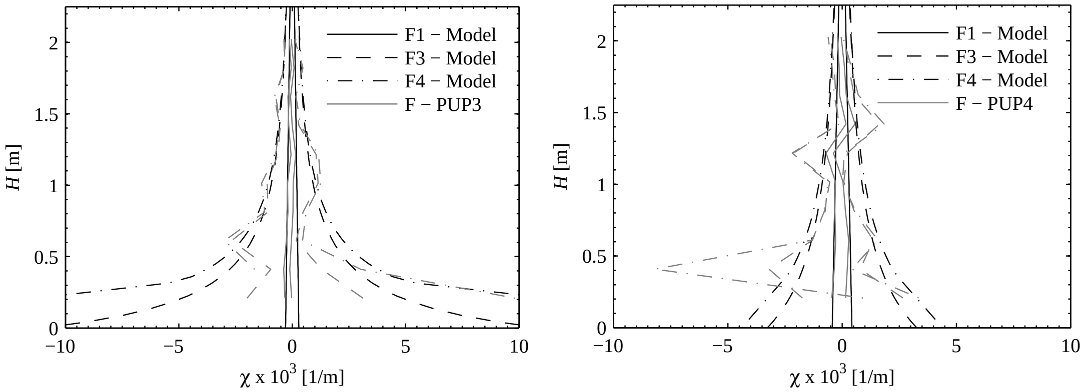

Figure 14. Curvature profiles at LS-F1, F3 and F4

5.2.3 Comparison of displacement fields

In Figs. 16 and 17, the theoretical deformed shape is estimated integrating the deformation profiles from Section 5.2.2. The unloaded part of the wall is indicated as shaded area. For larger displacements it can be seen that the predicted displacement field corresponds excellently to the experimentally obtained one. Differences are largest for the vertical displacement which was also observed in Section 5.1. A comparison of the displacement profiles indicates that the model underestimates somewhat the vertical shortening of the wall.

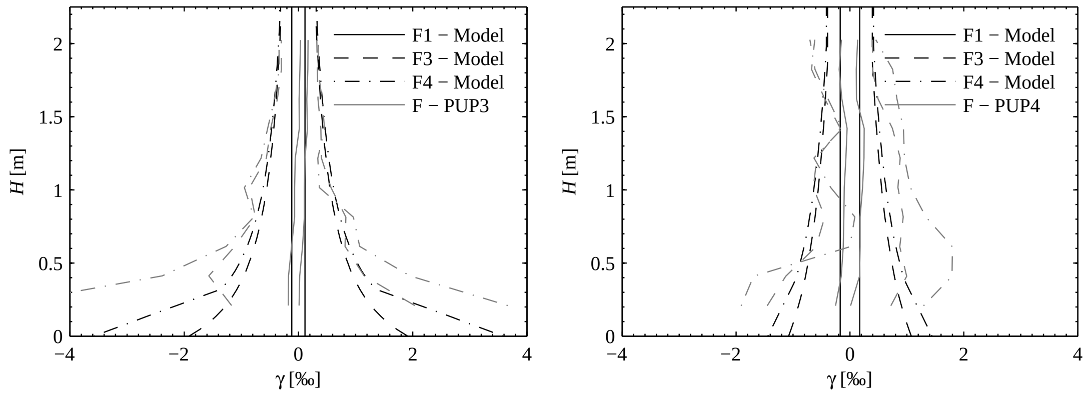

Figure 15. Average shear strains profiles at LS-F1, F3 and F4

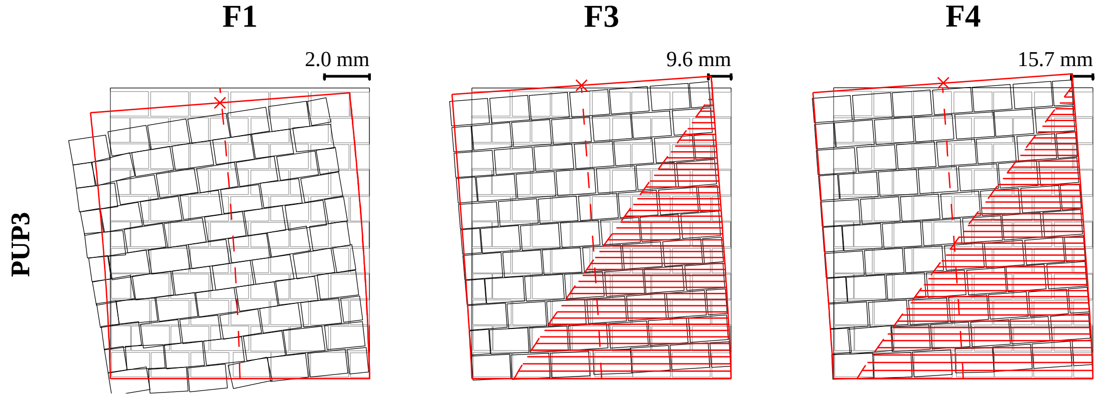

Figure 16. Amplified deformed shapes at the horizontal displacements predicted for LS-F1, F3 and F4 for the wall PUP3 (prediction in red, experimental measurement in black, original configuration in grey)

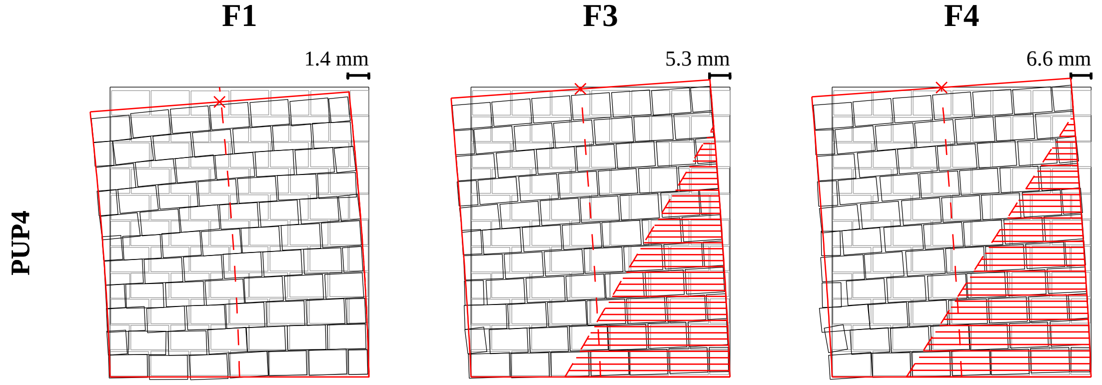

Figure 17. Amplified deformed shapes at the horizontal displacements predicted for LS-F1, F3 and F4 for the wall PUP4 (prediction in red, experimental measurement in black, original configuration in grey)

6 Experimental validation - Part II

In this section the newly proposed model is validated against a larger dataset of modern URM walls [PB14c]. Experimental and theoretical results are compared with regard to the effective elastic stiffness, the force capacity and the ultimate drift, i.e. the three parameters that define the bilinear approximation of the force-displacement response [PCK07]. Hence, the force-displacement curves for the walls from the data set are computed using the new model, which are then approximated by bilinear curves using the method described in [FM+09]. Therein the effective stiffness is defined as the secant stiffness at 70% of the peak force V_{max} and the ultimate resistance V_{ult} as the force for which the bilinear approximation yields the same energy as the original curve. The dataset in [PB14c] is based on the dataset by Frumento et al. [FM+09], to which some further wall tests were added. The dataset contains in total 64 walls which were all tested under quasi-static cyclic or monotonic lateral in-plane loading, while controlling the level of applied normal force and the shear span. Herein, only the 34 walls are used which developed a flexural (F) or hybrid (H) failure mode. For a number of tests some material properties are unknown, e.g. brick strength or elastic modulus of the masonry. For walls for which the compression strength of the brick is unknown, $f_{c,B} =$ 25 MPa was initially assumed (all concerned bricks had a void ratio of 40–55%). For tests, for which the elastic and shear modulus are not given, these values are estimated from the expected compression strength f_u. EC8-P3 [CEN05b] recommends a factor of 1000 between the characteristic compression strength f_k and the E-modulus. Assuming $f_u/f_k = 2$, the E-modulus can be estimate as $E = 500 f_u$. The shear modulus is again estimated as $G = 0.25E$ (Section 5).

6.1 Effective stiffness and strength

In Fig. 18 and Table 3, the effective stiffness and strength estimates of the new model are compared to existing models and code provisions. According to EC8-P3 [CEN05b], the effective stiffness can be taken as 50% of the uncracked stiffness EI and GA and the ultimate resistance as:

$$V_{ult,EC8} = \frac{LN}{2H_0}\left(1 - 1.15\frac{N}{LTf_u}\right) \tag{45}$$

The model by Penna et al. [PLG14] yields the entire force-displacement response and the effective stiffness is again determined as the secant stiffness at 70% of V_{max}. Figure 18 shows the cumulative distribution of the logarithmic ratio of predicted to experimental value. A ratio of zero corresponds therefore to a perfect match while ratios smaller (larger) than zero represent samples for which the model underestimates (overestimates) the experimentally obtained value. The figure shows that Eq. (41) tends to underestimate in average slightly the ultimate resistance and that the proposed model yields a better match. However, the differences are small and negligible. The stiffness according to EC8-P3 tends to underestimate the effective stiffness as does the model by Penna et al. [PLG14]. The latter results from the assumed simplified curvature profile, which is constant over the bottom and top half of the wall. The proposed model on the contrary yields in average a rather accurate prediction of the effective stiffness; the standard variation is, however, similar to the other two models.

6.2 Displacement capacity at horizontal failure

Figure 19 shows the comparison of the predicted displacement capacity at the ultimate stage LS-F4 to the displacement capacity obtained from the tests. The experimentally determined displacement capacity is defined as the displacement capacity for which the force dropped by 20%, e.g. [FM+09]. It is assumed that the limit state LS-F4 corresponds to such a drop in force.

Table 3. Comparison of experimental and predicted global EDPs for the walls

Test	f_u	$f_{c,B}$	E	V_{ult}			k_{eff}				u_{ult}					
Unit				EXP	Model **)	EC8-P3	EXP	Model **)	EC8-P3	PLG14	EXP	Model**)	EC8-P3	PB14	PCK07	BS08
	[MPa]	[MPa]	MPa]	[kN]	[kN]	[kN]	[MN/m]	[MN/m]	[MN/m]	[MN/m]	[mm]	[mm]	[mm]	[mm]	[mm]	[mm]
10-1	4.00	*)	3442	54	55	49	61	37	25	28	25.8	11.3	25.0	17.5	11.5	3.0
10-2	4.10	*)	3442	93	105	79	44	39	25	29	10.0	11.3	24.9	9.5	4.5	3.5
10-4	4.10	*)	3442	104	103	78	53	39	25	29	12.9	11.4	25.2	9.5	4.5	3.5
10-6	4.00	*)	3442	63	55	49	40	37	25	28	35.0	11.3	25.0	17.5	11.5	3.0
14-1	4.21	*)	2528	264	278	251	215	122	79	114	24.0	11.2	14.0	20.3	14.6	-
14-2	4.10	*)	2462	453	437	403	276	142	77	113	10.0	4.6	14.1	10.6	5.2	-
14-3	4.05	*)	2427	364	380	341	167	130	77	111	13.5	6.3	14.0	15.2	8.0	-
14-7	9.41	*)	5645	400	531	489	153	181	105	153	6.0	5.5	14.3	15.4	8.3	2.4
CL06	10.00	*)	5905	81	84	85	40	71	47	89	50.7	8.3	28.8	14.5	69.9	6.8
W2	8.25	37.4	4125	469	770	743	176	171	91	148	8.0	6.1	12.3	10.8	6.0	3.2
W4	8.25	37.4	4125	182	168	160	124	92	69	58	22.2	15.2	25.0	47.6	26.6	-
MI3	7.92	19.7	2991	-	121	114	-	21	13	26	14.8	16.2	32.0	11.4	21.7	10.7
ISP3	6.20	26.9	3100	-	121	108	-	35	22	44	10.5	13.6	21.3	8.8	12.6	5.7
PUP3	5.86	35.0	3550	112	109	99	47	35	23	21	16.2	12.7	40.3	27.5	13.7	-
PUP4	5.86	35.0	3550	135	137	129	54	41	23	22	7.9	6.2	40.3	19.1	7.9	-
10-7	4.25	*)	3592	97	97	74	58	37	24	28	10.0	11.2	26.1	10.0	4.8	3.6
10-8	4.25	*)	3592	97	96	74	64	37	24	28	12.5	11.2	26.1	10.0	4.8	3.6
10-9	4.25	*)	3592	71	97	74	14	37	24	28	14.6	11.1	25.9	10.0	4.8	3.6
10-10	6.26	*)	5233	100	96	85	37	54	34	39	10.0	7.7	26.0	15.2	8.5	3.4
10-11	6.26	*)	5233	102	96	85	33	53	34	39	11.8	7.7	26.0	15.2	8.5	3.4
10-12	6.26	*)	5233	104	97	85	32	54	34	39	9.9	7.7	26.0	15.2	8.4	3.3
14-6	3.86	*)	2334	327	286	245	386	100	61	87	11.5	8.4	12.9	14.6	7.3	-
15-8	5.24	*)	3665	89	93	83	23	65	42	50	34.0	7.2	16.1	14.9	7.6	2.1
15-9	5.18	*)	3627	133	117	98	86	65	41	50	23.2	7.3	16.1	12.3	5.3	2.2
15-10	5.41	*)	3785	135	147	116	51	69	43	54	16.0	7.1	16.1	9.7	3.9	2.4
MR-A1	9.40	20.2	4700	-	88	87	-	76	50	52	6.1	4.4	14.4	24.0	13.8	-
MR-B1	9.40	41.0	4700	-	61	60	-	76	53	58	10.1	9.2	15.8	28.7	35.2	-
10-13	6.26	*)	5200	93	97	85	45	53	34	39	6.0	7.7	26.0	15.2	8.5	3.4
10-14	6.26	*)	5200	98	97	85	31	53	34	39	9.2	7.8	26.1	15.2	8.5	3.4
10-15	6.26	*)	5200	98	97	85	32	53	34	39	8.7	7.7	26.0	15.2	8.5	3.4
14-5	2.41	*)	1445	231	209	187	175	72	43	62	30.1	6.5	14.5	15.2	8.0	-
15-5	5.53	*)	3871	112	98	87	45	69	44	53	16.6	6.8	16.1	14.9	7.6	2.1
15-6	5.64	*)	3945	122	126	107	67	71	45	55	18.4	6.8	16.1	12.3	5.3	2.2
15-7	5.74	*)	4019	147	155	123	54	73	46	57	18.5	6.7	16.1	9.7	3.9	2.4

*) Compression strength of brick is estimated as 15, 25 and 35 MPa.

**) The values reported in the table are obtained for a brick strength of 25 MPa, where the brick strength was unknown.

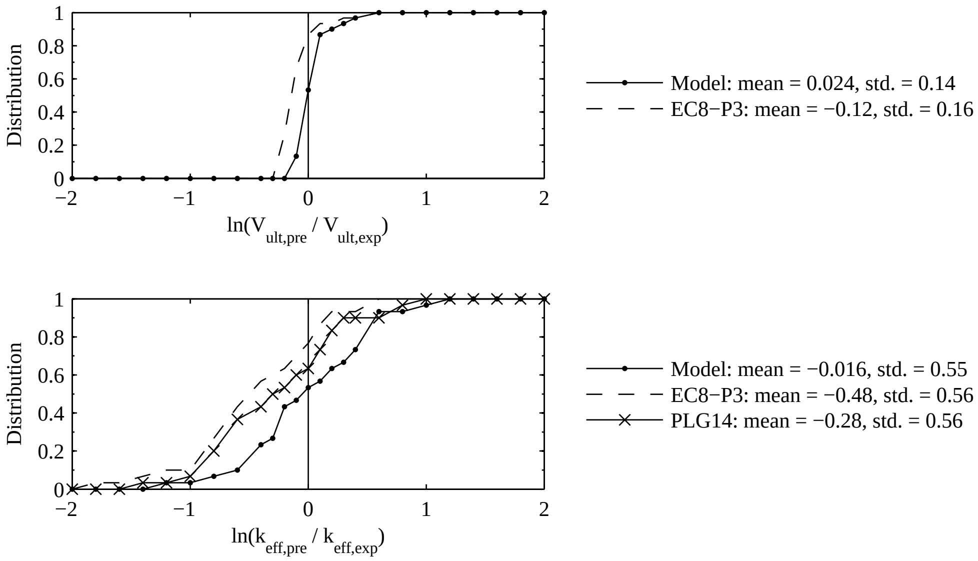

Figure 18. Distribution of the logarithmic ratio between predicted and experimental value of the ultimate lateral resistance V_{ult} and the effective stiffness k_{eff} according to the new proposed "Model", to EC8-P3 [CEN05b] and Penna et al. [PLG14]

The values of the individual test units are summarized in Table 3.

For only eight of the tests the brick strength was known while for the others the brick strength was not known. Figure 19 shows the ratio of predicted to observed displacement capacity for the group of tests for which the brick strength was known; for the group of tests for which it was unknown the prediction was tested for three different values of brick strength ($f_{c,B}$ =15 MPa, 25 MPa, 35 MPa). The figure shows that the displacement capacity is predicted very well for walls for which the brick strength is known. For walls for which the brick strength is not known, the deviation is significantly larger.

In Fig. 20, the displacement capacity at the ultimate stage LS-F4 obtained from the new model is compared to four other drift capacity models: (i) to the displacement capacity given in EC8-P3 [CEN05b] of $0.008 \times 4/3 \times H_0/L$ for flexural walls, (ii) to the formula proposed in [PB14c], (iii) to the interstory drift limit proposed in [PCK07] and (iv) to the ultimate displacement as defined in [BS08]. For tests for which the brick strength is not known, the values obtained for the model are based on $f_{c,B}$ =25 MPa. The comparison shows that the new model yields a slightly smaller standard deviation than existing empirical and mechanical models and that in average it tends to underestimate the displacement capacity. The latter results mainly from small test units, for which the displacement capacity is governed by the stress criterion at the base joint. It indicates that the confining effect of the foundation and its influence on the displacement capacity deserves a more in depth analysis. At present, however, there were no detailed test data on such small walls available.

The two existing mechanical models [PCK07, BS08] yield similar standard deviations as the new model but the model by Benedetti and Steli [BS08] underestimates in average the displacement capacity significantly. It is based on limiting the stresses at the external fiber at the wall base to the compression strength of the masonry and neglects therefore any confining effect of the foundation [PB14b]. The model by Priestley et al. [PCK07] also determines the

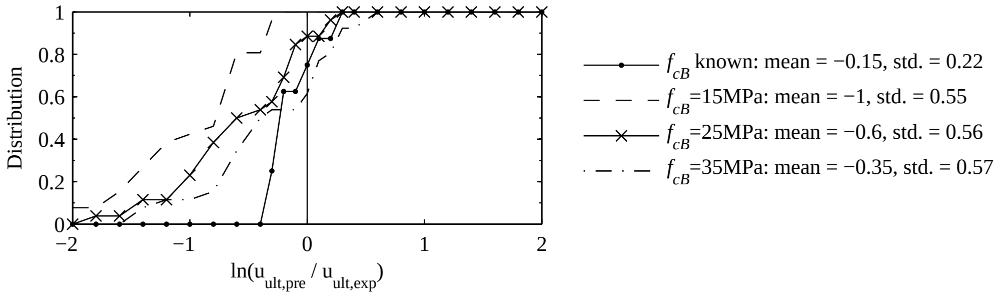

Figure 19. Distribution of the logarithmic ratio between prediction and experimental value of the ultimate displacement u_u according to the new proposed "Model", for the walls for which the $f_{c,B}$ was known and for the walls where $f_{c,B}$ was unknown and estimated at $f_{c,B}$ =15, 25 and 35 MPa

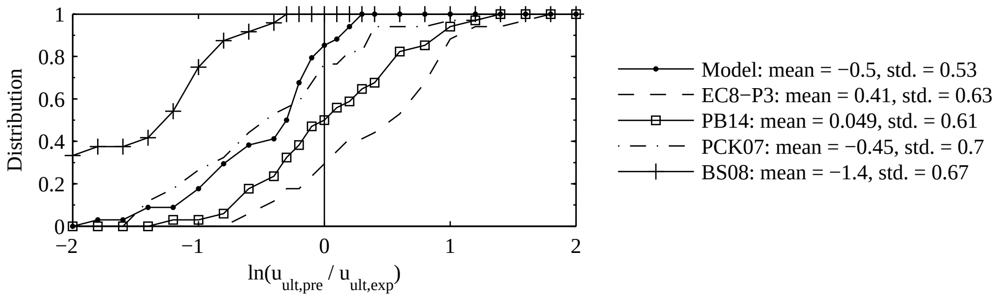

Figure 20. Distribution of the logarithmic ratio between prediction and experimental value of the ultimate displacement u_u according to the new proposed "Model", to EC8-P3 [CEN05b], to Petry and Beyer [PB14c], to Priestley et al. [PCK07] and to Benedetti and Steli [BS08]

displacement capacity by considering the masonry strength at the base. However, neglecting the influence of the confining effect of the foundation as well as of the shear deformations seems compensated by the assumed curvature profile, i.e. a linear profile over a height $(L - L_c)$, which could not be confirmed by experimental results (Fig. 14).

7 Determinant parameters for the ultimate drift capacity

The comparison with experimental results showed that the proposed model yields good estimates of the ultimate displacement capacity when the material parameters are known, i.e. the E-modulus of the masonry, the compression strength of masonry and bricks. All these material properties can be easily determined from standard material tests and in Fig. 21 the new proposed model is used in order to determine the influence of key parameters on the ultimate displacement capacity of URM walls. The investigated parameters are the axial stress ratio ($\beta = \sigma_0 / f_u$), the ratio of height of zero moment to wall height ($\alpha = H_0 / H$), the shear span of the wall (H_0 / L) and the size of the wall (H). The determining failure criterion, i.e. whether failure is attained at the base ($y = 0$) or at the second joint ($y = h_B$), is indicated by the color of the marker. The parametric study considers only wall configurations which would-according to EC8-P3 [CEN05b]—fail in flexure.

Figure 21a shows that for large walls ($H > 2$ m) subjected to relatively large axial stresses

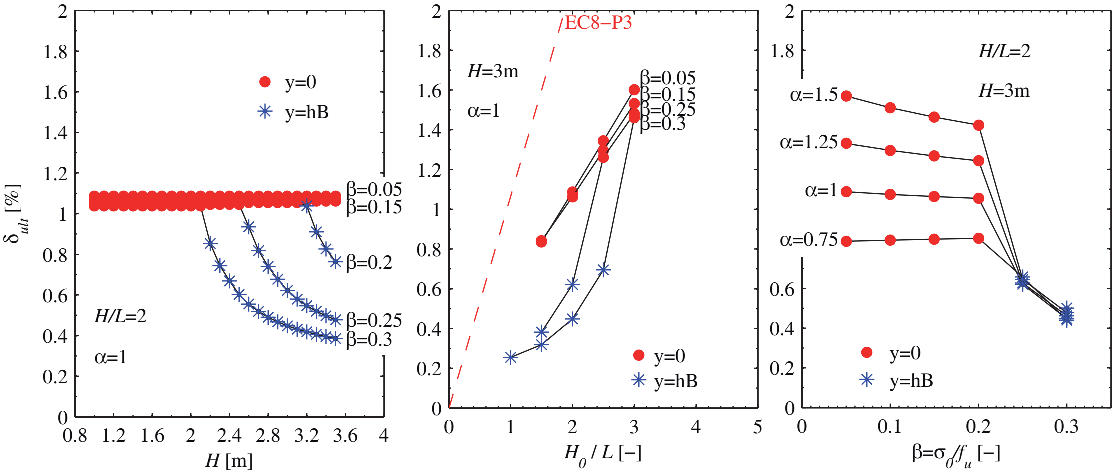

Figure 21. Predicted ultimate displacement capacity for flexural dominated walls in dependency of different parameters ($\alpha = H_0/H$, $\beta = \sigma_0/f_u$)

the failure will occur in the second joint before it can occur in the base joint. This confirms the influence of the wall size observed in [PB14c] and reveals also the importance of considering the failure criteria at both the base and the second joint. Figure 21b shows that the drift capacity increases with increasing aspect ratio. If the failure is governed by the base joint, there is a linear relationship between drift capacity and aspect ratio-as it is predicted by EC8-P3 [CEN05b]. The size of the wall with respect to the size of the brick (here $l_B = 0.3$ m, $h_B = 0.2$ m, $f_u = 6$ MPa, $f_{c,B} = 25$ MPa) affects the local failure mechanism and influences therefore the trends. Figure 21c shows that for small axial stress ratios ($\sigma_0/f_u \leq 0.2$) the influence of the axial stress ratio on the displacement capacity is negligible. However, for higher axial stress ratios failure will occur in the second joint before it can occur in the base joint, resulting thus in smaller drift capacities for higher axial stresses.

8 Conclusions and outlook

This article presents a new mechanical model for describing the force-displacement response up to the limit state ”Near Collapse” of in-plane loaded URM walls developing a flexural mode. The model is developed in two steps. First, an analytical formulation for the force-displacement response is derived and second, local limit states (LSs) that characterize the flexural failure are implemented. The new model allows therefore linking local LSs to global displacement capacities of modern URM walls with cement mortar and clay bricks.

The analytical formulation is based on the same hypotheses as existing models for rocking URM walls [BS08, BB13, PLG14], i.e. plane section hypothesis and a material with zero tensile strength and a linear-elastic behavior in compression. As a result, only the compressed part of the wall contributes to the resistance of the wall and the model accounts for a softening of the response due the reduction of the effective area after onset of decompression. Unlike existing models, the new formulation accounts for the variation in effective area along the height of the wall. Further, it is assumed that not only the flexural stiffness but also the shear stiffness depends on the effective area and not the gross area. Validation against results from 34 wall tests showed that this leads to an improved prediction of the effective stiffness. For two wall tests also detailed information on the displacement field was available allowing therefore a more detailed validation. Comparison of experimental to predicted values showed that the model is able to predict not only the global response but also the contributions of shear and flexural deformations to the total displacement as well as compressive strains and shear strains.

In a second step, criteria for local LSs were developed and implemented. These new criteria address the limit states that are characterized by the splitting and crushing of the bricks in the compressed toe of the masonry wall and account also for the confining effect of the foundation. Apart from the wall geometry and boundary conditions (axial load, shear span), the model requires as input material parameters that can be obtained from standard material tests, e.g., the stiffness and strength of the masonry as well as the brick strength. If these material properties are known the model yields a better prediction of the displacement capacity than any of the existing empirical or mechanical models. The model confirms that the drift capacity of walls failing in a flexural mode depends on the axial stress ratio and the ratio of shear span to height, which are key parameters in empirical models. The model further shows that there is indeed a size effect on the drift capacity of the wall, i.e. the drift capacity of walls constructed with the same brick size is dependent on the size of the wall. This results from (i) the confining effect of the foundation, (ii) the resulting observation that splitting of bricks initiates at the second joint half a brick inwards from the extreme fiber and (iii) that plastic deformations spread over at least over the height of one brick.

Research on mechanical drift capacity models for URM walls is still at the beginning and before such models can be implemented in codes many topics require further research. First and foremost, a drift capacity model for URM walls failing in shear is required but also other topics such as the effect of different construction materials, wall sections, cumulative damage demands and strain rates need to be investigated and their effect on the force-displacement response and the displacement capacity incorporated in the mechanical drift capacity models.

9 Acknowledgements

The authors would like to thank Prof. Andrea Penna, University of Pavia, Italy, for his helpful comments; our colleagues Shenghan Zhang—who modeled the walls from the PUP series in Vector2—and Francesco Vanin—who applied our model to other walls—for helping us to confirm our results; and Dr. Suikai Lu, consulting engineer, Vienna, who gave us indications on the possible range of compression strengths for clay masonry bricks.

References

[BB13] Benedetti, A and Benedetti, L. Interaction of shear and flexural collapse modes in the assessment of in-plane capacity of masonry walls. In *Proceedings of the 12th Canadian Masonry Symposium*, Vancouver, Canada, 2013.

[BP+14] Beyer, K, Petry, S, Tondelli, M and Paparo, A. *Towards displacement-based design of modern unreinforced masonry structures*. Istanbul, Turkey, 2014.

[BS08] Benedetti, A and Steli, E. Analytical models for shear-displacement curves of unreinforced and frp reinforced masonry panels. *Construction and Buildings Materials*, 22:175–185, 2008.

[CEN05a] CEN. Eurocode 6: Design of masonry structures - part 1-1: General rules for reinforced and unreinforced masonry structures. Technical Report EN 1996-1-1, European Committee for Standardisation, Brussels, Belgium, 2005.

[CEN05b] CEN. Eurocode 8: Design of structures for earthquake resistance, Part 3: Assessmemt and retrofitting of buildings. Technical Report EN 1998-3, European Committee for Standardisation, Brussels, Belgium, June 2005.

[FM+09] Frumento, S, Magenes, G, Morandi, P and Calvi, GM. *Interpretation of experimental shear tests on clay brick masonry walls and evaluation of q-factors for seismic design.* Technical Report, IUSS PRESS, Pavia, Italy, 2009.

[Gan85] Ganz, HR. *Mauerwerksscheiben unter Normalkraft und Schub.* Phd thesis, ETH Zürich, Institute of Structural Engineering, Zürich, Switzerland, 1985.

[GL97] Gambarotta, L and Lagomarsino, S. Damage models for the seismic response of brick masonry shear walls. Part I: The mortar joint model and its applications. *Earthquake Engineering and Structural Dynamics*, 26:423–439, 1997.

[Hey92] Heyman, J. Leaning towers. *Meccanica*, 27:153–159, 1992.

[Lan02] Lang, K. *Seismic vulnerability of existing structures.* Phd thesis, ETH Zürich, Institute of Structural Engineering, Zürich, Switzerland, February 2002.

[LP+13] Lagomarsino, S, Penna, A, Galasco, A and Cattari, S. Tremuri program: an equivalent frame model for the nonlinear seismic analysis of masonry buildings. *Engineering Structures*, 56:1787–1799, 2013.

[Mag06] Magenes, G. Masonry building design in seismic areas: recent experiences and prospects from a European standpoint. In *Keynote at the First European conference on earthquake engineering and seismology*, Geneva, Switzerland, 2006.

[Man14] Mandirola, M. *Non-linear macroelement modelling of experimental tests on masonry building specimens with rigid diaphragms.* Dissertation, University of Pavia, Pavia, Italy, 2014.

[MC97] Magenes, G and Calvi, GM. In-plane seismic response of brick masonry walls. *Earthquake Engineering and Structural Dynamics*, 26:1091–112, 1997.

[MM82] Mann, W and Müller, H. Failure of shear-stressed masonry—an enlarged theory, tests and application to shear walls. In *Proceedings British Ceramic Society*, volume 30, pages 223–235, 1982.

[PB14a] Petry, S and Beyer, K. Cyclic test data of six unreinforced masonry walls with different boundary conditions. *Earthquake Spectra*, 2014.

[PB14b] Petry, S and Beyer, k. Flexural deformations of URM piers: Comparison of analytical models with experiments. In *Proceedings of the 9th International Masonry Conference*, Guimarães, Portugal, 2014.

[PB14c] Petry, S and Beyer, K. Influence of boundary conditions and size effect on the drift capacity of URM walls. *Engineering Structures*, 65:76–88, 2014.

[PB14d] Petry, S and Beyer, K. Limit states of modern unreinforced clay brick masonry walls subjected to in-plane loading. *Bulletin of Earthquake Engineering February*, 2014.

[PCK07] Priestley, MJN, Calvi, GM and Kowalsky, MJ. *Displacement-Based Seismic Design of Structures.* Pavia, Italy, 2007.

[PLBL11] Pfyl-Lang, K, Braune, F and Lestuzzi, P. Evaluation de la sécurité parasismique des bâtiments en maçonnerie. Technical Report SIA D0237, Documentation, Swiss Society of Engineers and Architects SIA, Zürich, Switzerland, 2011.

[PLG14] Penna, A, Lagomarsino, S and Galasco, A. A nonlinear macroelement model for the seismic analysis of masonry buildings. *Earthquake Engineering and Structural Dynamics*, 43:159–179, 2014.

[TC71] Turnšek, V and Cašovič, F. Some experimental results on the strength of brick masonry walls. In *Second International Brick Masonry Conference*, pages 149–156, 1971.

[Tom09] Tomaževič, M. Shear resistance of masonry walls and eurocode 6: shear versus tensile strength of masonry. *Materials and Structures*, 42:889–907, 2009.

[TS81] Turnšek, V and Sheppard, P. The shear and flexural resistance of masonry walls. In *Proceedings of the International Research Conference on Earthquake Engineering*, pages 517–573, Skopje, 1981.

Chapter V

First ideas for a mechanical model capturing the formation of a diagonal shear crack

1 Introduction

In the previous paper a mechanical model is presented which describes the nonlinear response of flexural dominated URM walls up to Near Collapse [CEN05]. It is shown that even though the flexural rocking is governed by compression failure of masonry—which is known to be quite brittle—walls developing a flexural mode can develop significant ductility (see Fig. 1a). This is due to the fact that the tension strength of masonry is negligible and after onset of decompression in the base, the effective area which contributes to the total resistance of the wall reduces. Consecutively, the flexibility of the wall increases (see Fig. 2 of Paper IV). This phenomenon is well captured with the new model proposed in the previous paper.

In case of diagonal shear failure, the deformation mechanism is governed by the formation of diagonal shear cracks, which can be either associated to sliding between bricks and mortar [MM82, MC97] or the exceedance of the diagonal tensile strength [TC71, TS81]. Although on the material level the mechanisms associated to shear failure show a more ductile behavior than for compression failure (see Figs. 1a and 1b right), walls developing a shear mechanism are known to develop less ductility than flexural dominated walls (see Figs. 1a and 1b left) [MC97]. These ductile mechanisms are only triggered once the initial shear strength is exceeded locally.

In the following it is shown how these local mechanisms are triggered and how they influence the kinematics of shear dominated URM walls. Section 2 commences with a review of the local limit states (LSs) presented in Paper III. It is shown, how they influence the kinematics of the walls and how they could be predicted. In Section 3, a first model is proposed which attempts to capture the kinematics of the wall. The model is statically over determined and two possible assumptions to overcome that problem are discussed. In Section 4, a possible kinematic model is presented which could overcome the problems faced during the elaboration of the mechanical model, before this chapter is concluded in Section 5.

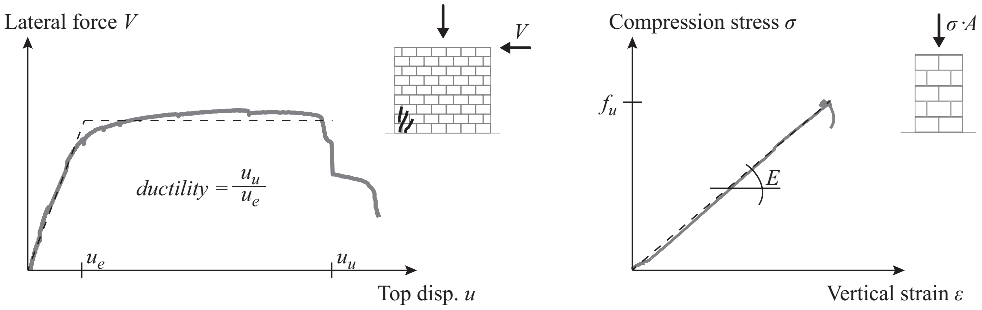

a) Global flexural rocking, dominated by the local compression behaviour of the masonry

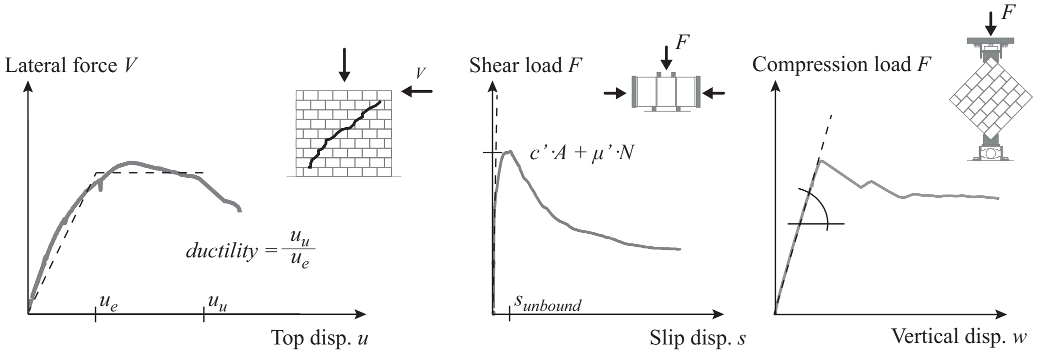

b) Global diagonal shear cracking, dominated by the local shear behaviour of the masonry

Figure 1. Comparison of the force-displacement behavior typically observed for a (a) flexural rocking and (b) diagonal shear behavior on (left) the global force-displacement response of shear walls and on (right) the local material behavior

2 Local limit states for shear dominated walls and their influence on the force-displacement response

In Paper III, a new set of local LSs is proposed which is typically observed for walls subjected to shear or flexural solicitations. For the reader's convenience the LSs associated to shear are again summarized in Table 1. Similar to flexural dominated walls (see Paper IV), it can be noted that three LSs are decisive for the global force-displacement response of URM walls until the point of significant drop of lateral resistance (normally referred as Near Collapse [CEN05]). These are: LS-S1 which initiates the separation of the wall into two triangles and causes thus the onset of a continuous softening; LS-S3 which is the local attendance of the peak shear strength in the center of the central diagonal crack and initiates thus a change of mechanism and the redistribution of internal forces and LS-S4 which is associated to the local shear failure of the corner regions and provokes thus a significant loss of lateral resistance. Last point is assumed to be equal to the point of "Near Collapse" as defined in EC8-P3 [CEN05].

2.1 Appearance of first diagonal shear cracks (LS-S1)

In Fig. 2, the force-displacement response of the walls PUP1, PUP2 and PUP5 is predicted using the flexural model from Paper IV. All three walls developed significant diagonal shear cracks. It can be noted that the global force-displacement curve obtained with the flexural model

Table 1. Local LSs for in-plane loaded URM walls with a dominating shear mode (Paper III)

Limit state	Local crack pattern	Influence on global response
LS-S1	First appearance of diagonal stair step cracks in mortar joints [MM82]	Preceded by a first reduction of stiffness
LS-S2	First appearance of vertical and inclined cracks through bricks along the diagonals	Negligible influence on force-displacement relationship
LS-S3	Deformations start concentrating in one diagonal crack	Peak load is typically attained shortly afterwards
LS-S4	Shearing off of the corners of the bricks	Significant loss of the lateral resistance
LS-S5	Crushing of bricks along the diagonal crack	Axial load failure

starts diverging already at an early stage from experiments. The displacement components are shown in Fig. 3 and it can be noted that also this prediction is not satisfying: PUP1 developed significantly more displacement due to shear than due to flexure and the flexural model captures the proportion in a satisfying manner until occurrence of LS-F1. For the walls where the differences between shear and flexural component was smaller (PUP2 and PUP5), the model yields a wrong distribution.

From experimental observation, it was noted that the appearance of first diagonal shear cracks (LS-S1) is always preceded by a softening of the global force-displacement curve (see Table 1). The first formation of the diagonal cracks initiates the separation of the URM walls into two triangles, which behave softer than an equivalent rectangular wall and this phenomenon is not captured with the flexural model proposed in Paper IV.

First diagonal stair step crack along the joints appear, when the vertical stress redistribute such that onset of decompression is obtained at one side of the bed joint [MM82]. Mann and Müller [MM82] explain this phenomenon as follows: the stresses which are transmitted through the head joint are negligible; thus, the shear stresses impose a local torque to the bricks which is balanced by a pair of vertical stresses (see Fig. 12 from Paper III). This reduces the vertical stresses at one side of the bricks and causes the appearance of diagonal stair step cracks. The vertical compression stresses σ_y after local redistribution can be estimated as follows [MM82]:

$$\sigma_y = \sigma_y^* \pm \tau_{xy} \cdot \frac{2h_B}{l_B} \tag{1}$$

where σ_y and σ_y^* are the local vertical stresses perpendicular to the bed joints after and before redistribution respectively and τ_{xy} are the local shear stresses parallel to bed joints. l_B and h_B are the height and length of the brick plus the mortar thickness respectively. Hence, LS-S1 occurs when following local condition applies:

$$\tau_{xy} = \sigma_y^* \cdot \frac{l_B}{2h_B} \tag{2}$$

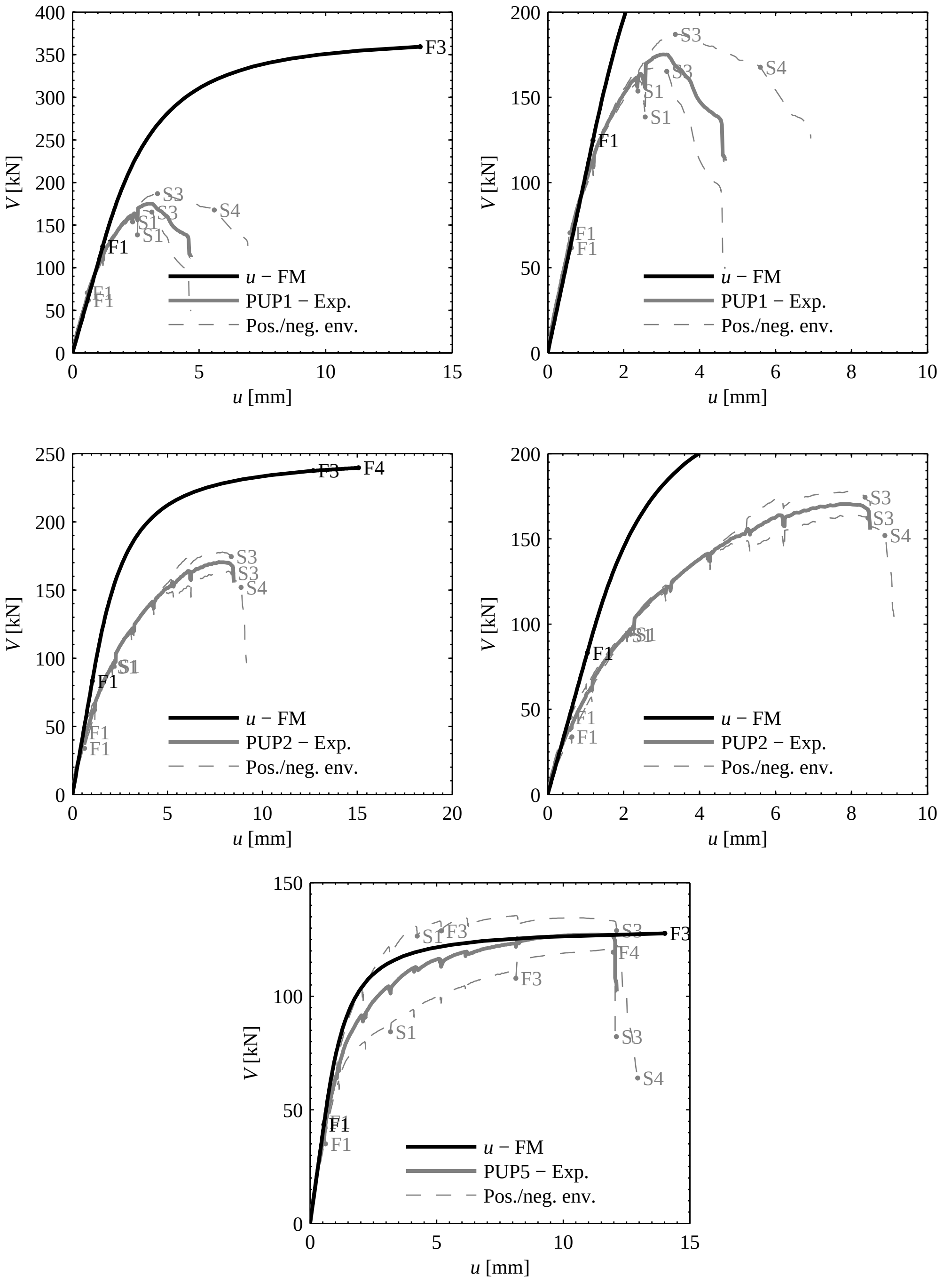

Figure 2. Prediction of the force-displacement response of URM walls developing a significant shear failure (FM refers to the flexural model from Paper IV; note that the scale of figures changes from left to right figure, where the model predicted significantly more force and displacement capacity)

From testing it was noted that the diagonal cracks appear always first in the center of the wall, where the lateral restraint is the smallest. Masonry is an inhomogeneous material

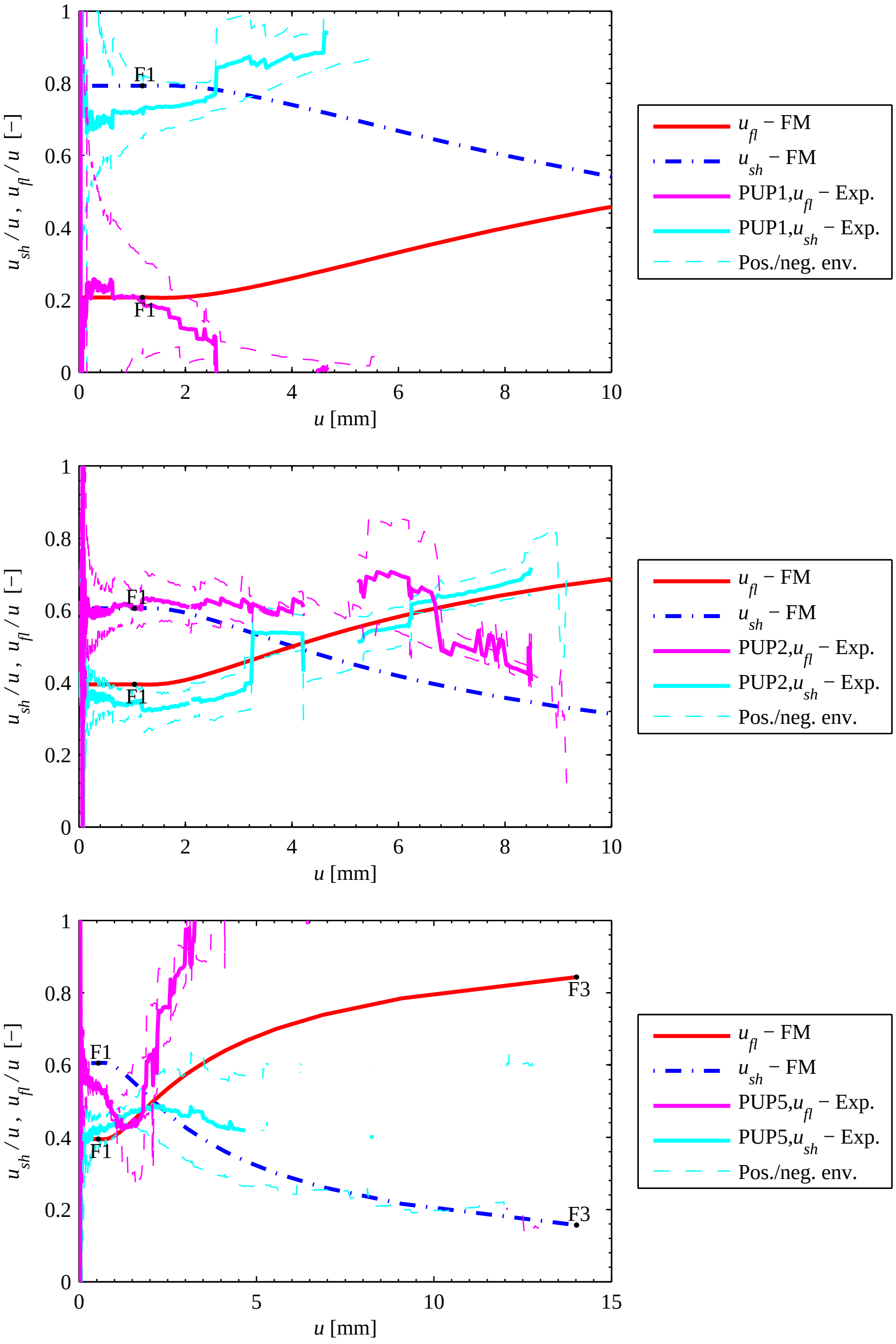

Figure 3. Ratio of displacement components caused by shear ($u_s h$) and flexural ($u_s h$) solicitations (FM refers to the flexural model from Paper IV)

which behaves differently with respect to the directions parallel or perpendicular to the bed joints [Gan85]. In Fig. 4b, the shear strains are shown at LS-S1 for a wall (PUP1) which developed a typical diagonal shear failure. It can be noted that the shear strains concentrate along the diagonal strut. This is related to the effect of local stress redistribution [MM82]: since no stresses are transferred through the vertical head joints, shear stresses are only

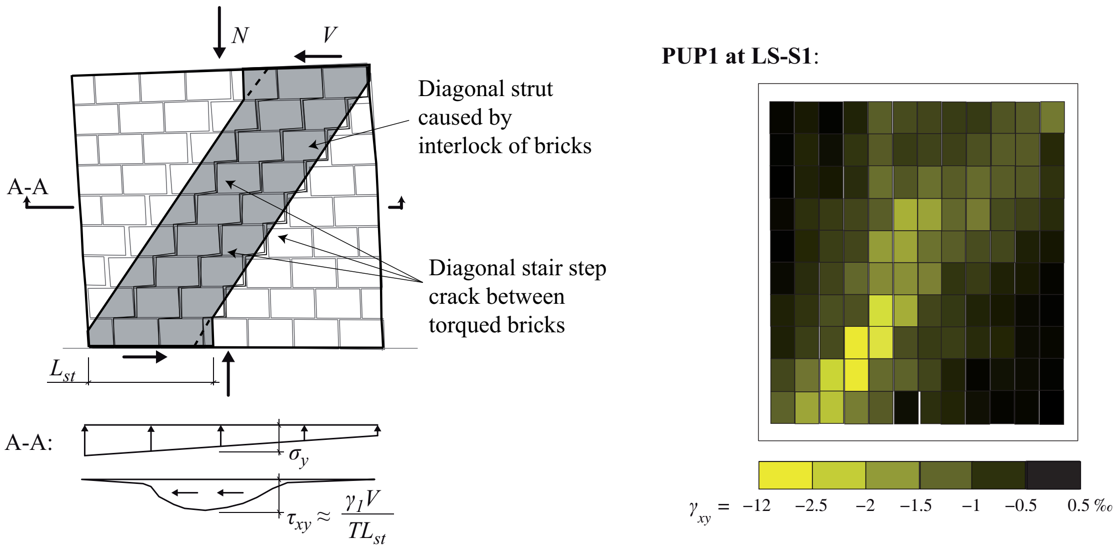

Figure 4. (a) Assumption for the diagonal shear stress strut for squat walls subjected to significant shear solicitations and (b) shear strain measurement (γ_{xy}) of a wall developing a significant shear mode at approximately LS-S1

transferred in the bed joint where local redistribution of normal stresses can take place, hence along the interlock region highlighted in Fig. 4a. While in continuum models this non-isotropic behavior of masonry is considered by means of orthotropic material laws, e.g. [FPV14], the concentration of shear stresses along the diagonal strut must be accounted for when translating Eq. (2) in a global criterion. It is suggested to do so using following estimation for the shear stresses at the center:

$$\tau_{xy} \approx \frac{V}{TL_{st}} \tag{3}$$

where L_{st} is the depth of the diagonal strut at the height of the second mortar joint. It depends on the number of bricks which can interlock between each other (see Fig. 4a) and is determined from the number of brick rows H/h_B and number of bricks in a row L/l_B:

$$L_{st} = l_B \cdot \left(\frac{L}{l_B} - \frac{H}{2h_B} + 1.0\right) \tag{4}$$

Thus, simplifying the vertical stresses at mid height of the wall to

$$\sigma_y \approx \frac{N}{TL_{c,\frac{H}{2}}} \tag{5}$$

Eq. (2) can be transformed into a global criterion such that the shear force V_{S1} at which the first diagonal crack in the center of the wall appears is estimated as:

$$V_{S1} \approx N \cdot \frac{L_{st}}{L_{c,\frac{H}{2}}} \cdot \frac{l_B}{2h_B} \tag{6}$$

In Fig. 5, the predicted occurrence of LS-S1 is shown for the three walls which developed the

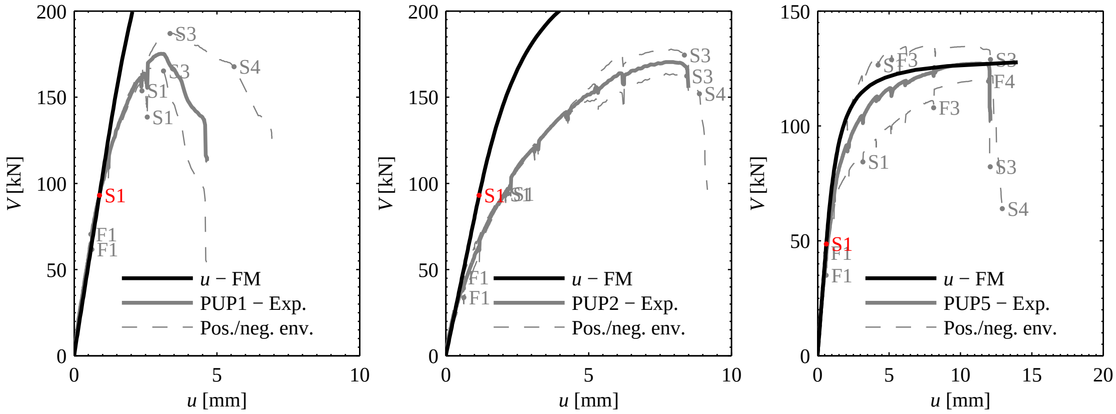

Figure 5. Prediction of LS-S1 in the force-displacement response of URM walls (FM refers to the analytical force-displacement formulation from Paper IV)

most significant shear mode. It can be noted that—with exception of PUP2—the predicted occurrence of LS-S1 is in accordance with the point where first softening occurs and where the flexural model from Paper IV starts diverging from the experiment. Note that the wall unit PUP2 was also surprisingly soft when compared to the corresponding wall unit PUM2 at half-scale, e.g. Paper II. In the previous section, it was noted that the flexural model yield in a wrong prediction of the displacement components if they were not so different from each other (see Fig. 3). However, LS-S1 occurs for rather small displacements and it is questionable if at that level, enough deformation develop in the walls that the experimental displacement components can be determined trustfully from the optical measurement.

2.2 Peak shear strength at opening of the diagonal crack in the center (LS-S3)

After the first appearance of a diagonal stair step crack (LS-S1), further parallel cracks develop and start also to propagate through bricks (LS-S2). With further increase of the shear force, the shear peak strength of the masonry is exceeded in the center of the wall (see Fig. 5) and deformation start concentrating along one crack, while the other cracks tend to reduce in width (see Paper III). This occurrence is associated to LS-S3 and corresponds to the point when the peak shear strength is exceeded along the central diagonal crack (Table 1):

$$\tau_{xy} = c + \mu \cdot \sigma_y \tag{7}$$

where c and μ are the cohesion and friction according to Mohr-Coulomb.

2.3 Shearing off of the corner bricks (LS-S4)

In Paper III, a significant loss of lateral strength is associated with the shearing off of the corners (LS-S4) and linked to the "Near Collapse" limit state according to EC8-P3 [CEN05]. It occurs when the shear strength is attained along the whole crack length (including central part and corner regions, see Fig. 6). At this point, the peak shear strength has been already exceeded along the central part of the diagonal shear crack at LS-S3, hence the shear stresses which are transferred through the diagonal crack are:

$$\tau_{xy} = \mu \cdot \sigma_y \tag{8}$$

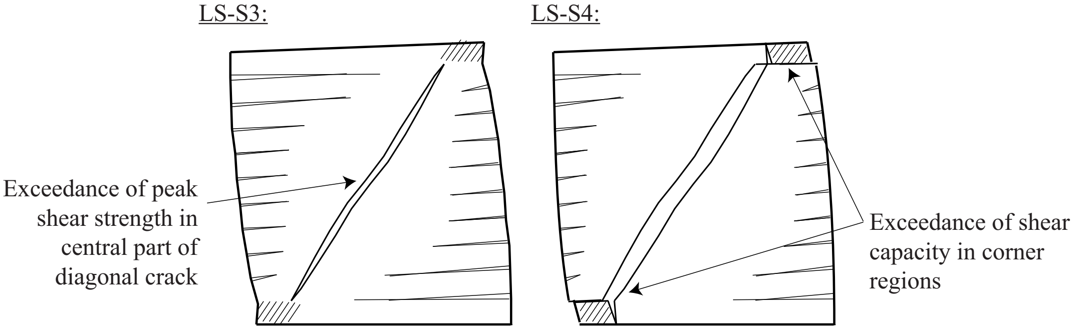

Figure 6. Schema illustrating the local mechanism at LS-S3 and LS-S4

In the corner regions, the shear capacity is still governed by the peak shear strength. However, due to the high solicitation of the bricks in corners, shear stresses in the corners should be also limited by the tensile strength $f_{t,B}$ of the bricks according to Mann and Müller [MM82]:

$$\tau_{xy} = \min\left(c + \mu \cdot \sigma_y; \frac{f_{t,B}}{2.3} \cdot \sqrt{1 + \frac{\sigma_y}{f_{tB}}}\right) \tag{9}$$

3 First propositions for a model based on equilibrium equations

In order to account for the softening due to the separation of the wall into two triangles, it is proposed to cut the wall along the diagonal crack into two separated triangles (see Fig. 7) and to replace the upper triangle by a set of forces. According to [MM82], the forces transferred through the vertical head joints are negligible and only horizontal shear forces $V_{1/2/3}$ and vertical normal forces $N_{1/2/3}$ are transferred through the crack. Thereby, three regions are distinguished along the crack: two corner regions (region 1 and 2) at the tips of the triangles through which $V_{1/2}$ and $N_{1/2}$ are transferred and the central region (region 3) along the diagonal crack through which V_3 and N_3 are transferred.

L_{st} in Eq. (3) is estimated such that the inclination of the central crack region is equal to $y : x = 2h_B / l_B$. This crack orientation corresponds also to the one observed during quasi-static cyclic tests of URM walls, e.g. Fig. 11a, or dynamic shake tests of whole URM wall structures, e.g. Fig. 11b, built with modern hollow core clay bricks.

The subdivision of the diagonal crack into the three regions allows to distinguish between the different local failure mechanisms which occur at LS-S3 and LS-S4. Hence, Eq. (7) is transformed in following global criterion for the shear force V_{S3} at LS-S3:

$$V_{S3} = V_1 + V_2 + c \cdot T(L - L_{st}) + \mu \cdot N_3 \tag{10}$$

and Eqs. (8) and (9) in following criterion for the shear force V_{S4} at LS-S4:

$$V_{S4} = V_1 + V_2 + \mu \cdot N_3 \tag{11}$$

where V_1 and V_2 are both limited by

$$V_{1/2} \leq \min\left(c \cdot \frac{TL_{st}}{2} + \mu \cdot N_{1/2}; f_{t,B} \cdot \frac{TL_{st}}{4.6} \cdot \sqrt{1 + \frac{2N_{1/2}}{TL_{st} f_{t,B}}}\right) \tag{12}$$

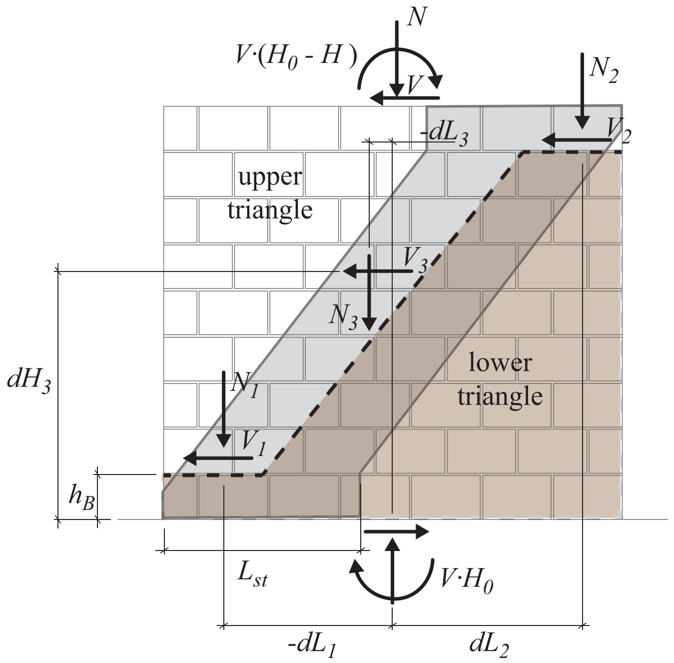

Figure 7 Separation of the rectangular wall into two triangles and force distribution along the cut

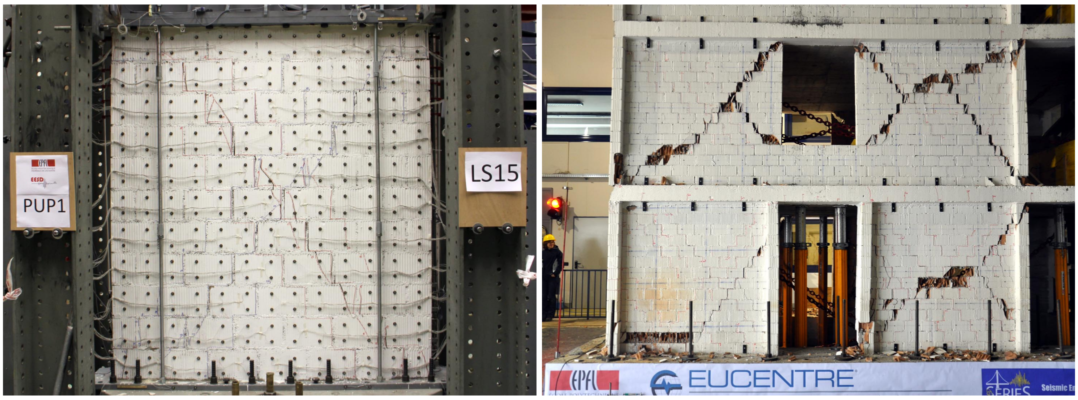

Figure 8. Crack pattern typically observed between LS-S3 and LS-S4 (left: URM full-scale wall from the EPFL test series, right: URM half-scale walls from the CoMa shake table test [BT+14])

3.1 Known and assumed relationships between the physical quantities

Considering that V can be determined from Eqs. (10) and (11), the quantities from Fig. 7 can be divided into a group of known and a group of unknown quantities:

5 Knowns: V, N, H_0, H, h_B and L_{st}

10 Unknowns: V_1, V_2, V_3, N_1, N_2, N_3, dH_3, dL_1, dL_2 and dL_3

In order to solve the problem, different relationships between these different quantities are summarized and/or proposed in the following. Some of these relationships derive from

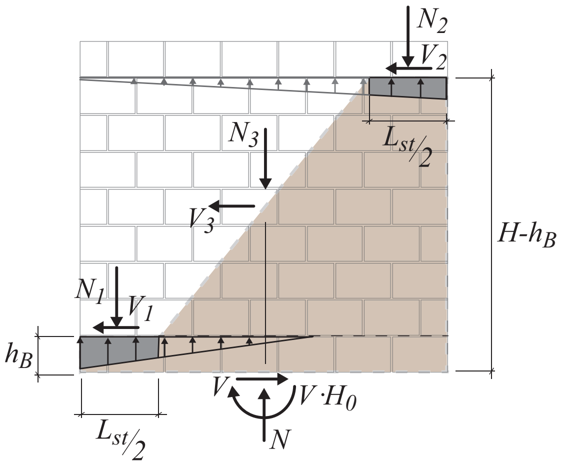

Figure 9 Estimation of $N_{1/2}$ using the plane section hypothesis and a linear-elastic constitutive law in compression

known facts—e.g. the force and moment equilibrium in Section 3.1.1—others are based on assumptions. In the later case, this is explicitly mentioned.

3.1.1 Equations from equilibrium

At first, three equations can be derived from force and moment equilibrium:

$$V = V_1 + V_2 + V_3 \tag{13}$$

$$N = N_1 + N_2 + N_3 \tag{14}$$

$$V \cdot H_0 = V_1 \cdot h_B + V_2 \cdot (H - h_B) + V_3 \cdot dH_3 - N_1 \cdot dL_1 - N_2 \cdot dL_2 - N_3 \cdot dL_3 \tag{15}$$

3.1.2 Assumptions for $N_{1/2}$ and $dL_{1/2}$

Assuming that the plane section hypothesis holds for the sections where both triangles are held together, i.e. at $y = h_B$ and $y = H - h_B$, the normal stresses in these sections can be estimated with a triangular stress distribution as shown in Fig. 9. The normal forces $N_{1/2}$ correspond thus to the sum of vertical stresses which pass through the corner regions (see Fig. 9):

$$N_1 = \int_{-\frac{L}{2}}^{-\frac{L_3}{2}} \sigma_y(x; h_B) \cdot T \, \mathrm{d}x \tag{16}$$

$$N_2 = \int_{\frac{L_3}{2}}^{\frac{L}{2}} \sigma_y(x; H - h_B) \cdot T \, \mathrm{d}x \tag{17}$$

where $\sigma_y(x; y)$ is the vertical stress in the section $y = h_B$ and $y = H - h_B$. $L_3 = L - L_{st}$ is the horizontal length of the diagonal central region.

Considering the small size of the corner regions, the eccentricity of N_1 and N_2 with respect to the center of the corner regions dL_1 and dL_2 can be neglected and the positions of N_1 and N_2 are simplified to:

$$dL_{1/2} = \mp \left(\frac{L}{2} - \frac{L_{st}}{4} \right) \tag{18}$$

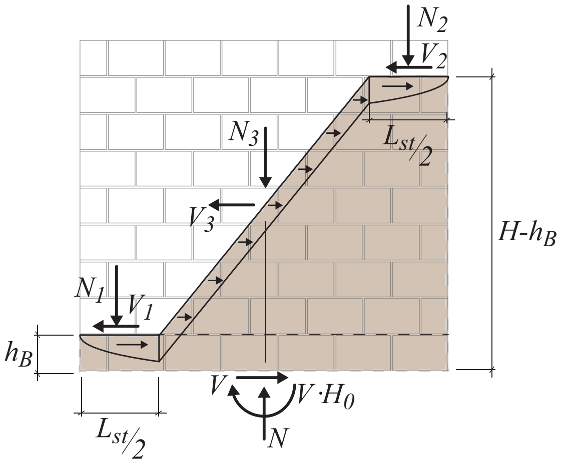

Figure 10 Simplification for the shear stress distribution along the diagonal shear crack

3.1.3 Assumption for the distribution of V for the different regions of the crack

From numerical simulation of the walls [ZPB14], it was concluded that the shear force distribution can be simplified as illustrated in Fig. 10. Hence, assuming a parabolic shear stress distribution in the corner regions and a constant shear stress distribution in the central region—while respecting Eq. (13), the three shear force components $V_{1/2/3}$ can be estimated as follows:

$$V_{1/2} = V \cdot \frac{L_{st}}{3 \cdot L - L_{st}} \tag{19}$$

$$V_3 = V \cdot \frac{3 \cdot L - 3 \cdot L_{st}}{3 \cdot L - L_{st}} \tag{20}$$

Note that assuming this shear stress distribution results also in following estimate for the position dH_3 at which V_3 applies:

$$dH_3 = \frac{H}{2} \tag{21}$$

3.1.4 Relationship between N_3^*, N_3 and V_3 according to Mann and Müller [MM82]

According to Mann and Müller [MM82] no forces are transferred through the head joints and local equilibrium at brick is preserved through a pair of vertical stresses which add or subtract to the vertical stresses (Eq. 1). Hence, the following relationship can be established between N_3 and V_3:

$$N_3 = N_3^* - V_3 \cdot \frac{2l_B}{h_B} \tag{22}$$

where N_3^* is the normal force which would be transferred through the central region of the crack if stresses transfer through head joints. The redistribution of axial stresses will decrease once first crack appear in bricks along the diagonal crack, i.e. occurrence of LS-S2 (see Table 1) and Eq. (22) gives only a lower bound for N_3. In order to account for this, it is proposed to

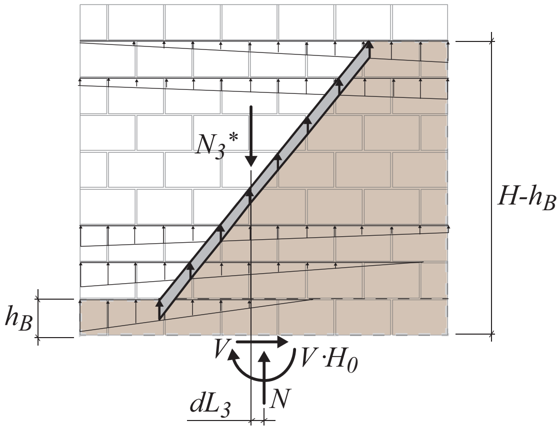

Figure 11 Estimation of N_3^* using the plane section hypothesis and a linear-elastic constitutive law in compression

introduce a redistribution factor $\eta_{MM} \leq 1.0$ in Eq. (22):

$$N_3 = N_3^* - \eta_{MM} \cdot V_3 \cdot \frac{2h_B}{l_B} \tag{23}$$

3.1.5 Assumptions for N_3^* and dL_3

Assuming that N_3^* is the normal force which would pass through the crack, if no local stress redistribution according to [MM82] would occur. It can be estimated using the same assumptions as for $N_{1/2}$ along the diagonal crack (see Fig. 11).

3.2 Estimation of the distribution of the forces using previous presented formulas

Previous presented relationships cannot all be taken as known and some are based on assumptions. In the following two methods are proposed which determine the different quantities from Fig. 7 while using different assumptions from Section 3.1. Thereafter, both approaches are used to predict the force-displacement curve and the obtained results are compared to the experiments.

3.2.1 Estimation of the force-distribution - Model 1

Based on the assumptions from Section 3.1.2, the forces can be distributed for the different regions as follows:

1. $N_{1/2}$ and $dL_{1/2}$ are estimated according to Section 3.1.2 using V and N
2. N_3 is obtained from the force equilibrium, i.e. Eq. (14)
3. $V_{1/2/3}$ and dH_3 are estimated according to Section 3.1.3 using V
4. dL_3 is obtained from moment equilibrium, i.e. Eq. (15)

3.2.2 Estimation of the force-distribution - Model 2

Assuming that Section 3.1.5 applies, the forces in the different regions can be estimated as follows:

1. N_3^* and dL_3 are estimated based on Section 3.1.5
2. $V_{1/2/3}$ and dH_3 are distributed according to Section 3.1.3
3. N_3 is computation from N_3^* and V_3 using the relationship described in Section 3.1.5 and assuming a factor for η_{MM} (for the following application a factor of 0.3 is assumed)
4. $N_{1/2}$ are computed from force and moment equilibrium (Eqs. 14 and 15)

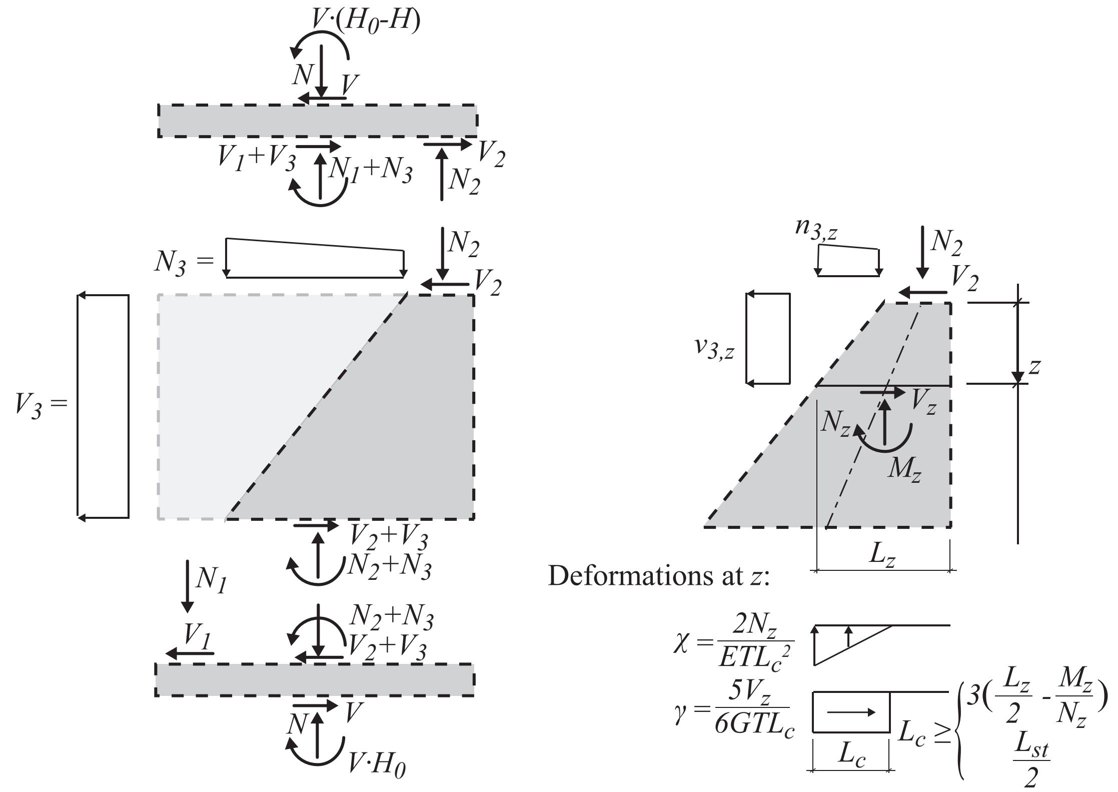

Figure 12. Assumptions for computing the displacement developing in both triangles

3.3 Force-displacement response obtained with the proposed models before LS-S3

Once the distribution of the forces is known, the axial force, shear force and moment diagrams of the lower triangle can be estimated and the displacement is obtained from numerical integration of curvatures and shear strains (see Fig. 12). Therefore, the axial force N_3 and the shear force V_3 which apply to the central region of the diagonal crack are simplified to linearly distributed forces $n_{3,z}$ and $v_{3,z}$ respectively. Assuming that the resultant V_3 applies at mid height (see Section 3.1.3) and considering the eccentricity of N_3, they can be estimated as follows:

$$v_{3,z} = \frac{V_3}{H_3} \tag{24}$$

$$n_{3,z} = \frac{12N_3 \cdot dL_3}{L_3^2 H_3} \cdot z - \frac{6N_3 \cdot dL_3}{L_3^2} + \frac{N_3}{L_3} \tag{25}$$

Note that $n_{3,z}$ is distributed along the horizontal length ($L_3 = L - L_{st}$) and $v_{3,z}$ along the vertical length ($H_3 = H - 2h_B$) of the central crack region.

3.4 Estimation of the distribution of the forces using previous presented formulas for a model before LS-S3 occurs

Figure 13 shows the force-displacement response estimated with the different models (FM refers to the analytical formulation from the flexural model from Paper IV, SM1 and SM2 refer

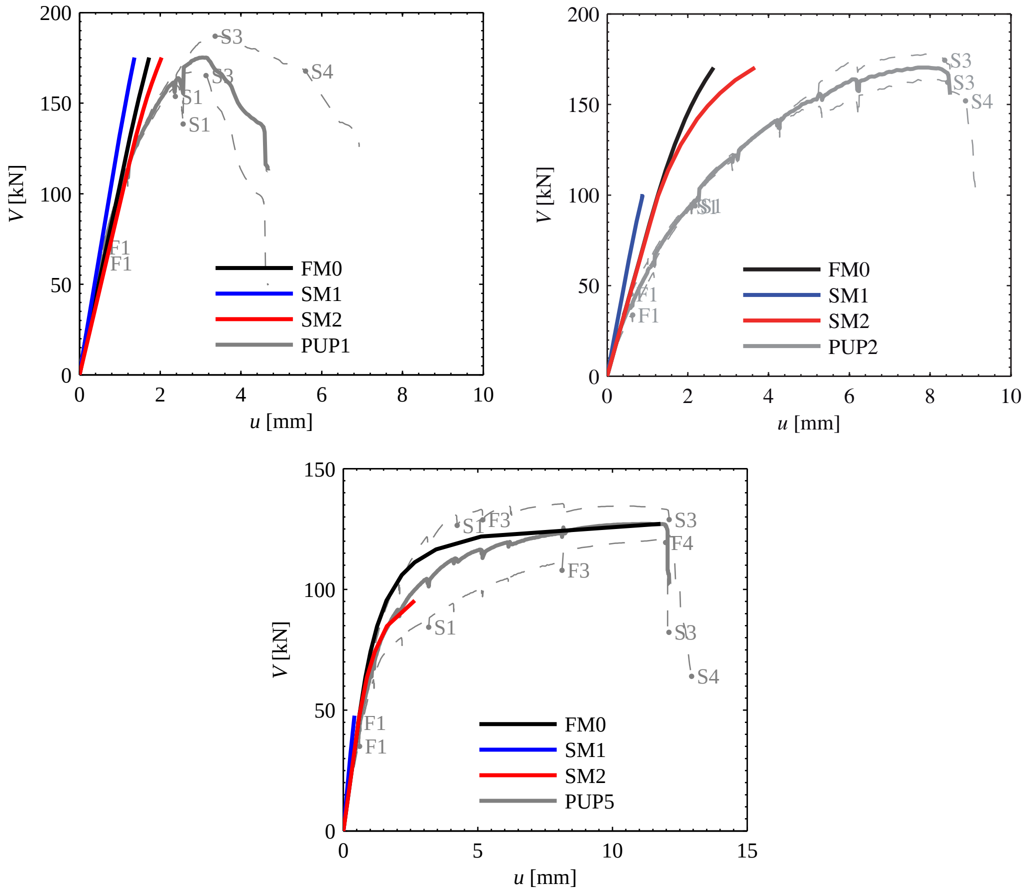

Figure 13. Force-displacement response estimated with the using the flexural model (FM), the shear model 1 (Section 3.2.1, SM1) and the shear model 2 (Section 3.2.2)

to the shear models in Sections 3.2.1 and 3.2.2 respectively). The displacement is estimated up to maximum shear force measured during the experiments. In some cases the force distribution caused the resultant of the axial force N_z was outside of the section of the triangle ($M_z/N_z \geq 0.5L_z$, see Fig. 12). In this case the curve are stopped for smaller forces. Figure 13 shows that SM1 predicts an increase in stiffness and SM2 a decrease with respect to FM. SM1 is based on the assumption that the normal forces N_1 and N_2 can be estimated using the plane section hypothesis and N_3 is computed thereafter from force equilibrium (Eq. 14). N_1 and N_2 apply both at the outer side with respect to the central axes of the triangles (see Fig. 12) and cause thus a bending in the opposite direction than expected. On the contrary, N_3 applies at the inside with the respect to the central axes of the triangles and enforces thus positive bending in the triangles (positive bending refers to $M_z > 0$ as shown in Fig. 12). Hence, SM1 overestimates the forces N_1 and N_2 and overestimates therefore also the stiffness of the wall (see 13). The assumptions in Section 3.1.2 do thus not hold, which is due to the relatively high flexibility of the bricks located at the edge of the wall. While bricks located in the center of the wall are hindered to torque by the surrounding bricks, this is not the case for the bricks located at the ends of one row. Thus, the central crack region reacts stiffer and will attract the forces. Consecutively, an increase of N_3 for increasing V would be expected (Fig. 14).

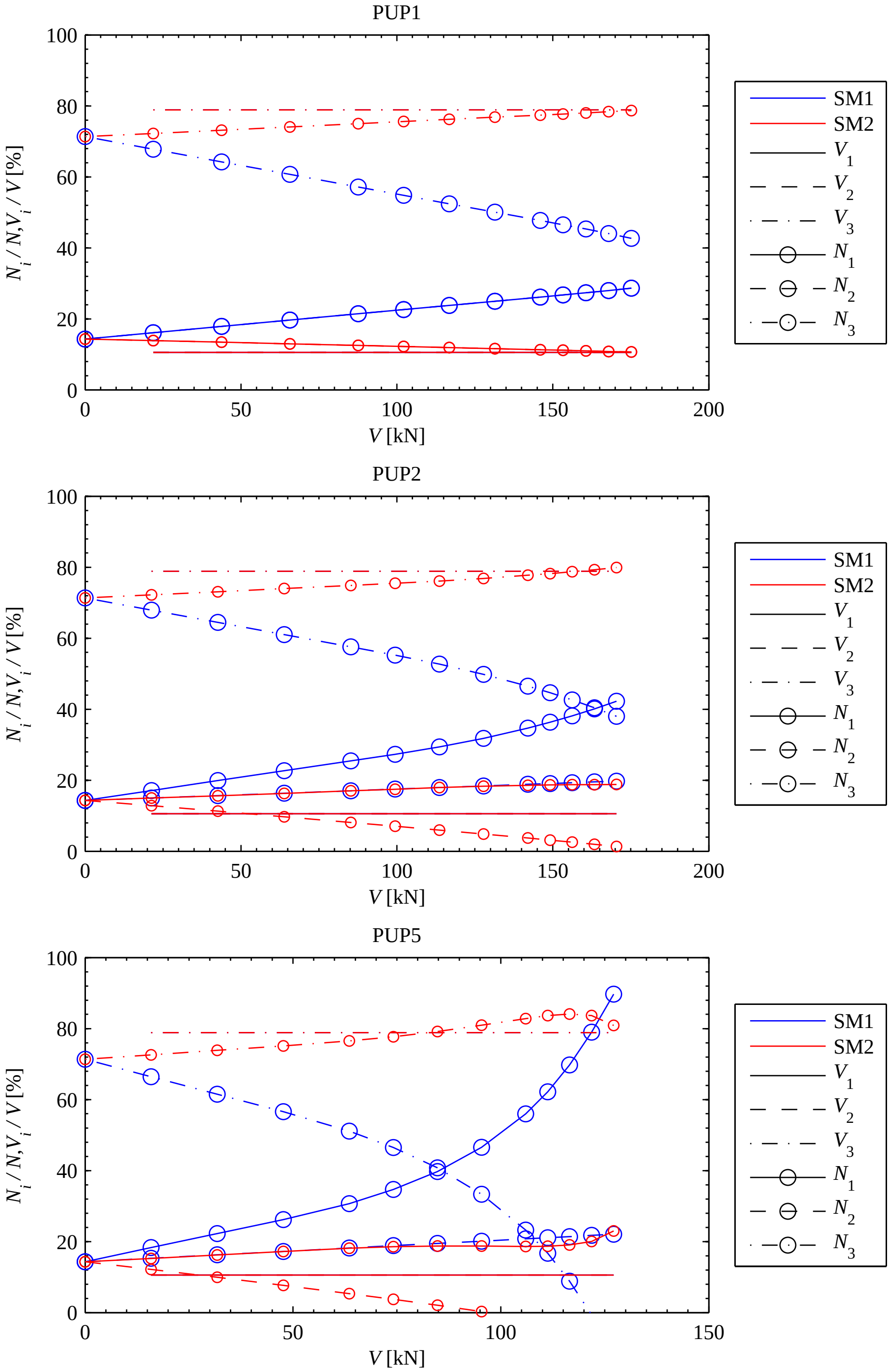

Figure 14. Distribution of the forces according to model 1 (Section 3.2.1, SM1) and to shear model 2 (Section 3.2.2, SM2)

In SM2, N_3^* is estimated using the plane section hypothesis in the central region of the crack and thereafter reduced by the pair of forces which balance locally the torque of the bricks [MM82] using Eq. (23). Assuming a rather low redistribution factor, i.e. $\eta_{MM} = 0.3$ (see Section 3.1.5), allows modeling the increase of N_3 (Fig. 14) and captures therefore also

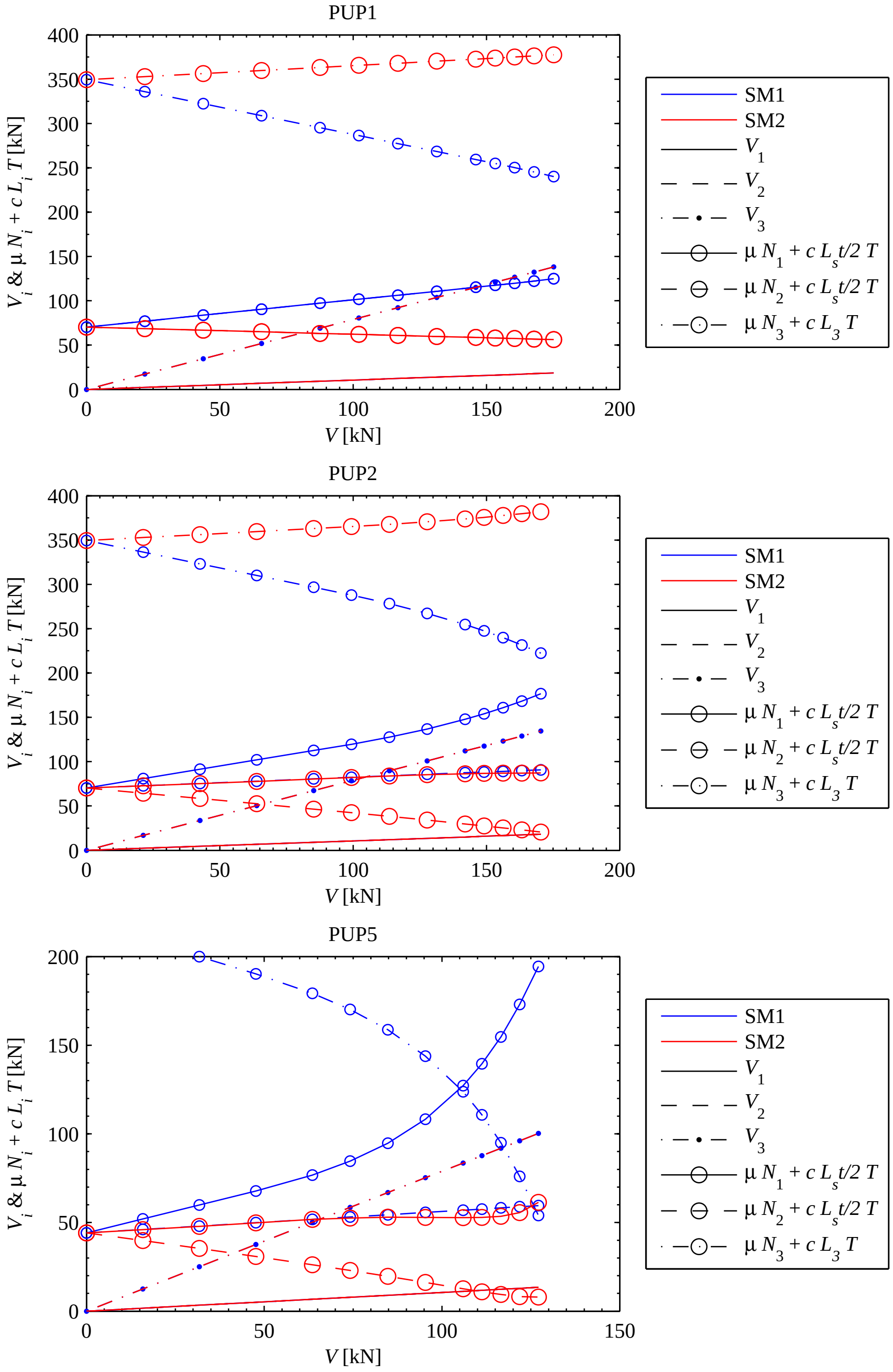

Figure 15. Shear force components against the shear strength for the different regions distributing the forces according to model 1 (Section 3.2.1, SM1) and to shear model 2 (Section 3.2.2, SM2)

the expected softening in the predicted global force-displacement response of the walls (see Fig. 14). Nevertheless, the relatively low value of η_{MM} which was needed in our to capture the increase of N_3, is surprising.

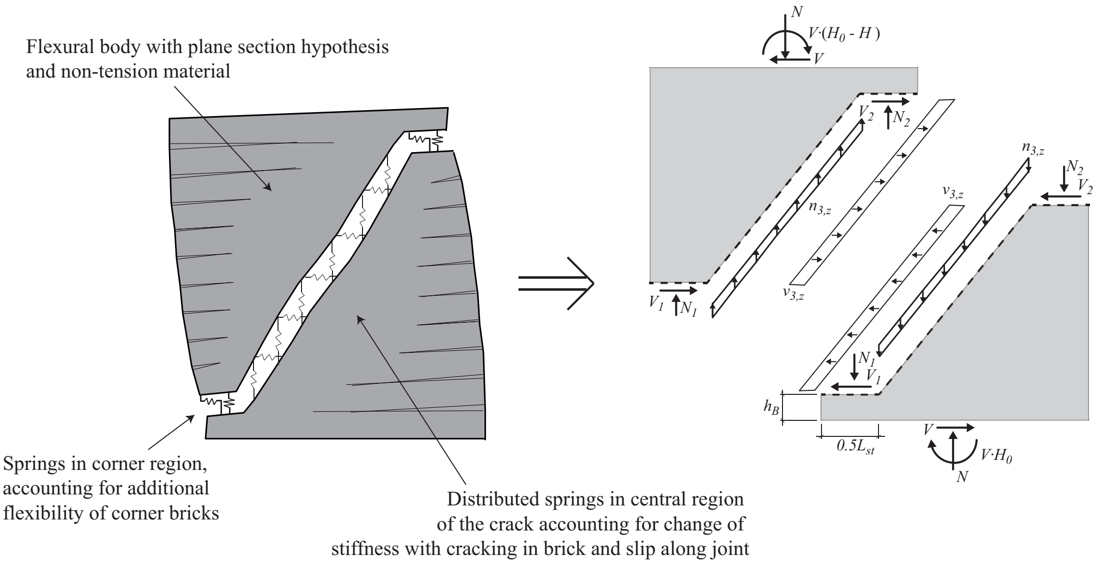

Figure 16. Possible kinematic model

In Fig. 15, the local peak shear strength is estimated for the three regions of the diagonal crack and compared to the shear forces which are transferred through the corresponding regions of the cut (see Fig. 7). The forces are distributed according to SM1 (Section 3.2.1) and SM2 (Section 3.2.2). Considering Eq. (10), LS-S3 should occur when the curve $\mu \cdot N_3 + c \cdot L_3 T$ intersects with V_3. It can be noted that this is only obtained in the case of PUP5, while for PUP1 and PUP2 LS-S3 should not be reached. This discrepancy between prediction and experimental observations—the occurrence of LS-S3 is marked in the experimentally determined load displacement curves in Fig. 13—origins probably from two simplifications: (i) the distribution of V according to Section 3.1.3 is too simplistic and (ii) the local stress criterion (Eq. 10) is not attained along the whole central region simultaneously as assumed in Eq. (10).

4 Possible approaches towards a mechanical capturing the formation of a diagonal shear crack

In the previous section, two possible models are discussed which are based on force equilibrium and cut the wall into two triangles, while replacing the upper triangle by a set of forces. However, both models are based on several assumptions which are quite simplistic and both models yield far from satisfying results in terms of force capacity or force-displacement response. In order to improve the model, two approaches should be pursued: (i) the local mechanism which occurs along the diagonal crack should be investigated more in depth and (ii) previous presented ideas for a model based on force equilibrium should be implemented in a kinematic model in order to consider the additional condition of equal displacement at both corner regions of the triangles.

Some of previous presented ideas base on the local redistribution of forces at bricks. However, the proposed equation by Mann and Müller [MM82] which captures this phenomenon is based on local equilibrium at brick solely and it is not suggested how to consider this phenomenon correctly at global level. In Section 3.1, several assumptions are done to overcome that problem, nevertheless, more detailed research is needed. For instance, the influence of cracking of bricks (LS-S2) should be investigated in depth in order to obtain a better feeling about appropriate values for η_{MM} (see Section 3.1.4). During experiments it is impossible to measure local stress distribution between bricks. Therefore, detailed numerical analysis will be needed, e.g. the micro-model approaches proposed in [Lou96, LR97], which capture the brick-mortar interaction and therefore the local mechanism of stress redistribution [MM82]. Furthermore, the influence of size of brick, cracks through bricks, etc. on the redistribution should be investigated in depth.

The models discussed in previous sections neglect the deformations in the upper triangle and equal displacement of both triangles at the corner regions is not considered. However, this is an additional condition which should be used and could be implemented in a kinematic model similar to the ones which have been recently developed for reinforced concrete walls, e.g. [MHB13]. A possible kinematic model is shown in Fig. 16. In this, both triangles are modeled as elastic bodies in which plane section hypothesis holds and the nonlinear behavior occurs only after onset of decompression in bed joints (see Paper IV). The diagonal crack is modeled with the help of nonlinear elastic-plastic springs which should consider the local behavior of masonry under shear stress solicitation (see Fig. 1) using for instance the model from Gambarotta and Lagomarsino [GL97]. The model in Fig. 16 distinguishes again between three different regions along the diagonal crack: the two corner regions 1 and 2 and the diagonal central region 3. Regions 1 and 2 could be modeled with one spring for the horizontal and one for the vertical direction. These springs should in addition to the nonlinear material behavior also account for the additional flexibility of the corner bricks. Along the central region, the springs should be linearly distributed such to consider the different solicitation along the crack. The constitutive law of these springs should account for changing geometry of the bricks (e.g. when bricks are divided by cracks) and for the nonlinear elastic-plastic slip-shear force relationship of the mortar brick interface.

5 Conclusions

In this chapter, it is shown that for URM walls assembled with modern hollow core clay bricks and with a high portion of shear solicitation the behavior is governed especially for small forces by an effect first described by Mann and Müller [MM82]: the stresses which are transferred through the vertical head joints are negligible and shear stresses are only transferred through bed joints and bricks; this introduces a moment to the bricks, which is balanced through local redistribution of normal stresses at top and bottom of bricks.

This phenomenon causes two mechanisms which are not captured with the flexural model proposed in Paper IV: (i) the shear stress concentrate along the diagonal compression strut where shear stresses can be directly transferred through interlock of bricks (see Fig. 4) and (ii) the redistribution of the normal stresses causes local decompression over half a brick length [MM82], which get apparent in form of diagonal stair step cracks (LS-S1). The flexural model overestimates the effective stiffness of the shear dominated URM walls after the formation of this first diagonal crack (LS-S1). In order to predict this point, a formula is proposed which accounts also for the concentration of shear stresses along the diagonal strut.

In Paper III, it is observed that the initiation of first diagonal stair step cracks separates the walls and causes a softening which is not captured with the flexural model. Thereafter, the behavior of the URM walls is governed by the deformation of both triangles which are hold together at $y = h_B$ and $H - h_B$. In order to account for this phenomenon, a model based on force equilibrium is proposed which cuts the wall into two triangles and replaces the upper triangle by a set of forces. Thereby three regions are distinguished along the crack: two corner regions and one diagonal central region. The model is statically over determined and two possible approaches are proposed how to estimate the forces.

The first approach assumes that the plane section hypothesis holds at the sections $y = h_B$ and $H - h_B$ and that the normal forces which are transferred through the corner regions can be estimated assuming a triangular stress distribution. However, the model does not account for the increased flexibility in the corner regions—the bricks situated at the end of a brick row are not hindered to torque which results in an increased torsional flexibility with respect to the bricks situated in the center of the wall. The first approach overestimates therefore the forces transferred through the corner regions. This reduces the displacements in the triangles and the model overestimates the overall stiffness of the wall. The second approach is based on the idea that the forces which are transferred through the central region of the crack can be estimated using the Mann and Müller criterion [MM82]. With respect to the first approach, the second approach predicts that more forces will be transferred through the central region of the crack and it yields the expected softening on the global force-displacement response. Nevertheless, this approach is based on assumptions which need more research, before they can be implemented trustfully in a model (e.g. amount of local stress redistribution [MM82]). To conclude a possible kinematic model is proposed which in addition should also account for (i) the displacement of the upper triangle, (ii) the nonlinear elastic-plastic behavior of the mortar-brick interface, (iii) the effect of the increased flexibility at corners and (iv) the effect of cracking in bricks on the local stress redistribution.

References

[BT+14] Beyer, K, Tondelli, M, Petry, S and Peloso, S. Dynamic testing of a four-storey building with reinforced concrete and unreinforced masonry walls: Prediction and test results. *Submitted to Bulletin of Earthquake Engineering*, 2014.

[CEN05] CEN. Eurocode 8: Design of structures for earthquake resistance, Part 3: Assessmemt and retrofitting of buildings. Technical Report EN 1998-3, European Committee for Standardisation, Brussels, Belgium, June 2005.

[FPV14] Facconi, L, Plizzari, G and Vecchio, F. Disturbed stress field model for unreinforced masonry. *Journal of Structural Engineering*, 140, 2014.

[Gan85] Ganz, HR. *Mauerwerksscheiben unter Normalkraft und Schub*. Phd thesis, ETH Zürich, Institute of Structural Engineering, Zürich, Switzerland, 1985.

[GL97] Gambarotta, L and Lagomarsino, S. Damage models for the seismic response of brick masonry shear walls. Part I: The mortar joint model and its applications. *Earthquake Engineering and Structural Dynamics*, 26:423–439, 1997.

[Lou96] Lourenço, PB. *Computational strategies for masonry structures*. Phd thesis, Faculty of Engineering, TU Delft, Netherlands, 1996.

[LR97] Lourenço, PB and Rots, JG. Multisurface interface model for analysis of masonry structures. *Journal of Engineering Mechanics*, 123:660–668, 1997.

[MC97] Magenes, G and Calvi, GM. In-plane seismic response of brick masonry walls. *Earthquake Engineering and Structural Dynamics*, 26:1091–112, 1997.

[MHB13] Mihaylov, BI, Hannewald, P and Beyer, K. Three-parameter kinematic theory for shear critical reinforced concrete walls. part i: Formulation. *Submitted to Journal of Structural Engineering*, 2013.

[MM82] Mann, W and Müller, H. Failure of shear-stressed masonry—an enlarged theory, tests and application to shear walls. In *Proceedings British Ceramic Society*, volume 30, pages 223–235, 1982.

[TC71] Turnšek, V and Cašovič, F. Some experimental results on the strength of brick masonry walls. In *Second International Brick Masonry Conference*, pages 149–156, 1971.

[TS81] Turnšek, V and Sheppard, P. The shear and flexural resistance of masonry walls. In *Proceedings of the International Research Conference on Earthquake Engineering*, pages 517–573, Skopje, 1981.

[ZPB14] Zhang, S, Petry, S and Beyer, K. Investigating the in-plane mechanical behavior of URM piers via DSFM. In *Proceedings of the 2nd European Conference on Earthquake Engineering and Seismology*, Istanbul, Turkey, 2014.

Summary

1 Summary of contributions

In countries of low to moderate seismicity, e.g. in Switzerland, unreinforced masonry (URM) is commonly used for the construction of low- to mid-rise buildings. Therefore, a large percentage of residential buildings contains modern URM walls as structural elements. When this kind of structures is subjected to seismic loading, the stiff URM walls attract considerable lateral forces. Thus, assuming that local out-of-plane failure is avoided, the overall response of the URM building will be governed by the in-plane behavior of the URM walls. In particular the URM walls situated at the ground floor, which are subjected to the highest forces, need to be considered in seismic design and assessment. Despite the wide use of URM in construction, the response of URM walls subjected to lateral in-plane loading is not yet fully understood. In particular the displacement capacity of URM walls requires further studies, which is a key input parameter for displacement-based methods but is not used explicitly in standard force-based design approaches.

This thesis contributes to the improvement of the design and assessment methods for URM wall structures built with modern hollow core clay bricks in several regards: First, an experimental campaign on the lateral nonlinear in-plane response of URM walls was performed; second, a literature review on URM wall tests was elaborated and an existing dataset on URM walls was extended and reanalyzed; third, a new mechanical model was developed that describes the full force-displacement response of flexural dominated URM walls up to a significant loss of lateral force. The individual conclusions of these three methodologies and their contributions to the global improvement on the design and assessment methods for URM walls are detailed in the following.

1.1 Contributions derived from the experimental campaign

In the framework of this thesis, two sets of URM walls were tested under quasi-static cyclic lateral in-plane loading. The first set of walls was constructed using modern hollow clay brick units and standard cement-based mortar (see Appendix A). The walls were built at full-scale and had all the same dimensions. The tests varied with regard to the applied boundary conditions, i.e. applied axial stress and shear span. The test setup had been designed such that these both parameters were constant throughout each test. The second set of walls was identical, but was built at half-scale using a scaled brick with similar mechanical properties than the full-scale brick (see Appendix B). The results drawn from the full-scale test series are presented in Papers I and III and their outcome can be summarized as follows:

(1) Two test series were performed which set themselves apart from other existing URM wall

tests, e.g. [GT84, MC92, BP+03, MMP08, GT13, SMS13], with regard to following aspects: (i) the displacement field of the URM walls was continuously measured during the whole test; (ii) the walls were tested applying a large range of different shear spans ($H_0 = 0.5$–$1.5H$) and (iii) all test data (raw and post-processed) was made publicly available and can be downloaded from the Zenodo platform (DOI: 10.5281/zenodo.8443).

(2) Based on observations from others [MM82, Hey92] and own observations, two new sets of limit states were proposed, which on the contrary to previous proposed limit states for URM walls [ATC98, GM+98, Cal99, Abr01, Lan02, BP+03, LG06, Tom07], are different for the two predominating failure modes (i.e. shear or flexure failure, see Fig. 1) and link local performance levels to characteristic points of the global force-displacement response of URM walls.

As preparation of a shake table test [BT+14, TP+14], the effect of scaling was investigated through the comparison of results from the half- and full-scale test series. These investigations led in addition to existing investigations on the scaling of masonry [BW58, HM65, HAH86, Tom87, ECA91, TV92, DHT95, Moh06, MH11] to the following conclusions:

(3) Hollow core clay bricks should be scaled by decreasing the number of webs while keeping the void ratio approximately the same. This assures (a) that half- and full-scale brick have similar brittleness and strength and (b) that the shear properties of the brick-mortar interface are similar for both types of masonries. Once model bricks are scaled properly, good similitude between the material properties of the half- and full-scale masonry is obtained. The influence of the scaling of the mortar joint thickness on the mechanical properties of the mortar-brick interface has only a secondary effect in the case of hollow clay brick masonry.

(4) The nonlinear response of URM walls under in-plane lateral loads at half- and full-scale matches rather well up to peak load (see Fig. 2). After peak load, the global displacement capacity depends on the local deformation capacity, e.g. maximum crack width, which was different for the half-scale masonry. Slightly higher drift capacities at ultimate stage and moreover higher maximum drift before axial load failure were obtained for URM walls built at reduced scale.

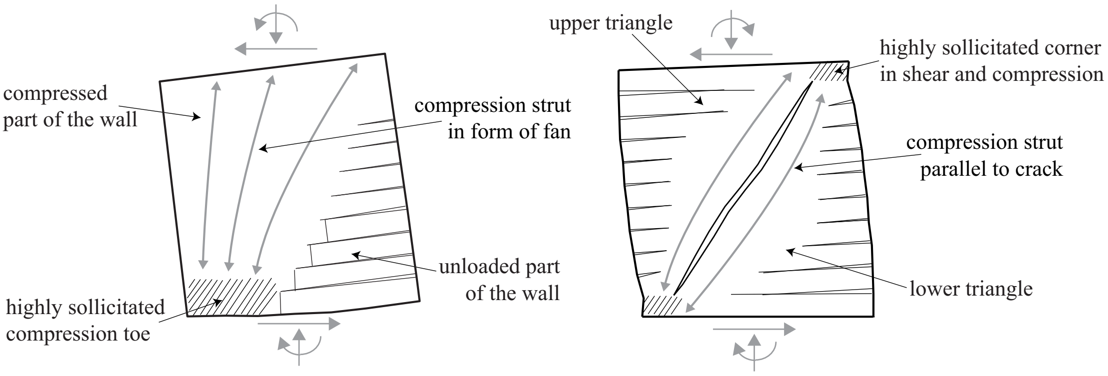

Figure 1. Mechanism for a flexural dominated wall and for a wall developing a significant shear crack

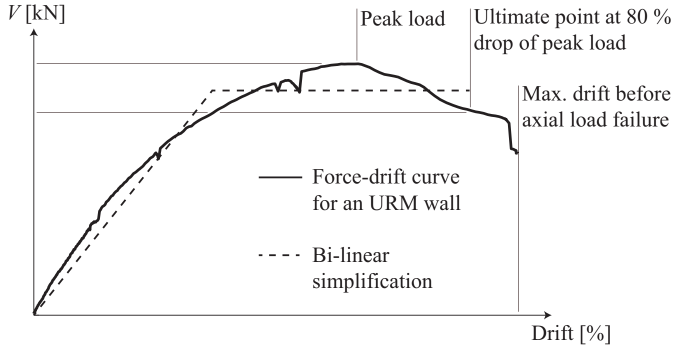

Figure 2 Force-drift curve for an URM wall subjected to lateral in-plane loading

1.2 Contributions derived from the dataset analysis

In order to confirm the results obtained from our own test series, these were compared with other existing experiments. To do so, a dataset with wall tests was setup. It was chosen to build on the existing dataset of wall tests on modern URM walls by [FM$^+$09] and to extend this set by our own tests and other wall tests reported in the literature [BT03, BT06, MDPG05, MMP08, GT84, SBG10, SG10, BP$^+$03, MC92, MC97]. The final dataset contains in total 64 walls and is limited to modern clay brick masonry with cement mortar bed joints of normal thickness (10–20 mm). The type of head joints varied between the different wall tests. Most walls were subjected to symmetric quasi-static in-plane loading. The dataset can be found in Paper I. Its elaboration led to the following conclusions:

(5) It was confirmed that attributing a fix ultimate drift capacity (see Fig. 2) to the failure modes, e.g. [CEN05], is too simplistic and that better estimates are obtained with empirical expressions which account for, e.g. applied axial stress and shear span [Lan02, Oro11, PLBL11]. In addition, the influence of the wall size [Lou97] and the load history [Abr96, PA90] was confirmed.

(6) A new empirical formulation was proposed which accounts in addition to other existing empirical models, e.g. [Lan02, CEN05, Oro11, PLBL11], also for the size of the wall units and the load history.

1.3 Contributions from the elaboration of the mechanical models

Based on the two different wall kinematics which were observed during the experimental campaign, two mechanical models were developed in Paper IV and Chapter V which aim at describing the nonlinear force-displacement response of URM walls developing a flexural mode and shear mode respectively.

The flexural model (Paper IV) was developed in two steps. First, an analytical formulation is derived based on the same hypotheses as existing models for rocking URM walls [BS08, PLG14], i.e. plane section hypothesis and a material with zero tensile strength and a linear-elastic behavior in compression. In a second step, local limit states that characterize changes in the kinematics of flexural dominated URM walls are developed and incorporated in the analytical expression. The new contributions of the flexural model can be summarized as follows:

(7) An analytical formulation was developed which is improved with respect to existing models [BS08, PLG14] with regard to the following two aspects: (i) it accounts for the variation in effective area along the height of the wall and (ii) couples the shear stiffness to the flexural stiffness. The new analytical formulation is thus compared to [BS08] applicable for walls subjected to different boundary conditions than cantilever or double-fixed. Furthermore,

it is shown that it yields not only good estimates of the global force-displacement response of URM walls but also of local deformation quantities, i.e. shear strain and curvature profile. The latter is important for the definition of limit states.

(8) Limit criteria which address the limit states that were characterized by the splitting and crushing of the bricks in the compressed toe of the masonry wall are implemented in the analytical formulation. In addition to previous existing local criteria [PCK07, BS08], the new criteria account for the confining effect of the foundation. Hence, it is considered that compression failure of the masonry will initiate from the second joint above the foundation, while it is assumed that failure in the base joint is governed by the compression strength of the brick. The new proposed mechanical model was validated against the 34 walls of the dataset of Paper I that developed a flexural failure. The comparison showed that the incorporated limit states yield better estimates of the displacement capacity and effective stiffness with regard to other existing models [PCK07, BS08, PLG14] or recommendations [CEN05, PLBL11].

Chapter V summarizes first ideas towards a model capturing the formation of a diagonal crack. The force-displacement response of URM walls subjected to significant shear load and assembled with relatively large modern hollow core clay bricks will diverge from the flexural model once diagonal stair step cracks develop in the walls. This results from the local stress redistribution according to [MM82] and causes a softening of the global force-displacement response of URM walls, which is not captured by the flexural wall model. The basic outcome of this chapter can be summarized as:

(9) An equation was proposed which predicts the formation of a first diagonal crack and thus the softening of shear dominated walls due to the separation into two triangles.

(10) A first kinematic model was proposed which models the wall as two triangles; further research is needed to complete this model.

2 Future work

Research on mechanical models for URM walls is in the fledgling stages and before such models can be possibly implemented in codes many topics require further research. To the author's opinion the most relevant topics are (i) the elaboration of a model which captures the response of URM walls developing a significant diagonal shear crack, (ii) the detailed investigations of the corner regions and their influence on the nonlinear force-displacement response of URM walls, and (iii) the influence of strain rate, loading history and the robustness of the bricks on the deformation capacity of the masonry after first crack develop through bricks.

In Chapter V, first ideas for a possible model capturing the formation of the diagonal crack are presented. However, these are just first ideas and to the author's opinion following two points could lead towards a complete mechanical model for shear dominated URM walls:

- The stress redistribution, which occurs locally at brick level and is due to the phenomenon first described by Mann and Müller [MM82], needs further investigation. Since it is not feasible to measure the stresses which develop between the bricks, it is suggested to do so using refined numerical modeling tools, e.g. simplified or non-simplified micro-modeling approaches [Lou96, LR97], which capture the complex brick-mortar interaction. Aspects which should be investigated more in depth are the influence of brick size with respect to the wall size and the influence of cracking of bricks in the central region of the diagonal crack.

- A model which would possibly overcome the problems faced in Chapter V could be a kinematic model, similar to the one developed for RC shear walls [MHB13]. The model should account for (i) the deformations of both triangles, (ii) the nonlinear elastic-plastic behavior of the mortar-brick interfaces, (iii) the higher torsional flexibility of the corner bricks (with respect to the bricks in the center of the wall, where local torque of brick is hindered by the surrounding bricks) and (iv) how cracks in bricks affect the local stress redistribution.

The experimental tests on URM walls underlined the importance of the corner regions; for flexural walls the ultimate capacity depends on the local deformation capacity of the bricks in the toe and for shear walls the ultimate displacement depends on the ability of the corner regions to hold both triangles together (see Fig. 1). Thus, more detailed investigations of the corner regions could help to further improve the proposed flexural model and also contribute to the development of a model capturing the post-peak behavior of shear dominated walls. The following two approaches are suggested:

- In the case of the herein presented wall tests only few measurement was available from the corner regions (e.g. the first LED was at around 5 cm from the base joint and 7.5 cm from the outer edge of the wall, see Appendix A). For future wall tests it would be interesting to complement the LED measurements by local detailed measurement of the corner regions using digital image correlation, e.g. similar to what has been recently done for RC walls [AP$^+$15] or the URM wall tests performed by [SMS13].
- Taking into account the influence of the local deformation capacity and strength of the corner region, it would be interesting to investigate the possibility of replacing locally bricks and mortar with higher performance materials (e.g. bricks of a stronger or/and softer material, fiber reinforced mortar) or to confine locally the mortar. This could improve the global seismic performance of URM walls, while minimizing the intervention for existing structures and additional construction costs for new buildings.

The different loading methodologies (monotonic vs. cyclic or symmetrical vs. asymmetrical loading, see Paper I) influenced the ultimate drift capacity. This observation is related to the crack propagation in bricks which is influenced by the robustness of bricks, the strain rate and the loading history. These issues should be further investigated:

- Identical tests on URM elements should be repeated several times while varying the number of load/displacement cycles at the same drift limit, rate of loading, duration of pause at peak displacement/load of each cycle, etc. In order to minimize the unknowns it might be interesting to start with small test units, e.g. as in [GT82] and to focus on a denser measurement, e.g. using digital image correlation similar to [SMS13, AP$^+$15].
- Standardized loading protocols should be developed for URM walls which propose an adequate loading protocol in dependency of the seismicity of the region [BP$^+$14, MB14] and which define also the boundary condition, e.g. the type of foundation.

References

[Abr96] Abrams, DA. Effects of scale and loading rate with tests of concrete and masonry structures. *Earthquake Spectra*, 12(1):13–28, 1996.

[Abr01] Abrams, DP. Performance-based engineering concepts for unreinforced masonry building structures. *Progress in Structural engineering and Materials*, 3:48–56, 2001.

[AP+15] Almeida, JP, Prodan, O, Rosso, A and Beyer, K. Tests on thin reinforced concrete walls subjected to in-plane and out-of-plane cyclic loading. *To be submitted to Earthquake Spectra*, 2015.

[ATC98] ATC. Evaluation of earthquake damaged concrete and masonry wall buildings. Technical Report FEMA-306, Basic Procedures Manual, Applied Technology Council (ATC), Washington, DC, USA, 1998.

[BP+03] Bosiljkov, V, Page, AW, Bokan-Bosiljkov, V and Zarnič, R. Performance based studies of in-plane loaded unreinforced masonry walls. *Masonry International*, 16(2):39–50, 2003.

[BP+14] Beyer, K, Petry, S, Tondelli, M and Paparo, A. *Towards displacement-based design of modern unreinforced masonry structures.* Istanbul, Turkey, 2014.

[BS08] Benedetti, A and Steli, E. Analytical models for shear-displacement curves of unreinforced and frp reinforced masonry panels. *Construction and Buildings Materials*, 22:175–185, 2008.

[BT03] Bosiljkov, V and Tomaževič, M. test report, Ljubljana, Slowenia, 2003.

[BT06] Bosiljkov, V and Tomaževič, M. Optimization of shape of masonry units and technology of construction for earthquake resistant masonry buildings. Research report - part three, ZAG, Ljubljana, Slowenia, 2006.

[BT+14] Beyer, K, Tondelli, M, Petry, S and Peloso, S. Dynamic testing of a four-storey building with reinforced concrete and unreinforced masonry walls: Prediction and test results. *Submitted to Bulletin of Earthquake Engineering*, 2014.

[BW58] Benjamin, JR and Williams, HA. The behavior of one-story brick shear walls. In *Journal Struct Division, Proceedings of the American Society of Civil Engineers*, pages 1–30, 1958.

[Cal99] Calvi, GM. A displacement-based approach for vulnerability evaluation of classes of buildings. *Journal of Earthquake Engineering*, 3:411–438, 1999.

[CEN05] CEN. Eurocode 8: Design of structures for earthquake resistance, Part 3: Assessmemt and retrofitting of buildings. Technical Report EN 1998-3, European Committee for Standardisation, Brussels, Belgium, June 2005.

[DHT95] Davies, M, Hughes, T and Taunton, P. Considerations in the small scale modelling of masonry arch bridges. In *Arch bridges*, pages 365–374, London, UK, 1995. Thomas Telford.

[ECA91] Egermann, R, Cook, D and Anzani, A. An investigation into the behaviour of scale model brick walls. In *Proceedings of the ninth international Brick/Block Masonry conferences*, pages 628–635, Berlin, Germany, 1991.

[FM+09] Frumento, S, Magenes, G, Morandi, P and Calvi, GM. *Interpretation of experimental shear tests on clay brick masonry walls and evaluation of q-factors for seismic design.* Technical Report, IUSS PRESS, Pavia, Italy, 2009.

[GM+98] Gruenthal, G, Musson, R, Schwarz, J and Stucchi, M. European macroseismic scale 1998. Technical report, Cahiers de Centre Européen de Géodynamique et de Seismologie, Luxembourg, 1998.

[GT82] Ganz, HR and Thürlimann, B. Versuche über die Festigkeit von zweiachsig beanspruchtem Mauerwerk. Technical Report Test Report 7502-3, ETH Zürich, Zürich, Switzerland, 1982.

[GT84] Ganz, HR and Thürlimann, B. Versuche an Mauerwerksscheiben unter Normalkraft und Querkraft. Technical Report Test Report 7502-4, ETH Zürich, Zürich, Switzerland, 1984.

[GT13] Gams, M and Tomaževič, M. Influence of different types of units and mortars on seismic resistance of masonry walls. In *Proceedings of the 12th Canadian Masonry Symposium*, Vancouver, Canada, 2013.

[HAH86] Hamid, AA, Abboud, B and HG, Harris. Direct small scale modeling of grouted concrete block masonry. In *U.S.-PRC joint workshop on seismic resistance of masonry structures*, Harbin, China, 1986.

[Hey92] Heyman, J. Leaning towers. *Meccanica*, 27:153–159, 1992.

[HM65] Hendry, AW and Murthy, CK. Comparative tests on 1/3- and 1/6-scale models brickwork piers and walls. In *Proceedings of the British Ceramic Society*, volume 4, pages 44–66, 1965.

[Lan02] Lang, K. *Seismic vulnerability of existing structures*. Phd thesis, ETH Zürich, Institute of Structural Engineering, Zürich, Switzerland, February 2002.

[LG06] Lagomarsino, S and Giovinazzi, S. Macroseismic and mechanical models for the vulnerability and damage assessment of current buildings. *Bulletin of Earthquake Engineering*, 4:415–443, 2006.

[Lou96] Lourenço, PB. *Computational strategies for masonry structures*. Phd thesis, Faculty of Engineering, TU Delft, Netherlands, 1996.

[Lou97] Lourenço, PB. *Two aspects related to the analysis of masonry structures: size effect and parameter sensitivity*. Technical report, tu-delft no 03.21.1.31.25/ tno-bouw no 97-nm-r1533, Faculty of Engineering, TU Delft, Netherlands, 1997.

[LR97] Lourenço, PB and Rots, JG. Multisurface interface model for analysis of masonry structures. *Journal of Engineering Mechanics*, 123:660–668, 1997.

[MB14] Mergos, PE and Beyer, K. Loading protocols for european regions of low to moderate seismicity. *Bulletin of Earthquake Engineering*, 2014.

[MC92] Magenes, G and Calvi, GM. Cyclic behaviour of brick masonry walls. In *Proceedings of the 10th world conference on earthquake engineering*, pages 3517–22, Madrid, Spain, 1992.

[MC97] Magenes, G and Calvi, GM. In-plane seismic response of brick masonry walls. *Earthquake Engineering and Structural Dynamics*, 26:1091–112, 1997.

[MDPG05] Modena, F, Da Porto, F and Garbin, F. Ricerca sperimentale sul comportamento di sistemi per muratura portante in zona sismica. Draft 2005/01, University of Padua, Padua, Italy, 2005.

[MH11] Mohammed, A and Hughes, T. Prototype and model masonry behaviour under different loading conditions. *Journal Civil Engineering Public Works Review*, 44:53–65, 2011.

[MHB13] Mihaylov, BI, Hannewald, P and Beyer, K. Three-parameter kinematic theory for shear critical reinforced concrete walls. part i: Formulation. *Submitted to Journal of Structural Engineering*, 2013.

[MM82] Mann, W and Müller, H. Failure of shear-stressed masonry—an enlarged theory, tests and application to shear walls. In *Proceedings British Ceramic Society*, volume 30, pages 223–235, 1982.

[MMP08] Magenes, G, Morandi, P and Penna, A. Enhanced safety and efficient construction of masonry structures in europe, 7.1c test results on the behaviour of masonry under static cyclic in plane lateral loads. Technical Report ESECMaSE D7.1c, University of Pavia, Pavia, Italy, 2008.

[Moh06] Mohammed, A. *Experimental comparison of brickwork behaviour at prototype and model scales*. Phd thesis, Cardiff University, UK, 2006.

[Oro11] Oropeza, M. *Fragility functions for seismic risk in regions with moderate seismicity*. Phd thesis, EPFL, School of Architecture, Civil and Environmental Engineering, Lausanne, Switzerland, September 2011.

[PA90] Paulson, TJ and Abrams, D. Correlation between static and dynamic response of model masonry structures. *Earthquake Spectra*, 6:573–591, 1990.

[PCK07] Priestley, MJN, Calvi, GM and Kowalsky, MJ. *Displacement-Based Seismic Design of Structures*. Pavia, Italy, 2007.

[PLBL11] Pfyl-Lang, K, Braune, F and Lestuzzi, P. Evaluation de la sécurité parasismique des bâtiments en maçonnerie. Technical Report SIA D0237, Documentation, Swiss Society of Engineers and Architects SIA, Zürich, Switzerland, 2011.

[PLG14] Penna, A, Lagomarsino, S and Galasco, A. A nonlinear macroelement model for the seismic analysis of masonry buildings. *Earthquake Engineering and Structural Dynamics*, 43:159–

179, 2014.

[SBG10] Suter, R, Broye, A and Grisanti, M. Essais de cisaillement de murs en maçonnerie renforcesm, serie experimentale mr–a. Technical Report Report Projet de recherche AGP 21´159, Ecole d´ingénieurs et d´architectes de Fribourg, Fribourg, Switzerland, 2010.

[SG10] Suter, R and Grisanti, M. Essais de cisaillement de murs en maçonnerie renforces, serie experimentale mr–b. Technical Report Report Projet de recherche AGP 21´159, Ecole d´ingénieurs et d´architectes de Fribourg, Fribourg, Switzerland, 2010.

[SMS13] Salmanpour, A, Mojsilovič, N and Schwartz, J. Deformation capacity of unreinforced masonry walls subjected to in-plane loading: a state-of-the-art review. *International Journal of Advanced Structural Engineering*, 5:1–12, 2013.

[Tom87] Tomaževič, M. Dynamic modelling of masonry buildings: storey mechanism model as a simple alternative. *Earthquake Engineering and Structural Dynamics*, 15:731–749, 1987.

[Tom07] Tomaževič, M. Damage as a measure for earthquake-resistant design of masonry structures: Slovenian experience. *Canadian Journal of Civil Engineering*, 34:1403–1412, 2007.

[TP$^+$14] Tondelli, M, Petry, S, Peloso, S and Beyer, K. Dynamic testing of a four-storey building with reinforced concrete and unreinforced masonry walls: Data set. *Submitted to Bulletin of Earthquake Engineering*, 2014.

[TV92] Tomaževič, M and Velechovsky, T. Some aspects of testing small-scale masonry building models on simple earthquake simulators. *Earthquake Engineering and Structural Dynamics*, 21:945–963, 1992.

Notations and abbreviations

Capital Latin letters:

E	Elasticity modulus
$F_{2,3}$	Forces of the two vertical actuators after processing
F_1	Force of the horizontal actuator after processing
G	Shear modulus
H	Height of the wall
H_0	Shear span or height of force application
H_{act}	Height between axes of the lateral piston and top of wall
L	Length of the wall
L_{act}	Horizontal distance between both vertical actuators
L_c	Length of the part of the wall which is in compression
M	Moment
N	Normal force
T	Thickness of the wall
T_e	Effective period
V	Lateral force

Small Latin letters:

f_{cB}	Compression strength of the brick parallel to perforation
f_{tB}	Tensile strength of the brick perpendicular to perforation
f_u	Mean compression strength of masonry
k_e	Effective stiffness
m_e	Equivalent mass
m_i	Story mass
u	Displacement
u_e	Elastic displacement
u_f	Displacement due to flexural solicitations
u_s	Displacement due to shear solicitations
u_u	Ultimate displacement

Capital Greek letters:

Δ_d	Target or demand displacement
Δ_i	Story displacement

Small Greek letters:

α	Normalized shear span
δ_e	Elastic interstory drift
δ_H	Interstory drift
δ_{nom}	Nominal drift
δ_u	Ultimate interstory drift
ϵ_{xx}	Horizontal strain
ϵ_{yy}	Vertical strain
γ_{xy}	Shear strain
ψ_{LH}	Factor accounting for the loading history
ψ_{SR}	Factor accounting for the strain rate effects
σ	Stress
σ_0	Average compression stress
σ_y	Vertical stresses, normally perpendicular to bed joints
τ_{xy}	Shear stresses, normally parallel to bed joints

Abbreviations:

AF	Amplification Factor
CT	Cyclic Test
CSM	Capacity Spectrum Method
DB	Displacement-Based
DBD	Displacement-Based Design
DDBD	Direct Displacement-Based Design
EDP	Engineering Demand Parameter
FB	Forced-Based
FBD	Forced-Based Design
LS	Limit State
MDOF	Multi Degree Of Freedom
NC	Near Collapse
PUM	Pier Unit Model
PUP	Pier Unit Prototype
RC	Reinforced Concrete
SD	Significant Damage
SDOF	Single Degree Of Freedom
URM	UnReinforced Masonry

Appendix A

Cyclic test data of six unreinforced masonry walls with different boundary conditions

Petry, S and Beyer, K; *Earthquake Spectra* (2014), DOI: 10.1193/101513EQS269

Abstract

Previous test data on unreinforced masonry walls focused on the global response of the wall. A new dataset on six wall tests, which is publically available, allows linking global to local deformations of masonry walls, which can be useful for advancing performance-based design and assessment methods for unreinforced masonry buildings. This data paper presents the results of a test series on six identical unreinforced masonry walls that were constructed using hollow clay brick units and standard cement-based mortar. The test units were subjected to quasi-static cycles of increasing drift demands and the tests differed with regard to the applied axial load and the moment restraint applied at the top of the walls. The walls were tested up to failure. Throughout the loading the deformations of the walls were recorded using a digital photogrammetric measurement system tracking the movement of 312 points per test unit.

1 Introduction

Performance-based design and assessment methods for unreinforced masonry structures require as input estimates of the drift capacity of masonry walls. Today's codes include only empirical drift capacity models for unreinforced masonry walls (e.g. [CEN05]) which result in significant dispersion of predicted to observed drift capacities [FM$^+$09, PB14]. To promote the use of performance-based design, better drift capacity models are required, which link explicitly the drift capacity of masonry walls based on assumed mechanisms and local deformation limits. Such models exist since several decades for reinforced concrete and steel structures (e.g. plastic hinge models with material strain limits, [PCK07]). To develop such models, test data for local and global deformation quantities are required. This paper presents such data for six unreinforced masonry wall tests.

2 Test objectives

When compared to previous tests on masonry walls (e.g. [GT84, VRJ93, BP$^+$03, MMP08, SMS13, GT13]), the tests series presented here is unique with respect to the following two aspects. First, all previous tests investigated only walls tested under a centric constant axial load with double-fixed or cantilever boundary conditions (which correspond to shear spans H_0 equal to 0.5 and 1.0 times the wall height H), while this series investigates a larger range of shear spans (H_0 = 0.5, 0.75 and 1.5H) and three axial load ratios. To the knowledge of the authors, the only wall that had been subjected to boundary conditions different to double-fixed or cantilever was test unit W4 by Ganz and Thürlimann [GT84], who studied the wall behavior under a constant axial load at a constant eccentricity and monotonically increasing horizontal displacement. Second, the tests are unique with regard to the local deformations recorded. A grid of four LEDs per full brick whose positions were recorded continuously by a digital photogrammetric measurement system allows computing the average strain sensor for each brick and crack width of all joints during loading. Salmanpour et al. [SMS13] and Gams and Tomaževič [GT13] used digital image correlation (DIC) for measuring local deformations of URM walls. The advantage of the LED-based system relates to the much smaller file size for one measurement frame allowing hence a larger measurement frequency.

3 Organization of the paper

The paper outlines the test program, the geometry and material test data of the six masonry walls, the instrumentation and the loading protocol. It describes the observed behavior and the recorded data. Two sets of data are provided: The first set or unprocessed data corresponds to the rawdata of the conventional and optical measurement data, which were recorded at different frequencies. In the second set of data (processed data), the optical measurement data was smoothed to remove inherent noise, the coordinate system was rotated to align the measurement axes with the axes of the test unit and the data synchronized with the data of the conventional instruments. The second set of conventional data has been carefully processed to remove any bias or data that is not linked to the actual behavior of the test data (e.g. offsets because conventional instruments were moved during testing). It also includes a number of additional channels computed from recorded channels such as the total applied axial force, the top and bottom moment of the walls and the average drift. This data is provided to allow potential users of the data to quickly evaluate the global response of the walls.

4 Test program and test setup

The experimental campaign comprised six tests on masonry walls that all had the same dimensions (H = 2.25 m, L = 2.01 m, T = 0.20 m). The walls were named PUP1–6 and represented the first story of an unreinforced masonry wall in a four-story building with reinforced concrete slabs [PB14]. The moment, axial force and shear force at the top of the walls were introduced by three actuators (Fig. 1). All actuators had a force capacity of ±1000 kN and a displacement capacity of ±500 mm. The distance between the axes of the two vertical cylinders was L_{act} = 2.4 m and the distance of the horizontal cylinder to the upper edge of the wall H_{act} = 0.275 m. The vertical actuators were controlled in such a way that the axial force applied to the wall during testing remained constant [WB11]. In addition, for PUP1 the vertical actuators maintained a zero rotation of the loading beam representing therefore double-fixed boundary conditions. For PUP2–5 the control of the vertical actuators was coupled to the force of the horizontal actuator in such a manner that the shear span H_0 remained constant throughout the test. In external walls of URM buildings the axial load N and the shear span H_0 depend on the loading direction, e.g. Petry and Beyer [PB14]. When the structure is loaded towards the considered external wall, N and H_0 increase and when loading of the structure is reversed, N and H_0 decrease. If these loading directions are regarded separately, PUP4 and PUP5 represent an external wall, once on the compression side and once on the tension side of the structure. In order to investigate the influence of varying axial force N and shear span H_0 of external walls on their force-displacement response, we defined N and H_0 of PUP6 as linear functions of the applied horizontal force F_1 using following formula:

$$N = \frac{N_{max} + N_{min}}{2} - F_1 \cdot \frac{N_{max} - N_{min}}{F_{1,max} - F_{1,min}} \tag{1}$$

$$N = \frac{H_{0,max} + H_{0,min}}{2} - F_1 \cdot \frac{H_{0,max} - H_{0,min}}{F_{1,max} - F_{1,min}} \tag{2}$$

where N_{max} = -619 kN, N_{min} = -219 kN, $H_{0,min}$ = 0.75H and $H_{0,max}$ = 1.5H correspond to the boundary conditions of PUP4 and PUP5, while $F_{1,max}$ = -$F_{1,min}$ = 133 kN was determined as the average of the lateral force capacities obtained from PUP4 and PUP5. Table 1 summarizes the applied axial load, the shear span and the equations for the control of the vertical actuators.

The masonry walls were constructed on steel plates that had been prepared by gluing a layer of quartz sand (d =1–3 mm) onto the steel plate (Figs. 2a and b). After waiting for at least 28 days (age at the day of testing: see Table 2) a layer of 5–10 mm cement mortar was added on top of the wall and another steel plate, which had been prepared in the same manner as the bottom steel plates, together with the loading beam were placed on top of the wall. The wall was prestressed vertically and then transported by crane to the test stand (Fig. 2c). In the test stand the bottom steel plate was bolted to a concrete foundation which remained fixed to the laboratory's strong floor. The prestress applied for transportation was removed after application of the axial stress (LS0 to LS1) and before the LS1 measurements were taken. Nevertheless, the applied prestress was only a small fraction of the stress applied during LS0 to LS1 and should have no influence on the LS0 measurements.

For the optical measurement, the walls were prepared as follows: (1) first a grid was drawn on the naked walls; (2) then small adhesive stickers were glued at each grid point in order to

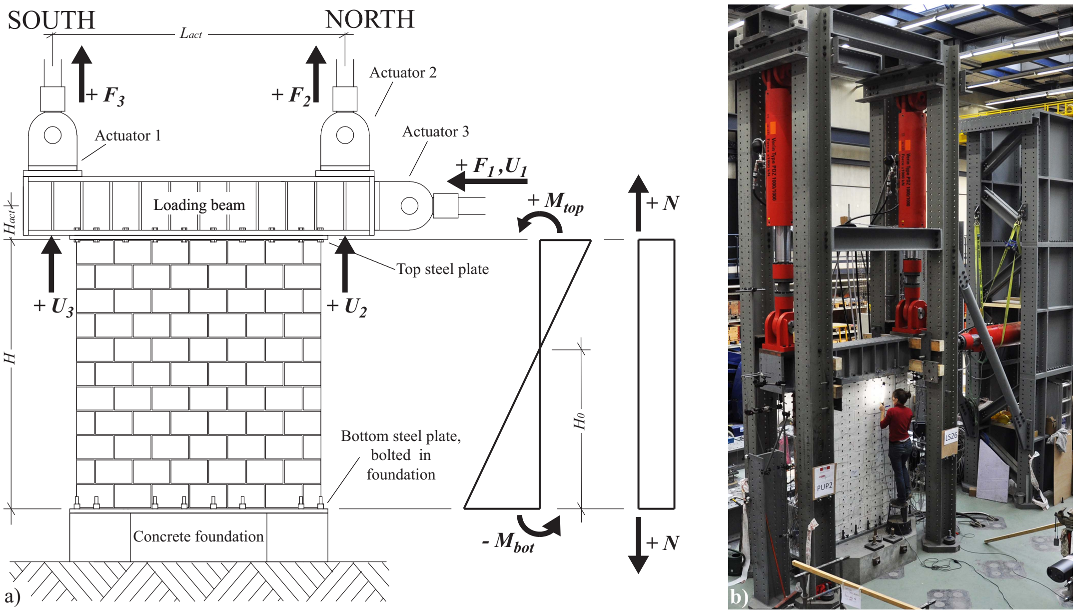

Figure 1. (a) Test setup with sign conventions after processing and (b) photo showing the test setup with the three actuators

Figure 2. (a) Steel plates with layer of quartz sand, (b) test units during construction and (c) transportation of test unit to test stand

indicate the positions of the LEDs; (3) the walls were painted white in order to improve the visibility of cracks during testing and the adhesive sticker were removed immediately after painting as long as the paint remained wet, leaving thus a small area (Ø = 1.9 cm) of naked brick surface; (4) cleaned and sandblasted steel discs (Ø = 2.0 cm) were glued directly onto the brick using a plasticine glue; (5) the plastic feet of the LEDs were fixed onto the steel discs using a hot-melt adhesive. After the test, the LEDs were removed from the plastic feet and reused. The aluminum supports of the linear variable differential transformer (LVDTs) at the short sides of the walls were fixed directly to the brick surface with a plasticine glue (the short sides of the walls remained unpainted for this reason, see Fig. 2c).

5 Material test data

The masonry walls were constructed using Swiss hollow clay brick units and the standard cement mortar WEBER MUR MAXIT 920. The brick units had dimensions of 300 x 190 x

Table 1. Test program

Specimen	Axial force N	Axial stress ratio σ_0/f_u	Shear span H_0	Equations for control of vertical actuators
PUP1	-419 kN	0.18	$0.5H$	Actuator 2: $F_2 = N - F_3$ Actuator 3: $U_3 = U_2$
PUP2	-419 kN	0.18	$0.75H$	Actuator 2 & 3: $F_{2,3} = \frac{N}{2} \pm c \cdot F_1$
PUP3	-419 kN	0.18	$1.5H$	
PUP4	-619 kN	0.26	$1.5H$	
PUP5	-219 kN	0.09	$0.75H$	
PUP6	-619 kN	0.26	1.5H	Actuator 2 & 3: $F_{2,3} = \frac{N}{2} + c_1 \cdot F_1 \pm c_2 \cdot F_1^2$
	-219 kN	0.09	$0.75H$	

H	Height of the wall
H_0	Shear span
$F_{2,3}$	Forces of the two vertical actuators
F_1	Force of the horizontal actuator
$U_{2,3}$	Vertical displacement of the two vertical actuators with respect to the ground
c	Constant describing the dependency between $F_{2,3}$ and F_1 which determines the moment profile. The value of this constant depends on H_0 and the geometry of the test setup.
c_1 and c_2	Constants describing the dependency between $F_{2,3}$ and F_1 including the variation of the shear span H_0 and the axial load N for PUP6.

195 mm ($L_B \times H_B \times W_B$, Fig. 3). The geometric and mechanical properties of the units are summarized in Table 3. Bed and head joints were fully mortared and had an average thickness of 10 to 12 mm. Mortar samples were taken while constructing walls and wallettes for material tests. The mortar samples were tested when testing the corresponding walls and wallettes. The mortar properties for all types of specimen are summarized in Table 4.

To determine the material properties of the masonry, three types of standard material tests were conducted (Fig. 4): (1) the compression strength, elasticity modulus and Poisson's ratio were determined with compression tests (WUP1–5) on masonry wallettes [CEN02], (2) the peak shear strength and residual shear strength of the mortar brick interface were determined with shear tests (TUP1–10) on masonry triplets [CEN07] and (3) the diagonal tensile strength

Table 2. Age at testing of the specimen for the compression tests (WUP), for the diagonal compression tests (QUP), for the shear tests (TUP) and for the six quasi-static cyclic tests on walls (PUP1–6)

	WUP	QUP	TUP	PUP1	PUP2	PUP3	PUP4	PUP5	PUP6	
Age at testing	169	206	50	40	73	104	112	122	135	days

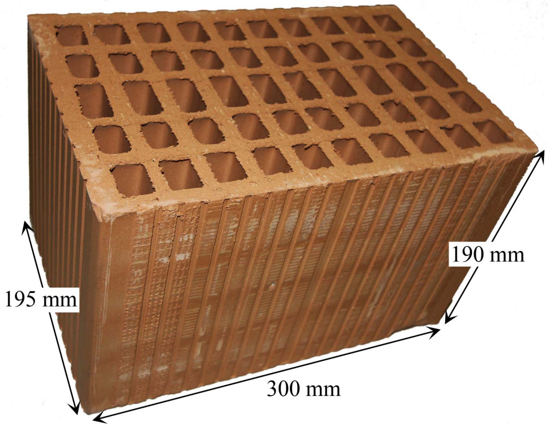

Figure 3 Investigated clay brick with average dimensions

Table 3. Derived brick and masonry properties

Brick properties			
Compression, ‖ to perforation	$f_{B,c,\parallel}$	35.0 ± 7%	MPa
Compression, ⊥ to perforation	$f_{B,c,\perp}$	9.4 ± 8%	MPa
Flexural tensile, ⊥ to perforation	$f_{B,ft}$	1.27 ± 38%	MPa
Masonry properties			
Compression strength	f_u	5.87 ± 5%	MPa
E-modulus	E	3550 ± 9%	MPa
Poisson ratio	ν	0.20 ± 19%	-
Peak strength	τ_{peak}	$0.94\sigma + 0.27$	
Residual strength	τ_{res}	0.91σ	
Diagonal tensile strength	f_t	0.50 ± 10%	MPa

was determined with diagonal compression tests (QUP1–5) on square masonry wallettes [RIL91]. Figures 5 to 7 show for each material test a photo of a specimen and the test results. The mean masonry properties and coefficients of variation are summarized in Table 3. The data from material tests are provided together with the data of the wall tests. The organization of all data is described in Section ”Test data”.

Note that the LVDTs indicated in Fig. 4c were only used for the first five triplet tests (TUP1–5), while for the test units TUP6–10 only the forces were recorded. Out of the ten triplet units, two units (TUP1 and TUP9) provided unreasonable results (the axial stress which we applied was too high and the bricks fractured before sliding in the joints could occur). These two units were omitted when computing residual and peak strength and are not shown in Fig. 6b.

6 Instrumentation

The test units (PUP1–6) were instrumented with 42 conventional channels, which were recorded at a frequency of 1 Hz. Next to global quantities (forces applied by actuators, displacements of top beam) some local deformations were measured with LVDTs and omega gauges. The locations of the conventional instruments and the base lengths (for instruments measuring local deformations) are indicated in Fig. 8. The sign convention for the actuator forces and displacements of the top beam are also included in Fig. 1. The exact position of the

Table 4. Mortar properties corresponding to the mortar used for the construction of the specimen (WUP) for the compression tests, (QUP) for the diagonal compression tests, (TUP) for the shear tests and (PUP1–6) for the six quasi-static cyclic tests on walls

		WUP	QUP	TUP	PUP1	PUP2	PUP3	PUP4	PUP5	PUP6	
Compression strength $f_{M,c}$	Mean	10.5	14.5	13.3	8.99	9.75	12.0	11.7	9.87	9.02	MPa
	Std. dev.	11	7	13	11	20	11	10	15	7	%
Flexural tensile strength $f_{M,ft}$	Mean	2.37	3.74	2.98	2.54	2.35	2.73	2.66	2.56	2.13	MPa
	Std. dev.	15	9	22	13	21	22	27	25	21	%

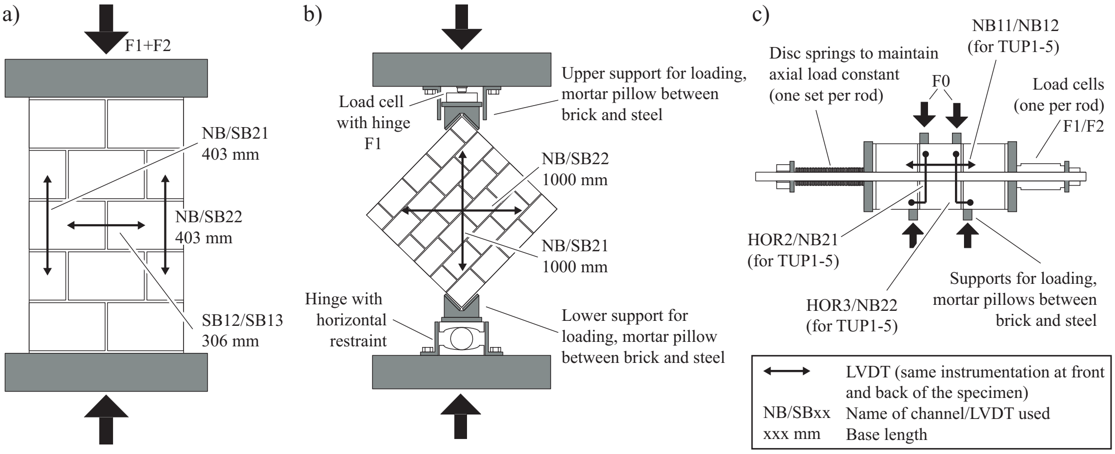

Figure 4. Test setups for the material tests

instruments U3, V3, U2 and V2 (Fig. 8) varied between walls and the horizontal distance from the instrument to the outer edge of the wall is specified in Table 5.

The optical measurements were performed with the commercially available system Optotrak from NDI (Optotrak Certus HD [NDI11]). The photogrammetric system worked with two position sensors consisting each of three digital cameras (see Fig. 9a), which measured the 3D-coordinates of LEDs (see Fig. 9b) glued onto the test unit, foundation and loading beam (see Fig. 10). During each measurement frame all LEDs illuminate one after each other and thus the positioning sensors recorded the x-, y- and z-coordinates of each LED with a measurement frequency of 2 Hz (PUP1) or 4 Hz (PUP2–6). This system or a similar system that is based on the same principals has been used in several test campaigns, for example on reinforced concrete walls and columns [LL$^+$12, GKN13], but to our knowledge so far only on

Table 5. Distances defining the location of the conventional measurement devices U2, U3, V2 and V3 (Fig. 8)

Distance	Channel number	Unit	PUP1	PUP2	PUP3	PUP4	PUP5	PUP6
d_{U2}	5	mm	75	205	218	150	145	147
d_{U3}	7	mm	75	230	218	155	140	140
d_{V2}	9	mm	45	150	150	230	250	254
d_{V3}	10	mm	45	150	150	234	257	270

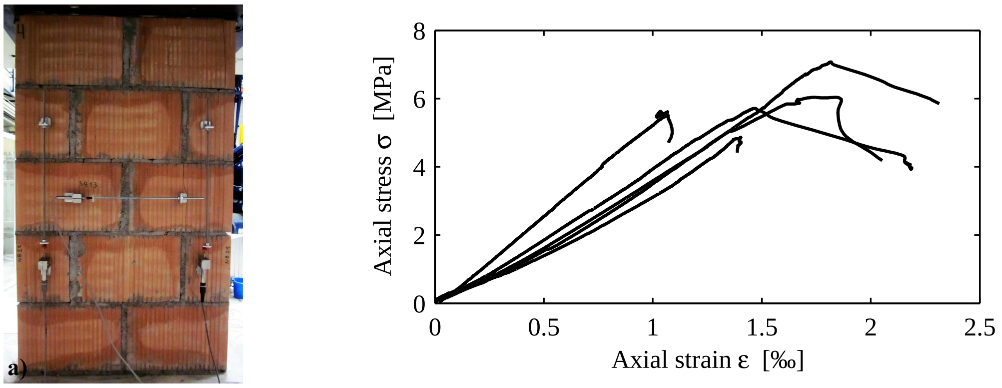

Figure 5. (a) Specimen for the compression tests with mounted measurement devices and (b) stress-strain relationships

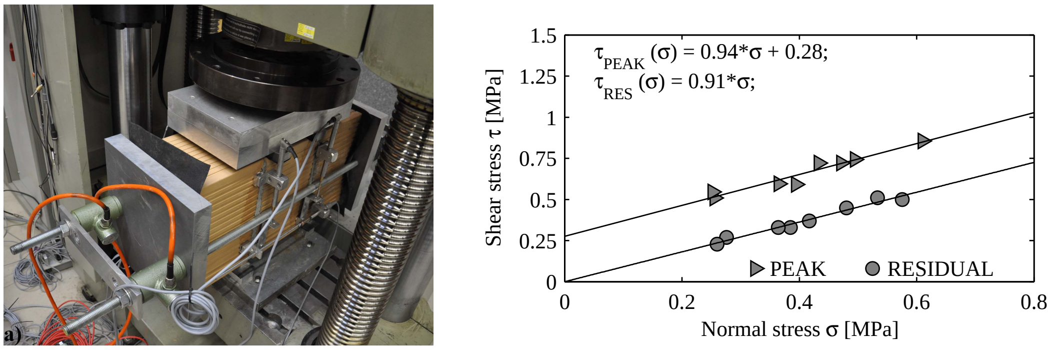

Figure 6. (a) Test setup for the shear tests with specimen and (b) applied normal stress versus resulting peak and residual shear strength of the mortar brick interface

masonry spandrels Beyer et al. [BD12a, BD12b] and not on masonry walls.

Both systems used for the optical and conventional measurement worked independently from each other. In order to synchronize them we used the so-called ”NDI-channel”. This channel sent a voltage signal from the optical measurement system to the conventional measurement system when the optical measurement system was recording data. The synchronization itself was done after the test during the post-processing phase with the help of a self-written Matlab script.

7 Testing procedure

All tests were performed applying the following procedure (Fig. 11): (0) Zero measurements were taken before any of the three actuators was connected to the test unit (load step LS0). (1) The vertical actuators were fixed to the loading beam at the top of the wall. (2) The axial force was applied by means of an identical force in both vertical actuators (LS1, $F_{2,3} = N/2$). The resulting axial force acted therefore at the center line of the wall. (3) The horizontal actuator was connected to the loading beam. (4) The control functions for the vertical actuators were changed to the control functions indicated in Table 1. (5) The lateral loading history was started (LS2 – end). A load step of the drift controlled loading history corresponds to the peak of one half-cycle. At each load step, the loading was stopped, cracks were marked and photos were taken. During this period the conventional instruments were continuously recorded. The

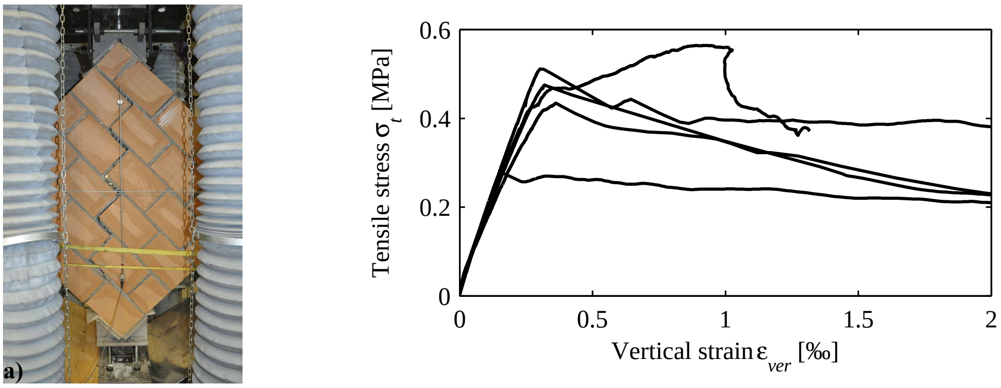

Figure 7. (a) Specimen for the diagonal compression tests with typical stair stepped crack along mortar joints and (b) stress-strain relationships

LEDs were only recorded for a period of approximately two minutes just before the test unit was unloaded (see Fig. 11). The loading velocity was chosen in such a way that loading from one peak to the next took between 10 to 30 min. All tests lasted for two to three days. Each evening all three actuators were unloaded in such a way that first the horizontal actuator was stopped between two loadsteps ($F_1 \approx 0$ kN) and then the axial load was removed until $F_{2,3} \approx 0$ kN. During the night the actuators were switched off, but remained fixed to the test unit. The next day the axial load was reapplied ($F_2 = F_3$) and horizontal loading continued. Care was taken that the actuators were not switched off between peak load and horizontal load failure. The amplitudes of the half-cycles corresponded to the following drift levels: 0.025%, 0.05%, 0.1%, 0.15%, 0.2%, 0.3%, 0.4%, 0.6%, 0.8% and 1.0% (see Fig. 11). Note that the cycles with amplitudes of 0.15% and 0.25% were not included in the loading history applied to PUP1, but added from PUP2 onwards since the performance of PUP1 deteriorated rapidly within the cycles with amplitudes of 0.2% and 0.3%.

8 Test observations and summary of results

8.1 Test observations

In the following we summarize the most important observations during testing. All cracks were marked on the walls and the crack tip annotated with the load step number. Photos were taken at all load steps and at zero load in between load steps and are provided along with the test data (for the organization of the data and photo see Section ”Test data”). The first wall, PUP1, was tested under double-fixed boundary conditions. Hence, the shear span was at approximately $0.5H$. During the cycle with a nominal drift of 0.2%, the horizontal actuator was not stopped in time and the wall was accidentally loaded up to a drift of 0.3%. After a second full cycle of 0.2%, the wall collapsed before reaching again a drift of 0.3%. The crack pattern developed as follows: the first horizontal cracks in the joints at the top and the bottom of the wall appeared already during the cycles of 0.025% and 0.05% peak drift. The first diagonal cracks formed during the cycles of 0.1% peak drift and developed for both directions in form of two or three parallel stair stepped cracks through the mortar joints. At this stage, all cracks closed again when the loading was reversed. At the onset of strength degradation, i.e. after the peak strength was reached, the deformations started to concentrate in one diagonal crack, which did no longer close when the loading was reversed. This phenomenon developed in both loading directions and it was observed that axial load failure was provoked through the

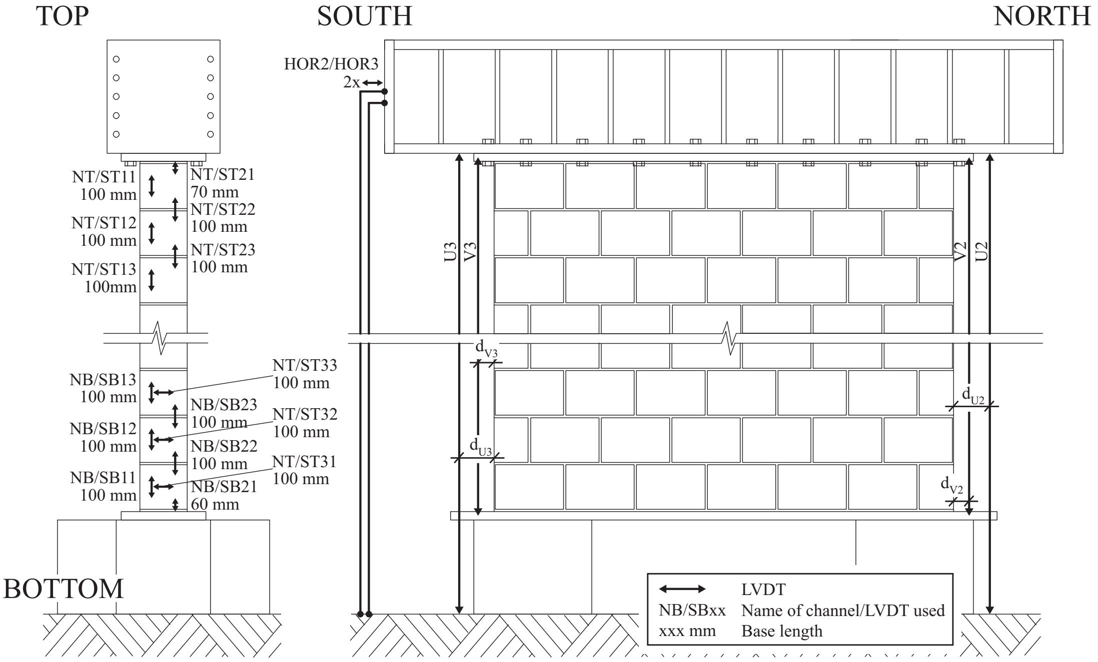

Figure 8. Location of the conventional measurement devices

continuous deterioration of the zone where the diagonal cracks intersected (see Fig. 12a).

The second wall, PUP2, was tested with a shear span of $0.75H$. The cracks developed in a similar fashion as in the first wall. The first cracks to appear were horizontal cracks in the joints of both bottom corners. Unlike for PUP1, however, the top part of the wall remained uncracked during the small amplitude cycles as the top moment was smaller than the bottom moment. With increasing drifts, the horizontal cracks grew in length and width and spread over an increasing height of the wall. At a drift of 0.1%, the first diagonal cracks appeared as two or three parallel stair stepped cracks. When the lateral resistance dropped, the deformations for each loading direction, as for PUP1, concentrated in one diagonal crack and the axial load failure was caused by a continuous deterioration of the zone where the two diagonal cracks intersected (see Fig. 12b). When compared to PUP1, the first stair stepped cracks which appeared in PUP2 were steeper (3:2 ≈ ver:hor) and turned with further displacement demand into a diagonal crack. Finally, the deformations started concentrating along one diagonal crack and a quite similar crack pattern was obtained at axial load failure for PUP2 and PUP1 (compare Figs. 12a and b).

The third wall, PUP3, was tested with a shear span of $1.5H$. PUP3 showed up to a drift of ±0.4% a behavior dominated by flexural deformations. The deformations concentrated in the bed joints and the cracks extended over almost the entire height of the wall. First stair stepped cracks appeared only at drifts of ± 0.4%. The bottom corner started crushing, before the deformations could concentrate in one diagonal crack, as it was observed for PUP1 and PUP2. The drop of lateral resistance was caused by the deterioration of these corners. Finally, axial load failure was provoked by the crushing of the central bricks at about one quarter of the height of the wall (see Fig. 12c).

For the fourth wall, PUP4, the normal force was increased by around 50% to -619 kN. The

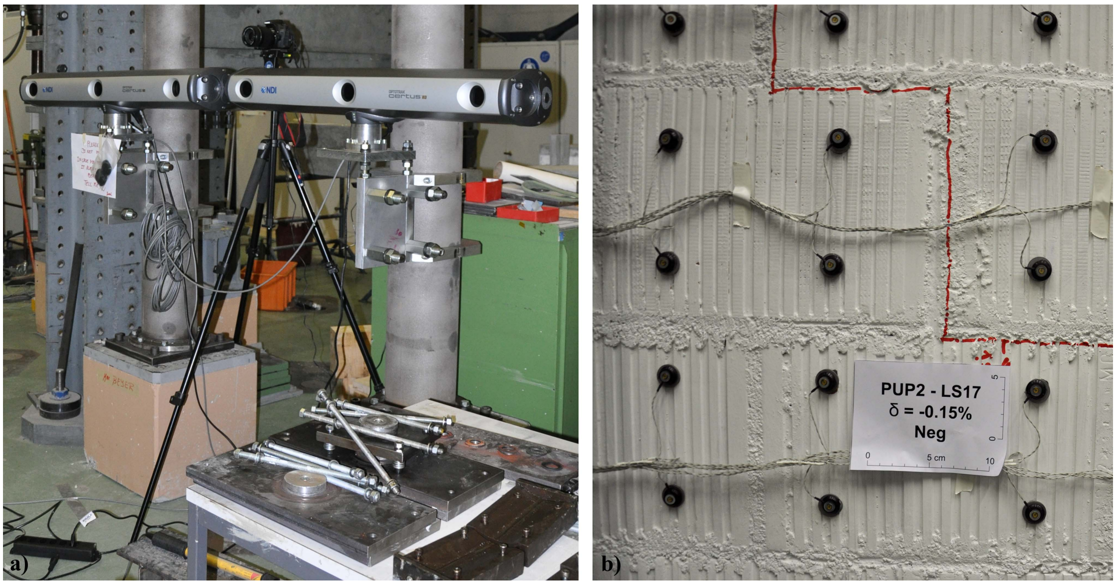

Figure 9. Measurement device used for the optical measurement system: (a) two position sensors consisting each of three cameras and (b) LEDs glued onto the masonry wall

shear span was kept constant at approximately $1.5H$. PUP4 showed first a typical flexural behavior and, as for PUP3, the deformations concentrated mainly in horizontal cracks, which spread over almost the entire height of the wall. Diagonal cracks appeared first at the bottom of the wall at a nominal drift of 0.15%. At a nominal drift of 0.25%, vertical splitting cracks appeared at both bottom corners leading to the successive failure of the brick from the outer edge inwards. Axial load failure seemed to be caused by the continuous deterioration of the areas where vertical splitting cracks and diagonal cracks from both directions intersected (see Fig. 12d).

For the fifth wall, PUP5, the normal force was decreased by around 50% of the load applied to PUP1–3 to -219 kN and the shear span was $0.75H$. At the end of the cycle with drift amplitude 0.6% (at LS37) the hydraulic system accidentally lost its pressure, which caused a sudden release of force in all three actuators (see last loop in Fig. 13f). After reloading in the positive direction (towards LS38 with a nominal drift of +0.8%), a significant residual drift remained. However, a significant drop in lateral force resistance was observed before (at LS37). The crack pattern developed as follows: the first horizontal cracks appeared during the cycles of 0.05% nominal drift in the base joint of the wall. The first stair stepped cracks formed during the cycles of 0.15% nominal drift. With further loading, more and more diagonal stair stepped cracks appeared, while the flexural deformations remained concentrated in horizontal cracks in the lower half of the wall. For both loading directions the lateral force dropped by more than 20% during the cycles of 0.6%; this was also the cycle when deformations started to concentrate in one diagonal crack (see Fig. 12e).

The sixth wall, PUP6, was subjected to an asymmetric loading since the normal force and shear span were linearly dependent of the applied horizontal force during testing (see Eqs. (1) and (2)). In the negative direction, the boundary conditions approached those of PUP4 and in the positive direction those of PUP5. In both directions, first stair stepped cracks appeared during the cycles of 0.1% drift. In the positive direction, further parallel stair stepped

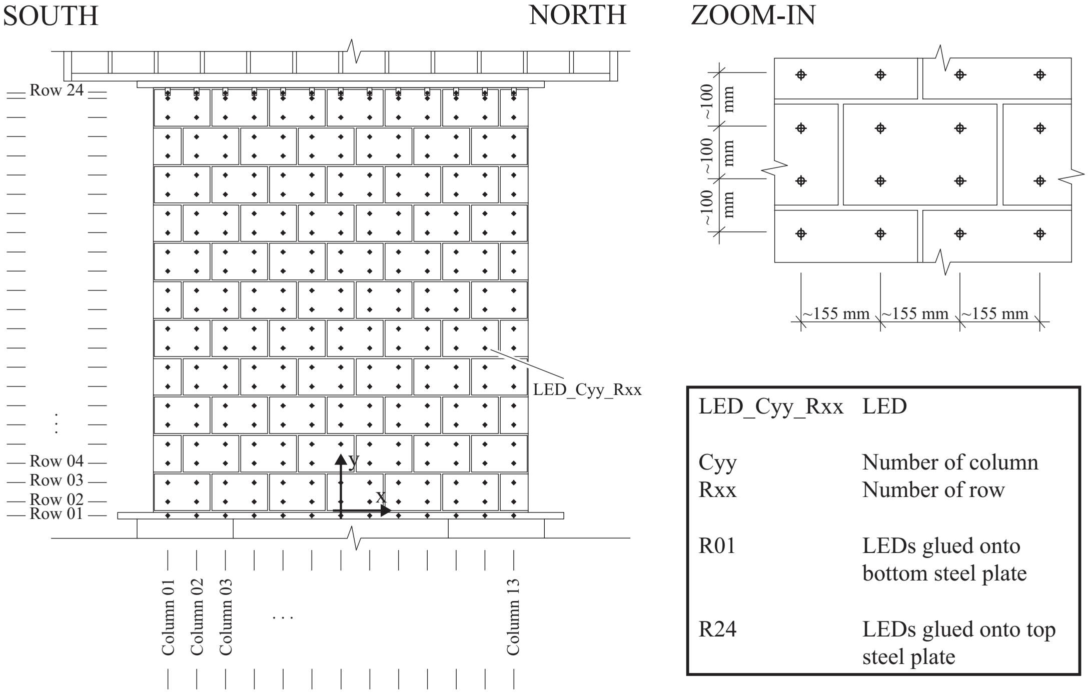

LED_Cyy_Rxx	LED
Cyy	Number of column
Rxx	Number of row
R01	LEDs glued onto bottom steel plate
R24	LEDs glued onto top steel plate

Figure 10. Positions of the LEDs for the optical measurement

cracks appeared during the cycles of 0.15–0.25% peak drift. In the negative direction, the behavior was dominated by vertical splitting cracks at the compressed corner which started to form during cycles with 0.2% nominal drift. While loading from a nominal drift of +0.25% (LS24) to -0.25% (LS25), the loading was accidentally started in the wrong direction. When this was noted, the applied drift was already +0.35% and loading was stopped immediately and reversed towards -0.25% (LS25). During the cycles with a nominal drift of 0.8%, the deformations started concentrating along one diagonal crack when loading in the positive direction, while in the negative direction vertical splitting cracks developed now over the entire height of the wall (see 12f). A significant horizontal failure was attained while loading towards LS42 (nominal drift of 1.0%) thus, it was decided to change loading direction before the axial load failure could occur in the same direction. Accordingly, horizontal and axial load failure occurred for the negative loading direction during cycles with ±0.8%. Note that these limit state drifts are approximately twice as large as those of PUP4.

8.2 Summary of results

The force-displacement hysteresis obtained from the optical and conventional measurement devices are shown in Fig. 13. For the optical measurements, the horizontal displacements of LEDs glued onto the top steel plate were averaged (see row 24 in Fig. 10), while the conventional displacement was measured at mid-height of the top beam (see position HOR2/3 in Fig. 8). Hence, small differences can be noticed for large rotations of the top beam (e.g. PUP4). Figure 14 shows the moments at the top and bottom against the top rotation of the walls. Apart from PUP6 (see Section ”Test program and test setup”), the ratio of top to bottom moment remained constant throughout one test. Failure modes, peak load and drift at peak load, horizontal failure and maximum drift are summarized in Table 6. A comparison with a

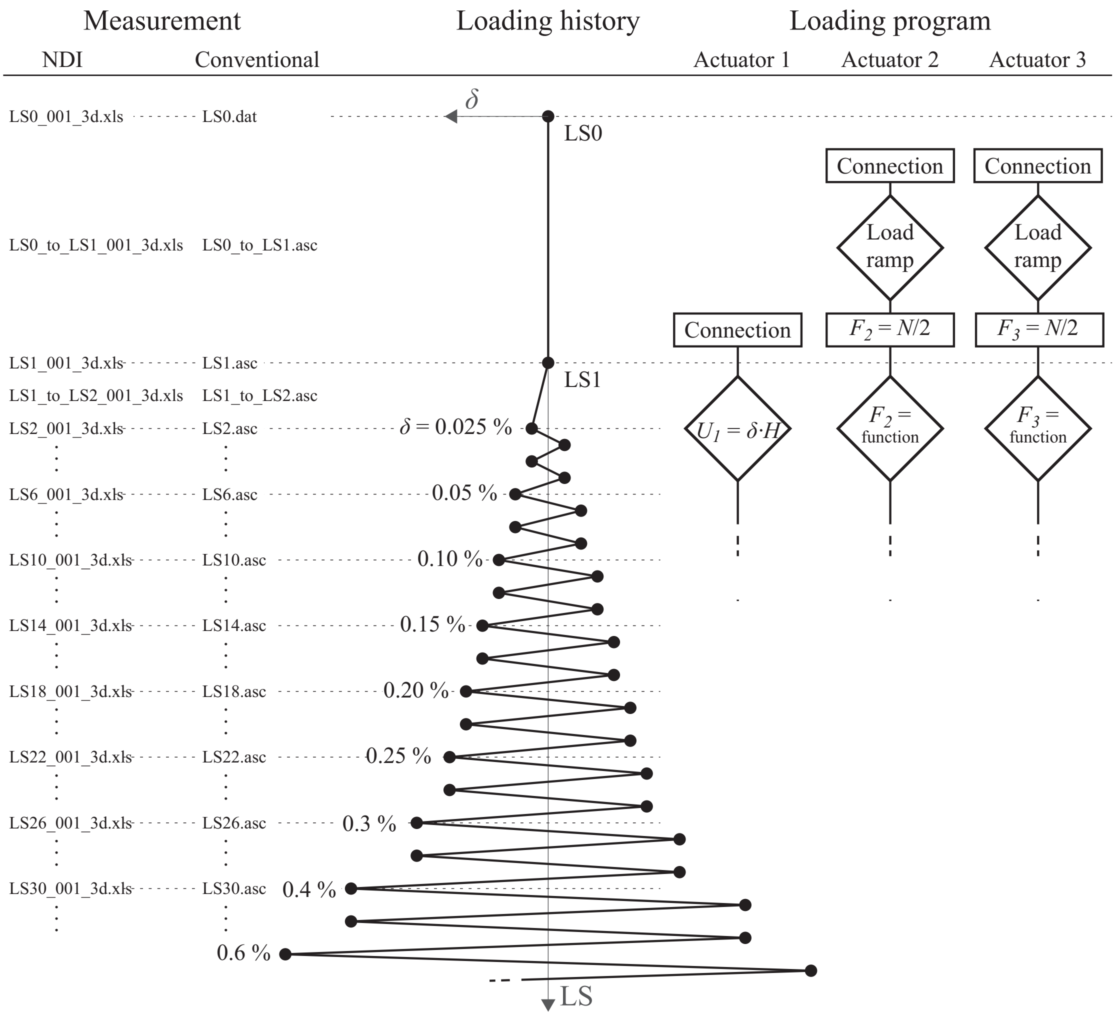

Figure 11. Testing procedure

database of 64 tests can be found in Petry and Beyer [PB14].

9 Test data

9.1 Organization of data

The data can be downloaded as one zip file from www.zenodo.org using the DOI 10.5281/zenodo.8443 (10 files of 0.98–1.3 GB). The platform ZENODO (www.zenodo.org) was developed under the European FP7 project (http://www.openaire.eu/) and is hosted by the research facility CERN which operates a Large Hadron Collider.

Upon unzipping, the folder structure unfolds as follows (Fig. 15): The data is organized first by specimen (PUP1–6 for the six walls, QUP for the diagonal compression tests, TUP for the triplet tests and WUP for the compression tests). For each wall specimen there are three subfolders (”photos”, ”unprocessed_data” and ”processed_data”) and for each type of material tests two subfolders (”unprocessed_data” and ”processed_data”). The following sections outline the organization of the data within the individual folders and the processing applied to the data. Each wall folder contains one file ”Metadata_conventional_channels.xls” which

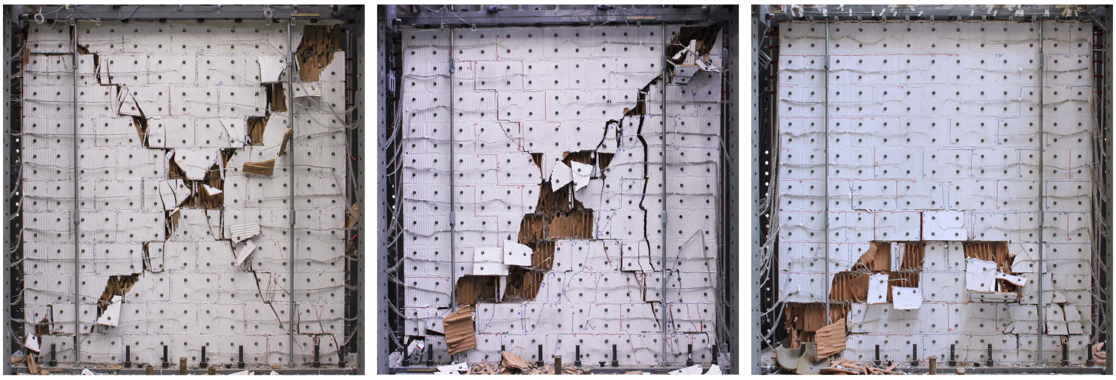

a) PUP1: $H_0/H = 0.5$, $N = -419$ kN **b) PUP2**: $H_0/H = 0.75$, $N = -419$ kN **c) PUP3**: $H_0/H = 1.5$, $N = -419$ kN

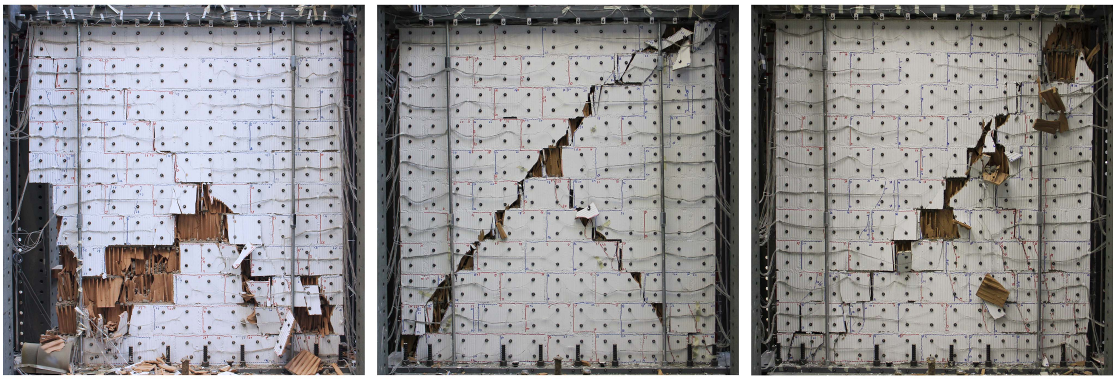

d) PUP4: $H_0/H = 1.5$, $N = -619$ kN **e) PUP5**: $H_0/H = 0.75$, $N = -219$ kN **f) PUP6**: $H_0/H = var.$, $N = var.$

Figure 12. Picture of all six walls when they could no longer sustain the applied axial load

contains information on all instruments used (type of instrument, producer, measurement range, measurement unit, base length for displacement measurements, sign convention).

9.2 Photos

In addition to the data from conventional and optical measurements, photos are used to document the damage to the walls. Photos were taken at each load step, i.e. at peak displacements. These photos are labeled with ”LSxx.JPG” where xx stands for the load step (see Fig. 11 for the numbering of the load steps). To document the residual damage at zero horizontal force when passing from one load step to the other, the loading was shortly stopped for PUP2–6 when reaching $F_1 \approx 0$ kN. The photo at $F_1 \approx 0$ kN between load steps xx and xx+1 is labeled ”LSxx_to_LSxx+1.JPG”.

During testing, the cracks were traced using blue and red pens in order to render the cracks visible on photos. Cracks that were noticed for the first time at load steps in the positive loading direction (LS2, LS4, ...) were marked with a blue line and cracks that were noticed for the first time at load steps in the negative direction (LS3, LS5, ...) were marked in red. Cracks that appeared in the base joint during transportation or while fixing the bottom steel plate to the concrete foundation are marked and are annotated with 0. Such cracks appeared for PUP3–6 but they remained limited to hairline cracks extending only over a small part of the wall length.

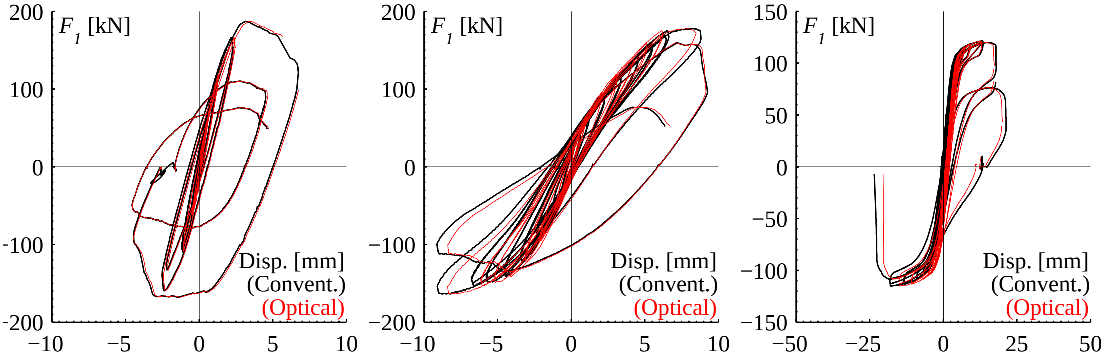

a) **PUP1**: $\sigma_0/f_u = 0.18$; $H_0 = 0.5H$ b) **PUP2**: $\sigma_0/f_u = 0.18$; $H_0 = 0.75H$ c) **PUP3**: $\sigma_0/f_u = 0.18$; $H_0 = 1.5H$

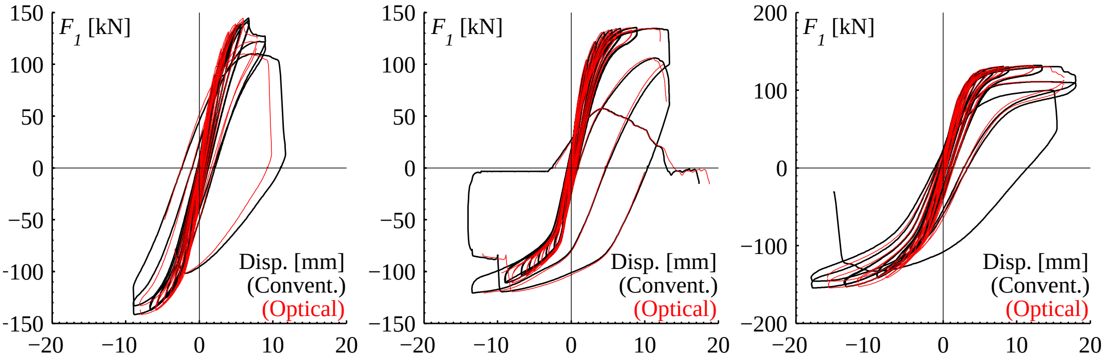

d) **PUP4**: $\sigma_0/f_u = 0.26$; $H_0 = 1.5H$ e) **PUP5**: $\sigma_0/f_u = 0.09$; $H_0 = 0.75H$ f) **PUP6**: $\sigma_0/f_u =$ var.; $H_0 =$ var.

Figure 13. Displacement-force hysteresis; x-axes: CH2 and y-axes: CH45 in black and CH55 in red with LS1 as reference

9.3 Unprocessed data

The unprocessed data contains the original files recorded during the testing of the walls. The folder "unprocessed_data" contains two subfolders "conventional" and "optical".

9.3.1 Conventional measurement data

The conventional measurements were recorded using the system "CATMAN" [HBM00] and the files contain the unmodified output files of this system. They comprise the actuator forces (F_1, F_2 and F_3), the voltage channel "NDI-channel" (see Section "Instrumentation"), the measurement from the internal displacement transducer of actuator 1 (U1), the measurements from the external displacement transducers (U2, U3, HOR2, HOR3, V2 and V3) and the local displacement measurements at the corners of the wall (NB11 to ST33), see Fig. 8. The voltage channel "NDI-channel" was exported from the NDI system and indicated when the optical measurement system was recording. The conventional measurement system was always started before and stopped after the optical measurement system and this voltage signal was therefore used to synchronize the two measurement systems. The folder "conventional" stores the following types of files, which are all ascii-files: The files containing the measurement during loading are labeled "LSxx_to_LSxx+1.asc". While holding the position at one load step, the data was written to a file labeled "LSxx.asc". When loading was interrupted during the night, the files labeled "LSxx_to_unload.asc" and "Restart_to_LSxx+1.asc" contain the corresponding half loadstep with the unloading/reloading part.

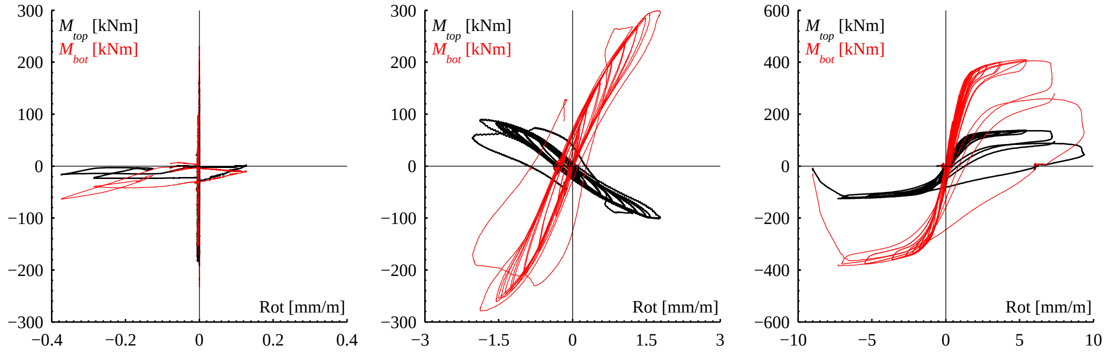

a) **PUP1**: $\sigma_0/f_u = 0.18$; $H_0 = 0.5H$ b) **PUP2**: $\sigma_0/f_u = 0.18$; $H_0 = 0.75H$ c) **PUP3**: $\sigma_0/f_u = 0.18$; $H_0 = 1.5H$

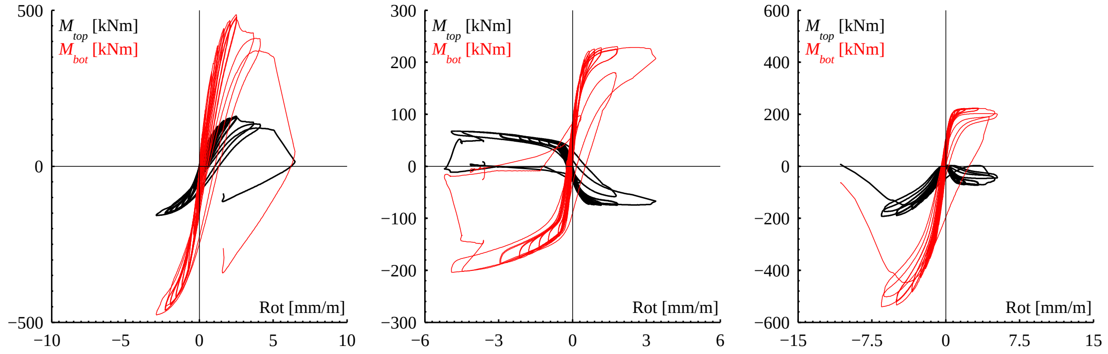

d) **PUP4**: $\sigma_0/f_u = 0.26$; $H_0 = 1.5H$ e) **PUP5**: $\sigma_0/f_u = 0.09$; $H_0 = 0.75H$ f) **PUP6**: $\sigma_0/f_u =$ var.; $H_0 =$ var.

Figure 14. Top rotation-top moment hysteresis; x-axes: CH50 and y-axes CH47 in black and CH48 in red with LS1 as reference

9.3.2 Optical measurement data

The folder ”optical” contains the output of the NDI measurement system. For each recording sequence a separate folder was created which stores the NDI-specific file formats (raw data and sensor settings) and the measurement data exported to Excel. The folders are named ”LSxx_to_LSxx+1” for measurements when loading from one load step to the next and ”LSxx” for measurements at one load step. For the latter, the data was recorded for 90 to 120 seconds. The Excel-files carry the same names as the folders plus the suffix ”_001_3d.xls”: ”LSxx_to_LSxx+1_001_3d.xls” and ”LSxx_001_3d_xls”.

Each Excel-file contains three header lines which indicate the number of frames included in this file, the recording frequency in Hz (2 Hz for PUP1 and 4 Hz for PUP2–6) and the units of the coordinate measurements (mm). After one blank line, the actual measurement data is organized in columns. The first column stores an index starting always from 1. The second and following columns give the coordinate measurements of the LEDs. Always three columns store the x-, y-, and z-coordinate measurements of one LED. The labels of these columns are for LED number 1 Marker_1x, Marker_1y, Marker_1z. Note that the LED numbers are at this stage random and the numbering indicated in Fig. 10 only applies to the processed data. If the LED-coordinates could not be measured because the LED was not visible for the position sensor, the columns corresponding to this LED do not contain any entries.

Table 6. Summary of test results [PB14]

Specimen	Failure mechanism	σ_0/f_u	H_0/H	Peak load	Drift at peak load	Drift at hor. failure	Max. drift
PUP1	Diagonal shear	0.18	$0.5H$	187 kN	0.15%	0.29%	0.31%
				-167 kN	-0.12%	-0.17%	-0.21%
PUP2	Diagonal shear	0.18	$0.75H$	178 kN	0.35%	0.40%	0.41%
				-164 kN	-0.37%	-	-0.38%
PUP3	Flexural Rocking	0.18	$1.5H$	121 kN	0.51%	0.72%	0.84%
				-115 kN	-0.72%	-0.93%	-0.94%
PUP4	Hybrid shear	0.26	$1.5H$	145 kN	0.27%	0.35%	0.44%
				-142 kN	-0.36%	-	-0.38%
PUP5	Diagonal shear	0.09	$0.75H$	135 kN	0.37%	0.56%	0.58%
				-121 kN	-0.53%	-0.54%	-0.55%
PUP6	Hybrid shear	0.26	$1.5H$	132 kN	0.54%	-	0.74%
		0.09	$0.75H$	-154 kN	-0.70%	-	-0.71%

9.3.3 Irregularities with regard to the measurements

When the horizontal actuator was not stopped in time for PUP1 (during the cycle with a nominal drift of 0.2%, LS13 to LS14) and the wall was accidentally loaded up to a drift of 0.3%, the optical and conventional measurement systems were not recording during this phase. For PUP3, no measurements are available for LS9_to_LS10, LS39_to_LS40 and parts of the optical measurement for LS20_to_LS21 and LS34_to_LS35 are missing. While testing PUP5, the NDI measurement for LS36_to_LS37 was started only after unloading and reaching $F_1 \approx 0$ kN.

9.4 Processed data

The processing of the data served four objectives: (1) synchronization of the optical data with the conventional measurement data; (2) reducing the data to make it more manageable; (3) to reorganize the data in two data sets - one for measurements at load steps and one for measurements containing the actual loading process between load steps; (4) to remove any bias or data that is not linked to the actual behavior of the test unit.

For each test, the data acquired during loading is appended to one continuous vector of 10000–15000 data points. The data recorded at a load step was averaged and hence, condensed to one single measurement point. A second file contains these measurement points for all load steps (19 to 50 data points, depending on the number of loadsteps until failure). In addition, the data recorded at $F_1 \approx 0$ kN between two successive load steps was identified and also condensed to one point. This data describes the residual deformations for zero horizontal force and is contained in a third file. The suffix of each file ("_at_LS", "_at_F0" or none for the loading phase from peak to peak) indicates the type of file (see Fig. 15).

9.4.1 Processing of the conventional measurement data

With the exception of the channels containing the forces F_1, F_2 and F_3, the signal coming from the NDI measurement and the time, all channels were shifted to zero in such a way that the displacement at LS0 corresponds to zero. The sign of the force of actuator 1, F_1, the displacement measurements V2 and V3 and the deformation measurements NB11 to ST33 were inverted in

Table 7. Computed channels

Channel number	Channel name	Unit	Shortcut	Formulae/Explanation	Sign convention
44	Average HOR	mm	-	$\frac{(\text{HOR2+HOR3})}{2}$	+ = towards South - = towards North
46	Normal force	kN	N	$F_2 + F_3$	+ = pulling to top - = pushing to bottom
47	Top moment	kNm	M_{top}	$(F_2 - F_3) \cdot \frac{L_{act}}{2} + F_1 \cdot H_{act}$	See Fig. 1a
48	Bottom moment	kNm	M_{bot}	$(F_2 - F_3) \cdot \frac{L_{act}}{2} + F_1 \cdot (H + H_{act})$	See Fig. 1a
49	Shear span	m	H_0	$\frac{M_{bot}}{M_{bot} - M_{top}} \cdot H$	-
50	Rotation from U2 and U3	mm/m	-	$\frac{(\text{U2+U3})}{d_{U2}+d_{U3}+L}$	+ = counter clockwise - = clockwise
51	Rotation from V2 and V3	mm/m	-	$\frac{(\text{V2+V3})}{d_{V2}+d_{V3}+L}$	+ = counter clockwise - = clockwise
53	Disp at top plate	mm	-	Average displacement obtained from LEDs glued onto the top steel plate	+ = towards South - = towards North
54	Missing disp	mm	-	Displacement obtained from CH44, where measurement from LEDs is missing	+ = towards South - = towards North
55	Disp at top plate	mm	-	Displacement obtained from CH53 and CH54	+ = towards South - = towards North
56	Drift	%	-	$\frac{\text{CH55}}{\text{MarkersPosition}}$	+ = towards South - = towards North

order to match the sign convention described in ”Metadata_conventional_channels.xls” (see also Fig. 1). Furthermore, the conventional data was carefully processed to remove any bias or data that is not linked to the actual behavior of the test data (e.g. offsets because conventional instruments were moved during testing). This process involved certain judgment; in case of doubt the data was not modified.

The self-weight of the loading beam (19 kN) was added to the axial load applied at the top of the walls; the weight of the horizontal actuator was neglected since it was supported by straps (Fig. 1b). Thus, the force applied by the two vertical actuators 2 and 3 was adjusted as follows:

$$F_{2,3} = F_{2,3} - \frac{19\text{kN}}{2} \tag{3}$$

In addition to the recorded channels, a set of computed channels was added to the processed data. The objective of these computed channels is to allow the user to quickly plot fundamental graphs such as the shear force-average drift hysteresis of the wall. Table 7 defines these computed channels: CH53 was obtained by averaging the displacement from all LEDs glued onto the top steel plate. CH54 contains entries only when the optical measurements were missing, hence, when CH53 indicates a NaN-value (NaN=Not a Number). In this case, CH44 is taken as replacement and shifted in such a way as to remove any offsets between CH53 and CH54. The final displacement of the top plate of the wall is channel CH55, which assembles channels CH53 and CH54. CH56 stores the average drift which was obtained by dividing the displacement of the top plate (CH55) by the average height of the wall as obtained from LS0 measurements.

9.4.2 Processing of the optical measurement data

To remove any inherent noise, the optical measurement data was smoothed over a range of 20 data points using the Matlab-function ”smooth” [Mat10]. The coordinate system was then rotated and shifted to align the axes with the xy-axes as indicated in Fig. 10. Finally, the data was synchronized with the processed conventional measurements. In order to have the same number of entries for the conventional and optical measurements, the measurement frequency of the optical measurements was reduced leading to 150–500 data points between peak displacements. LEDs that fell off during testing were identified and the corresponding entries were replaced by NaN-entries. NaN-entries were also assigned when LED-coordinates were not recorded. Finally, the LEDs were renumbered indicating the position of the LED by a row and a column number (Fig. 10). The coordinate histories of each LED are stored in an ascii-file with three columns for the x-, y-, and z-coordinate.

The files are named ”LED_Cyy_Rxx.asc”, where xx corresponds to the row number and yy to the column number (see Fig. 10). For PUP1 and PUP2 only four LEDs were glued onto the top and bottom steel plate. These two times four LEDs are saved in the files LED_R01_Cyy and LED_R24_Cyy which corresponded to the nearest position of the LEDs. The remaining files were filled with NaN-values in order to simplify the batch processing of the walls.

9.5 Data for material tests (QUP, TUP and WUP)

Data from the material tests was processed similar to the conventional data from the wall tests. Hence, all channels were set to zero at zero load and any bias or data that is not linked to the actual behavior of the test data was eliminated (e.g. offsets because conventional instruments were moved during testing).

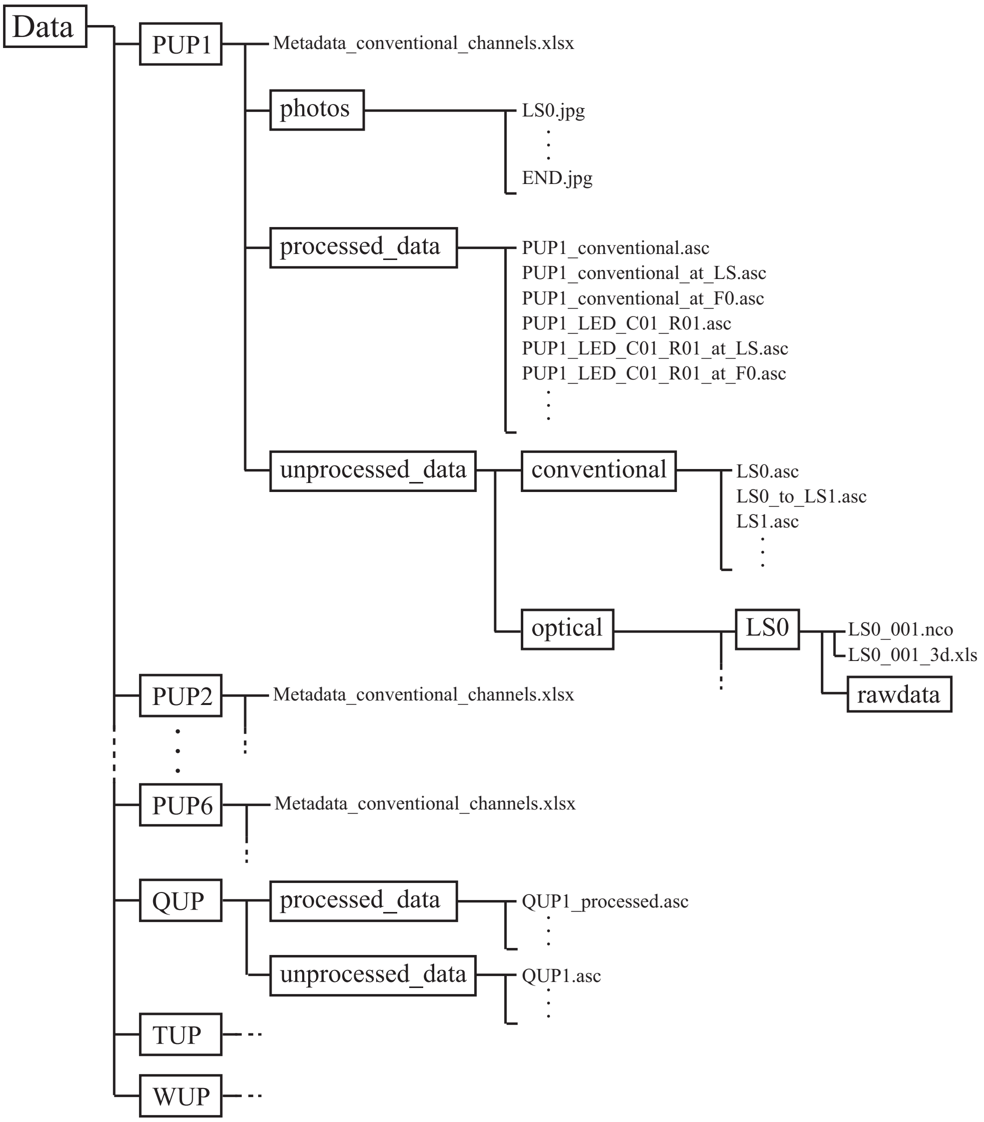

Figure 15. Organization of the data

10 Examples for derived data

This section gives some examples of graphs and figures that can be produced using the experimental data; further examples can be found in Petry and Beyer [PB14]. All plots are created using the derived data.

10.1 Example plots for global behavior

Current codes (e.g. [CEN05]) suggest that the deformation capacity of masonry walls is directly linked to the failure mechanism of the wall. However, recent research showed that this approximation is insufficient and that the displacement capacity of URM walls depends on more than only the failure mechanism [PB14]. The development of deformation mechanisms could up to now only be inferred from crack patterns. The optical measurements taken during this series allow drawing amplified deformed shapes of the walls. Figure 16 shows as example the amplified deformed shapes of PUP4 at different load steps; PUP4 was chosen because the behavior was initially dominated by flexural deformations while the test unit developed subsequently important diagonal shear cracks. Figure 16 shows the deformed shapes at LS18 and 19 (δ_{nom} = 0.2%) and 30 and 31 (δ_{nom} = 0.6%). The photos that were taken at the same load steps are shown in Fig. 17. The amplified deformed shapes were computed as follows: The rigid body translation and rotation of each brick were computed from the average displacements of the four LEDs on the brick. From the same four LEDs, the average strain state of the brick was computed (ϵ_x, ϵ_y, τ_{xy}). It was assumed that the entire brick was subjected to this strain state. The deformed shape of the brick and its rigid body movement were amplified by a factor AF and the deformed brick was plotted at its new position. All bricks together give the amplified deformed shape (Fig. 16). Such plots allow identifying clearly the development of failure mechanisms and can be regarded as an important complement to photos of crack patterns (Fig. 17).

10.2 Example plots for local behavior

The LED-data can also be used to compute local deformations such as average strains and crack widths. Figure 18 shows as example average strains at the compressed face of the wall. The strains were computed from the LEDs in column 1 and 13 for loading towards South (even load steps) and North (uneven load steps), respectively. The strains were computed as average strains between the center lines of bricks bridging therefore always one brick and one bed joint. The plots show clearly that the compressive strains concentrate in the bottom four brick rows. They also show that the bed joints 7 and 8 were particularly weak, most likely due to poor quality of the mortar used for the construction of these bed joints. Figure 19 shows the deformations in the bed joints which were computed using the same assumptions as for the deformed shapes (uniform strain state in bricks).

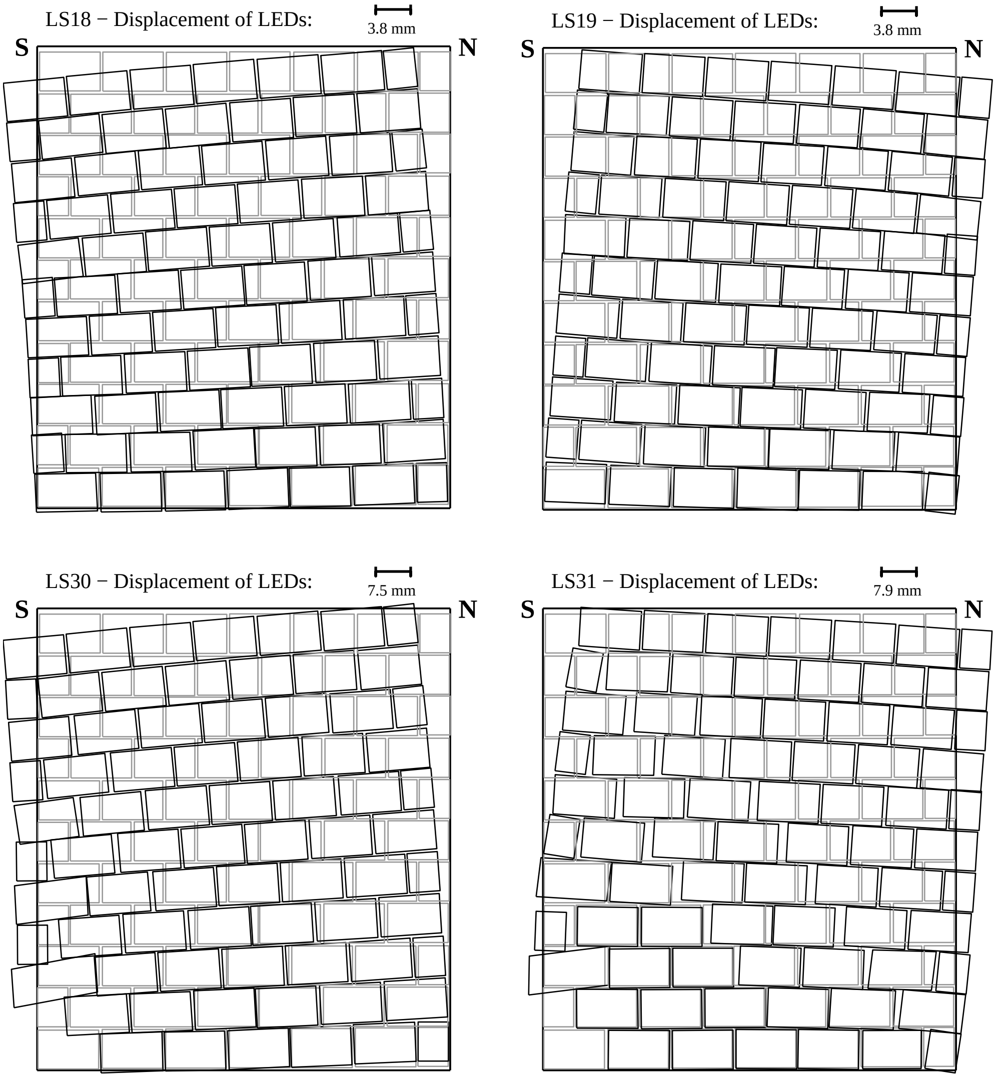

LS18 − Displacement of LEDs:

LS19 − Displacement of LEDs:

LS30 − Displacement of LEDs:

LS31 − Displacement of LEDs:

Figure 16. Amplified deformed shapes for LS18 and LS19 (AF ≈ 45) and LS30 and LS31 (AF ≈ 22) (PUP4, reference load step: LS0)

a) PUP4: $H_0/H = 1.5$, $N = -619$ kN, LS18 **b) PUP4**: $H_0/H = 1.5$, $N = -619$ kN, LS19

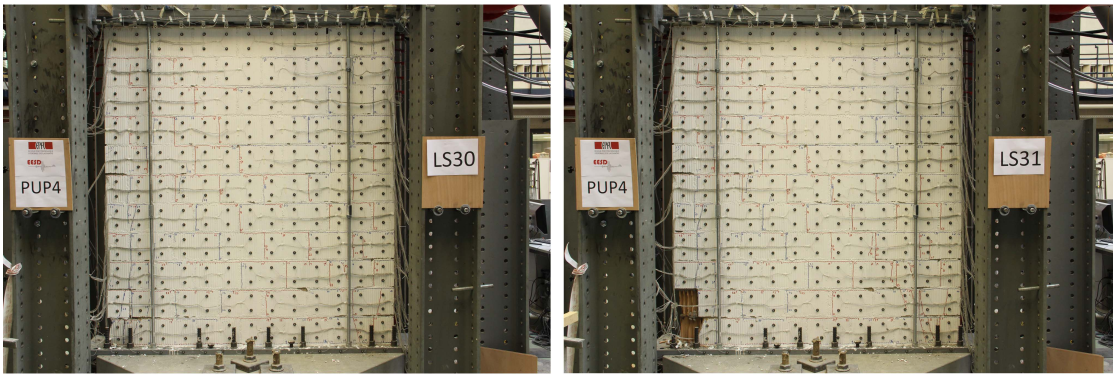

c) PUP4: $H_0/H = 1.5$, $N = -619$ kN, LS30 **d) PUP4**: $H_0/H = 1.5$, $N = -619$ kN, LS31

Figure 17. Photos of PUP4 taken at the load steps LS18, LS19, LS30 and LS31

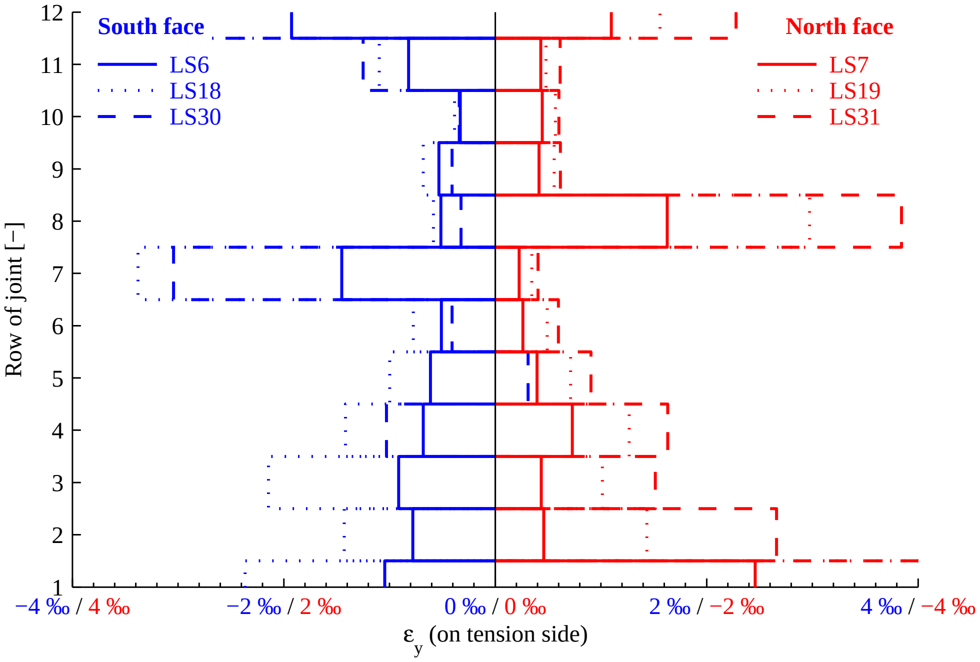

Figure 18. Strain at compressed edge of the wall (PUP4, reference load step LS0)

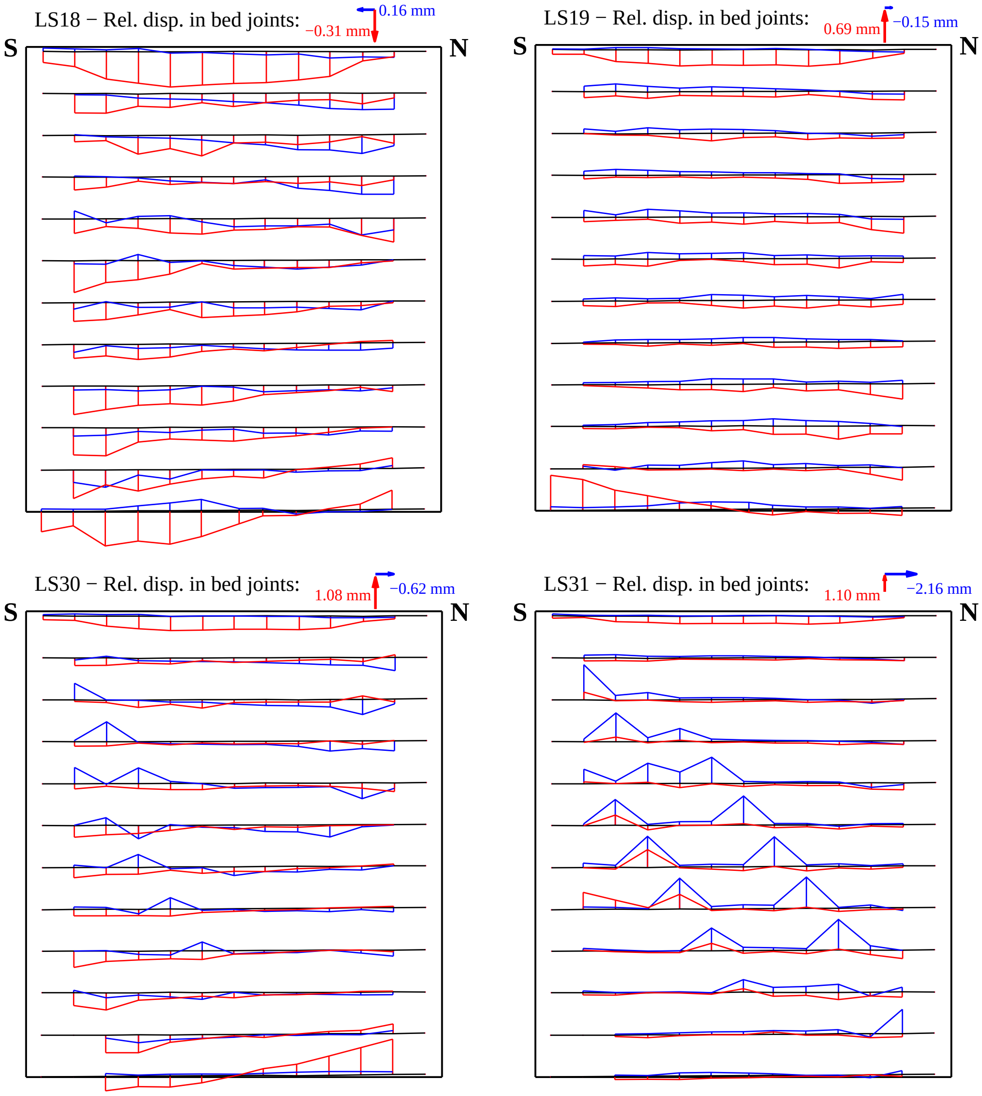

Figure 19. Horizontal slip (in blue) and vertical opening/compression (in red) of the bed joints for different load steps (PUP4, reference load step LS0)

11 Summary

The paper presents the data of six quasi-static cyclic tests on masonry walls, which is publically accessible through the ZENODO platform. The data is unique with regard to the boundary conditions applied to the walls and the detail of local deformation measurements recorded. Example plots show how these local deformation measurements can be used to analyze in depth the behavior of the masonry walls. Such data is crucial for advancing numerical and analytical models for the deformation capacity of masonry walls-the latter are an important step towards performance-based design and assessment procedures for unreinforced masonry structures.

12 Acknowledgments

The authors thank Morandi Frères SA for the donation of the bricks and all engineers, technicians and students who helped with the laboratory testing. The authors would like to thank in particular Dr. Pia Hannewald, Sylvain Demierre, Gérald Rouge, Nikita Saugy and Nicholas Molyneaux.

References

[BD12a] Beyer, K and Dazio, A. Quasi-static cyclic tests on masonry spandrels. *Earthquake Spectra*, 28:907–929, 2012.

[BD12b] Beyer, K and Dazio, A. Quasi-static monotonic and cyclic tests on composite spandrels. *Earthquake Spectra*, 28:885–906, 2012.

[BP+03] Bosiljkov, V, Page, AW, Bokan-Bosiljkov, V and Zarnič, R. Performance based studies of in-plane loaded unreinforced masonry walls. *Masonry International*, 16(2):39–50, 2003.

[CEN02] CEN. EN 1052-1: Methods of test for masonry, Part 1: Determination of compressive strength. Technical Report EN 1052-1:1998-12, European Committee for Standardisation, Brussels, Belgium, 2002.

[CEN05] CEN. Eurocode 8: Design of structures for earthquake resistance, Part 3: Assessmemt and retrofitting of buildings. Technical Report EN 1998-3, European Committee for Standardisation, Brussels, Belgium, June 2005.

[CEN07] CEN. EN 1052-3: Methods of test for masonry, Part 3: Determination of the initial shear strength. Technical Report EN 1052-3:2002+A1:2007 D, European Committee for Standardisation, Brussels, Belgium, 2007.

[FM+09] Frumento, S, Magenes, G, Morandi, P and Calvi, GM. *Interpretation of experimental shear tests on clay brick masonry walls and evaluation of q-factors for seismic design*. Technical Report, IUSS PRESS, Pavia, Italy, 2009.

[GKN13] Goodnight, J, Kowalsky, M and Nau, J. Effect of load history on performance limit states of circular bridge columns. *Journal of Bridge Engineering, SPECIAL SECTION: Eurocodes and Their Implications for Bridge Design: Background, Implementation, and Comparison to North American Practice*, 18:1383–1396, 2013.

[GT84] Ganz, HR and Thürlimann, B. Versuche an Mauerwerksscheiben unter Normalkraft und Querkraft. Technical Report Test Report 7502-4, ETH Zürich, Zürich, Switzerland, 1984.

[GT13] Gams, M and Tomaževič, M. Influence of different types of units and mortars on seismic resistance of masonry walls. In *Proceedings of the 12th Canadian Masonry Symposium*, Vancouver, Canada, 2013.

[HBM00] HBM. Catman data acquisition software. Technical report, Hottinger Baldwin Messtechnik GmbH, Darmstadt, Deutschland, http://www.hbm.com/en/menu/products/software/data-acquisition-software, 2000.

[LL+12] Lowes, LN, Lehman, DE, Birely, AC, Kuchma, DA, Marley, KP and Hart, CR. Earthquake response of slender planar concrete walls with modern detailing. *Engineering Structures*, 43:31–47, 2012.

[Mat10] Matlab. Matlab version 7.10.0.499 (r2010a). Technical report, The Mathwork Inc., Natick, Massachusetts, United States, http://www.mathworks.ch, 2010.

[MMP08] Magenes, G, Morandi, P and Penna, A. Enhanced safety and efficient construction of masonry structures in europe, 7.1c test results on the behaviour of masonry under static cyclic in plane lateral loads. Technical Report ESECMaSE D7.1c, University of Pavia, Pavia, Italy, 2008.

[NDI11] NDI. Optotrak certus hd. Technical report, Northern Digital Inc., Waterloo, Ontario, Canada, http://www.ndigital.com/industrial/certushd.php, 2011.

[PB14] Petry, S and Beyer, K. Influence of boundary conditions and size effect on the drift capacity of URM walls. *Engineering Structures*, 65:76–88, 2014.

[PCK07] Priestley, MJN, Calvi, GM and Kowalsky, MJ. *Displacement-Based Seismic Design of Structures*. Pavia, Italy, 2007.

[RIL91] RILEM. RILEM TC76-LUM: Diagonal tensile strength tests of small wall specimens. Technical Report TC76-LUM, RILEM Publications SARL, Brussels, Belgium, 1991.

[SMS13] Salmanpour, A, Mojsilovič, N and Schwartz, J. Deformation capacity of unreinforced masonry walls subjected to in-plane loading: a state-of-the-art review. *International Journal of Advanced Structural Engineering*, 5:1–12, 2013.

[VRJ93] Vermeltfoort, AT, Raijmakers, TMJ and Janssen, HJM. Shear tests on masonry walls. In *Proceedings of the Sixth North American Masonry Conference*, pages 1183–1193, Philadelphia, Pennsylvania, 1993.

[WB11] Walter and Bai. 3 servo-hydraulic differential actuators type dpz 1000/1000 with 3-channel hydraulic svice manifold and command unit type az 150-3-280 and software dion7. Technical report, Walter+Bai AG Testing Machines, Löhnnigen, Switzerland, http://www.walterbai.com, 2011.

Appendix B

Cyclic test data of five URM walls at half-scale

Summary

In addition to the test data of the full-scale unreinforced masonry (URM) walls [PB14a], also the test data obtained with the half-scale walls was made publicly available. The data has been assigned the DOI 10.5281/zenodo.12873 and can be downloaded with the following link:

https://zenodo.org/record/12873

This appendix describes the test program, material tests and organization of the test data. When using the data please cite as follows [PB14b]:

Petry, S and Beyer, K; Scaling unreinforced masonry for reduced-scale seismic testing. *Bulletin of Earthquake Engineering* (2014), 12(6):2557–2581, DOI: 10.1007/s10518-014-9605-1

1 Introduction

In the framework of the investigations on the scale effects [PB14b], five out the six full-scale wall test presented in [PB14a] were repeated at half-scale. The test data of the full-scale tests has been made publicly available [PB14a] and this appendix presents the data for the five unreinforced masonry half-scale wall tests.

The appendix is organized similarly to the paper on the full-scale walls [PB14a]. References to [PB14b] and [PB14a] are used to keep the length of the document to a minimum without compromising on the explanations required for reusing the data.

2 Test objectives

The objectives of repeating the test series at half-scale are outlined in detail in [PB14b] and are thus not repeated here.

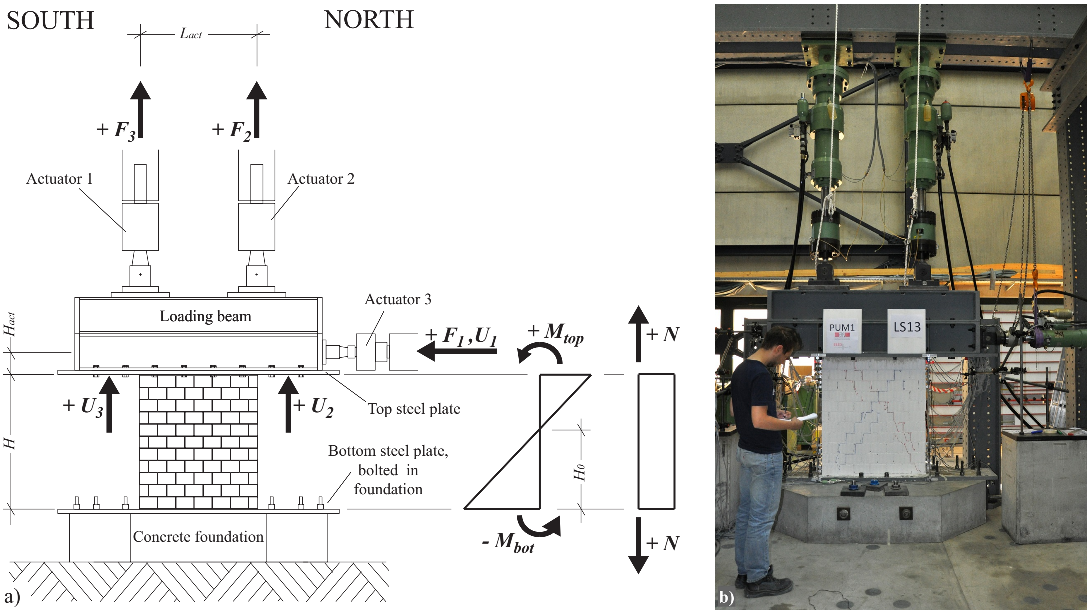

Figure 1. (a) Test setup with sign conventions after processing of the data and (b) photo showing the test setup of the half-scale wall tests with the three actuators

3 Organization of the appendix

The outline of this appendix follows the structure of [PB14a]. Hence, first the test program, the geometry and material of the five half-scale masonry walls is described. Then specifications concerning the instrumentation and the loading protocol are given and differences to the full-scale wall tests [PB14a] highlighted.

4 Test program and test setup

The experimental campaign comprised five tests on masonry walls that all had the same dimensions (H = 1.113 m, L = 1.005 m, T = 0.10 m). The walls were named PUM1–5 and represented the test units PUP1–5 from the full-scale series [PB14a]. The moment, axial force and shear force at the top of the walls were introduced by three actuators (Fig. 1). The two vertical actuators had a force capacity of ±450 kN and a displacement capacity of ±100 mm. The horizontal actuator had a force capacity of ±100 kN and a displacement capacity of ±100 mm. The distance between the axes of the two vertical cylinders was L_{act} = 0.96 m and the distance of the horizontal cylinder to the upper edge of the wall H_{act} = 0.185 m. The vertical actuators were controlled in such a way that the axial force applied to the wall during testing remained constant. In addition, the control of the vertical actuators was coupled to the force of the horizontal actuator in such a manner that the shear span H_0 remained constant throughout the test. The axial stress N/A_{gross} and normalized shear span H_0/H were the same for the half-scale and full-scale walls [PB14b]. The applied boundary conditions are summarized in Table1. Note that also for PUM1 the boundary condition were chosen such that the shear span remained constant at H_0=0.5H, while PUP1 was tested applying a zero rotation at the top [PB14b].

For the construction of the walls the same procedure as for the full-scale walls was used [PB14a]. Photos of the construction are shown in Fig. 2. The age at testing of the individual

Table 1. Test program

Specimen	Axial force N	Axial stress ratio σ_0/f_u	Shear span H_0	Eq. for control of vertical actuators
PUM1	-105 kN	0.18	$0.5H$	Actuator 2 & 3: $F_{2,3} = \frac{N}{2} \pm c \cdot F_1$
PUM2	-105 kN	0.18	$0.75H$	
PUM3	-105 kN	0.18	$1.5H$	
PUM4	-155 kN	0.26	$1.5H$	
PUM5	-55 kN	0.09	$0.75H$	

H	Height of the wall
H_0	Shear span
$F_{2,3}$	Forces of the two vertical actuators after processing
F_1	Force of the horizontal actuator after processing
c	Constant describing the dependency between $F_{2,3}$ and F_1 which determines the moment profile. The value of this constant depends on H_0 and the geometry of the test setup.

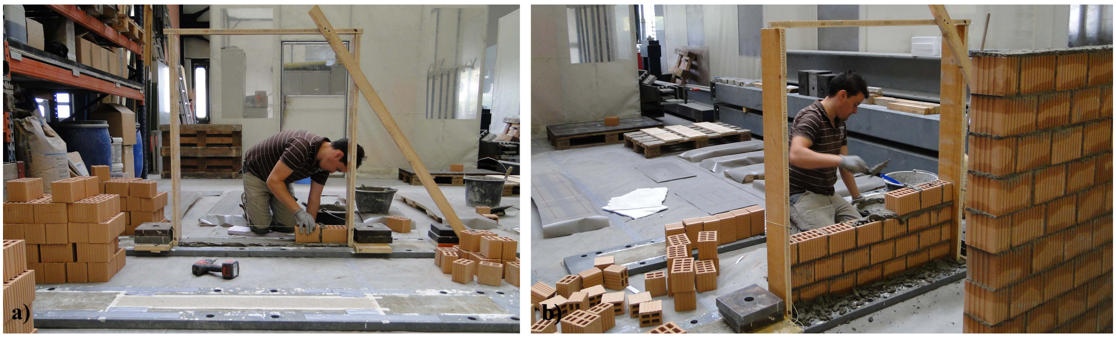

Figure 2. Steel plates with layer of quartz sand and test units during construction

test specimens is summarized in Table 2.

For the optical measurements, the walls were prepared similar to the full-scale walls with the difference that the distance of the LED grid was have the length. Note that due to the fine grid, the distance between the LEDs was too small to draw the cracks. Therefore, it was chosen to fix the LEDs on the other side than from which the pictures were taken.

5 Material test data

The masonry walls were constructed using a scaled brick unit which had similar properties than the hollow clay brick unit at full-scale, which was used for the construction of the full-scale walls [PB14a]. The half-scale brick is shown in Fig. 3. The brick units had dimensions of 150 x 95 x 95 mm ($L_B \times H_B \times W_B$). The geometric and mechanical properties of the units are summarized in [PB14b]. The same mortar as for the full-scale series was used (WEBER MUR MAXIT 920). Bed and head joints were fully filled and had an average thickness of 5 to 7 mm. Mortar samples were taken while constructing walls and wallettes for material tests. The mortar samples were tested when testing the corresponding walls and wallettes. The mortar properties for all types of specimens are summarized in Table 3.

Table 2. Age at testing of the specimens for the compression tests (WUM), for the diagonal compression tests (QUM), for the shear tests (TUM) and for the five quasi-static cyclic wall tests (PUM1–5)

	WUM	QUM	TUM	PUM1	PUM2	PUM3	PUM4	PUM5	
Age at testing	154	50	50	60	70	88	98	112	days

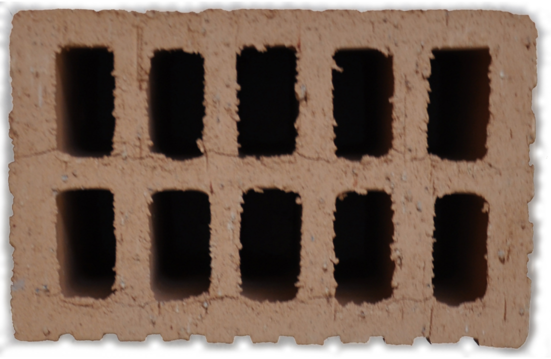

Figure 3 Investigated clay brick at half-scale

To determine the material properties of the masonry, the same three types of standard masonry material tests were conducted as for the full-scale wall tests [PB14a]: (1) the compression strength, elasticity modulus and Poisson's ratio were determined with compression tests (WUM1–5) on masonry wallettes [CEN02], (2) the peak shear strength and residual shear strength of the mortar brick interface were determined with shear tests (TUM1–10) on masonry triplets [CEN07] and (3) the diagonal tensile strength was determined with diagonal compression tests (QUM1–5) on square masonry wallettes [RIL91]. Figures 4 to 6 show for each material test a photo of a specimen and the test results. The mean masonry properties and coefficients of variation are summarized in Table 3 of [PB14b]. The data obtained from material tests are provided together with the data of the half-scale wall tests (see Section 8).

Note that the LVDTs indicated in Fig. 4c of [PB14a] were only used for the first five triplet tests (TUM1–5), while for the test units TUM6–10 only the forces were recorded. Out of the ten triplet units, two units (TUM5 and TUM8) provided unreasonable results (the axial stress which we applied was too high and the bricks fractured before sliding in the joints could occur). These two units were omitted when computing residual and peak strength and are not shown in Fig. 5b.

Table 3. Mortar properties corresponding to the mortar used for the construction of the specimens for the compression tests (WUM), for the diagonal compression tests (QUM), for the shear tests (TUM) and for the six quasi-static cyclic wall tests (PUM1–5)

		WUM	QUM	TUM	PUM1	PUM2	PUM3	PUM4	PUM5	
Compression strength $f_{M,c}$	Mean	14.0	13.7	13.0	9.27	11.3	12.3	9.45	11.9	MPa
	Std. dev.	5	9	6	8	10	9	7	18	%
Flexural tensile strength $f_{M,ft}$	Mean	3.57	3.36	3.23	2.89	3.55	3.40	3.01	3.79	MPa
	Std. dev.	19	7	19	8	13	12	12	15	%

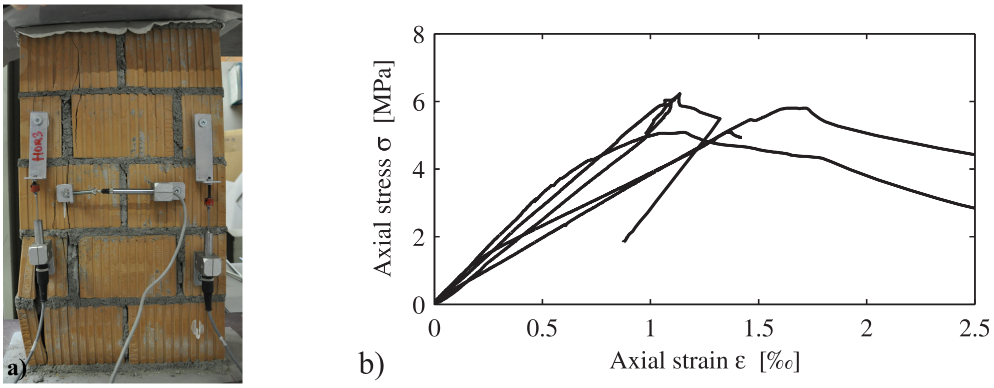

Figure 4. (a) Specimen for the compression tests with mounted measurement devices and (b) stress-strain relationships

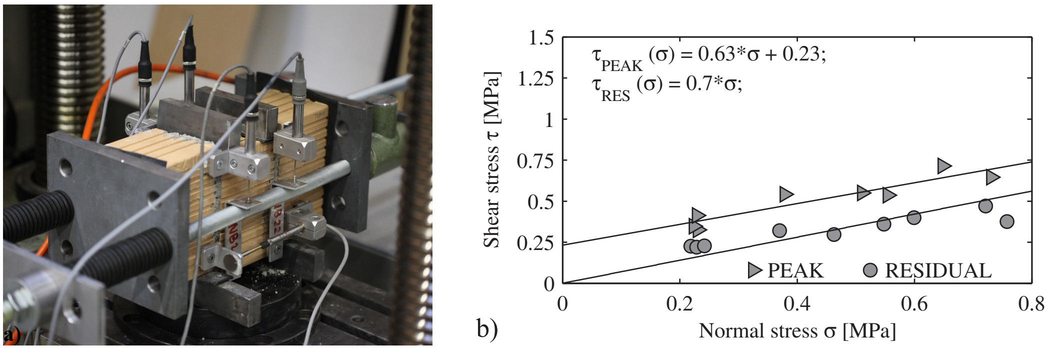

Figure 5. (a) Test setup for the shear tests with specimen and (b) applied normal stress versus resulting peak and residual shear strength of the mortar brick interface

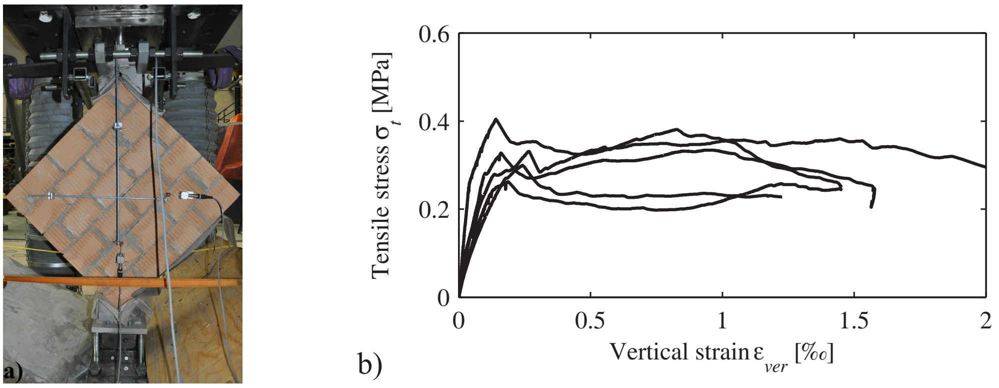

Figure 6. (a) Specimen for the diagonal compression tests with typical stair stepped crack along mortar joints and (b) stress-strain relationships

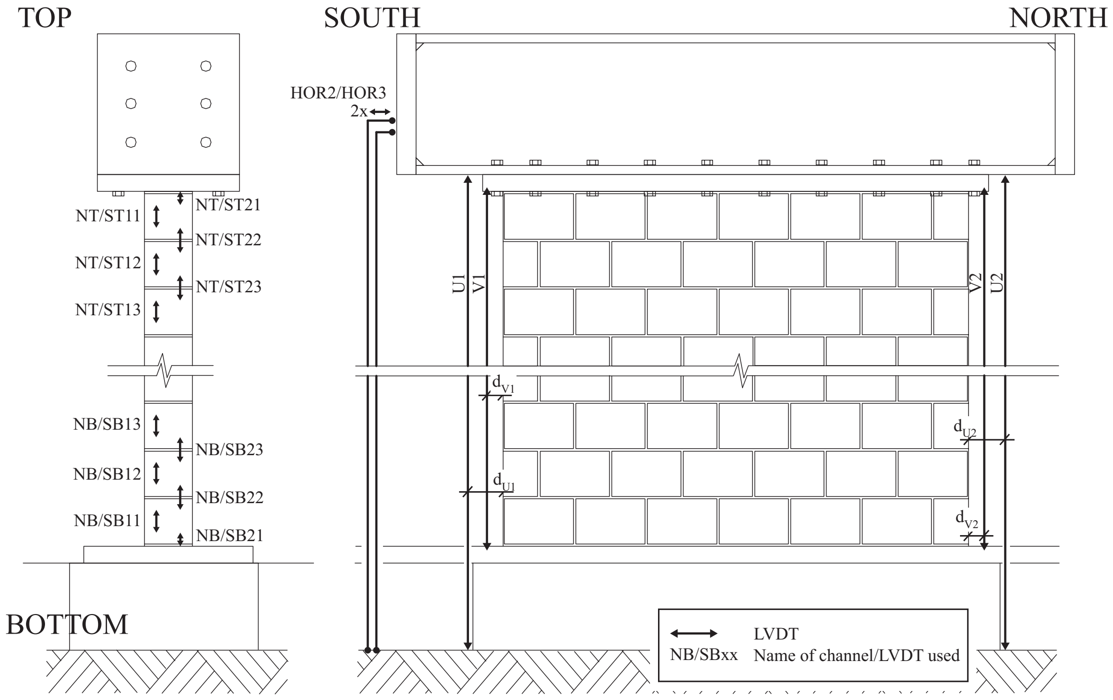

Figure 7. Location of the conventional measurement devices

6 Instrumentation

The test units (PUM1–5) were instrumented with 42 conventional channels, which were recorded at a frequency of 1 Hz. Next to global quantities (forces applied by actuators, horizontal displacements of top beam) some local deformations were measured with LVDTs and omega gauges. The locations of the conventional instruments are indicated in Fig. 7. The base lengths for the instruments measuring local deformations are summarized in Table 4. Note that due to the small width of the half-scale walls, the horizontal strains at the narrow sides were not measured and therefore the channels 30–32 and 40–42 are empty. The sign convention for the actuator forces and displacements of the top beam are shown in Fig. 1. The exact position of the instruments U3, V3, U2 and V2 (Fig. 7) varied slightly between walls and the horizontal distance from the instrument to the outer edge of the wall is specified in Table 5.

The optical measurements were performed with the commercially available system Optotrak from NDI (Optotrak Certus HD [NDI11]). The photogrammetric system works with one position sensors consisting of three digital cameras (see Fig. 8a), which measured the 3D-coordinates of the LEDs (see Fig. 8b) glued onto the test unit, foundation and loading beam. The LEDs were glued onto the wall in the same way as for the full-scale walls [PB14a]. During each measurement frame all LEDs illuminate one after each other and the positioning sensors recorded the x-, y- and z-coordinates of each LED with a measurement frequency of 4 Hz.

The measurement systems used for the optical and conventional measurements worked independently from each other and were synchronized after the test during the post-processing phase with the help of a self-written Matlab script. For more details on this procedure please refer to [PB14a].

Table 4. Base length for the local measurement devices(Fig. 7)

Channel name	Channel number	Unit	PUM1	PUM2	PUM3	PUM4	PUM5
NB11	13	mm	51	45	48	51	50
NB12	14	mm	50	47	48	52	51
NB13	15	mm	41	48	47	48	50
NB21	16	mm	28	26	30	16	30
NB22	17	mm	56	63	53	55	53
NB23	18	mm	55	53	57	53	53
SB11	19	mm	44	53	46	52	50
SB12	20	mm	45	50	47	50	55
SB13	21	mm	50	50	48	47	50
SB21	22	mm	35	28	30	21	31
SB22	23	mm	59	63	58	55	49
SB23	24	mm	53	56	49	50	54
NT11	25	mm	49	50	49	51	51
NT12	26	mm	50	49	50	49	53
NT13	27	mm	49	47	51	49	54
NT21	28	mm	40	54	35	32	38
NT22	29	mm	52	51	50	51	50
NT23	30	mm	51	49	51	51	50
ST11	34	mm	46	48	47	51	50
ST12	35	mm	51	40	48	50	52
ST13	36	mm	46	44	43	53	50
ST21	37	mm	34	58	35	25	40
ST22	38	mm	52	53	52	50	49
ST23	39	mm	50	51	51	50	48

7 Testing procedure

All tests were performed applying the same procedure as for the full-scale walls [PB14a]. The displacement amplitudes of the half-cycles corresponded to the following drift levels: 0.025%, 0.05%, 0.1%, 0.15%, 0.2%, 0.3%, 0.4%, 0.6%, 0.8% and 1.0%. Note that the cycles with amplitudes of 0.15% and 0.25% were not included in the loading history applied to PUM1, but added from PUM2 onwards. This corresponds to the load histories applied to the full-scale walls.

8 Test data

8.1 Organization of data

The data can be downloaded as one zip file from www.zenodo.org using the DOI xxxx (7 files of 0.26–1.33 GB). The platform ZENODO (www.zenodo.org) was developed under the European FP7 project (http://www.openaire.eu/) and is hosted by the research facility CERN which operates a Large Hadron Collider.

Upon unzipping, the folder structure unfolds as follows (Fig. 9): The data is organized first by specimen (PUM1–5 for the five walls, QUM for the diagonal compression tests, TUM for the triplet tests and WUM for the compression tests). For each wall specimen there are three

Table 5. Distances defining the location of the conventional measurement devices U2, U3, V2 and V3 (Fig. 7)

Distance	Channel number	Unit	PUM1	PUM2	PUM3	PUM4	PUM5
d_{U1}	5	mm	10	495	495	485	510
d_{U2}	7	mm	10	405	395	385	400
d_{V1}	9	mm	500	15	-15	50	40
d_{V2}	10	mm	500	27	45	55	70

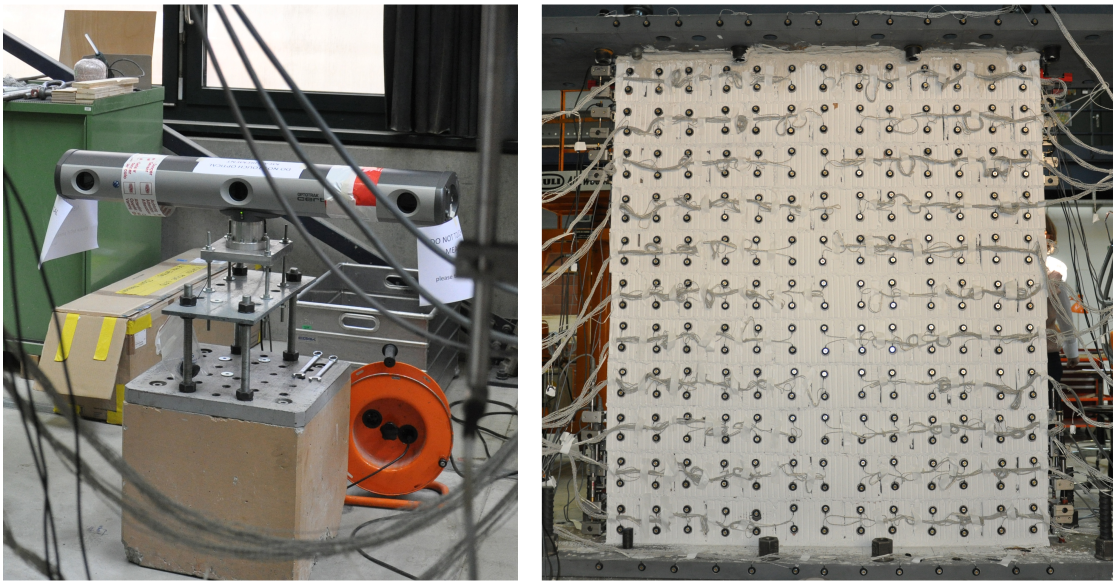

Figure 8. Measurement device used for the optical measurement system: (a) position sensors consisting of three cameras and (b) LEDs glued onto the back side of the masonry wall

subfolders (”photos”, ”unprocessed_data” and ”processed_data”) and for each type of material tests two subfolders (”unprocessed_data” and ”processed_data”). The following sections outline the organization of the data within the individual folders and the processing applied to the data. Each wall folder contains one file ”Metadata_conventional_channels.xls” which contains information on all instruments used (type of instrument, producer, measurement range, measurement unit, base length for displacement measurements, sign convention).

8.2 Photos

In addition to the data from conventional and optical measurements, photos are used to document the damage to the walls. Photos were taken at each load step, i.e. at peak displacements. These photos are labeled with ”LSxx.JPG” where xx stands for the load step. To document the residual damage at zero horizontal force when passing from one load step to the other, the loading was shortly stopped for PUM1–5 when reaching $F_1 \approx 0$ kN. The photo at $F_1 \approx 0$ kN between load steps xx and xx+1 is labeled ”LSxx_to_LSxx+1.JPG”.

At each load step, the cracks were traced using blue and red pens in order to render the cracks visible on photos. Cracks that were noticed for the first time at load steps in the positive loading direction (LS2, LS4, ...) were marked with a blue line and cracks that were noticed for the first time at load steps in the negative direction (LS3, LS5, ...) were marked in red. Cracks that appeared in the base joint during transportation or while fixing the bottom steel plate to the concrete foundation are marked in black and are annotated with 0. Such cracks appeared for all walls but they remained limited to hairline cracks extending only over a small part of the wall length.

8.3 Unprocessed data

The unprocessed data contains the original files recorded during the testing of the walls. The folder ”unprocessed_data” contains two subfolders ”conventional” and ”optical”.

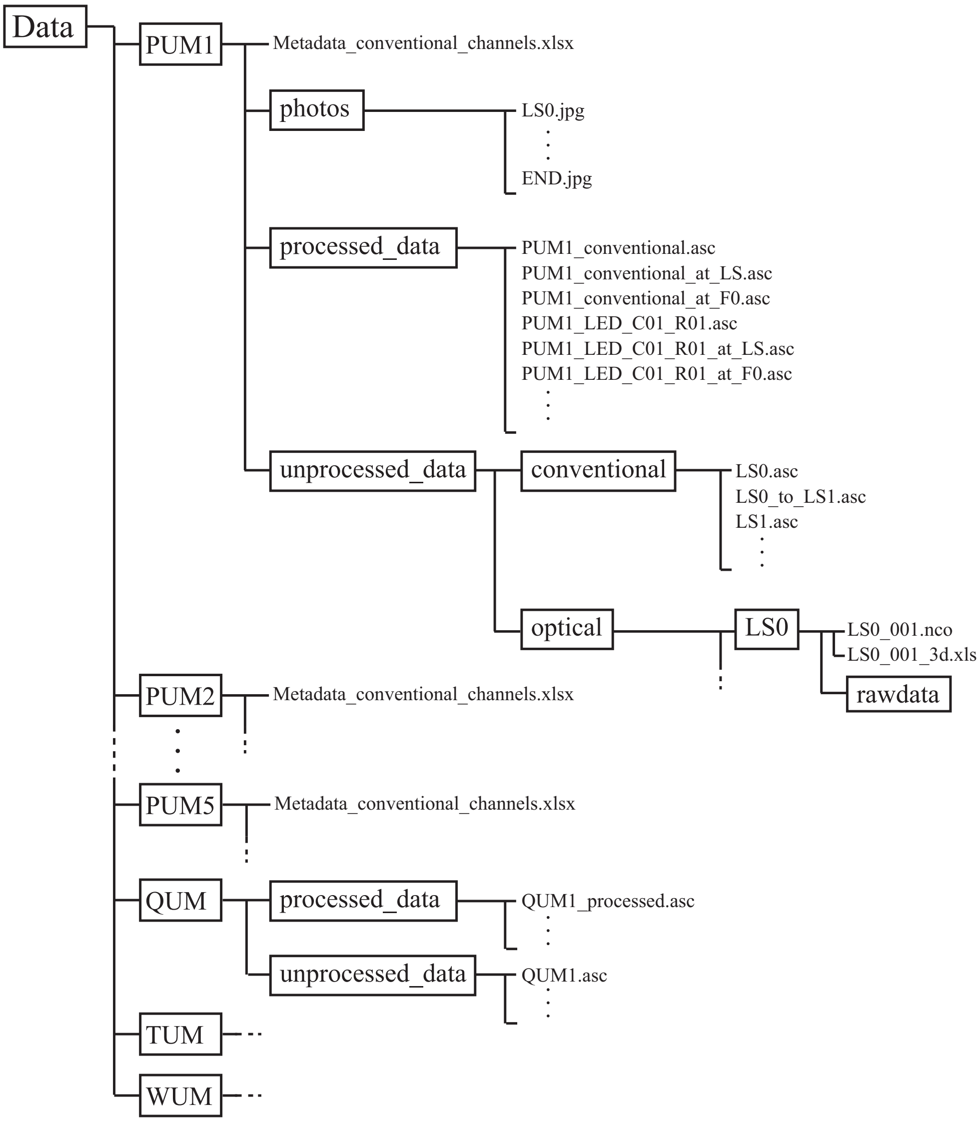

Figure 9. Organization of the data for the half-scale test series

8.3.1 Conventional measurement data

The conventional measurements were recorded using the system ”CATMAN” [HBM00] and the files contain the unmodified output files of this system. They comprise the actuator forces (F_1, F_2 and F_3), the voltage channel ”NDI-channel” (see Section ”Instrumentation”), the measurement from the internal displacement transducer of actuator 3 (U3), the measurements from the external displacement transducers (U1, U2, HOR2, HOR3, V2 and V3) and the local displacement measurements at the corners of the wall (NB11 to ST33). The voltage channel ”NDI-channel” was exported from the NDI system and indicated when the optical measurement system was recording. The conventional measurement system was always started before and stopped after the optical measurement system and this voltage signal was therefore used to synchronize the two measurement systems. The folder ”conventional” stores the following types of files, which are all ascii-files: The files containing the measurement during loading are labeled ”LSxx_to_LSxx+1.asc”. While holding the position at one load step, the data was written to a file labeled ”LSxx.asc”. When loading was interrupted during the night, the files labeled ”LSxx_to_unload.asc” and ”Restart_to_LSxx+1.asc” contain the corresponding half loadstep with the unloading/reloading part.

8.3.2 Optical measurement data

The folder ”optical” contains the output of the NDI measurement system. For each recording sequence a separate folder was created which stores the NDI-specific file formats (raw data and sensor settings) and the measurement data exported to Excel. The folders are named ”LSxx_to_LSxx+1” for measurements when loading from one load step to the next and ”LSxx” for measurements at one load step. For the latter, the data was recorded for 90 to 120 seconds. The Excel-files carry the same names as the folders plus the suffix ”_001_3d.xls”: ”LSxx_to_LSxx+1_001_3d.xls” and ”LSxx_001_3d_xls”.

Each Excel-file contains three header lines which indicate the number of frames included in this file, the recording frequency in Hz (4 Hz for PUM1–5) and the units of the coordinate measurements (mm). After one blank line, the actual measurement data is organized in columns. The first column stores an index starting always from 1. The second and following columns give the coordinate measurements of the LEDs. Always three columns store the x-, y-, and z-coordinate measurements of one LED. The labels of these columns are for LED number 1 Marker_1x, Marker_1y, Marker_1z. At this stage the LED numbers are random (see also App A). If the LED-coordinates could not be measured because the LED was not visible for the position sensor, the columns corresponding to this LED do not contain any entries. Note that for the small-scale walls the LEDs were glued at the back side of the LEDs. Therefore the coordinate system is rotated with respect to the one from the full-scale series and the sign of the x-axes is inverted (see 10).

8.4 Processed data

The processing of the data is done in analogy to the full-scale series [PB14a]. Thus, for each test, the data acquired during loading is appended to one continuous vector of 10000–15000 data points. The data recorded at a load step was averaged and hence, condensed to one single measurement point. A second file contains these measurement points for all load steps (22 to 48 data points, depending on the number of loadsteps until failure). In addition, the data recorded at $F_1 \approx 0$ kN between two successive load steps was identified and also condensed to one point. This data describes the residual deformations for zero horizontal force and is

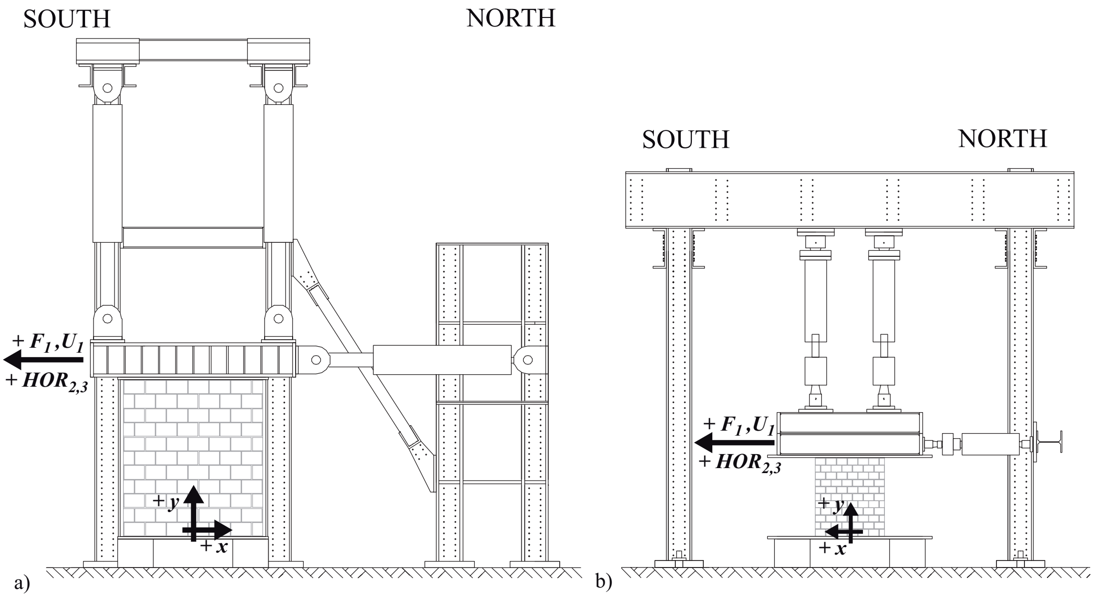

Figure 10. Sign convention and coordinates orientation for (a) the full-scale wall tests (PUP1–6) and (b) the half-scale wall tests (PUM1–5)

contained in a third file. The suffix of each file (”_at_LS”, ”_at_F0” or none for the loading phase from peak to peak) indicates the type of file (see Fig. 9).

8.4.1 Processing of the conventional measurement data

With the exception of the channels containing the forces F_1, F_2 and F_3, the signal coming from the NDI measurement and the time, all channels were shifted to zero in such a way that the displacement at LS0 corresponds to zero. In the setup of the small scale series, the actuators 1–3 were numbered in the inverse direction than for the full-scale series. In order to make comparison easier, the order the force channels in the small-scale series were changed thus that F_1 represents the force in the horizontal actuator and F_2 and F_3 the force in the vertical actuator at the North and the South respectively (see numeration of actuators after processing in Fig. 1). After that, the sign of the force of the horizontal actuator, F_1, the displacement measurements V1 and V2 and the deformation measurements NB11 to ST33 were inverted in order to match the sign convention described in ”Metadata_conventional_channels.xls”. In addition, the conventional data was carefully processed to remove any bias or data that is not linked to the actual behavior of the test data (e.g. offsets because conventional instruments were moved during testing). This process involved certain judgment; in case of doubt the data was not modified.

The self-weight of the loading beam (8.8 kN) was added to the axial load applied at the top of the walls; the weight of the horizontal actuator was negligible. Thus, the force applied by the two vertical actuators F_2 and F_3 was adjusted as follows:

$$F_{2,3} = F_{2,3} - \frac{8.8\text{kN}}{2} \tag{1}$$

In addition to the recorded channels, a set of computed channels was added to the processed data. The objective of these computed channels is to allow the user to quickly plot fundamental

Table 6. Computed channels

Channel number	Channel name	Unit	Shortcut	Formulae/Explanation	Sign convention
44	Average HOR	mm	-	$\frac{\text{(HOR2+HOR3)}}{2}$	+ = towards South - = towards North
46	Normal force	kN	N	$F_2 + F_3$	+ = pulling to top - = pushing to bottom
47	Top moment	kNm	M_{top}	$(F_2 - F_3) \cdot \frac{L_{act}}{2} + F_1 \cdot H_{act}$	See Fig. 1a of [PB14a]
48	Bottom moment	kNm	M_{bot}	$(F_2 - F_3) \cdot \frac{L_{act}}{2} + F_1 \cdot (H + H_{act})$	See Fig. 1a of [PB14a]
49	Shear span	m	H_0	$\frac{M_{bot}}{M_{bot} - M_{top}} \cdot H$	-
50	Rotation from U2 and U3	mm/m	-	$\frac{\text{(U2+U3)}}{d_{U2} + d_{U3} + L}$	+ = counter clockwise - = clockwise
51	Rotation from V2 and V3	mm/m	-	$\frac{\text{(V2+V3)}}{d_{V2} + d_{V3} + L}$	+ = counter clockwise - = clockwise
53	Disp at top plate	mm	-	Average displacement obtained from LEDs glued onto the top steel plate	+ = towards South - = towards North
54	Missing disp	mm	-	Displacement obtained from CH44, where measurement from LEDs is missing	+ = towards South - = towards North
55	Disp at top plate	mm	-	Displacement obtained from CH53 and CH54	+ = towards South - = towards North
56	Drift	%	-	$\frac{\text{CH55}}{\text{MarkersPosition}}$	+ = towards South - = towards North

graphs such as the shear force-average drift hysteresis of the wall. Table 6 defines these computed channels: CH53 was obtained by averaging the displacement from all LEDs glued onto the top steel plate. CH54 contains entries only when the optical measurements were missing, hence, when CH53 indicates a NaN-value (NaN=Not a Number). In this case, CH44 is taken as replacement and shifted in such a way as to remove any offsets between CH53 and CH54. The final displacement of the top plate of the wall is channel CH55, which assembles channels CH53 and CH54. CH56 stores the average drift which was obtained by dividing the displacement of the top plate (CH55) by the average height of the wall as obtained from LS0 measurements.

8.4.2 Processing of the optical measurement data

To remove any inherent noise, the optical measurement data was smoothed over a range of 50 data points using the Matlab-function ”smooth” [Mat10]. The coordinate system was then rotated and shifted to align the axes with the xy-axes as indicated in Fig. 10b. Finally, the data was synchronized with the processed conventional measurements. In order to have the same number of entries for the conventional and optical measurements, the measurement frequency of the optical measurements was reduced leading to 150–500 data points between peak displacements. LEDs that fell off during testing were identified and the corresponding entries were replaced by NaN-entries. NaN-entries were also assigned when LED-coordinates were not recorded. Finally, the LEDs were renumbered indicating the position of the LED by a row and a column number. The coordinate histories of each LED are stored in an ascii-file with three columns for the x-, y-, and z-coordinate.

The files are named ”LED_Rxx_Cyy.asc”, where xx corresponds to the row number and yy to the column number.

8.5 Data for material tests (QUM, TUM and WUM)

Data from the material tests was processed similar to the conventional data from the wall tests. Hence, all channels were set to zero at zero load and any bias or data that is not linked to the actual behavior of the test data was eliminated (e.g. offsets because conventional instruments were moved during testing).

9 Acknowledgments

The author thank Morandi Frères SA for the donation of the bricks and all engineers, technicians and students who helped with the laboratory testing. The author would like to thank in particular Salvatore Marino for his help during all wall tests and François Perrin for his help while mounting the test setup.

References

[CEN02] CEN. EN 1052-1: Methods of test for masonry, Part 1: Determination of compressive strength. Technical Report EN 1052-1:1998-12, European Committee for Standardisation, Brussels, Belgium, 2002.

[CEN07] CEN. EN 1052-3: Methods of test for masonry, Part 3: Determination of the initial shear strength. Technical Report EN 1052-3:2002+A1:2007 D, European Committee for Standardisation, Brussels, Belgium, 2007.

[HBM00] HBM. Catman data acquisition software. Technical report, Hottinger Baldwin Messtechnik GmbH, Darmstadt, Deutschland, http://www.hbm.com/en/menu/products/software/data-acquisition-software, 2000.

[Mat10] Matlab. Matlab version 7.10.0.499 (r2010a). Technical report, The Mathwork Inc., Natick, Massachusetts, United States, http://www.mathworks.ch, 2010.

[NDI11] NDI. Optotrak certus hd. Technical report, Northern Digital Inc., Waterloo, Ontario, Canada, http://www.ndigital.com/industrial/certushd.php, 2011.

[PB14a] Petry, S and Beyer, K. Cyclic test data of six unreinforced masonry walls with different boundary conditions. *Earthquake Spectra*, 2014.

[PB14b] Petry, S and Beyer, K. Scaling unreinforced masonry for reduced-scale seismic testing. *Bulletin of Earthquake Engineering*, 12:2557–2581, 2014.

[RIL91] RILEM. RILEM TC76-LUM: Diagonal tensile strength tests of small wall specimens. Technical Report TC76-LUM, RILEM Publications SARL, Brussels, Belgium, 1991.

Curriculum Vitae – Sarah Petry

PhD student – École Polytechnique Fédérale de Lausanne

CH-1024 Ecublens, Switzerland
Phone: +41-78-8460073
Email: sarah.petry@ymail.com
Born, 24-11-1984, in St. Martin d'Hères, France
Marial status: Married
Nationality: German

Education

École Polytechnique Fédérale de Lausanne [EPFL], Lausanne, Switzerland 2010-2014
- PhD, Earthquake Engineering and Structural Dynamics (to be accomplish End of 2014)

École des Ponts – ParisTech [ENPC], Paris, France 2008-2010
- Diplôme des Ponts, equivalent to M.Sc., French-German studies in Civil and Structural Engineering

Technische Universität München [TUM], Munich, Germany 2004-2010
- Vordiplom (03/2006, intermediate degree): 1,6 – level A, Civil and Structural Engineering
- Diplom, equivalent to M.Sc.: 1,4 – level A, Civil and Structural Engineering

Research Experience

École Polytechnique Fédérale de Lausanne [EPFL], Lausanne, Switzerland 2010-2014
PhD Project: Displacement capacity of unreinforced masonry (URM) walls
- Planning and execution of two test series of quasi-static tests on full- and half-scale URM walls
- Small-scale testing: review and recommendations for the use of hollow-brick masonry at reduced scale
- Cooperation on the planning and execution of a shake table test at the EUCENTRE, Italy, of a mixed four storey structure at half-scale
- Review and development of a kinematic model to determine the displacement capacity of URM walls

Technische Universität München [TUM], Munich, Germany 2006-2007
Centre and laboratory for hydromechanics
- Cooperation on a research programme for the determination of a cleaning process for stone mastic asphalt: numerical and physical simulations

Professional Experience

RFR Shanghai, Shanghai, China 2010

- Final year project (six months) - Pavilion and Façade Treatment of the Starhill Gallery in Kuala Lumpur, Malaysia
- Developing and optimization of 3D-model in GSA

AVLS, Acoustique Vibration Logiciel Scientifique, Paris, France 2009

- Two month internship as a civil engineer in structural dynamics

BBI, Bauer Beratende Ingenieure, Landshut, Germany 2007

- Two month internship as a structural engineer

Teaching Experience

École Polytechnique Fédérale de Lausanne [EPFL], Lausanne, Switzerland 2010-2014

- Teaching Assistant for the Master level course Earthquake Engineering
- Supervision of 3 Master thesis (2 out of 3 obtained the Prix Master SGEB for excellent Master Projects in the field of Earthquake Engineering)

Technische Universität München [TUM], Munich, Germany 2006-2009

- Tutorials for the mechanics lecture level I to III
- Tutorials for the hydromechanics lecture

Award

École Polytechnique Fédérale de Lausanne [EPFL], School of Architecture, Civil and Environmental Engineering (ENAC), PhD student award 2011, 2nd price

Journal Articles

- S. Petry and K. Beyer. Force-displacement response for in-plane loaded URM walls with a dominating flexural mode. *Submitted to Earthquake Engineering and Structural Dynamics September 2014.*
- K. Beyer, M. Tondelli, S. Petry and S. Peloso. Dynamic testing of a four-storey building with reinforced concrete and unreinforced masonry walls: Prediction and test results. *Submitted to Bulletin of Earthquake Engineering September 2014.*
- M. Tondelli, S. Petry, S. Peloso and K. Beyer. Dynamic testing of a four-storey building with reinforced concrete and unreinforced masonry walls: Data set. *Submitted to Bull Earthquake Eng September 2014.*
- S. Petry and K. Beyer. Limit states of modern unreinforced clay brick masonry walls subjected to seismic in-plane loading. *Special Issue of Vienna Congress 2013 in Bull Earthquake Eng September* 2014. DOI: 10.1007/s10518-014-9695-9
- S. Petry and K. Beyer. Cyclic test data of six unreinforced masonry walls with different boundary conditions, *Earthquake Spectra* 2014. DOI: 10.1193/101513EQS269
- S. Petry and K. Beyer. Scaling unreinforced masonry for reduced-scale seismic testing. *Bull Earthquake Eng* 2014; 12(6): 2557-2581. DOI: 10.1007/s10518-014-9605-1
- S. Petry and K. Beyer. Influence of boundary conditions and size effect on the drift capacity of URM walls. *Engineering Structures* 2014; 65: 76-88. DOI: 10.1016/j.engstruct.2014.01.048
- K. Beyer, M. Tondelli and S. Petry. Rütteltischversuche an einem Gebäude mit Mauerwerks- und Stahlbetonwänden (Shake table tests on a building with masonry and reinforced concrete walls), *Bauingenieur* 2013; 88(10): 2-7

International conference papers

- S. Petry and K. Beyer. Review and improvement of simple mechanical models for predicting the force-displacement response of URM walls subjected to in-plane loading. In *Proceedings of the 2nd European Conference on Earthquake Engineering and Seismology*, Istanbul, Turkey, 2014.
- S. Zhang, S. Petry and K. Beyer. Investigating the in-plane mechanical behavior of URM piers via DSFM. In *Proceedings of the 2nd European Conference on Earthquake Engineering and Seismology*, Istanbul, Turkey, 2014.
- K. Beyer, M. Tondelli, S. Petry and S. Peloso. Seismic response of a 4 storey building with reinforced concrete and unreinforced masonry walls, In *Proceedings of the 9th International Masonry Conference*, Guimarães, Portugal, 2014
- K. Beyer, M. Tondelli, S. Petry and S. Peloso. Seismic response of a 4 storey building with reinforced concrete and unreinforced masonry walls. In *Proceedings of the 9th International Masonry Conference*, Guimarães, Portugal, 2014.
- S. Petry and K. Beyer. Scaling unreinforced masonry structures with hollow-core clay bricks for laboratory testing. In *Proceedings of the Vienna Congress on Recent Advances in Earthquake Engineering and Structural Dynamics*, Vienna, Austria, 2013
- S. Petry and K. Beyer. Influence of coupling on the displacement capacities of URM piers – comparison of experimental results with existing recommendations. In *Proceedings of the Vienna Congress on Recent Advances in Earthquake Engineering and Structural Dynamics*, Vienna, Austria, 2013
- M. Tondelli, S. Petry, S. Peloso and K. Beyer. Shake-table test on a four-storey structure with reinforced concrete and unreinforced masonry walls. In *Proceedings of the Vienna Congress on Recent Advances in Earthquake Engineering and Structural Dynamics*, Vienna, Austria, 2013
- S. Petry and K. Beyer. Comparison of seismic tests on URM piers at half- and full-scale. In *Proceedings of the 12th Canadian Masonry Symposium*, Vancouver, Canada, 2013
- S. Petry and K. Beyer. Influence of the boundary conditions on the displacement capacity of URM piers. In *Proceedings of the 12th Canadian Masonry Symposium*, Vancouver, Canada, 2013
- S. Petry and K. Beyer. Testing unreinforced masonry structures at reduced scale. In *Proceedings of the 15th World Conference on Earthquake Engineering*, Lisbon, Portugal, 2012

Languages Written and Spoken

- German: Native proficiency
- French: Full professional proficiency
- English: Full professional proficiency
- Spanish: Limited working proficiency

Interests

Mountaineering, hiking, skiing
Horse-riding (more than 20 years of experience)
Cello (more than 15 years of experience) and Chorus singing
Dancing (salsa and saloon dances)
Cooking